

INFLUENCE OF GERMANIUM CONCENTRATION AND HOMOGENEOUS BORON
DOPING ON MICROSTRUCTURE, KINETICS, AND SHEET RESISTANCE OF NICKEL
GERMANOSILICIDE THIN FILMS

By

JOHN SAMUEL MOORE

A DISSERTATION PRESENTED TO THE GRADUATE SCHOOL
OF THE UNIVERSITY OF FLORIDA IN PARTIAL FULFILLMENT
OF THE REQUIREMENTS FOR THE DEGREE OF
DOCTOR OF PHILOSOPHY

UNIVERSITY OF FLORIDA

2008

© 2008 John Samuel Moore

In memory of Dr. Richard Connell. May all who teach aspire to his example.

ACKNOWLEDGMENTS

Life is a long journey, and one not traveled alone. On a personal level, I thank my family first and foremost. Without their love and support, this document would never have been possible. I also express gratitude to the innumerable teachers who have helped me through my 23 years of education. I particularly recognize some of my high school Advanced Placement English, science, and math teachers, Ms. Miles, Mrs. O'Connor, Mrs. Slotnick, and Mr. Lederberg, who gave me the tools and foundation for a successful undergraduate and graduate education. My thanks are also extended to the late Dr. Richard Connell, for whom this work is dedicated, for being an outstanding professor and role model throughout my undergraduate degree. My dear friend and staunch supporter, Dr. Michelle Phen, is also acknowledged for her unending assistance with the development and editing of this work.

On a professional level, I thank Hans Weijtmans and Dr. Mark Visokay, formerly of Texas Instruments, Inc., for growing the experimental structures used in this work. I also thank the staff, especially Kerry Siebein and Dr. Jerry Bourne, of the Major Analytical Instrumentation Center (MAIC) at the University of Florida for their assistance in TEM and SEM sample analysis. I also thank Mikhail Klimov of AMPAC at the University of Central Florida for his assistance with the SIMS analysis presented in this work. I also acknowledge the staff and students of the Software and Analysis of Advanced Materials Processing (SWAMP) research group and my advisory committee for their assistance with this work.

TABLE OF CONTENTS

	<u>page</u>
ACKNOWLEDGMENTS	4
LIST OF TABLES	8
LIST OF FIGURES	9
ABSTRACT	13
CHAPTER	
1 INTRODUCTION	15
1.1 Device Interconnections and Silicides	15
1.2 Silicon-Germanium in Semiconductor Technologies	17
1.2.1 Low Resistivity Junctions	17
1.2.2 Uniaxially Strained Devices	18
1.3 Nickel as a Silicidation Metal	19
1.4 Motivation of This Work	20
2 LITERATURE SURVEY	25
2.1 Binary Systems	25
2.1.1 Silicon-Germanium Binary System	25
2.1.2 Nickel-Silicon Binary System	25
2.1.3 Nickel-Germanium Binary System	26
2.2 Ternary System: Ni-Si-Ge	28
2.2.1 Physical Properties	28
2.2.2 Phase Diagram	28
2.2.3 Microstructure	29
2.2.3.1 Initial film formation	30
2.2.3.2 Film agglomeration	31
2.2.4 Sheet Resistance	34
2.2.5 Influential Variables	34
2.2.5.1 Silicon-germanium layer strain and thickness.	35
2.2.5.2 Germanium content of $\text{Si}_{1-x}\text{Ge}_x$ layer	36
2.2.5.3 Crystalline quality of the $\text{Si}_{1-x}\text{Ge}_x$ layer.	37
2.2.5.4 Nickel layer thickness.	38
2.2.5.5 Implanted Dopants.	39
2.2.5.6 In-situ Doping.	40
2.3 Outstanding Issues	42
3 DESIGN OF EXPERIMENTS	68
3.1 Research Objectives	68

3.2 Factors and Levels	69
3.2.1 Factors Altered	69
3.2.2 Factors Held Constant	70
3.3 Experimental Structure	71
3.4 Characterization Techniques	71
3.4.1 Cross-Section Transmission Electron Microscopy	72
3.4.2 Scanning Electron Microscopy.....	73
3.4.3 Electron Dispersive Spectroscopy.....	75
3.4.4 Secondary Ion Mass Spectroscopy.....	76
3.4.5 Four Point Probe.....	77
3.4.6 Image Processing and Quantification.....	79
3.4.7 Statistical Analysis	81
3.5 Analysis of As-Grown Samples.....	83
4 INFLUENCE OF GE, B ON MICROSTRUCTURE AND KINETICS	91
4.1 Analysis using XTEM/EDS.....	92
4.2 Plan View SEM Analysis	94
4.2.1 Phase Identification using EDS.....	95
4.2.2 Imaging and Phase Quantification using SEM/BSE	95
4.2.2.1 Influence of Ge content.....	97
4.2.2.2 Influence of B content.....	98
4.3 Reaction Kinetics.....	101
4.3.1 Reaction Order.....	103
4.3.1.1 Precipitation reaction.....	105
4.3.1.2 Agglomeration reaction.....	106
4.3.2 Activation Energy.....	106
4.3.2.1 Precipitation reaction.....	107
4.3.2.2 Agglomeration reaction.....	109
4.4 Summary.....	110
5 RELATIONSHIP OF SHEET RESISTANCE AND MICROSTRUCTURE AND THE INFLUENCE OF GE AND B	134
5.1 Sheet Resistance Analysis	135
5.1.1 Influence of Ge	136
5.1.2 Influence of B	137
5.2 Sheet Resistance/Microstructure Relationship	138
5.2.1 Stage I (Precipitation).....	141
5.2.1.1 Influence of Ge.....	141
5.2.1.2 Influence of B.....	143
5.2.1.3 Tortuosity Analysis	144
5.2.2 Stage II (Agglomeration).....	147
5.2.2.1 Influence of Ge.....	147
5.2.2.2 Influence of B.....	148

5.2.3 Boron Conduction Path	150
5.2.3.1 Potential Conduction Paths	151
5.2.3.2 Evaluation of Potential Paths	153
5.3 Summary.....	155
6 CONCLUSIONS AND FUTURE WORK	183
6.1 Conclusions.....	183
6.1.1 Microstructure and Kinetics	183
6.1.2 Structure/Property Relationship	185
6.1.3 Influence of Homogeneous B Doping.....	186
6.2 Future Work.....	187
APPENDIX	
A ERROR IN SEM/BSE IMAGE QUANTIFICATION	189
B GAUGE REPEATABILITY AND REPRODUCIBILITY ANALYSIS OF 4PP MEASUREMENT.....	193
C AVRAMI PLOT ERROR	198
LIST OF REFERENCES.....	200
BIOGRAPHICAL SKETCH	205

LIST OF TABLES

<u>Table</u>	<u>page</u>
1-1: Properties of common silicides used in silicide processing.....	24
2-1: Measurement of average Ni(Si _{1-x} Ge _x)/Si _{1-x} Ge _x interface roughness for undoped and B-doped samples calculated via AFM after annealing at 400 and 500 °C for 30 seconds	67
3-2: Results from SIMS analysis of as-grown samples	90
4-1: Linear regression results for isothermal transformation curves plotted on a graphs of log(log(1/(1-AF))) vs. log(t) for the precipitation reaction.....	130
4-2: Values of n (reaction order) for reactions obeying Avrami kinetics	131
4-3: Linear regression results for isothermal transformation curves plotted on a graphs of log(log(1/(1-AF))) vs. log(t) for the agglomeration reaction.....	132
4-4: Activation energies derived from linear regression of series on the plot of ln(k) vs. (1/KT)	133
5-1: Linear regression results for best fit lines shown for Stage I (precipitation reaction) in Figure 5-9.....	179
5-2: Stage I (precipitation reaction) linear regression results for the compiled undoped and doped data shown in Figure 5-11.....	180
5-3: Measurements of Si _{1-z} Ge _z area fraction, tortuosity, and sheet resistance for selected undoped and doped 25% Ge samples.	181
5-4: Regression results for Stage II (agglomeration reaction) best fit lines shown in Figure 5-15.....	182

LIST OF FIGURES

<u>Figure</u>	<u>page</u>
1-1: Diagram and SEM image of Si diffusion into Al	21
1-2: Salicide process flow	22
1-3: Cross-section of uniaxially strained device showing Si recess etch, SiGe epitaxial growth, and image of actual device	23
2-1: Binary phase diagram of Si-Ge system showing complete solid solubility of Si and Ge in the solid phase.....	43
2-2: Binary phase diagram of Ni-Si System.	44
2-3: Schematic of the evolution of Ni-Si binary system on thermal annealing	45
2-4: XRD results plotting the squared normalized intensity of characteristic diffraction peaks for Ni, Ni ₂ Si, and NiSi as a function of anneal time.....	46
2-5: Sheet resistance of nickel silicide samples as a function of annealing temperature and initial Ni layer thickness	47
2-6: Binary phase diagram of the Ni-Ge system.....	48
2-7: XRD results plotting the squared normalized intensity of characteristic diffraction peaks for Ni, Ni ₅ Ge ₃ , and NiGe as a function of anneal time.....	49
2-8: Sheet resistance of Ni-Ge system as a function of annealing temperature for two initial Ni layer thicknesses	50
2-9: Free energy for a system of one gram-atom of NiSi _{0.5} Ge _{0.5} in contact with one gram-atom of Si _{0.5} Ge _{0.5} at 600 °C as a function of w (fraction of Ge atoms transferred from NiSi _{1-x} Ge _x to Si _{1-x} Ge _x)	51
2-10: Partial isotherms calculated for the Ni-Si-Ge ternary system	52
2-11: Partial isotherms calculated for the Ni-Si-Ge ternary system without inclusion of the NiSi ₂ phase.....	53
2-12: Partial calculated isotherm at 600 °C showing the initial and final equilibrium state for one gram-atom of NiSi _{0.5} Ge _{0.5} in contact with one gram-atom of Si _{0.5} Ge _{0.5}	54
2-13: XRD θ -2 θ scans showing evolution of Ni-Si-Ge system for 60 second RTAs from 300-500 °C	55
2-14: Cross-section TEM images of Ni-silicided Si _{1-x} Ge _x films annealed at 400 °C for 60 seconds.....	56

2-15: Analysis of films annealed at 500 °C including HRXTEM	57
2-16: XTEM images of Ni(Si _{0.75} Ge _{0.25}) films annealed for 60 seconds	58
2-17: Plan-view SEM analysis of Ni(Si _{0.9} Ge _{0.1}) grains annealed for 30 seconds at temperatures ranging from 650 to 750 °C.....	59
2-18: AES maps of Ge, Ni, and Si for Ni(Si _{0.75} Ge _{0.25}) samples annealed at 500, 700, and 900 °C for 60 seconds	60
2-19: Sheet resistance of single crystal Si _{1-x} Ge _x (x = 0, 10, 20 at %Ge) layers silicided with 25 nm of Ni for 30 seconds as a function of annealing temperatures.....	61
2-20: Sheet resistance of nickel germanosilicide films as a function of anneal temperatures for samples with varying initial Si _{1-x} Ge _x film strain.....	62
2-21: Plan-view SEM images of nickel germanosilicide samples with varying concentrations of Ge annealed at 650, 700 and 750 °C for 60 seconds	63
2-23: Plan-view SEM images of nickel germanosilicide films on As and B implanted single-crystal Si _{1-x} Ge _x	65
2-24: Sheet resistance of As and B doped nickel germanosilicide films as a function of anneal temperature	66
3-1: SEM/BSE image from this work.....	85
3-2: Examples of images from this work before and after Image J threshold operation	86
3-3: Example tortuosity measurement	87
3-4: XTEM image of sample from as-grown wafer with x = 25 at% Ge and no B doping.....	88
4-1: On-axis <110> XTEM images of 25% Ge samples annealed at 450 °C for 10 minutes.....	112
4-2: On-axis <110> images of 25% Ge samples with and without B doping annealed at 550 °C for 10 or 1020 minutes.....	113
4-3: XTEM images taken at 10° tilt from <110> zone axis of undoped and doped 25% Ge samples RTA annealed at 600 °C for 60 seconds	114
4-4: SEM images of undoped 25% Ge sample after 1020 minute anneal at 550 °C in SE and BSE modes.....	115
4-5: SEM/BSE images of samples annealed at 450 °C.....	116
4-6: SEM/BSE images of samples annealed at 550 °C.....	117
4-7: SEM/BSE images of samples annealed at 650 °C.....	118

4-8: SEM/BSE images of samples annealed at 750 °C.....	119
4-9: Area fraction of Ge-rich Si _{1-z} Ge _z phase as a function of anneal time at temperatures of 450, 500, and 650 °C.....	120
4-10: Paired t-test results (n=36) comparing the Ge-rich Si _{1-z} Ge _z area fraction of 15 and 25% Ge samples at all points on the thermal matrix imaged with SEM/BSE.	121
4-11: Area fraction of Ge-rich Si _{1-z} Ge _z phase as a function of anneal time at temperatures of 450, 500, and 650 °C.....	122
4-12: Paired t-test results (n=36) comparing the undoped and doped samples at all conditions imaged with SEM/BSE.....	123
4-13: Plot of log(log(1/(1-AF))) vs. log(t) for samples containing 15% Ge.....	124
4-14: Plot of log(log(1/(1-AF))) vs. log(t) for samples containing 25% Ge.....	125
4-15: Plot of area fraction of initial Ni(Si _{1-x} Ge _x) phase present as a function of Ge-rich Si _{1-z} Ge _z area fraction.	126
4-16: Plot of log(log(1/(1-AF))) vs. log(t) for Ge-rich Si _{1-z} Ge _z area fractions less than 60%.....	127
4-17: Plot of log(log(1/(1-AF))) vs. log(t) for Ge-rich Si _{1-z} Ge _z area fractions greater than 60%.....	128
4-18: Plots of ln(k) vs. 1/(kT).....	129
5-1: Isochronal anneal series of sheet resistance of undoped 15 and 25% Ge samples.....	158
5-2: Isochronal anneal series of sheet resistance of doped 15 and 25% Ge samples.....	159
5-3: Isochronal anneal series of sheet resistance of undoped and doped 15% Ge samples.....	160
5-4: Isochronal anneal series of sheet resistance of undoped and doped 25% Ge samples.....	161
5-5: Plot of sample sheet resistance vs. Si _{1-z} Ge _z grain size.	162
5-6: Plot of sample sheet resistance vs. area fraction of Ni(Si _{1-u} Ge _u) or Si _{1-z} Ge _z	163
5-7: Plot of sample sheet resistance vs. area fraction of Si _{1-z} Ge _z	164
5-8: Plot of sample sheet resistance vs. area fraction of Si _{1-z} Ge _z for the precipitation stage (Stage I) of the transformation.....	165
5-9: Plot of Stage I sample sheet resistance vs. area fraction of Si _{1-z} Ge _z for undoped and doped samples.....	166
5-10: Plot of Stage I linear regression intercept and slope of the results given in Table 5-1.....	167

5-11: Plot of Stage I sample sheet resistance vs. area fraction of $\text{Si}_{1-z}\text{Ge}_z$ for all samples.....	168
5-12: Plot of linear regression intercept and slope of the results given in Table 5-2	169
5-13: Image of an undoped 25% Ge sample annealed at 450 °C for 1020 minutes before and after ImageJ processing.....	170
5-14: Plots of conductive path tortuosity vs. area fraction $\text{Si}_{1-z}\text{Ge}_z$ and sample sheet resistance vs. tortuosity for selected undoped and doped 25% Ge samples	171
5-15: Sheet resistance of undoped and doped 15 and 25% Ge samples as a function of $\text{Si}_{1-z}\text{Ge}_z$ area fraction for the agglomeration stage (Stage II) of the film transformation.....	172
5-16: Sheet resistance as a function of $\text{Si}_{1-z}\text{Ge}_z$ area fraction for all samples in Stage II (agglomeration) of the film transformation.	173
5-17: SEM/BSE images of undoped 25% Ge samples annealed at 650 °C or 750 °C for 10 minutes before and after ImageJ processing.....	174
5-18: SIMS analysis results of B doping distribution after silicidation with Ni metal showing silicidation induced dopant segregation.....	175
5-19: XTEM and SIMS analysis results for doped 25% Ge sample annealed at 450 °C for 10 minutes.....	176
5-20: Cartoon schematics of nickel germanosilicide samples exhibiting segregation induced dopant segregation	177
5-21: Isochronal anneal series of doped 15% Ge samples with calculated sheet resistance values for the potential alternative conduction paths.....	178
A-1: Individual plot results divided by sample and region for area fraction of Ni-rich phase and area fraction of Ge-rich SiGe phase.....	191
A-2: Minitab results for fully nested ANOVA results for area fraction of Ni-rich phase and area fraction of Ge-rich SiGe phase.....	192
B-1: Gauge R&R ANOVA analysis of sheet resistance measurements for the five samples which all operators measured successfully in all trials.....	195
B-2: Gauge R&R ANOVA analysis of sheet resistance measurements including data from all 10 samples for the operator who successfully measured all samples for all trials.	196
B-3: Gauge R&R ANOVA analysis of sheet resistance measurements, excluding data from sample 9, for the operator who successfully measured all samples for all trials.....	197
C-1: Transformed error range for a constant +/- 3.35% range of area fraction as a function of nominal area fraction.....	199

Abstract of Dissertation Presented to the Graduate School
of the University of Florida in Partial Fulfillment of the
Requirements for the Degree of Doctor of Philosophy

INFLUENCE OF GERMANIUM CONCENTRATION AND HOMOGENEOUS BORON
DOPING ON MICROSTRUCTURE, KINETICS, AND SHEET RESISTANCE OF NICKEL
GERMANOSILICIDE THIN FILMS

By

John Samuel Moore

August 2008

Chair: Kevin Jones

Major: Materials Science and Engineering

This work studied the influence of Ge concentration and homogeneous B doping on the microstructure, kinetics, and sheet resistance of nickel germanosilicide thin films. Experimental structures consisted of 150 nm of single crystal relaxed $\text{Si}_{1-x}\text{Ge}_x$ ($x = 15$ or 25 at%) layers with and without in-situ homogeneous B doping of $4.5\text{E}19$ atoms/ cm^2 and capped by 10 nm of sputtered Ni metal. Samples were furnace annealed under a N_2 atmosphere at temperatures between 450 and 800 degrees Celsius in 50 degree increments for times of 10, 30, 90, 270, and 1020 minutes.

Microstructure analysis showed that increasing Ge content increased the amount of film transformation while the addition of B doping had no effect on morphology. Distinct reactions were observed before and after full consumption of the parent $\text{Ni}(\text{Si}_{1-x}\text{Ge}_x)$ film during kinetic analysis of isothermal transformation curves. The first reaction, in which Si-rich $\text{Ni}(\text{Si}_{1-u}\text{Ge}_u)$ and Ge-rich $\text{Si}_{1-z}\text{Ge}_z$ were found to precipitate from the $\text{Ni}(\text{Si}_{1-x}\text{Ge}_x)$ film, was determined to have concentration dependant activation energies of 1.96 and 0.76 eV for the 15 and 25% Ge samples, respectively. In this stage, the sheet resistance was found to linearly increase with increasing area fraction of $\text{Si}_{1-z}\text{Ge}_z$ for all samples. The cause for the increase was determined to

be related to the conductive path tortuosity. Increasing Ge content did not affect the structure/property relationship, but the addition of B caused a decrease in sheet resistance. The second reaction, in which $\text{Ni}(\text{Si}_{1-u}\text{Ge}_u)$ grains were found to agglomerate after the $\text{Ni}(\text{Si}_{1-x}\text{Ge}_x)$ layer was fully consumed, was determined to have an activation energy of 0.125 eV for both the 15 and 25% Ge samples. The undoped samples in this stage were found to have uniformly very high sheet resistance values. This result was attributed to the lack of a conduction path between isolated $\text{Ni}(\text{Si}_{1-u}\text{Ge}_u)$ grains. A strong linear relationship, however, was determined for the doped samples, and increasing Ge content had a small effect on the relationship for these samples. It was determined that the stabilizing influence of B doping was caused by the availability of a conduction path through the unreacted doped $\text{Si}_{1-x}\text{Ge}_x$ layer.

CHAPTER 1 INTRODUCTION

Nickel germanosilicides are formed when Ni metal and SiGe compounds react during thermal processing. They are predominantly of interest to semiconductor technology where they are used as an intermediate layer between devices and metal device interconnections. This work investigates the influence of Ge content and in-situ B doping on the thermal stability of nickel germanosilicides. The following sections in this chapter discuss why interconnections and intermediate layers (silicides) are needed, why SiGe and in-situ B doping of the SiGe are used in modern device designs, and why Ni metal is of interest as a silicidation metal.

1.1 Device Interconnections and Silicides

For modern microprocessor designs, tens of millions of individual transistors must be linked together to form a single processor. The interconnections are made using complex, interconnected, multi-layered patterns of metal. The metal must also be connected to the source, gate, and drain contacts of each transistor. Direct contact, however, between the semiconductor and the metal- such as that between Al and Si- can lead to the formation of Schottky barriers which impede the flow of charge carriers. The height of the barrier depends upon the work function difference between the semiconductor and the metal. Thus, barrier height is a function of the materials selected and will vary from system to system. Regardless, Schottky barriers degrade device performance by requiring electrons or holes to overcome an energy barrier as they pass across the interface, raising overall circuit resistance and decreasing the time constant (switching speed) of the device. The thermal stability of a metal-semiconductor interface may also be poor and lead to failure of the device. In the Al-Si system at 450-500 °C, the solubility of Si in Al is between 0.5 and 1.0 at% [Mey90]. As shown in Figure 1-1(a), Si therefore diffuses

from the substrate into the Al layer, creating pits in the silicon substrate. These pits, shown in a Scanning Electron Microscopy (SEM) image in Figure 1-1(b), can disrupt device function.

Alternatively, an intermediate layer may be used to form low-resistance Ohmic contacts (or Schottky contacts with known, lower, barrier heights) between the substrate, silicide, and metal. Depending upon the materials selected, use of an intermediate layer can also result in improved interface stability. To form the intermediate layer, a layer of metal is deposited onto a semiconductor substrate where electrical contact is to be made. The metal, which is often different than that used for interconnection, is then diffused into the substrate using a thermal anneal. This results in the formation of a metal-semiconductor compound called, in the case of a Si substrate, a silicide (alternatively, for a Ge substrate, a germanicide). Depending on the metal and substrate, one or more stoichiometric compounds are possible, and more than one stoichiometric compound may be initially formed.

One method of forming silicides is called a “salicide” (self-aligned silicide) process. Figure 1-2 presents a simplified salicide process flow. The process flow begins once the device’s gate, source, drain, and SiO₂ isolation has been fabricated. First, a metal layer is uniformly deposited over entire structure, usually by a sputtering technique. Second, a thermal anneal produces silicides at any metal/silicon interface. Metal not in contact with Si does not react (hence the self-aligned nature of the technique). Once the silicide has been formed, the remaining unreacted metal is removed using a selective etch.

Once formed, however, silicide layers (or germanicide, etc.) are subjected to additional thermal processing during the remaining fabrication of the device. It is important, therefore, to understand how the silicide may react or evolve due to subsequent thermal processing. For example, when NiSi is annealed to temperatures above ~700 °C a phase transformation from

NiSi to NiSi₂ occurs and increases the resistance of the silicide [Gam98]. For other silicides, such as TiSi₂, additional thermal processing can cause the agglomeration of silicide grains that also results in higher resistivity contacts [Gam98]. Thus, knowledge of the thermal stability of a silicide is very important to process design.

1.2 Silicon-Germanium in Semiconductor Technologies

Silicon-Germanium (SiGe or, more specifically, Si_{1-x}Ge_x where x = at% Ge) are alloys of varying atomic ratios of Si and Ge which are used in some semiconductor applications. The properties of these alloys will be discussed in further depth in the following chapter. SiGe is used for a variety of applications including photodiodes [Hua95], work-function-tunable gates [Hel97, Pon00], and SiGe-channel heterojunction MOSFETs [Pea86, Ver94]. This work, however, will focus on the use of SiGe in p-MOSFET logic technologies.

1.2.1 Low Resistivity Junctions

As critical device dimensions for MOSFET logic technology decreased below 130 nm, new methods of forming shallow, low-resistance source/drain regions became necessary [NTR97]. To overcome this problem, Raaijmakers et al. suggested the use of elevated source/drain regions that would provide shallow junction depth and low sheet and contact resistance [Raa99]. The raised regions, formed by selective epitaxial growth of in-situ B doped Si above the contact region of the device, would also act as a sacrificial layer during silicidation. Raaijmakers et al. also suggested that Ge should be added to the elevated source/drain region for several reasons. First, the amount of electrically active B in SiGe alloys can be larger than that in pure Si [Hel97b, Sal97, Man98]; higher concentrations of active dopant leads to lower contact resistance to the silicide. In situ doping of the SiGe alloys also allows the elimination of an activation anneal as most of the dopant is incorporated in substitutional positions (electrically active) [Hel97b]. This effect, which is stable, is due to substitutional B compensating lattice

strain in the SiGe alloy. Second, the addition of Ge has been shown to shift the valence band of the region to higher energy, decreasing Schottky barrier height and improving device performance [Hel97b].

Further work, by Gannavaram et al., suggested using an isotropic Si plasma etch to define the extension junction recess [Gan00]. The recess would then be filled using in situ B doped epitaxial deposition of SiGe, maintaining the previously discussed benefits. Ozturk et al. suggested that this technology could meet the demands of future technology nodes as small as 30 nm [Ozt01]. Isotropic plasma etching, however, can damage the Si substrate and result in defect formation at the Si/SiGe interface. Loo et al. proposed an alternative etch technique using HCL chemical vapor etching which produces defect-free epitaxial in situ doped SiGe regions [Loo04]. This work also confirmed the benefits of Ge addition and in situ B doping on source/drain contact resistance.

1.2.2 Uniaxially Strained Devices

The possible benefits of the embedded process proposed by Gannavaram et al. led Intel Corporation to evaluate the technology for use in commercial process flows [Tho06]. The technology, however, resulted in larger than expected performance enhancement. The additional enhancement was attributed to uniaxial compressive channel stress induced by the SiGe wells [Tho02]. Uniaxial stress causes improved hole mobility at both low strain and high vertical electric fields due to the reduction in effective mass from the warping of the Si valence band under strain [Tho04, Uch06]. Improved mobility, in turn, improves the switching speed of the device [Mei04, Won04, Aub05, Lee05, Web05]. A more in-depth discussion of strained-Si technology can be found in a review by Thompson et al. [Tho06].

Uniaxial strained silicon technology, therefore, has been introduced into commercial use for 90nm logic technologies [Tho02]. A cross-section of a strained-Si device is shown in Figure

1-3. While first-generation devices used ~17 at% Ge in the source/drain region, future generation designs will likely increase the Ge concentration and bring the recessed region closer to the channel [Bai04, Chi04, Tho06]. Additionally, by in situ doping of the SiGe region with B, the benefits discussed in the previous section may be maintained.

1.3 Nickel as a Silicidation Metal

A number of metals have been researched as candidates for use as a silicidation metal for both salicide and other processes. Table 1-1 presents important properties of silicides commonly used in salicide processes. Both TiSi_2 and CoSi_2 have been used in commercially produced products. TiSi_2 has several benefits including low resistivity, relatively high thermal stability, and the ability to reduce native oxides due to the high solubility of oxygen in Ti [Iwa85, Bar87 Mass90]. High temperature anneals ($>800\text{ }^\circ\text{C}$), however, are required to form the lowest conductivity C54 phase. Even higher formation temperatures are reported to be required as silicide thickness decreases, as linewidth decreases, and as the concentration on n-type dopants increases [Las91, Gan93, Mae93].

An alternative silicide is CoSi_2 , which shares a similar resistivity and thermal stability to TiSi_2 . The sheet resistance of CoSi_2 , however, is relatively insensitive to decreasing linewidth [Las91, Mae93] and CoSi_2 can be used as a dopant diffusion source to form shallow junctions [Las91, Jia92a, Jia92b, Jia92c]. Disadvantages of CoSi_2 in relation to TiSi_2 include consumption of more Si to produce an equivalent sheet resistance and the need for better surface preparation, as CoSi_2 does not reduce interfacial oxides. Though lower than that required for TiSi_2 , a relatively high temperature anneal ($600\text{-}800\text{ }^\circ\text{C}$) is also required to form the lowest resistance phase [Gam98].

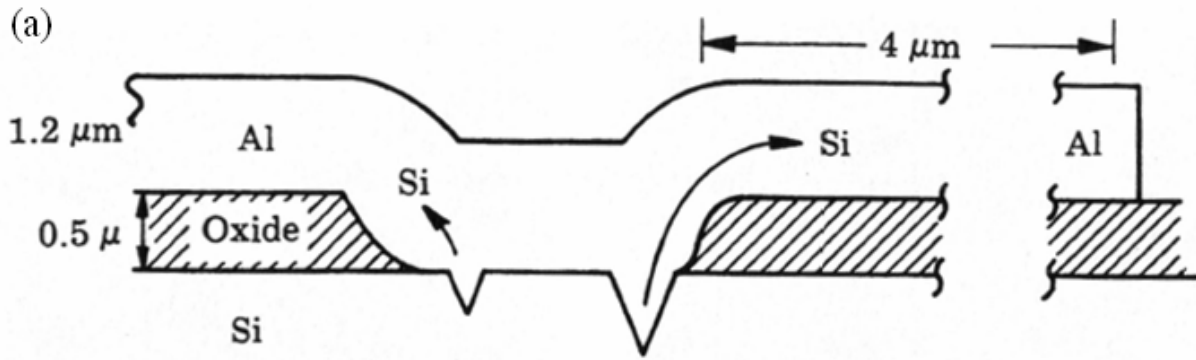
A third option for a silicidation metal is Ni, forming NiSi . NiSi has a low resistivity, with sheet resistance comparable to both of the previously discussed silicides. As with CoSi_2 , the

sheet resistance of the silicide is also relatively insensitive to linewidth. Furthermore, the formation of NiSi requires less Si consumption than either TiSi₂ or CoSi₂ which allows the formation of much shallower contacts [Gam98]. Finally, NiSi can be formed in a one-step anneal at much lower temperatures (400-600 °C) than either TiSi₂ or CoSi₂. Disadvantages of NiSi include poor thermal stability including transformation to relatively high resistivity NiSi₂ at temperatures around 700 °C. Further comparisons of NiSi, TiSi₂, and CoSi₂ are available in the review articles by Gambino et al. [Gam98] and Iwai et al. [Iwa02].

1.4 Motivation of This Work

Individual transistors (and other devices) must be linked together to form a working unit through the use of metal interconnections. The interconnections and the semiconductor substrate can react, however, to form barriers to charge carrier flow and may also have poor thermal stability. To prevent this, intermediate layers called silicides are used to decrease (or eliminate) barrier height and improve interface stability. Most commonly, silicides are formed on the source, drain, and gate regions of a semiconductor device through the use of a silicide process.

Recent developments in semiconductor technology suggest that the addition of Ge to the source/drain contact regions of the device can provide increased dopant solubility and activation. The use of embedded SiGe source/drain contacts also strains the channel of the device, leading to additional performance gains. Due to a large number of benefits, there is also interest in the use of nickel as a silicidation material. Thus, it is of particular interest to determine how the introduction of Ge into the source/drain well will affect the Ni silicidation of these regions and to determine if in situ B doping of the regions impacts the silicidation process. While investigation of this topic has already begun (and will be discussed in the next chapter), questions remain about the behavior of nickel germanosilicides. The motivation of this work, therefore, is to answer some of these outstanding questions.



$T_{\text{anneal}} \cong 450^\circ\text{C}$

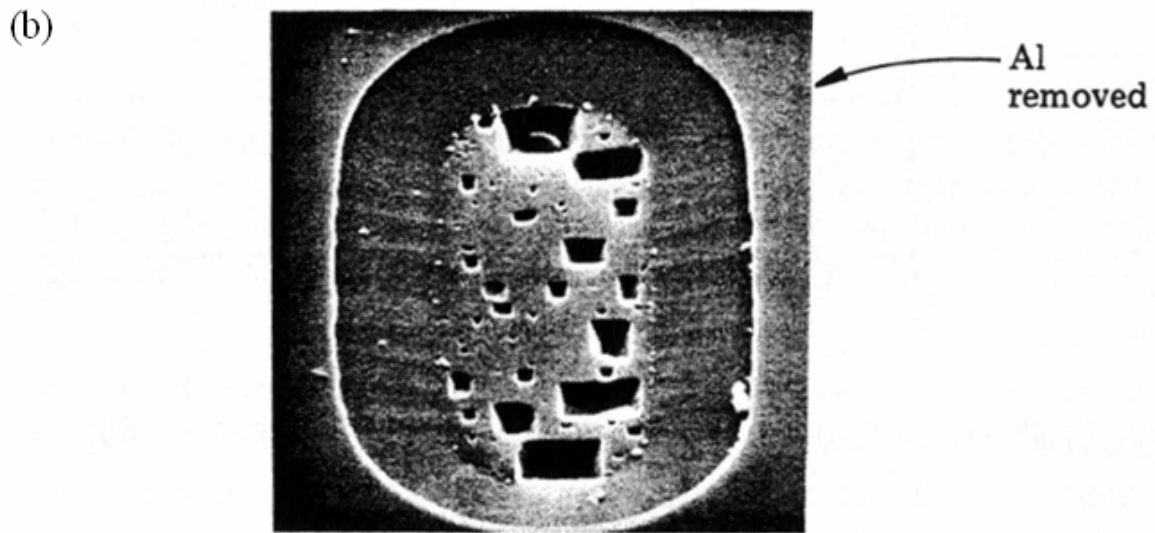


Figure 1-1: (a) Diagram showing diffusion of Si into Al and subsequent pit formation in the Si substrate (b) SEM image of pits in Si substrate after removal of Al layer. [Mey90]

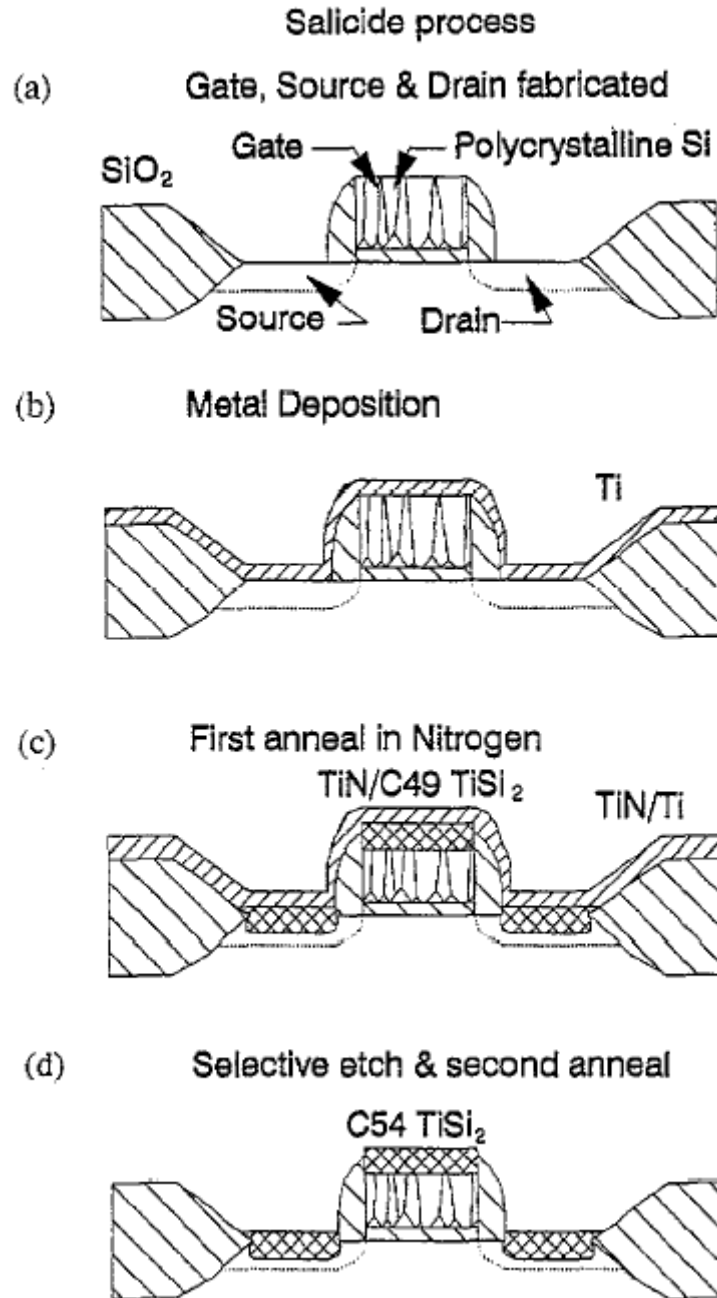


Figure 1-2: Salicide process flow (a) device with gate, source, drain, and SiO_2 isolation fabricated (b) deposition of Ti layer over entire structure (c) thermal anneal under N_2 ambient producing silicides at metal/silicon interfaces (cross-hatched regions) (d) device after selective etch to remove unreacted metal. [Gam98]

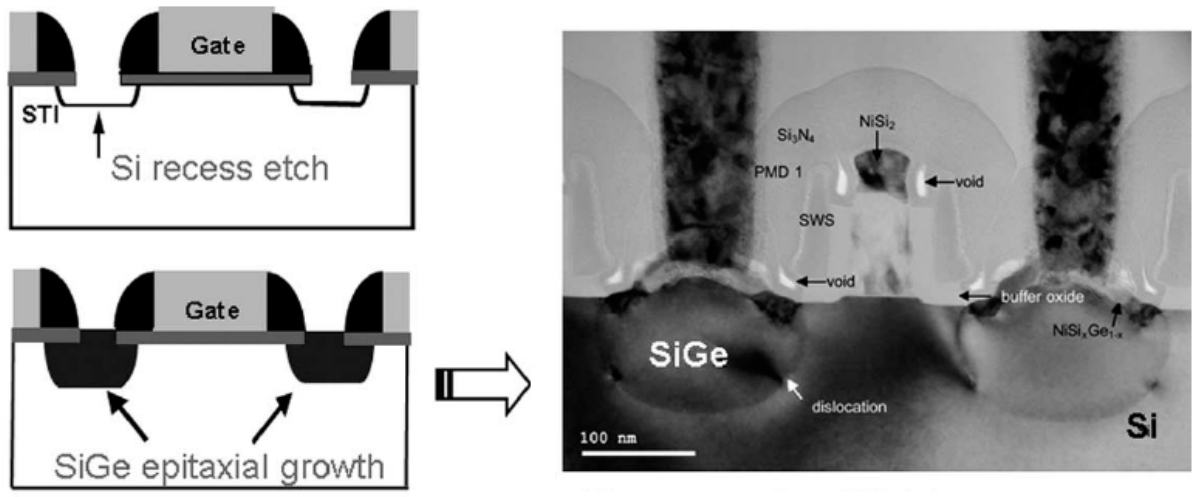


Figure 1-3: Cross-section of uniaxially strained device showing Si recess etch, SiGe epitaxial growth, and image of actual device [Tho06]

Table 1-1: Properties of common silicides used in salicide processing [Gam98].

Silicide	CoSi ₂	Pd ₂ Si	PtSi	NiSi	NiSi ₂	TiSi ₂
Thin film resistivity ($\mu\text{ohm-cm}$)	14-20	25-35	28-35	14-20	35-50	13-20 C54-TiSi ₂
Si consumed per nm of metal (nm)	3.6	0.7	1.3	1.8	3.6	2.3
Formation temperature ($^{\circ}\text{C}$)	600-700	200-500	300-600	400-600	600-700	600-700
Melting temperature ($^{\circ}\text{C}$)	1326	1394	1229	992	992	1500
Eutectic temperature ($^{\circ}\text{C}$)	1204	816	830	964	964	1330
Schottky barrier height on n-type Si	0.64	0.74	0.87	0.67	0.7	0.6
B.p. of most volatile fluoride ($^{\circ}\text{C}$)	CoF ₂	PdF ₂	PtF ₆	NiF ₂	NiF ₂	TiF ₄
	1400	red heat	58m	1000s	1000s	284s
B.p. of most volatile chloride ($^{\circ}\text{C}$)	CoCl ₂	PdCl ₂	PtCl ₃	NiCl ₂	NiCl ₂	TiCl ₄
	1049	500d	435m	973s	973s	136
B.p. of most volatile bromide ($^{\circ}\text{C}$)	CoBr ₂	PdBr ₂	PtBr ₄	NiBr ₂	NiBr ₂	TiBr ₄
	678		180d	963	963	230

CHAPTER 2 LITERATURE SURVEY

The ternary Ni-Si-Ge system includes three binary systems: Si-Ge, Ni-Si, and Ni-Ge. Knowledge of the properties of the three binary systems will allow a deeper understanding of the properties seen in the ternary. Thus, each of these four systems will be discussed in this chapter, with emphasis on the microstructural evolution and electrical properties of the ternary system.

2.1 Binary Systems

2.1.1 Silicon-Germanium Binary System

The binary phase diagram of the Si-Ge system is shown in Figure 2-1. It can be seen from this diagram that Si and Ge form a complete solid solution across all compositions of the alloy. This is due to the satisfaction of the Hume-Rothery rules: the two elements share the same diamond cubic crystal structure and valence state and have similar values of electronegativity and atomic diameter. The properties of SiGe vary between those of Si and Ge. For some properties, such as lattice parameter, the values vary linearly between that of Si and Ge in accordance with Vegard's Law [Dis64]. For other properties, such as the melting point seen in Figure 2-3, the relationship is nonlinear.

2.1.2 Nickel-Silicon Binary System

The binary phase diagram of the Ni-Si system is shown in Figure 2-2. Six intermediate compounds are evident in the diagram ranging in composition from Ni-rich Ni_3Si to Si-rich NiSi_2 [Mey90]. Kinetically, however, only three compounds are of interest when Si is present in excess amounts (as is the case during silicidation reactions): Ni_2Si , NiSi , and NiSi_2 [Gas98, Nem06]. The evolution of these phases from the initial layers is shown schematically in Figure 2-3. Generally speaking, when a thin Ni layer is annealed in contact with excess Si the Ni_2Si phase forms until all Ni metal is consumed. This reaction begins around 210 °C [Nem06]. Once

all Ni metal has been consumed, the Ni_2Si phase reacts with the Si substrate to produce NiSi. These reactions are sequential; NiSi does not form until all Ni metal has reacted to form Ni_2Si . Experimental observation of the transitions are reported by Nemouchi et al. [Nem06] and shown in Figure 2-4. Upon annealing above $\sim 700^\circ\text{C}$, NiSi transforms to NiSi_2 [dHe82, dHe89]. While other intermediate phases may appear during the reaction, the presence of these phases is transient and usually neglected [Lav03, Ger04, Nem06]. The reaction rates of these transformations (measured as a function of layer thickness) have been found to be proportional to linear time (surface reaction controlled) or the square root of time (diffusion controlled) [Mey90]. The formation of NiSi_2 has also been found to be nucleation controlled [dHe84] and Ni to be the dominant diffusing species for all phases [Fin81, dHe82, Mey90].

The electronic properties of the Ni-Si system are also of interest. Figure 2-5 presents the sheet resistance of the system as a function of annealing temperature for three initial Ni layer thicknesses as measured by Chen et al. [Che97]. All samples were annealed for 40 seconds. Two observations can be determined from this plot. First, increasing the initial thickness of the Ni layer increases the sheet resistance of the system for all temperatures. Second, three regimes of sheet resistance are seen. These correspond to each of the three phases present in the evolution of the Ni-Si system. Ni_2Si , present at low temperature, and NiSi_2 , present at high temperatures, both have sheet resistances higher than that of the intermediate NiSi phase [Nem06]. For this reason, NiSi is the desired phase for semiconductor technology applications.

2.1.3 Nickel-Germanium Binary System

The phase diagram of the Ni-Ge system is shown in Figure 2-6; seven intermediate compounds are evident in the diagram. As with the Ni-Si system, all of the phases in the diagram are not seen experimentally. Unlike the Ni-Si system, however, some controversy exists as to which phase initially forms during the reaction of Ni metal with excess Ge. Reported initial

phases include orthorhombic Ni_2Ge [Hsi88, Li89], monoclinic Ni_5Ge_3 [Patt94], and hexagonal Ni_3Ge_2 [Nem06]. Nemouchi et al. suggest that this confusion arises from the fact that the major XRD diffraction lines are identical for all three of these phases [Nem06]. TEM/EELS analysis in the same work showed the Ni_5Ge_3 phase to form first at a temperature around 140 °C.

Regardless, all of these authors agree that NiGe is the second and final phase formed in the evolution of the films. Also unlike the Ni-Si system, the phases present in the thermal evolution of the Ni-Ge system do not form sequentially [Nem06]. Instead, the initial N-rich phase (most likely Ni_5Ge_3) and NiGe form simultaneously with the Ni-rich phase between that of the unreacted Ni and NiGe. Once the Ni metal has been consumed, the Ni-rich phase transforms into NiGe. This evolution is shown in Figure 2-7. It has been experimentally identified that Ni is the diffusing species during the evolution of all phases [Tho88].

Figure 2-8 plots the sheet resistance of the Ni-Ge system as a function of annealing temperature for two Ni layer thicknesses [Zha05]. A sample of Ni on Si was also included for comparison. All samples were RTA processed for 30 seconds. It can be observed from this plot that, as with the Ni-Si system, three regimes are present. At low temperature, the Ni-rich germanicide has a higher sheet resistance than the NiGe phase present at intermediate temperatures. At higher temperatures (~500-600 °C), a rapid increase in sheet resistance is apparent. Unlike the Ni-Si system, this increase is not attributed to phase transformation as NiGe_2 has only been reported to form at high temperatures and pressures [Tak00]. Instead, this rapid increase in sheet resistance is due to the agglomeration of NiGe which has been shown to begin at temperatures as low as 400 °C [Zha05].

2.2 Ternary System: Ni-Si-Ge

2.2.1 Physical Properties

When Ni is reacted with SiGe, a ternary alloy of Ni, Si, and Ge is formed. While the composition of the Ni-rich initial phase is a matter of some debate [Cha04, Zha02], it is agreed that the silicidation process produces $\text{Ni}(\text{Si}_{1-x}\text{Ge}_x)$ with the ratio of Si to Ge identical to that of the silicided $\text{Si}_{1-x}\text{Ge}_x$ alloy at temperatures around 400 °C [Zha02, Cha04, Liu05]. Since both NiSi and NiGe have the same space group (pnma) and prototype crystal (MnP) [Mas90] and Si and Ge form a complete solid solution, it is thought that $\text{Ni}(\text{Si}_{1-x}\text{Ge}_x)$ is a complete solid solution of NiSi and NiGe in the appropriate ratio [Seg02]. It has also been shown that the formation of NiGe_2 is limited to high temperatures and pressures not seen during silicidation processing [Tak00]. Exhaustive experimental evidence has furthermore shown that small quantities of Ge (~1 at% +) prevents the formation of NiSi_2 at temperatures up to 800 °C or more [Jar02, Seg02, Ish03, Seg03], most likely due to the lack of the corresponding NiGe_2 phase. Several of these authors have therefore proposed that $\text{Ni}(\text{Si}_{1-x}\text{Ge}_x)$ will not transform to $\text{Ni}(\text{Si}_{1-x}\text{Ge}_x)_2$ and at this date no experimental evidence has been shown to the contrary for annealing temperatures up to 850 °C for 30 seconds [Jar02].

2.2.2 Phase Diagram

S.-L. Zhang performed a series of thermodynamic calculations treating $\text{Ni}(\text{Si}_{1-x}\text{Ge}_x)$ as a complete solid solution of NiSi and NiGe [Zha03]. If the $\text{Ni}(\text{Si}_{1-x}\text{Ge}_x)$ layer is in contact with $\text{Si}_{1-x}\text{Ge}_x$, as is usually the case in silicidation, the equilibrium minimum free energy of the $\text{Ni}(\text{Si}_{1-x}\text{Ge}_x)$ - $\text{Si}_{1-x}\text{Ge}_x$ system can be calculated with this method. The graphical results for an example calculation with one gram-atom of $\text{Ni}(\text{Si}_{0.5}\text{Ge}_{0.5})$ in contact with one gram-atom of $\text{Si}_{0.5}\text{Ge}_{0.5}$ at 600 °C is presented in Figure 2-9. From this graph, it can be determined that the system will reach equilibrium with one gram-atom of $\text{Ni}(\text{Si}_{0.90}\text{Ge}_{0.10})$ and one gram-atom of $\text{Si}_{0.30}\text{Ge}_{0.70}$

[Zha03]. The driving force for the rejection of Ge from the nickel germanosilicide is the difference in the heats of formation for NiSi (-45 kJ/gram-atom) and NiGe (-32 kJ/gram-atom) [45 from Zha06].

Using similar methodology, partial isotherms for the ternary phase diagram can be calculated. Examples of calculated isotherms are shown in Figure 2-10. The horizontal line between NiSi and NiGe represents all possible compositions of the complete solid solution (any composition of $\text{Ni}(\text{Si}_{1-x}\text{Ge}_x)$). It should be noted that the presence and behavior of Ni-rich phases (e.g. Ni_2Si and Ni_5Ge_3) are neglected and not shown. As mentioned previously, the presence of Ge has been shown to severely inhibit the formation of NiSi_2 . Eliminating NiSi_2 from the calculations produces the isotherms shown in Figure 2-11. This change affects only nickel germanosilicides with very small concentrations of Ge ($x < \sim 0.05$) and it has been suggested that confirmation of this change may be difficult [Jar02]. For the previous example of $\text{NiSi}_{0.5}\text{Ge}_{0.5}$ in contact with $\text{Si}_{0.5}\text{Ge}_{0.5}$, use of either 600 °C isotherm, shown in Figure 2-12 for the modified calculations, indicates the resulting equilibrium states of $\text{NiSi}_{0.9}\text{Ge}_{0.1}$ and $\text{Si}_{0.3}\text{Ge}_{0.7}$.

2.2.3 Microstructure

Knowledge of the microstructure of $\text{Ni}(\text{Si}_{1-x}\text{Ge}_x)$ and its thermal stability is important to determine the possible processing window of the material. While no transformation to a high-resistance digermanosilicide analogous to NiSi_2 has been reported in literature, nickel germanosilicide films have relatively poor thermal stability due to the thermodynamic impetus for Ge rejection as calculated by Zhang. Thus, many researchers have investigated the microstructure of $\text{Ni}(\text{Si}_{1-x}\text{Ge}_x)$ and its thermal evolution over a range of processing conditions. The results from these investigations will be discussed in the following sections.

2.2.3.1 Initial film formation

The initial reaction of a Ni metal layer with a $\text{Si}_{1-x}\text{Ge}_x$ alloy produces a Ni-rich phase analogous to the Ni-rich Ni_2Si and Ni_5Ge_3 phases reported for the Ni-Si and Ni-Ge systems, respectively. For a 325 °C 30 second anneal, this phase has been reported to be $\text{Ni}_2(\text{Si}_{1-x}\text{Ge}_x)$ by Chamirian et al. [Cha04]. For a 300 °C 60 second anneal the presence of both $\text{Ni}_2(\text{Si}_{1-x}\text{Ge}_x)$ and $\text{Ni}_3(\text{Si}_{1-x}\text{Ge}_x)_2$ has been reported by Zhao et al. [Zha02]. The existence of Ni_2Si , Ni_2Ge , Ni_3Si_2 and Ni_3Ge_2 are all reported on the respective phase diagrams and so solid solutions of either pair seem reasonable. Further information on Ni-rich phase formation is not available in literature at this time; one or both phases may form sequentially or simultaneously or other intermediate phases may also occur.

Regardless of the composition and evolution of the initial Ni-rich phase, on annealing to temperatures at 450 °C for 30 seconds, and as high as 700 °C for 30 seconds, Chamirian et al. and Zhao et al. both report that the Ni-rich phase disappears and $\text{Ni}(\text{Si}_{1-x}\text{Ge}_x)$ predominates for all samples. XRD spectra confirming the sole presence (disregarding SiGe and Si peaks) of $\text{Ni}(\text{Si}_{1-x}\text{Ge}_x)$ at temperatures over 400 °C and ranging as high as 800 °C have been reported by several additional authors [Liu04, Ok04, Pey02, Cho06, He05, Yao07]. One set of XRD spectra containing this evolution is included in Figure 2-13. Since $\text{Ni}(\text{Si}_{1-x}\text{Ge}_x)$ is the phase of interest for use as an intermediate silicide layer in semiconductor applications, most work on nickel germanosilicides has therefore focused on thermal anneals at temperatures higher than 400-500 °C where no Ni-rich nickel germanosilicide forms.

$\text{Ni}(\text{Si}_{1-x}\text{Ge}_x)$ films formed by annealing at temperatures from 400-450 °C and times of 30-60 seconds on crystalline $\text{Si}_{1-x}\text{Ge}_x$ substrates (with x ranging from 10 to 20 at % Ge) have been analyzed with XTEM/EDS by several authors [Zha02, Jon04, Ok04, Ko06, Yao07]. These authors all agree that $\text{Ni}(\text{Si}_{1-x}\text{Ge}_x)$ films produced in this annealing range have homogeneous

compositions with Si to Ge ratios identical to that of the $\text{Si}_{1-x}\text{Ge}_x$ substrate. The films are also shown in these works to be granular, continuous, and of uniform thickness. XTEM images of representative films formed within this range are shown in Figure 2-14.

2.2.3.2 Film agglomeration

As shown by the previously discussed thermodynamic calculations of Zhang [Zha06], the uniform $\text{Ni}(\text{Si}_{1-x}\text{Ge}_x)$ films produced at temperature ranges from 400-450 °C are not thermodynamically stable when in contact with unreacted $\text{Si}_{1-x}\text{Ge}_x$. Instead, at longer times or elevated temperatures, nickel germanosilicide films undergo Ge rejection and form $\text{Si}_{1-z}\text{Ge}_z$ grains that are Ge-rich relative to the $\text{Si}_{1-x}\text{Ge}_x$ substrate ($z > x$) interspersed between remaining Si-rich $\text{Ni}(\text{Si}_{1-u}\text{Ge}_u)$ grains ($u < x$). This process has been experimentally observed by a large number of researchers [Pey02, Zha02, Pey04, Jin05, Yao07]. Furthermore, the equilibrium concentrations of the $\text{Ni}(\text{Si}_{1-u}\text{Ge}_u)$ and $\text{Si}_{1-z}\text{Ge}_z$ grains predicted by Zhang's ternary isotherms have been shown to be in good agreement with observed experimental values [Pey04]. While the overall process of the rejection of Ge and the formation of $\text{Si}_{1-z}\text{Ge}_z$ is commonly referred to in literature as "agglomeration" of the germanosilicides, it would be more accurate to label the process as an eutectoid-type solid state phase transformation.

The initial stages of the transformation have been observed by Yao et al. for samples with 20 at% Ge annealed at 500 °C for 20 seconds [Yao07]. Using HRXTEM, the researchers observed sharp v-shaped grooves forming at the intersection of $\text{Ni}(\text{Si}_{1-x}\text{Ge}_x)$ grain boundaries and the $\text{Ni}(\text{Si}_{1-x}\text{Ge}_x)/\text{Si}_{1-x}\text{Ge}_x$. One such groove is shown in Figure 2-15(a). Similar grooving is also observed in NiSi and NiGe samples; examples of these grooves are shown in Figure 2-15 (b) and (c), respectively. The grain boundary angles, indicated as θ in the figures, was found to be smaller in the germanosilicide than in the silicide or germanide. The overall shape of the interfaces in the germanosilicide was also found to be more planar. These findings led Yao et al.

to suggest that grooving occurs much more rapidly in the germanosilicide and sufficient time is not available to diffusively smooth the interfaces. Yao et al. also performed EDS on the HRXTEM samples to determine the distribution of Ge in the vicinity of the grain boundary/groove. The results, shown in Figure 2-15(d), indicate that the grain boundary above the groove is depleted of Ge while the region immediately below the groove is enriched in Ge. These findings suggest that Ge rejection occurs along the grain boundaries of the $\text{Ni}(\text{Si}_{1-x}\text{Ge}_x)$ grains.

Later stages of the transformation have been observed by a number of researchers [Zha02, Pey02, Ok03, Pey04, Jin05]. In these studies, with Ge compositions ranging from 20 to 25 at %, anneal temperatures ranging from 500 to 800 °C, and anneal times ranging from 30 to 60 seconds, XTEM analysis shows Ge-rich $\text{Si}_{1-z}\text{Ge}_z$ grains have formed between grains of Si-rich $\text{Ni}(\text{Si}_{1-u}\text{Ge}_u)$ [Ok03, Pey04]. One representative set of XTEM images, from Pey et al. [Pey04] is shown in Figure 2-16. At lower temperatures (500 to 700 °C, Figure 2-16 (a)-(c)), distinct Ge-rich $\text{Si}_{1-z}\text{Ge}_z$ grains are distinguishable in the film. The number and spacing of $\text{Si}_{1-z}\text{Ge}_z$ grains is also observed to increase in this range. While not explicitly discussed in any of the works, misfit dislocations can be noted between the $\text{Si}_{1-z}\text{Ge}_z$ grains and the $\text{Si}_{1-x}\text{Ge}_x$ layer. These results, when combined with the observations of Yao et al., suggest that in this annealing range the Ge-rich regions below the grooved grain boundary form Ge-rich $\text{Si}_{1-z}\text{Ge}_z$ grains which are distinct from the $\text{Si}_{1-x}\text{Ge}_x$ layer. At higher temperatures (~800 °C, Figure 2-16(d)), the misfit dislocations between the grains and the layer are not observed, suggesting that the Ge concentration gradient may have lessened due to diffusion. The spacing between $\text{Ni}(\text{Si}_{1-u}\text{Ge}_u)$ grains is also larger in this temperature range.

The transformation has also been studied by plan-view techniques including SEM and AES. Several researchers have used plan-view SEM to observe the extent of the transformation as a function of temperature [Ok03, Cha04, Pey04, Ko06, Yao07]. The samples observed in these works ranged from 10 to 25 at% Ge and were annealed at temperatures from 500 to 800 °C for times ranging from 20 to 60 seconds. As with the XTEM work discussed previously, the results from these studies generally agree. A representative set of images, from Ok et al. [Ok03], is shown in Figure 2-17. Evidence of the beginnings of the phase transformation (in the form of phase contrast between grains in the image) is present within all images at all times and temperatures. These observations are also seen all of the images from all of the other works. The degree of agglomeration, as judged from the size of the grains in the images, is seen to increase with increasing temperature. It is important to note, however, that the magnification of the images in all studies is relatively low, with scale bars in the 1 to 2 μm range. Also, no researcher attempted to quantify the size of the grains observed in the SEM images. The importance of these matters will be discussed in later sections.

Plan-view AES elemental mapping was performed by Pey et al [Pey02]. In this study, mapping was performed on samples of 25 at% Ge annealed for 60 seconds at temperatures from 500 to 900 °C in 100 °C increments. The results from the mapping, some of which are shown in Figure 2-18, show non-uniform distributions of Ni and Ge which become coarser with increasing temperature. These images correspond generally well with the plan-view SEM images previously discussed and confirm the contrast seen in the previous images is due to phase contrast and not sample topography. While Pey et al. conclude that agglomeration begins around 700 °C, it is apparent from the maps that the transformation has begun prior to this point (the distribution at 600 °C is clearly not uniform).

2.2.4 Sheet Resistance

One commonly studied electrical property of nickel germanosilicide films is sheet resistance, likely due to the ease of measurement via four point probe analysis. Sheet resistance is measured in Ohms/sq and, given the thickness of the film, the resistivity of the film can be extracted from the value. Ok et al. performed an experiment where the sheet resistance of nickel germanosilicide films was measured as a function of annealing temperature [Ok03]. The structures used in the study were comprised of 25 nm of Ni deposited on $\text{Si}_{1-x}\text{Ge}_x$ films with 0, 10, and 20 at% Ge and samples were annealed for 30 seconds. The measurements from the study are presented in Figure 2-19. Below 600 °C, the sheet resistance of each film is stable. Above this temperature, the sheet resistance of all sample conditions increases with increasing temperature (the difference in values between the samples as a function of Ge content will be discussed later). For the samples with 0 at% Ge (Ni on Si), the increase is attributed to the previously discussed transformation of NiSi to higher resistance NiSi₂ around 700 °C. The Ni-Si-Ge system, however, was previously shown to lack a corresponding high resistance digermanosilicide. Thus, the increase of sheet resistance for the nickel germanosilicide structures was attributed to the agglomeration (decomposition) of the film. Similar results and conclusions have been presented by a number of researchers [Pey02, Zha02, Cha04, Cha04b, Zha04, Seg04, Liu05, Cho06, Ko06, Lau06, Yao06].

2.2.5 Influential Variables

Several variables have been determined to be influential in the stability and evolution of nickel germanosilicide thin films. These variables include the strain state, thickness, Ge content, thickness, and crystalline quality of the $\text{Si}_{1-x}\text{Ge}_x$ layer and the thickness of the Ni layer. The impact of doping via both implantation and in-situ methods has also been studied. The following

sections briefly discuss the most important variables and their impact on the films, both in terms of microstructure and sheet resistance.

2.2.5.1 Silicon-germanium layer strain and thickness.

Zhao et al. performed a study using XTEM analysis to determine if the strain state (prior to silicidation) of the $\text{Si}_{1-x}\text{Ge}_x$ layer impacted the stability of the films [Zha04]. The study used structures with a $\text{Si}_{0.73}\text{Ge}_{0.27}$ layer which was partially relaxed (50 or 75%) for some samples prior to deposition of 20 nm of Ni metal. Samples were then annealed at temperatures from 400-650 °C for 60 seconds. The authors concluded that increasing layer strain enhanced agglomeration due to an increase in interface energy. This conclusion, however, is not well-supported by the XTEM images presented by the authors as no distinct morphological difference is evident in the images. Plan-view analysis of the samples was not performed. The authors also noted that, for fully-strained layers annealed at 600 °C for 60 seconds, misfit and threading dislocations formed at the $\text{Si}_{1-x}\text{Ge}_x/\text{Si}$ interface in locations where germanosilicide grains approached the interface. These results suggest that the depth of the silicidation may affect strain relaxation of the $\text{Si}_{1-x}\text{Ge}_x$ layer. In conjunction with the authors' conclusion that increasing layer strain increases agglomeration, this suggests that the proximity of the germanosilicide layer to the $\text{Si}_{1-x}\text{Ge}_x/\text{Si}$ may affect agglomeration behavior.

Zhao et al. also studied the sheet resistance of the film as a function of initial $\text{Si}_{1-x}\text{Ge}_x$ layer strain. The sheet resistance measurements, shown in Figure 2-20, are stable (~70 Ohm/sq) for temperatures below 550 °C. At higher temperatures the sheet resistance of the films increased with increasing temperature. The fully strained samples were reported to show the highest increase (to around 47 Ohm/sq) and the 50 and 75% samples both increased to similar values (around 15 Ohm/sq). The increase in sheet resistance was attributed to the agglomeration of the layers, with the increased agglomeration of the fully strained layer responsible for causing the

highest increase of sheet resistance. No direct relationship between agglomeration and sheet resistance was established.

2.2.5.2 Germanium content of $\text{Si}_{1-x}\text{Ge}_x$ layer.

Ok et al. used plan view SEM to establish the effect of increasing the Ge content in the $\text{Si}_{1-x}\text{Ge}_x$ film on germanosilicide formation and stability [Ok03]. Images from the study are shown in Figure 2-21 for samples with $\text{Si}_{1-x}\text{Ge}_x$ compositions of 10 and 20 at% Ge annealed at 650, 700, and 750 °C for 30 seconds. The authors noted that the surface of the samples with increased Ge content showed a qualitatively greater number of dark regions (corresponding to areas of $\text{Si}_{1-x}\text{Ge}_x$ uncovered by the phase transformation) when compared to the images of samples with lower Ge content and identical anneals. From these observations, it was concluded that increasing Ge content caused the germanosilicide to become degraded at lower temperatures. No quantitative study of the images, however, was performed. Careful examination of the images also reveals evidence of non-uniform Ge content for both samples annealed at 650 °C, the lowest temperature shown. This observation suggests that the reaction has already begun for these samples.

As previously shown in Figure 2-19, Ok et al. also measured the sheet resistance of the samples used in the study. The measurements showed that the magnitude of the sheet resistance in the stable region (anneal temperature less than 700 °C) increased with increasing Ge content in the initial $\text{Si}_{1-x}\text{Ge}_x$ layer. No explanation for this behavior was presented in the work. The measurements also showed that, once sheet resistance began to increase at higher temperatures, the sample with larger Ge content increased more rapidly. Though no direct relationship was established, the increases were again attributed to agglomeration of the films at higher temperatures; the greater increase in sheet resistance of the higher concentration Ge sample was ascribed to the increased agglomeration seen in those samples.

While the previously discussed work by Zhao et al. [Zha04] only studied the microstructure evolution for Ni-silicided $\text{Si}_{0.73}\text{Ge}_{0.27}$ layers with various levels of initial strain, the study also measured the sheet resistance of identically processed samples with $\text{Si}_{0.81}\text{Ge}_{0.19}$ layers. All samples showed an increase in sheet resistance beginning around 550 °C, once more attributed to film agglomeration. The sheet resistance measurements of the films with higher initial Ge content, however, were shown to increase more than those with lower concentrations for each strain condition. The difference was credited to increased agglomeration in the samples with higher initial Ge content in the $\text{Si}_{1-x}\text{Ge}_x$ film. This conclusion, while in agreement with the conclusions of Ok et al., was not supported by microstructure analysis of the lower concentration samples. Additionally, no direct relationship between microstructure and sheet resistance was determined.

2.2.5.3 Crystalline quality of the $\text{Si}_{1-x}\text{Ge}_x$ layer.

The works previously discussed in this literature survey have all used single-crystal $\text{Si}_{1-x}\text{Ge}_x$ layers as the basis for germanosilicide layer formation. The formation of germanosilicide layers on poly-crystalline $\text{Si}_{1-x}\text{Ge}_x$ layers, however, has also been studied and found to exhibit significantly different behavior. Using XTEM/EDS analysis, Jarmar et al. have shown that, as with nickel germanosilicide layers formed on single-crystal $\text{Si}_{1-x}\text{Ge}_x$ layers, those formed on poly-crystalline $\text{Si}_{1-x}\text{Ge}_x$ layers also initially form a continuous $\text{Ni}(\text{Si}_{1-x}\text{Ge}_x)$ layer that rejects Ge and agglomerates [Jar02]. A notable difference, however, is that the Ni-rich $\text{Ni}(\text{Si}_{1-u}\text{Ge}_u)$ grains were shown to be much more mobile and migrated to the wafer surface and $\text{Si}_{1-x}\text{Ge}_x/\text{Si}$ interface. Thus, it can be concluded that the quality of the $\text{Si}_{1-x}\text{Ge}_x$ layer can clearly affect the evolution of the nickel germanosilicide layer. No sheet resistance measurements were included in the study.

2.2.5.4 Nickel layer thickness.

The influence of the thickness of the initial Ni layer on germanosilicide film evolution has been studied by Ko et al. [Ko06]. In the work, two thicknesses of Ni metal (11 and 21 nm) were deposited on samples of relaxed $\text{Si}_{0.75}\text{Ge}_{0.25}$ and germanosilicides were formed using a two-stage anneal. Samples were first annealed at 400 °C for 60 seconds to form a homogeneous $\text{Ni}(\text{Si}_{0.75}\text{Ge}_{0.25})$ layer. The samples were then annealed at 750 °C for an unreported time. One annealed, the samples were imaged with FE-SEM in BSE mode. The images, not included here due to their poor quality, show that the grain size of the samples with the thicker Ni layer was qualitatively larger than those of with the thinner Ni layer. Since a thicker initial Ni layer will produce a thicker nickel germanosilicide film (as more Ni is available to react), these results suggest that the thickness of the germanosilicide may affect the stability and evolution of the film. No quantification of the different morphologies was attempted.

The study by Ko et al. also investigated the effect of varying the initial Ni layer thickness on the sheet resistance of the layers as a function of annealing temperature. The samples and thermal processing used in this portion of the study were identical to those previously discussed with the exception of either 11 or 21 nm of Ni being deposited prior to silicidation. The measurements show that increasing the thickness of the Ni layer did not affect sheet resistance (stable at ~ 5-10 Ohm/sq) for any sample at temperatures below 600 °C. Between 600 to 650 °C, samples with the thinner initial Ni layer showed an abrupt rise in sheet resistance to around 75 Ohm/sq. The sheet resistance of these samples was then stable (at ~75 Ohm/sq) to temperatures as high as 800 °C. In contrast, samples with the thicker Ni layer showed only a gradual increase in sheet resistance above 600 °C, with a maximum value of ~75 Ohm/sq reached at 800 °C. The difference in behavior was attributed to two causes. First, the increased availability of Ni in the films formed from thicker Ni layers produces thicker germanosilicide layers and thus decreases

sheet resistance. Second, the samples with thicker initial Ni layers displayed a larger grain size after annealing, causing an increase in film interconnectivity and thus a more stable sheet resistance. More simply, increasing Ni thickness decreased agglomeration and thus lowered sheet resistance. Again, no attempt to directly link the two properties was made.

Liu and Ozturk also varied the initial Ni layer thicknesses (10 and 20 nm) in a study using fully relaxed $\text{Si}_{1-x}\text{Ge}_x$ layers with Ge concentrations greater than 40% with and without in-situ B doping [Liu05]. The effect of B doping will be discussed later. No comparative microstructure analysis of the samples with varying initial Ni layer thickness was made, however the sheet resistance of the samples was measured as a function of temperature for 30 second anneals. The results from the experiment, shown in Figure 2-22, show that the samples with thicker Ni layers had lower sheet resistance measurements at all temperatures. For the undoped samples, the samples with the thicker initial Ni layer did not show an increase in sheet resistance until ~ 450 °C while the samples with the thinner layer started to display and increase around 350 °C. These results agree well with those found by Ko et al. and were attributed to the same factors: thicker and more stable germanosilicide layers produced by the increased initial thickness of Ni.

2.2.5.5 Implanted Dopants.

Chamirian et al. studied the effect of implanting $\text{Si}_{1-x}\text{Ge}_x$ films with dopants prior to Ni deposition and germanosilicide formation [Cha04]. In the study, both single- and polycrystalline films of $\text{Si}_{0.8}\text{Ge}_{0.2}$ were ion implanted with either As (4×10^{15} atoms/cm², 20 keV) or B (2×10^{15} atoms/cm², 2 keV). Next, a spike anneal to 1100 °C was performed to activate the dopants prior to deposition of 10 nm of Ni metal. Samples were then annealed at 450 °C for 30 seconds to produce a $\text{Ni}(\text{Si}_{0.8}\text{Ge}_{0.2})$ film. To study the thermal stability, the samples were annealed a second time at temperatures of 450, 600, and 700 °C for 30 seconds. Plan view SEM images of the films formed on single-crystal $\text{Si}_{1-x}\text{Ge}_x$ substrates are shown in Figure 2-23. No

quantitative analysis of the images was performed. Qualitatively, however, the morphology of the films does not appear to differ between the As and B implanted films (no non-implanted control samples were included in the study). Plan view SEM images of the films formed on polycrystalline substrates were also included in the work, though they are not reproduced here. These images also showed no qualitative difference in film morphology between the corresponding As and B implanted samples, though the overall grain size of the films appeared to be smaller than those formed on the single-crystal layers.

The sheet resistance of the samples used in the study by Chamirian et al. was also measured. These measurements, presented in Figure 2-24, show no significant difference between the As and B doped samples for the films formed on either single- or poly-crystalline $\text{Si}_{1-x}\text{Ge}_x$ layers. The plateau at temperatures below ~ 375 °C was attributed to the Ni-rich germanosilicide phases present at these temperatures having a higher resistivity than the $\text{Ni}(\text{Si}_{1-x}\text{Ge}_x)$ phase previously shown to be present at temperatures greater than around 400 °C. The increase in sheet resistance seen around 600 °C for all samples was attributed to the agglomeration of the film. The similarity in sheet resistance between the As and B doped samples was attributed to the previously discussed similarity in the morphology of the films. No quantitative relationship between sheet resistance and film morphology was established in the study.

2.2.5.6 In-situ Doping.

The impact of heavily doping the $\text{Si}_{1-x}\text{Ge}_x$ layer during its epitaxial growth (in-situ doping) on germanosilicide stability was studied by Liu and Ozturk [Liu05]. In the work, fully relaxed $\text{Si}_{1-x}\text{Ge}_x$ layers with Ge concentrations greater than 40% were doped with approximately 2 at% B (1×10^{21} atoms/cm²). Undoped samples with identical Ge concentration were also grown for comparison. A 20 nm thick layer of Ni was then deposited and the samples were annealed at

temperatures from 300 to 750 °C for 30 seconds to form nickel germanosilicide films. SIMS analysis of the B-doped sample annealed at 500 °C showed the formation of a shoulder and significantly longer tail for the Ni distribution when compared to the analysis of the B-doped sample annealed at 450 °C. It should be noted that the SIMS analysis was reported as a plot of analysis time vs. counts and was not converted to depth vs. concentration. Regardless, this change was attributed to significant interface roughening. The Ni(Si_{1-x}Ge_x)/Si_{1-x}Ge_x interface was further studied by selectively etching the germanosilicide and performing Atomic Force Microscopy (AFM) analysis of the exposed interface. Table 2-1 presents the average interface roughness values for doped and undoped samples annealed at 400 and 500 °C. The average roughness of the doped samples is significantly less than that of the undoped samples at each temperature. Liu and Ozturk attributed these results to the high levels of boron doping decreasing agglomeration through strain compensation. This theory is supported by the well-established ability of boron doping to compensate strain in Si_{1-x}Ge_x films at concentrations lower than 1 at% [Cho06a, Cho06b] and the previously discussed conclusions of Zhao et al. [Zha06] who stated that increasing strain increased the amount of film degradation. Other work has determined a similar effect in nickel germanosilicide samples highly doped with C [Tol04].

The sheet resistance of the samples used in the experiment by Liu and Ozturk was also measured as a function of anneal temperature. The measurements, previously shown in Figure 2-22, indicate that the addition of the in-situ B doping stabilized the sheet resistance of the films above 350 and 450 °C for the samples with 10 and 20 nm thick initial Ni layers, respectively. While the sheet resistance of the samples with B-doped Si_{1-x}Ge_x layers continues to gradually increase with increasing temperature, a sharp rise in the property is not seen. The stabilization

was attributed by Liu and Ozturk to their conclusion that the heavy B doping reduced the agglomeration of the films.

2.3 Outstanding Issues

While a substantial amount of work has been accomplished with the intent of understanding the formation and stability of nickel germanosilicide films, a number of questions remain unanswered in literature. First, can a direct relationship between film agglomeration and the increase in sheet resistance be established? While many works have proposed a qualitative link between the two properties, no quantitative relationship has been put forth. Without the establishment of a direct, quantitative relationship the connection between the two properties cannot be absolutely established. Second, does the addition of high levels of B doping truly affect the amount of agglomeration in nickel germanosilicide films? The study by Liu and Ozturk utilized only indirect measurement techniques during their investigation of the morphology of the films. If there is indeed an effect, does any quantitative relationship between agglomeration and sheet resistance still hold true? If there is not an effect, what is then causing the stabilization of sheet resistance in the films? Finally, the studies available in literature all utilize isochronal experiments with very short annealing times. What happens if the experiments are performed over a larger range of time and temperatures? Answers to these questions will further clarify the behavior of nickel germanosilicide thin films.

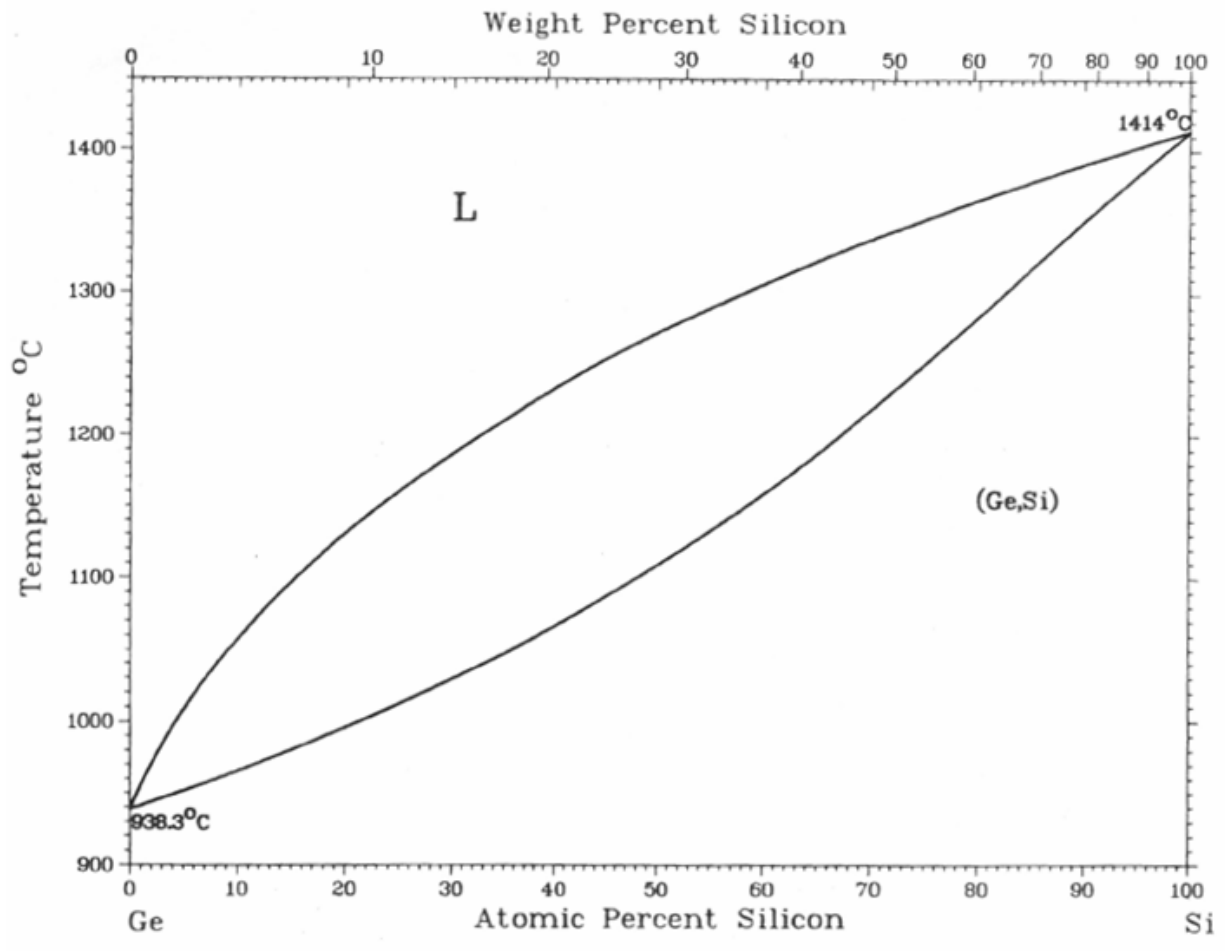


Figure 2-1: Binary phase diagram of Si-Ge system showing complete solid solubility of Si and Ge in the solid phase [Mas90].

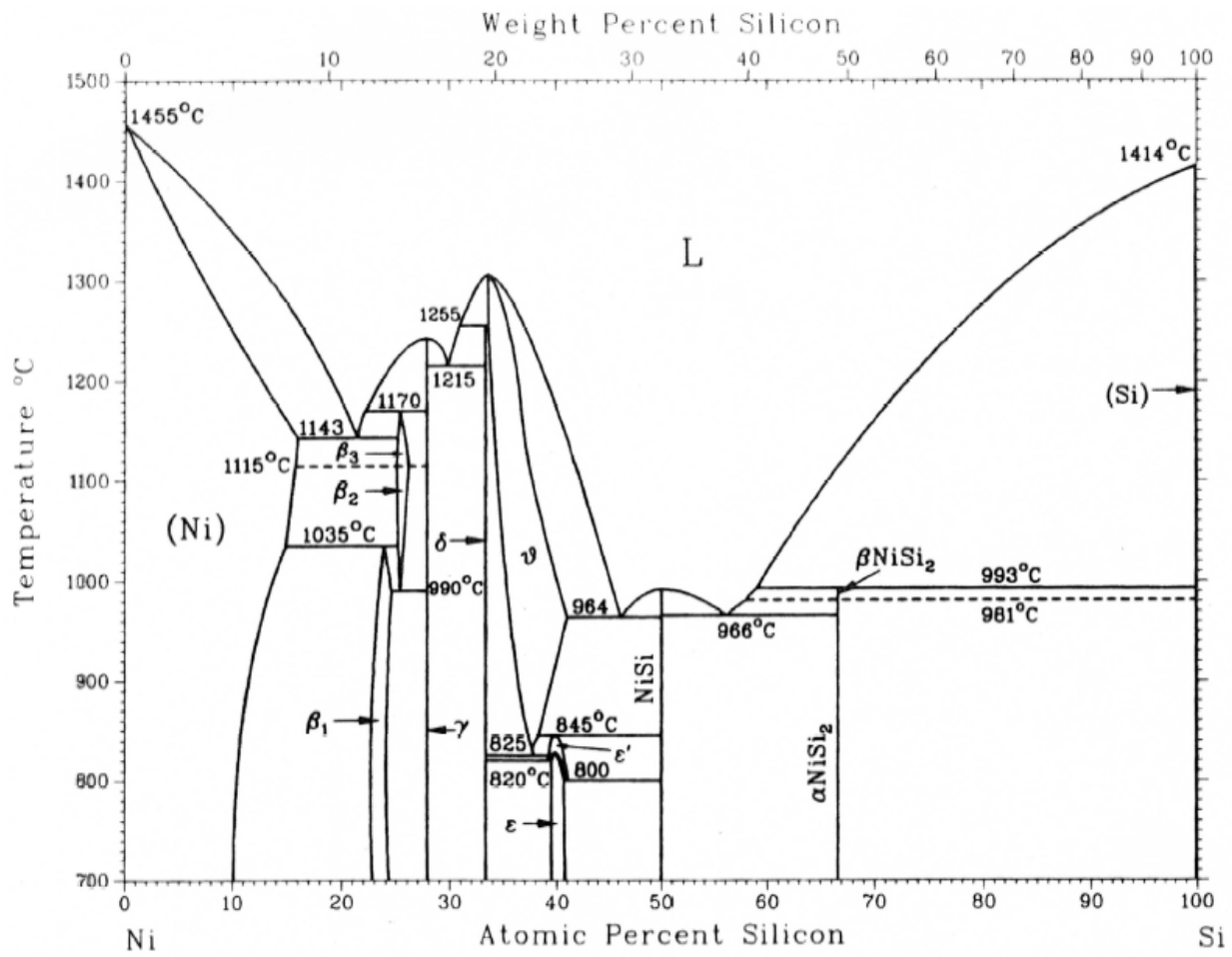


Figure 2-2: Binary phase diagram of Ni-Si System [Mas90].

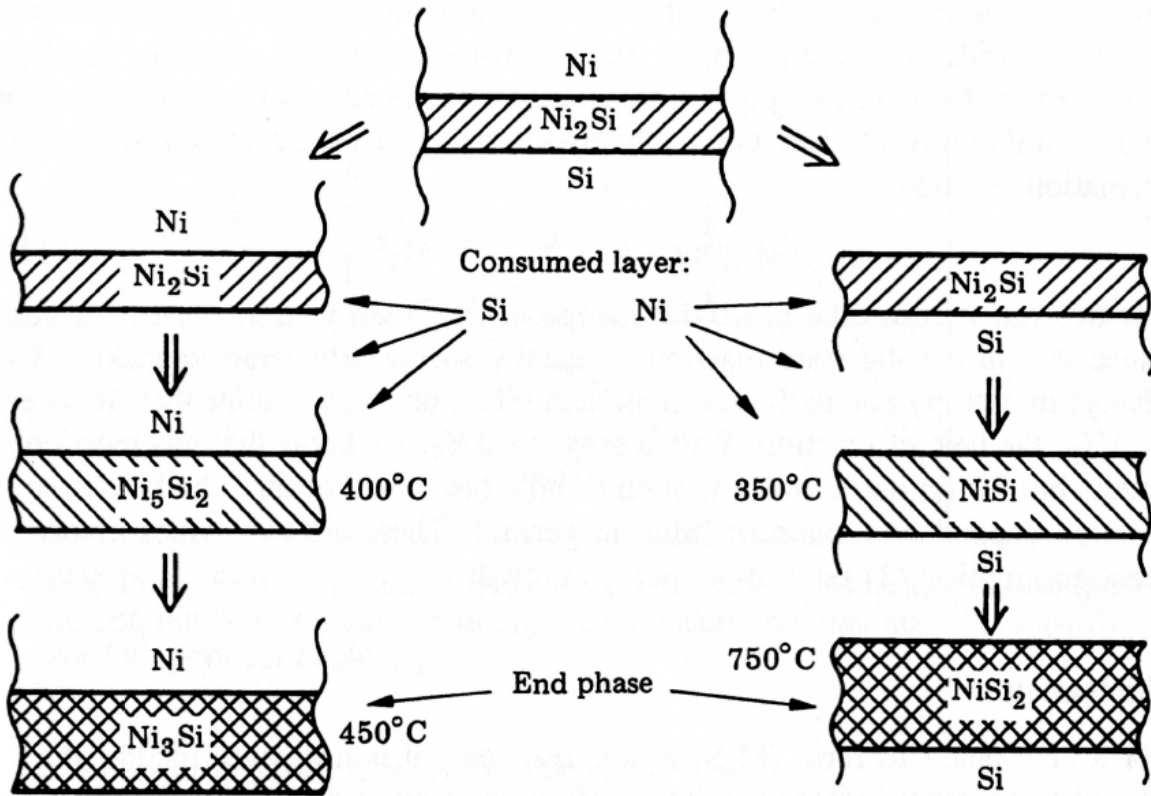


Figure 2-3: Schematic of the evolution of Ni-Si binary system on thermal annealing. The right hand path (excess Si, Ni layer consumed) is followed for silicidation processes [Mey90]

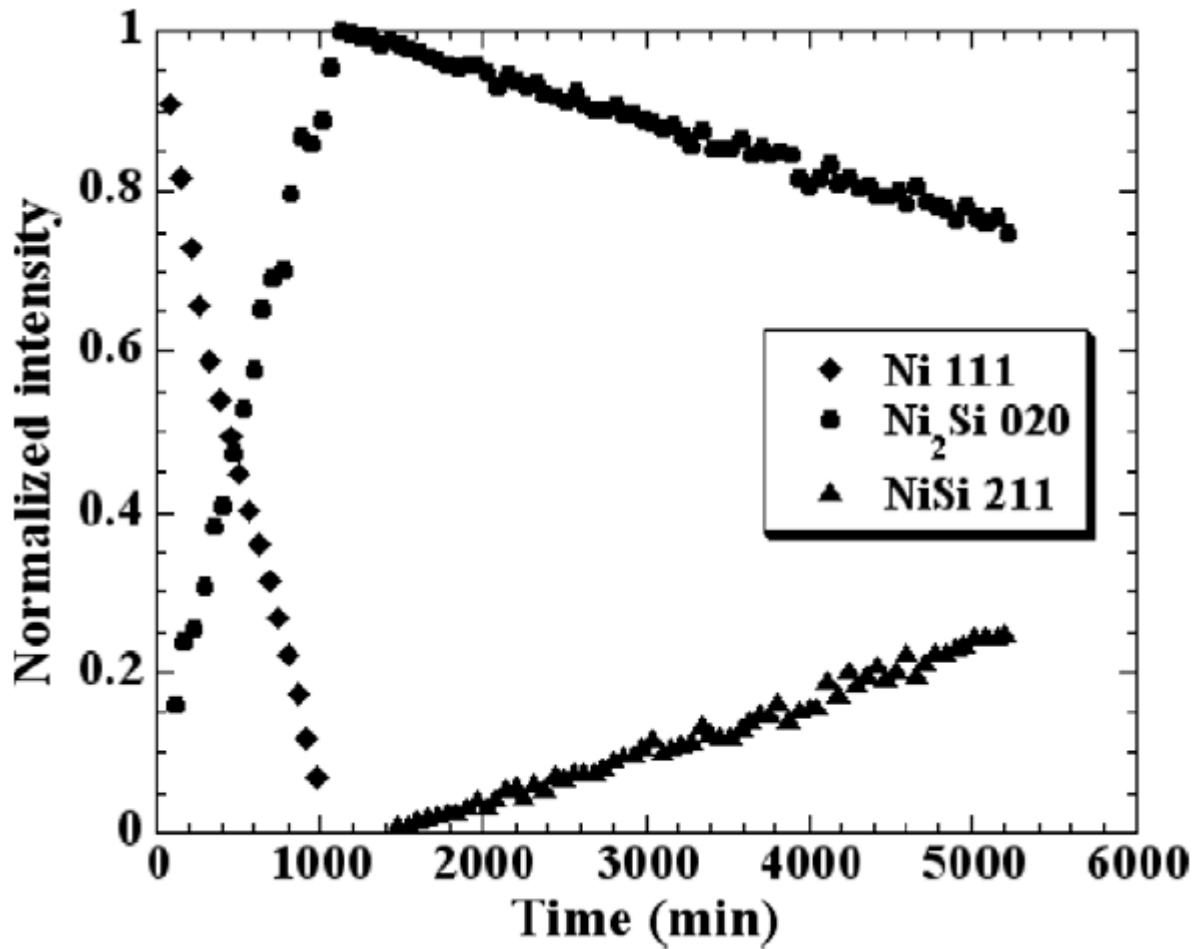


Figure 2-4: XRD results plotting the squared normalized intensity of characteristic diffraction peaks for Ni, Ni₂Si, and NiSi as a function of anneal time. Samples were 50 nm of Ni on a-Si substrate annealed at 230 °C. Note that the Ni signal disappears prior to the appearance of NiSi [Nem06].

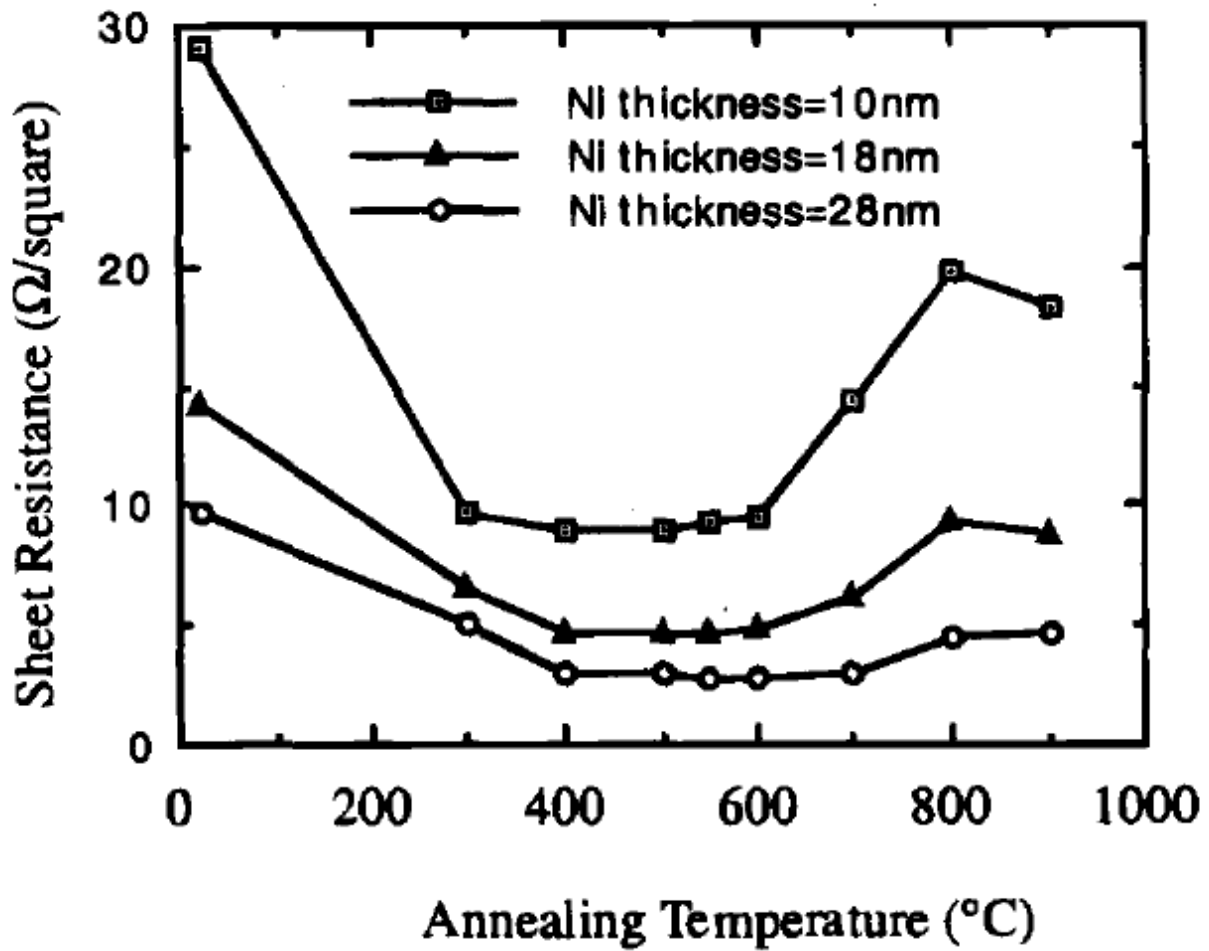


Figure 2-5: Sheet resistance of nickel silicide samples as a function of annealing temperature and initial Ni layer thickness. Anneals were performed for 40 seconds [Che97].

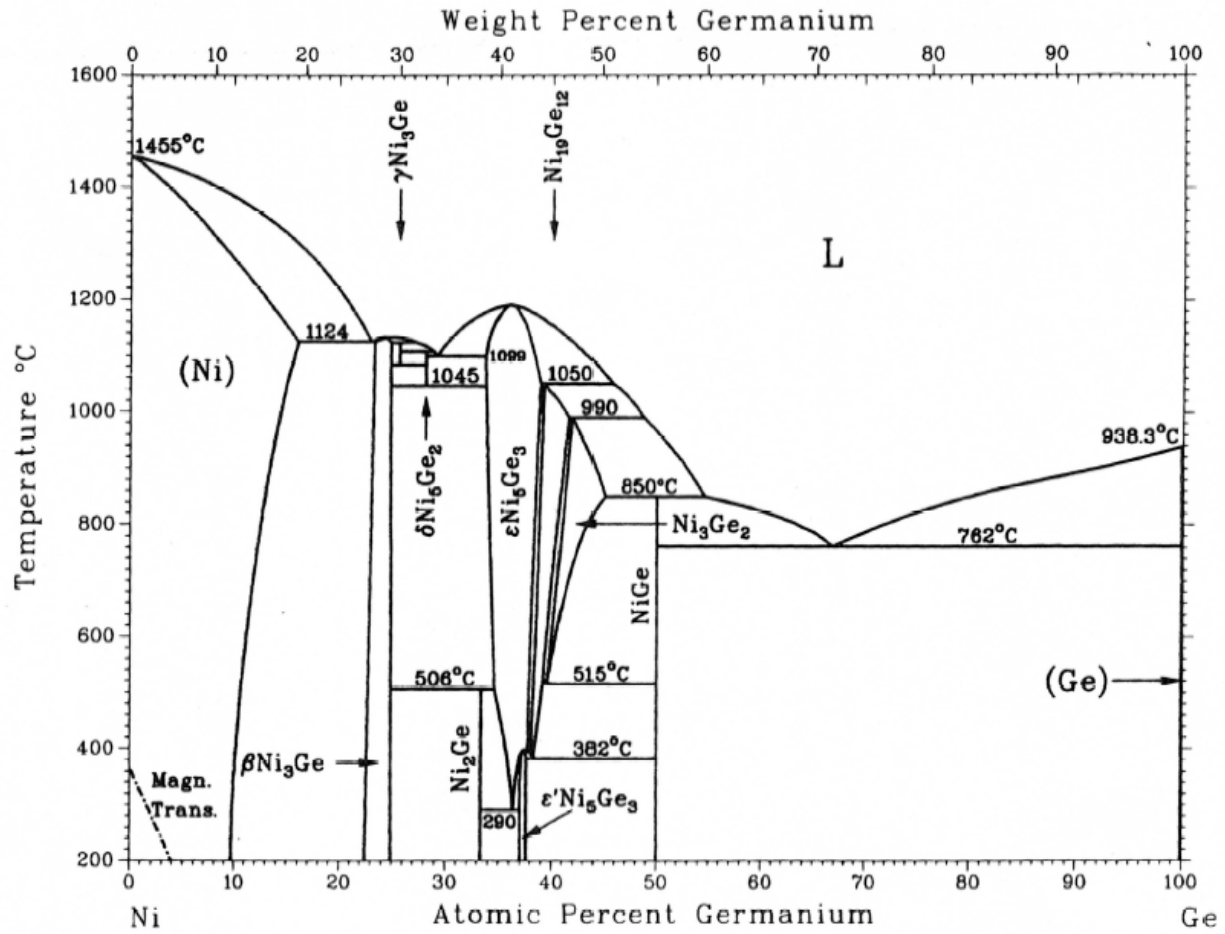


Figure 2-6: Binary phase diagram of the Ni-Ge system [Mas90].

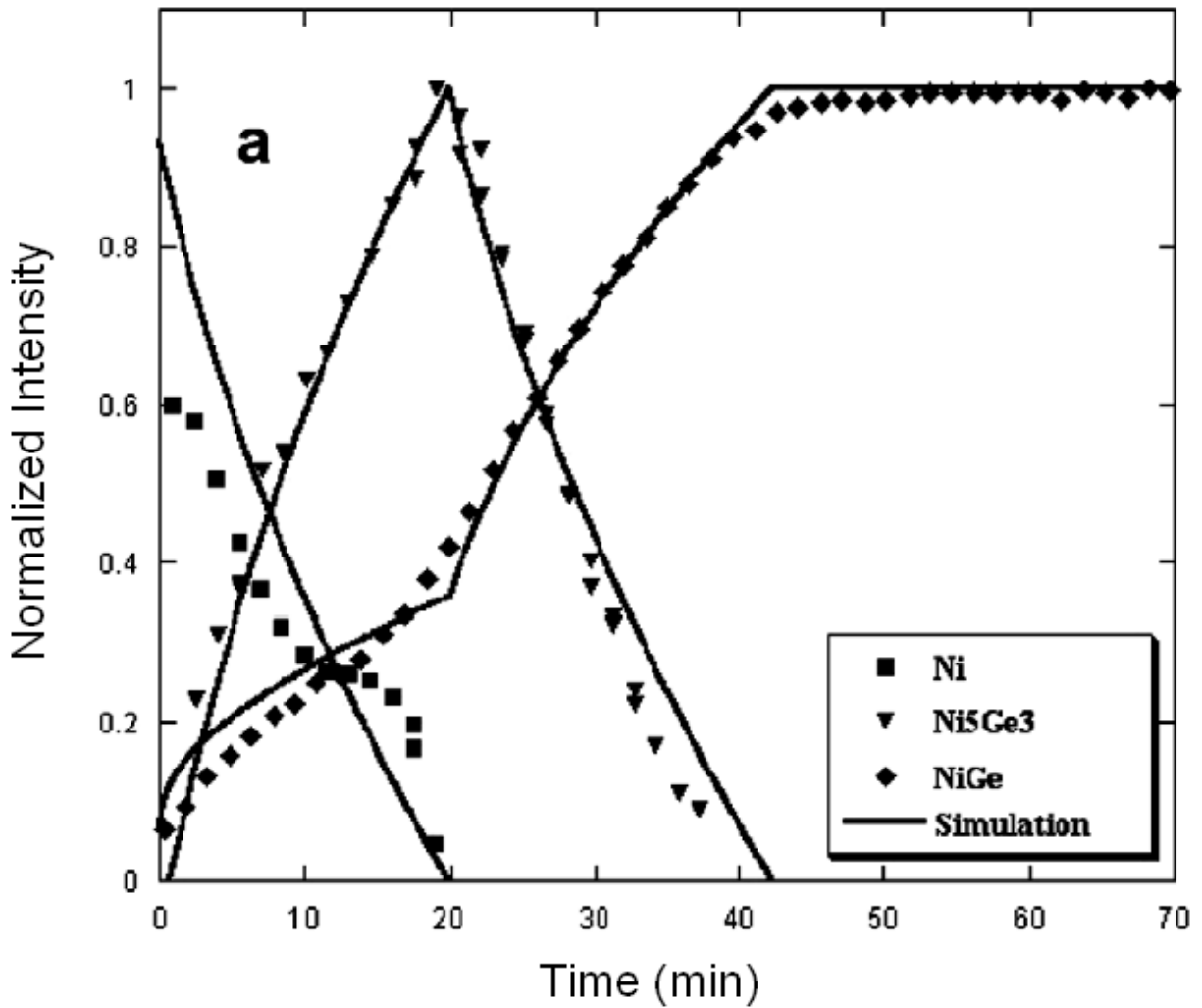


Figure 2-7: XRD results plotting the squared normalized intensity of characteristic diffraction peaks for Ni, Ni₅Ge₃, and NiGe as a function of anneal time. Samples were 50 nm of Ni on a-Ge substrate annealed at 160 °C. Note that the germanicide phases arise simultaneously [Nem06].

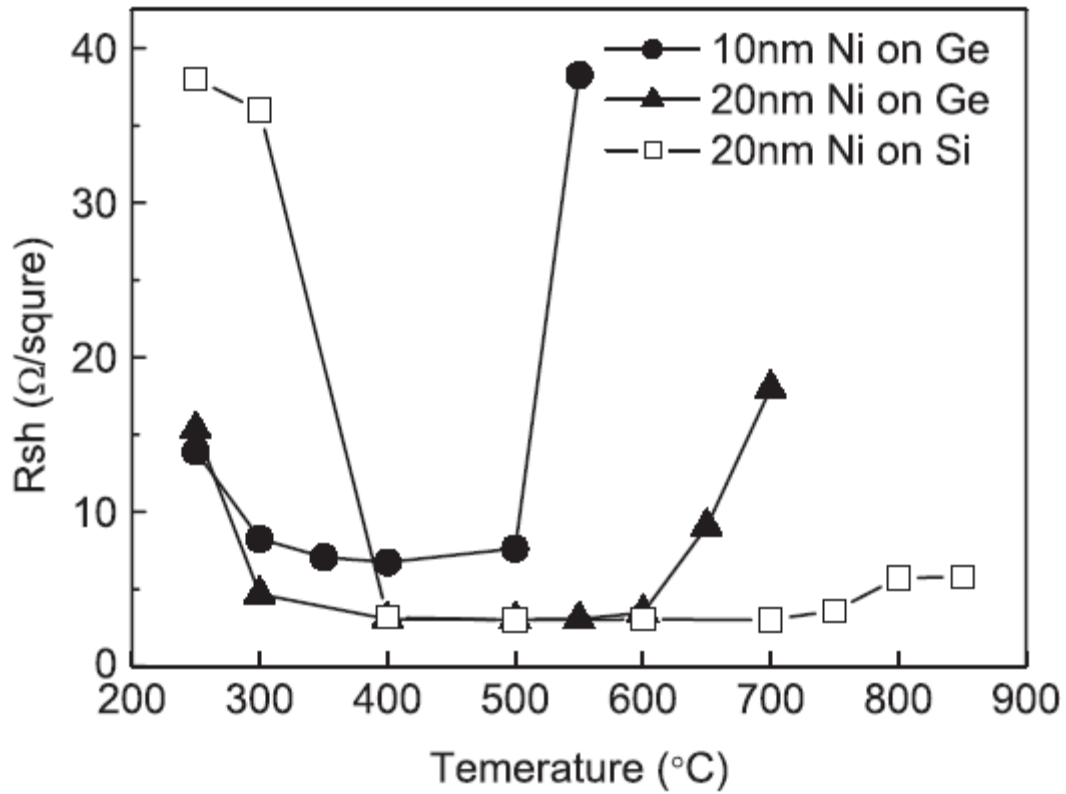


Figure 2-8: Sheet resistance of Ni-Ge system as a function of annealing temperature for two initial Ni layer thicknesses. Sheet resistance of Ni on Si is also shown for comparison. All samples were annealed for 30 seconds [Zha05].

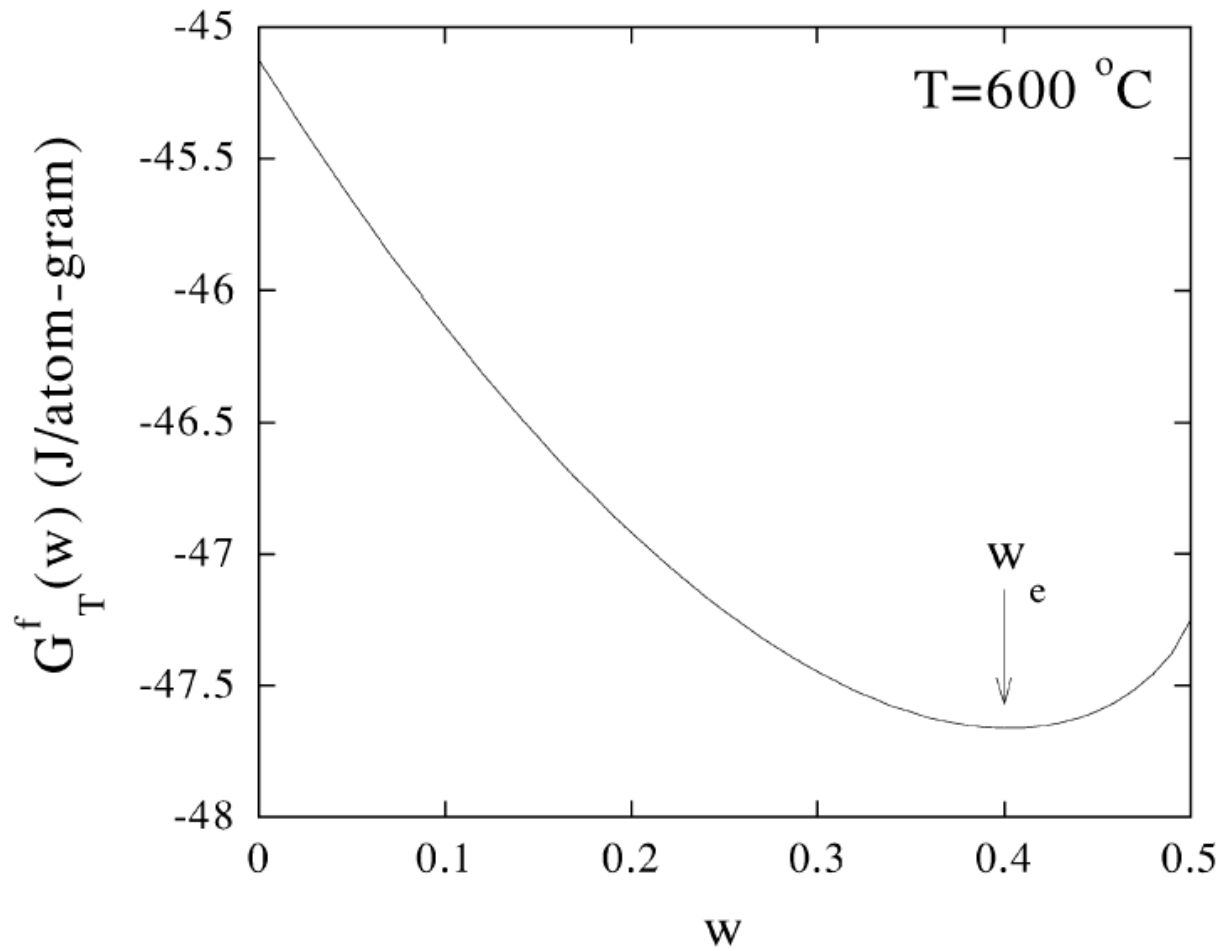


Figure 2-9: Free energy for a system of one gram-atom of $\text{NiSi}_{0.5}\text{Ge}_{0.5}$ in contact with one gram-atom of $\text{Si}_{0.5}\text{Ge}_{0.5}$ at $600\text{ }^\circ\text{C}$ as a function of w (fraction of Ge atoms transferred from $\text{NiSi}_{1-x}\text{Ge}_x$ to $\text{Si}_{1-x}\text{Ge}_x$). Minimum free energy is achieved with $w = 0.4$, resulting in one gram-atom of $\text{NiSi}_{0.9}\text{Ge}_{0.1}$ in contact with one gram-atom of $\text{Si}_{0.3}\text{Ge}_{0.5}$ at equilibrium [Zha03]

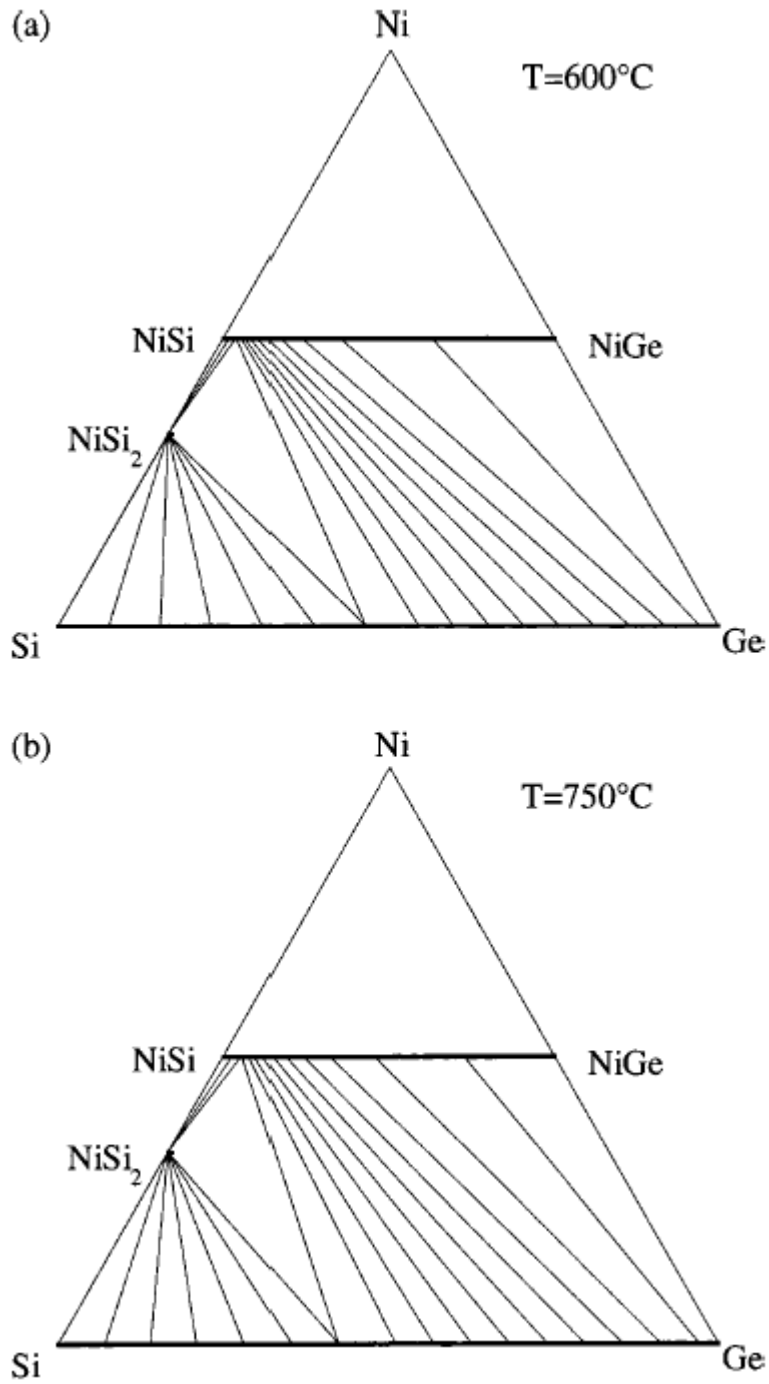


Figure 2-10: Partial isotherms calculated for the Ni-Si-Ge ternary system for (a) 600°C and (b) 750°C . Note that the presence and behavior of Ni-rich phases (e.g. Ni_2Si , Ni_5Ge_3) are neglected [Jar02]

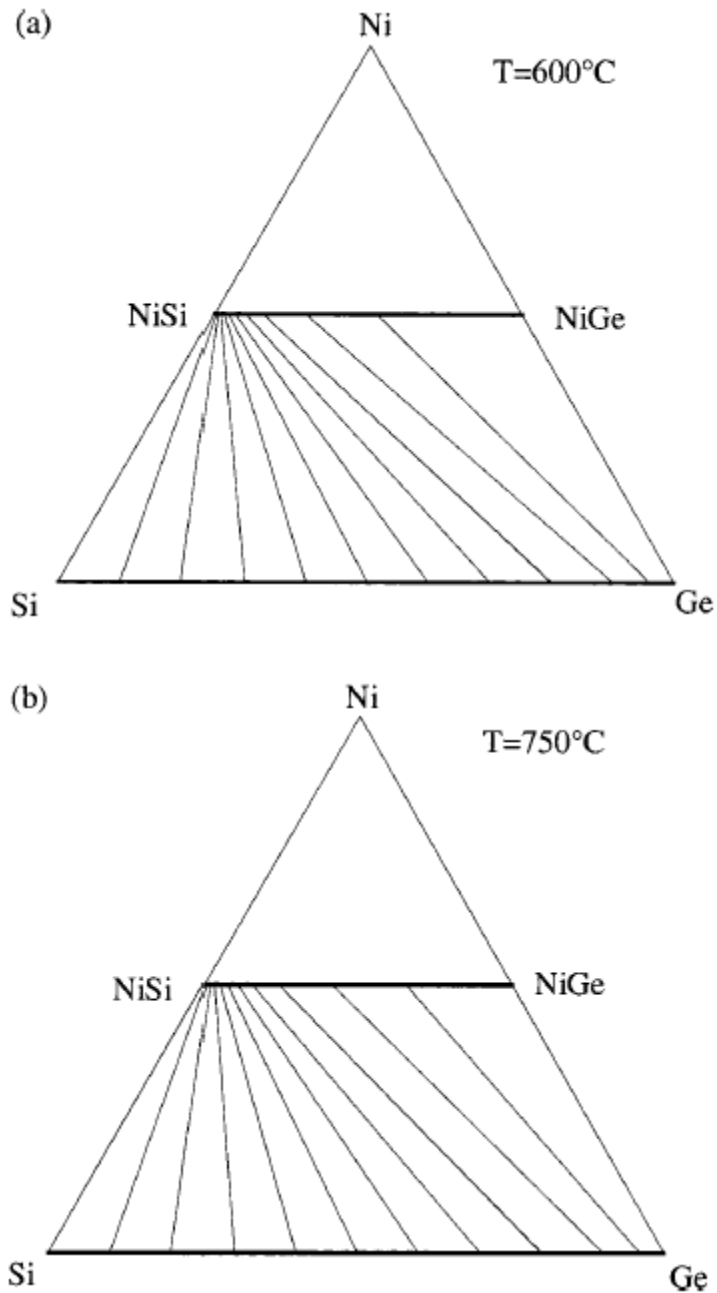


Figure 2-11: Partial isotherms calculated for the Ni-Si-Ge ternary system without inclusion of the NiSi_2 phase for (a) 600°C and (b) 750°C [Jar02]

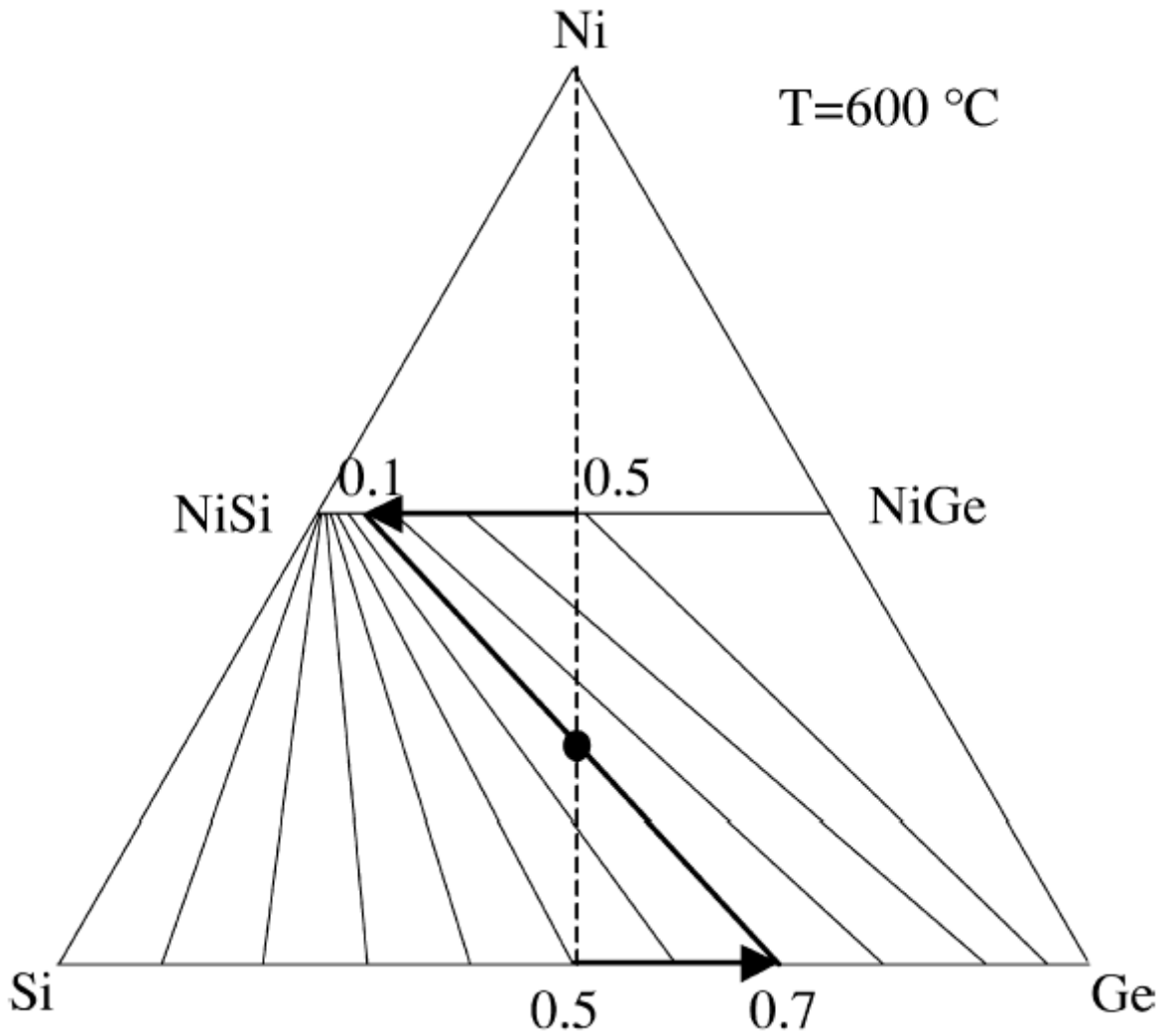


Figure 2-12: Partial calculated isotherm at 600 °C showing the initial and final equilibrium state for one gram-atom of $\text{NiSi}_{0.5}\text{Ge}_{0.5}$ in contact with one gram-atom of $\text{Si}_{0.5}\text{Ge}_{0.5}$ [Zha03].

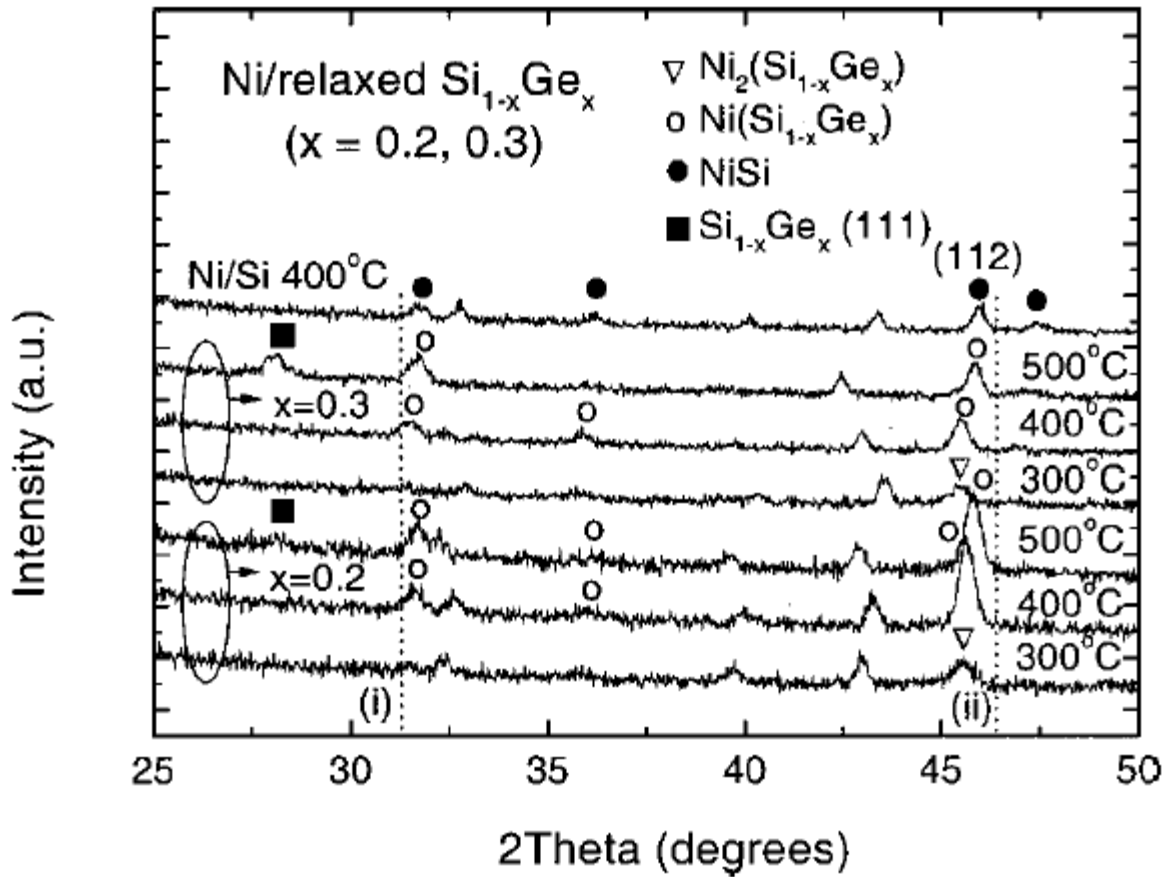


Figure 2-13: XRD θ - 2θ scans showing evolution of Ni-Si-Ge system for 60 second RTAs from 300-500 °C. $\text{Ni}_2(\text{SiGe})$ is shown to predominate at 300 °C while only $\text{Ni}(\text{SiGe})$ is apparent at higher temperatures [Zha02].

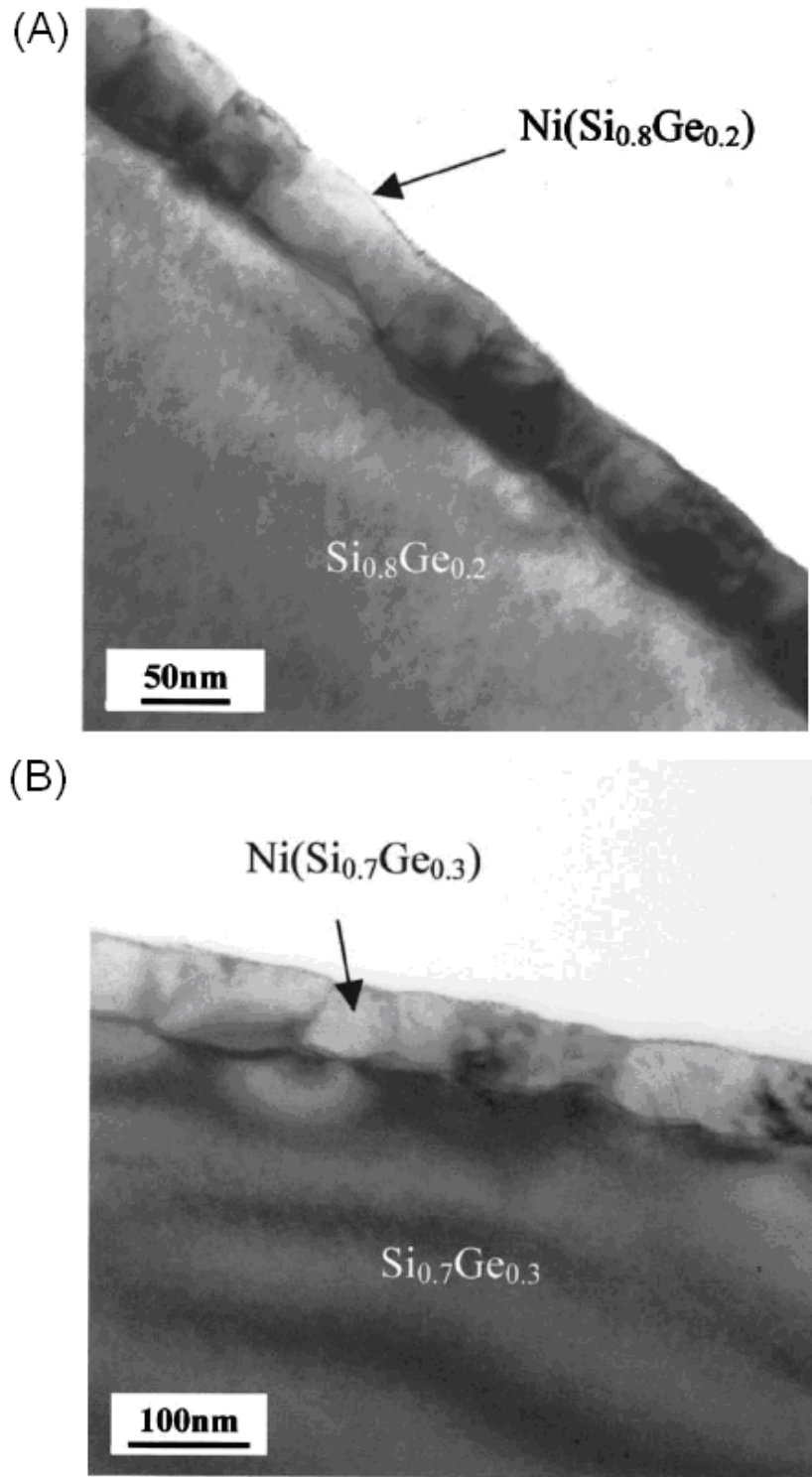


Figure 2-14: Cross-section TEM images of Ni-silicided $\text{Si}_{1-x}\text{Ge}_x$ films annealed at 400 °C for 60 seconds with (a) $x = 20$ at% and (b) $x = 30$ at% [Zha02].

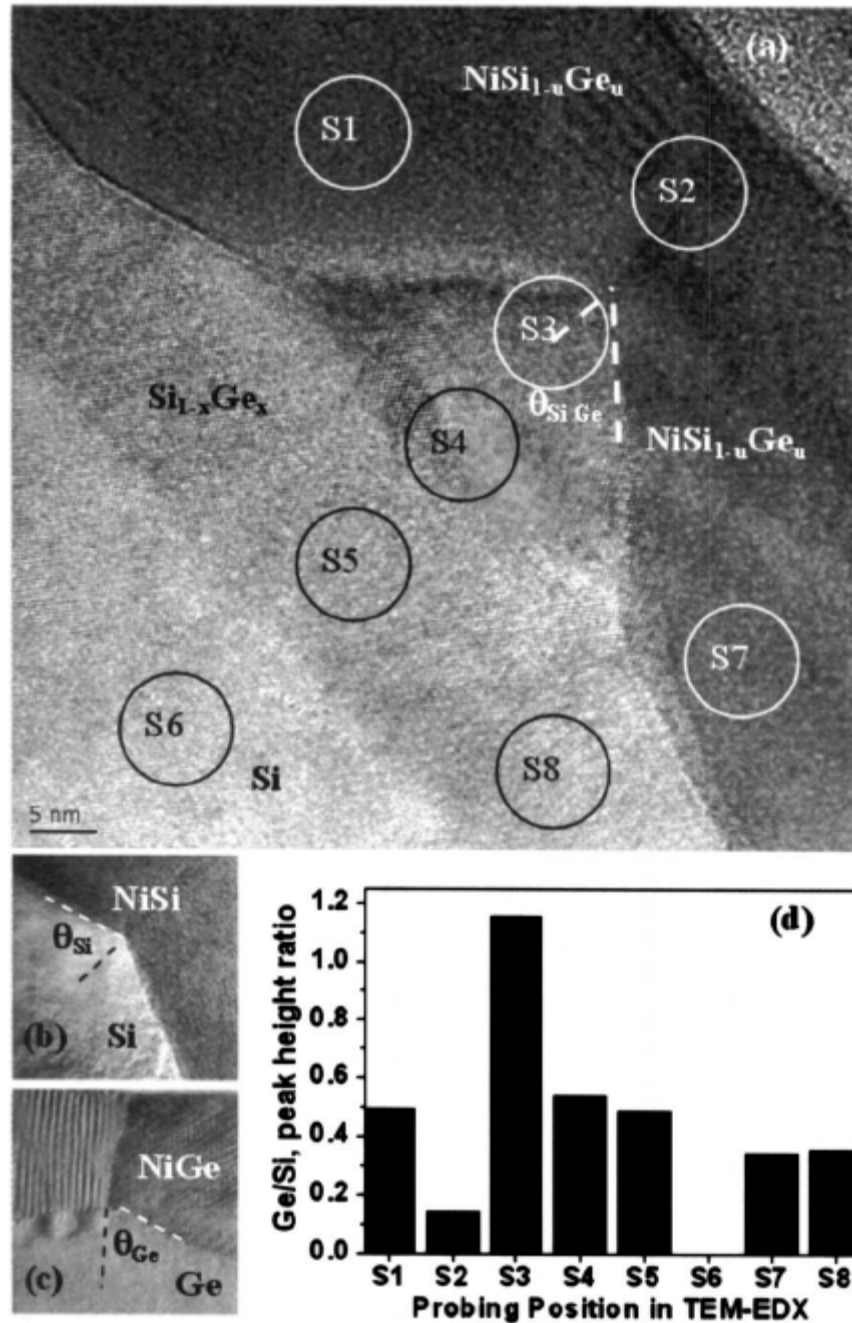
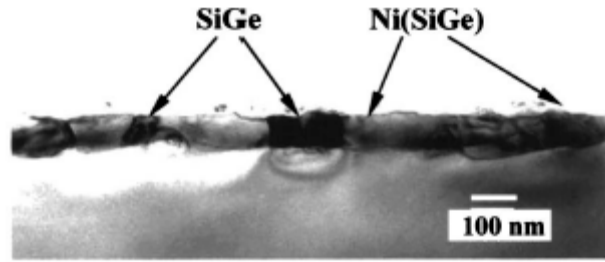
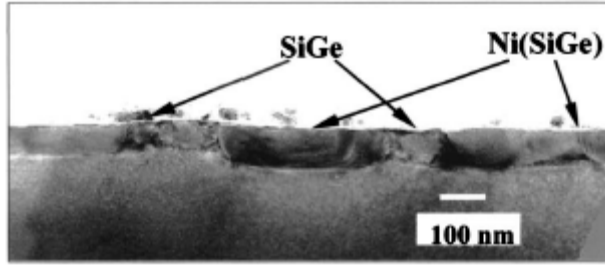


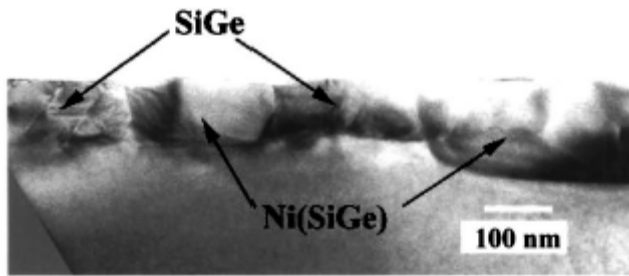
Figure 2-15: Analysis of films annealed at 500 °C including HRXTEM of (a) $\text{Ni}(\text{Si}_{0.8}\text{Ge}_{0.2})$ (b) NiSi (c) NiGe . Grain boundary angle is indicated as θ for each sample. (d) EDS analysis of $\text{Ni}(\text{Si}_{0.8}\text{Ge}_{0.2})$ sample at locations as noted. [Yao07]



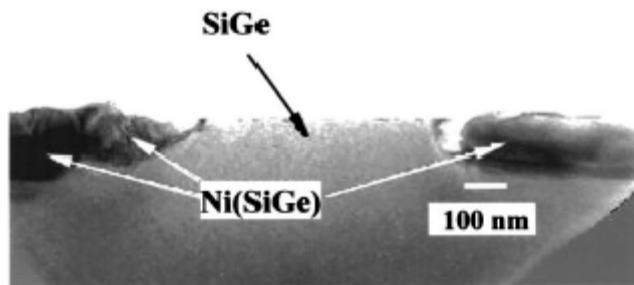
(a)



(b)



(c)



(d)

Figure 2-16: XTEM images of $\text{Ni}(\text{Si}_{0.75}\text{Ge}_{0.25})$ films annealed for 60 seconds at (a) 500°C (b) 600°C (c) 700°C and (d) 800°C [Pey04].

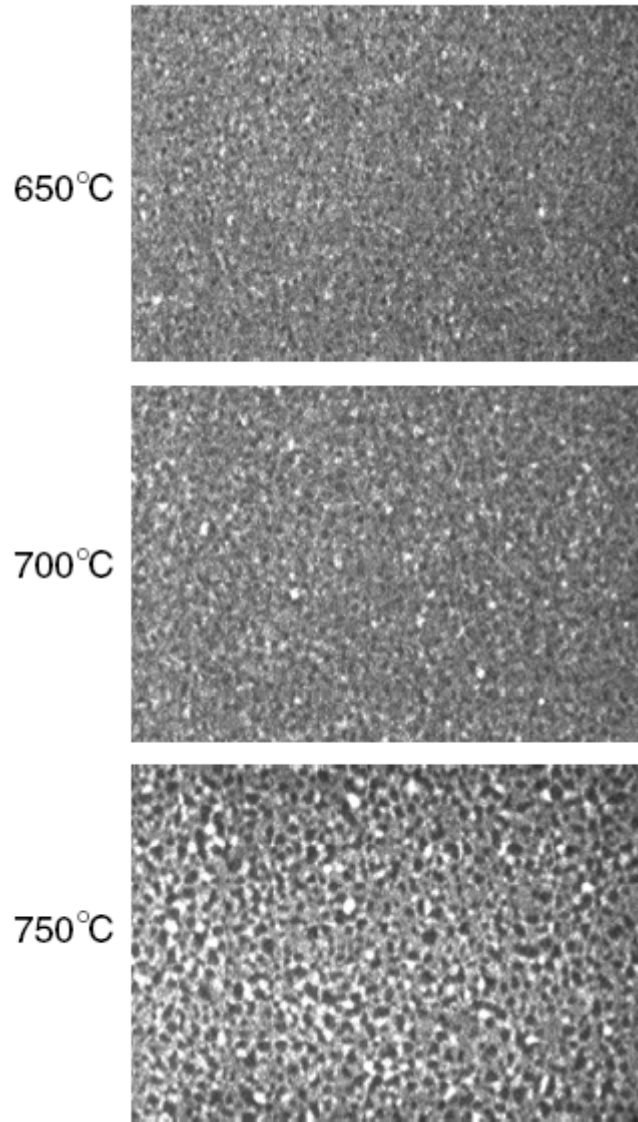


Figure 2-17: Plan-view SEM analysis of $\text{Ni}(\text{Si}_{0.9}\text{Ge}_{0.1})$ grains annealed for 30 seconds at temperatures ranging from 650 to 750 °C [Ok03].

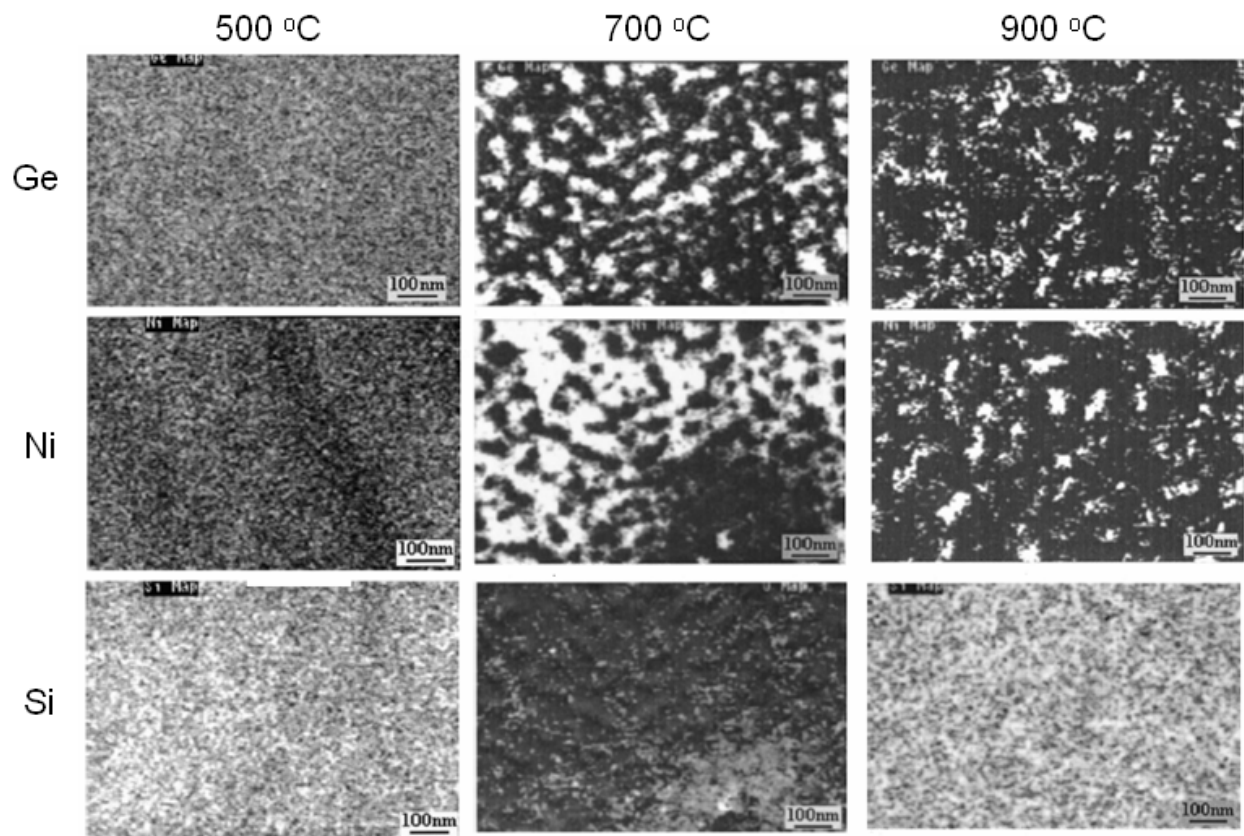


Figure 2-18: AES maps of Ge, Ni, and Si for Ni(Si_{0.75}Ge_{0.25}) samples annealed at 500, 700, and 900 °C for 60 seconds [Pey02].

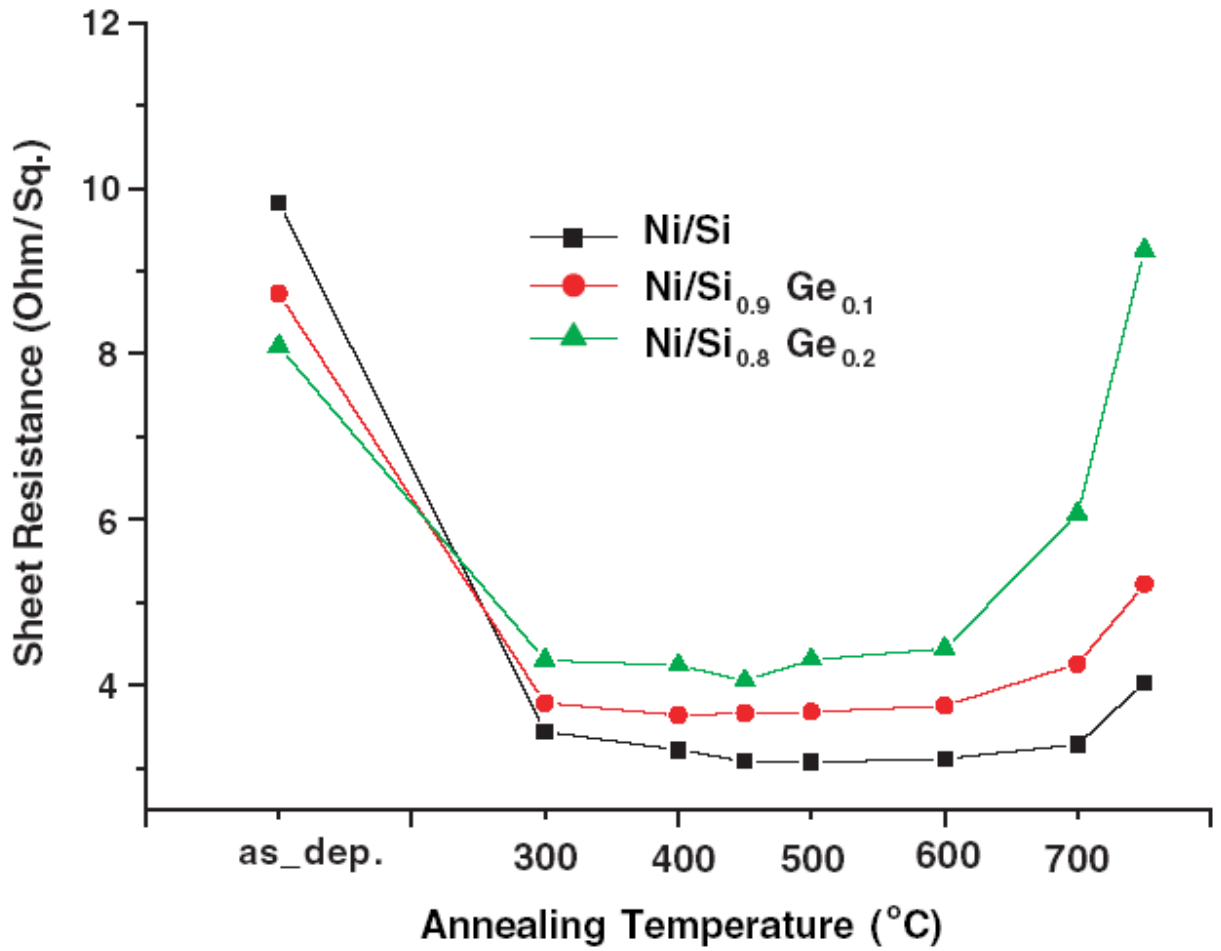


Figure 2-19: Sheet resistance of single crystal Si_{1-x}Ge_x (x = 0, 10, 20 at %Ge) layers silicided with 25 nm of Ni for 30 seconds as a function of annealing temperatures [Ok03].

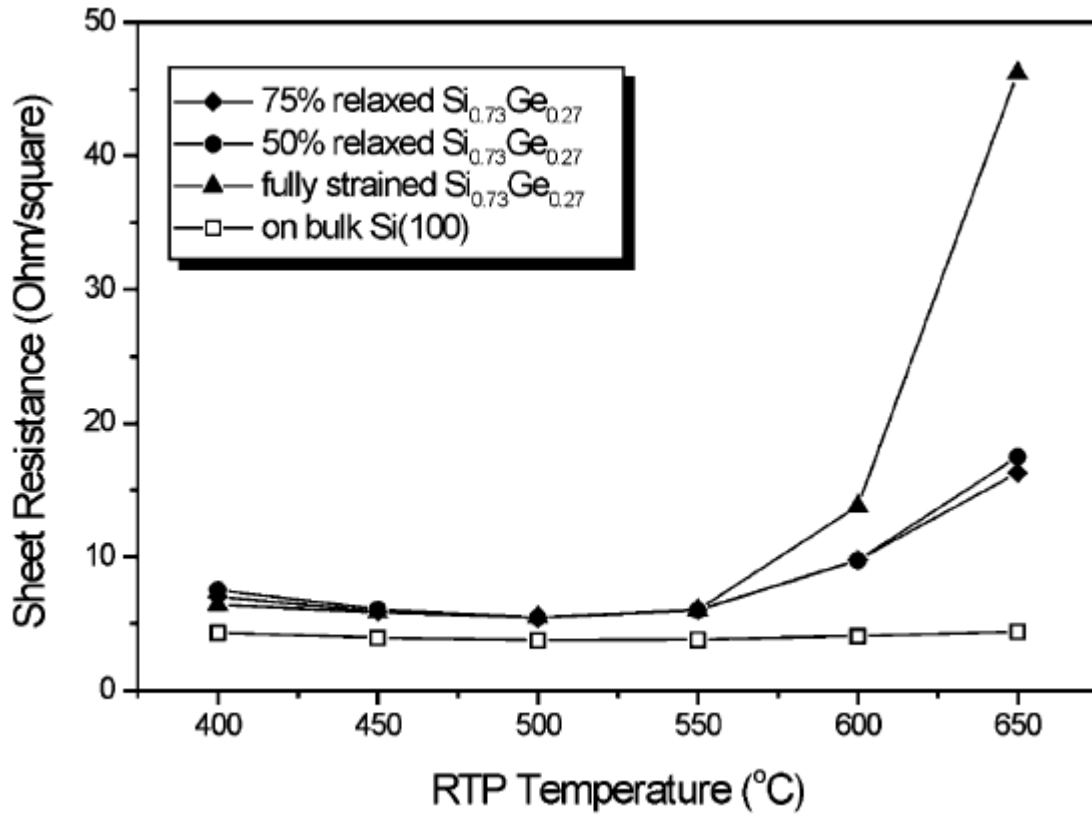


Figure 2-20: Sheet resistance of nickel germanosilicide films as a function of anneal temperatures for samples with varying initial $\text{Si}_{1-x}\text{Ge}_x$ film strain. Samples were annealed for 60 seconds [Zha04].

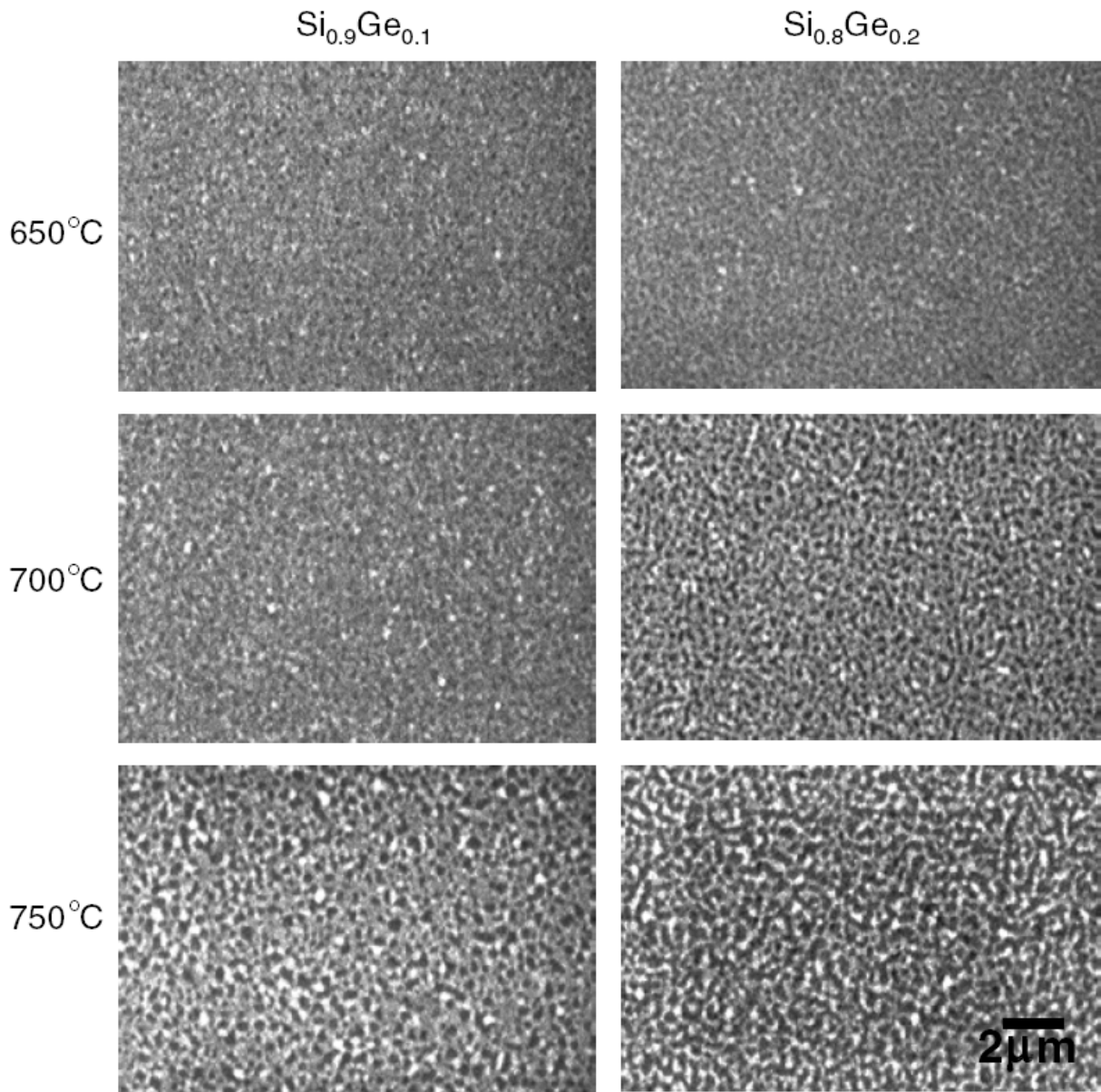


Figure 2-21: Plan-view SEM images of nickel germanosilicide samples with varying concentrations of Ge (10 and 20 at%) in the initial $\text{Si}_{1-x}\text{Ge}_x$ layer annealed at 650, 700 and 750 °C for 60 seconds [Ok03].

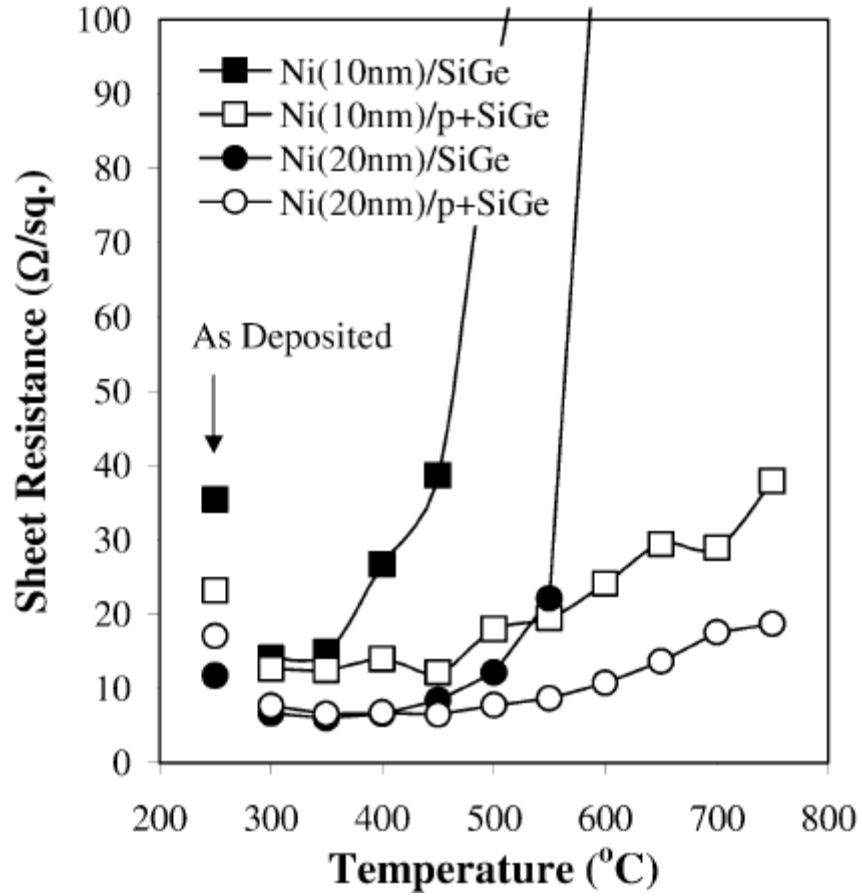


Figure 2-22: Sheet resistance of nickel germanosilicide films as a function of temperature for samples with and without B doping and two initial Ni layer thicknesses. [Liu05]

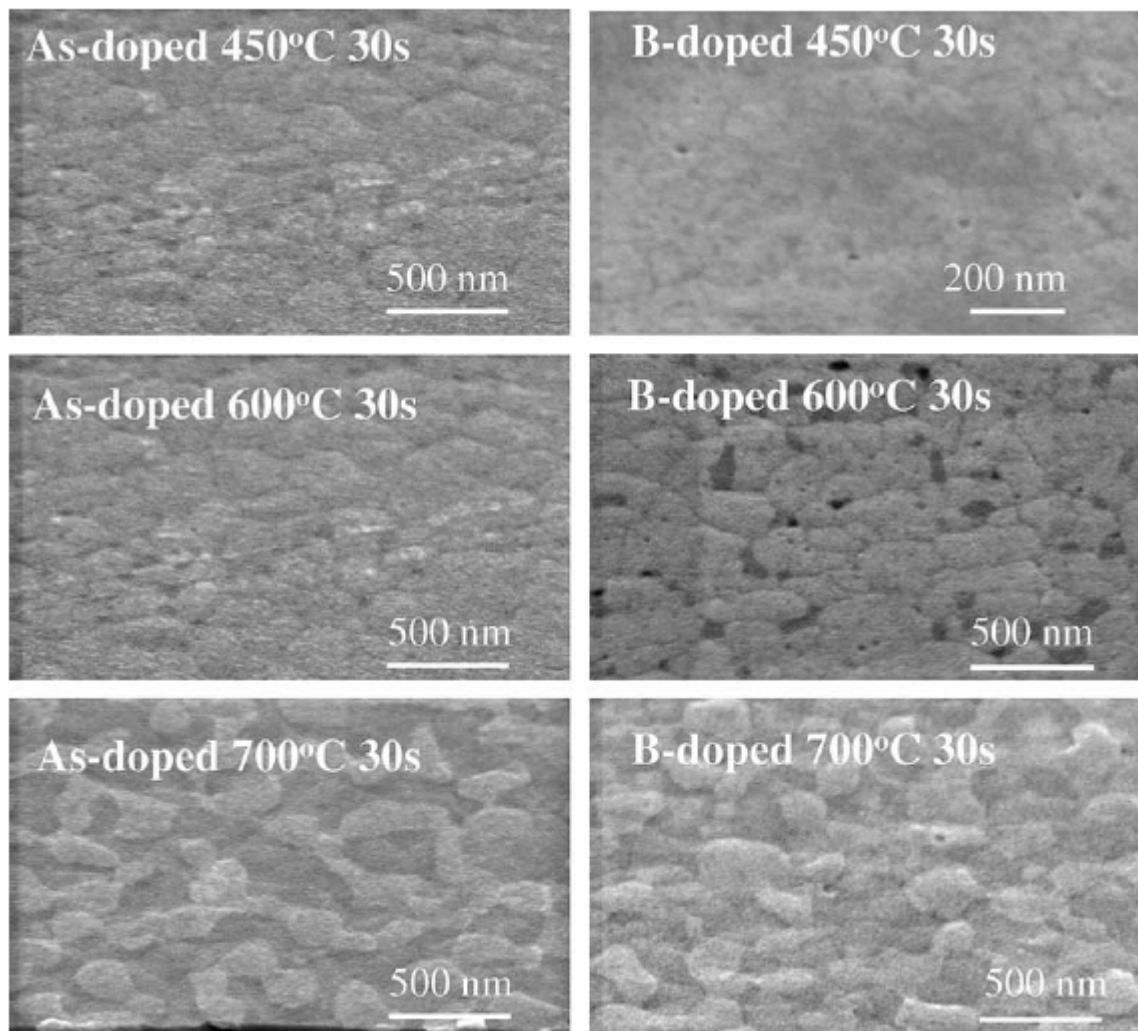


Figure 2-23: Plan-view SEM images of nickel germanosilicide films on As and B implanted single-crystal $\text{Si}_{1-x}\text{Ge}_x$. Samples underwent a two-stage anneal at 400 °C for 60 seconds and 450, 600, or 700 °C for 30 seconds.

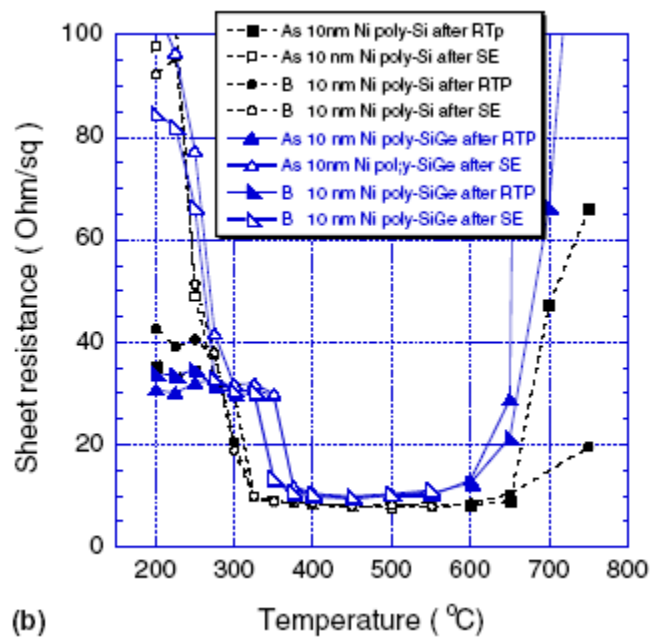
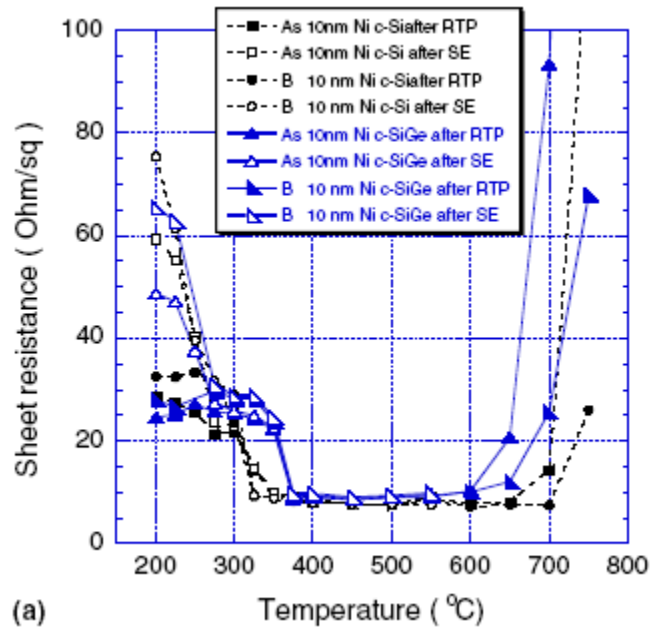


Figure 2-24: Sheet resistance of As and B doped nickel germanosilicide films as a function of anneal temperature for samples with (a) crystalline and (b) polycrystalline $\text{Si}_{1-x}\text{Ge}_x$ layers. [Cha04]

Table 2-1: Measurement of average Ni(Si_{1-x}Ge_x)/Si_{1-x}Ge_x interface roughness for undoped and B-doped samples calculated via AFM after annealing at 400 and 500 °C for 30 seconds. [Liu05]

AFM Roughness		
Temperature	Undoped	Doped
400 °C	12.0 nm	4.4 nm
500 °C	18.0 nm	5.0 nm

CHAPTER 3 DESIGN OF EXPERIMENTS

3.1 Research Objectives

The objective of this work is to clarify certain outstanding issues regarding the morphological stability and electronic properties of nickel germanosilicide thin films. Specifically, this work aims to clarify the relationship between the rejection of Ge from the initial film which results in the formation of Ge-rich $\text{Si}_{1-z}\text{Ge}_z$ grains (commonly referred to as film agglomeration) and observed increases in the sheet resistance of the film. While prior works have proposed a qualitative link between the two properties, no quantitative relationship has been put forth.

This work also aims to confirm whether the addition of high levels of B doping can suppress the agglomeration process as suggested by Liu and Ozturk [Liu05]. Their work did not utilize direct measurement techniques when evaluating film agglomeration and so the degree of suppression, if any, is not well quantified. Regardless if suppression is confirmed to occur, this work also aims to determine if the quantitative relationship between agglomeration and sheet resistance is maintained for B doped samples.

Finally, prior studies available in literature utilize isochronal experiments with very short annealing times. This work aims to expand the knowledge base of the behavior of nickel germanosilicide films over a much larger range of anneal times and temperatures, including both isochronal and isothermal series. By increasing the thermal matrix, information regarding the kinetics of the phase transformation may be obtained.

Achieving these research objectives will lead to greater understanding of the stability and properties of nickel germanosilicide thin films. This understanding, in turn, can be used to further evaluate the use of the layers as intermediate contacts in semiconductor devices.

3.2 Factors and Levels

The choice of factors and levels used in this work were strictly constrained due to the lack of availability of in-house wafer processing capability. Many factors known to affect the behavior of nickel germanosilicide films, such as initial nickel layer thickness or $\text{Si}_{1-x}\text{Ge}_x$ crystal quality, require separate wafers to study each level. Thus, only the two such factors thought to be most important were selected for this work: Ge concentration of the initial $\text{Si}_{1-x}\text{Ge}_x$ layer and homogeneous boron doping of the $\text{Si}_{1-x}\text{Ge}_x$ layer during growth. As each of these factors was varied at two levels, only four wafers were needed for all experiments performed in this work. The other factors studied in this work, anneal temperature and anneal time, were able to be varied over many levels as ample thermal processing ability was available.

It would have been possible to include other factors in the study with a relatively small number of additional wafers through use of an experimental design allowing the screening of multiple factors, such as a fractional factorial design. Such a design, however, was rejected as the intent of this work was not to determine which factors are critical to nickel germanosilicide growth (this knowledge is available in the literature) but to explore a few known factors in greater depth.

3.2.1 Factors Altered

Four factors were varied in the experiment: anneal temperature, anneal time, Ge content in the $\text{Si}_{1-x}\text{Ge}_x$ film, and boron doping of the $\text{Si}_{1-x}\text{Ge}_x$ film. The factors were varied over a range of levels dependent upon the availability of resources. For temperature, levels of 450 to 800 °C in increments of 50 °C were used. All thermal anneals were performed in a quartz-tube furnace under a N_2 ambient atmosphere. For time, levels of 10, 30, 90, 270, and 1020 minutes were chosen. Anneal lengths were timed using a laboratory timer. For Ge content, levels of 15 and 25 at% were used. Higher Ge concentrations were not available due to limitations in reactor

processing capability. It is known that Ge composition is a critical factor in nickel germanosilicide behavior as increasing Ge content will increase the thermodynamic driving force for the rejection of Ge. This, in turn, results in increased reaction rates and the formation of $\text{Si}_{1-z}\text{Ge}_z$ grains with higher Ge content. It was expected that these differences would also affect the sheet resistance of the films. The effect of increasing Ge concentration is also important since, as previously discussed, it is expected that future device designs will utilize higher Ge concentrations to increase the strain state of the device structures. For boron doping, levels of undoped and homogeneously doped at a concentration of $\sim 4.5 \times 10^{19}$ atoms/cm² were selected. While this concentration was lower than the $\sim 1 \times 10^{21}$ atoms/cm² used by Liu and Ozturk [Liu95], it represents the maximum level possible with the reactor used to grow the material. Homogeneous boron doping during growth is an important factor as it is likely to be included in future device generations since, as previously discussed, it eliminates the need for implantation and activation of source/drain well dopants.

All possible combinations of the factors and levels were performed and analyzed in this work, resulting in each of the four experimental structures being studied over a significant thermal matrix. Thus, the overall matrix may also be treated as either five isochronal or eight isothermal anneal series. Analysis of the repeatability of the anneal process was also verified; the results of this analysis is available in Appendix A.

3.2.2 Factors Held Constant

Additional factors determined by prior research to affect nickel germanosilicide formation, stability, and electronic properties were not varied in this work. The factors held constant include the initial Ni layer thickness and the crystalline quality, strain state, and thickness of the $\text{Si}_{1-x}\text{Ge}_x$ layer. While these factors are known to affect nickel germanosilicide film stability, they

are expected to be either less influential than those varied in this work, less likely to be varied in future device designs, or both.

3.3 Experimental Structure

The relaxed $\text{Si}_{1-x}\text{Ge}_x$ layers used in this work were grown using an ASM Epsilon 3200 RP-CVD tool at Texas Instruments, Inc. Prior to deposition, (001) Si substrate wafers underwent a HF clean and H_2 bake at 1050 °C for 3 minutes to remove both the native Si oxide and any contaminants from the wafer surface. Once cleaned, single crystal $\text{Si}_{1-x}\text{Ge}_x$ layers were grown using dichlorosilane and germane precursors in a hydrogen carrier gas with a flow of 40 standard liters per minute. Borane was also included during growth for the boron doped samples. Growth was carried out at 700 °C and a fixed pressure of 10 Torr. Final $\text{Si}_{1-x}\text{Ge}_x$ layer thickness was 150 nm. Subsequent to $\text{Si}_{1-x}\text{Ge}_x$ layer growth, all wafers were capped with 10 nm of sputtered Ni metal and 10 nm of TiN. It should be noted that the initial structure design called for only 0.5 nm of TiN deposition. As will be discussed in later chapters, however, the presence of the excess TiN was not found to affect the behavior of the nickel germanosilicide nor did it impact the analytical techniques utilized in this work.

3.4 Characterization Techniques

Several types of characterization techniques have been used to analyze the nickel germanosilicide films studied in this work. These techniques include Cross-Section Transmission Electron Microscopy (XTEM), Scanning Electron Microscopy (SEM), Electron Dispersive Spectroscopy (EDS), Secondary Ion Mass Spectrometry (SIMS), Four Point Probe (4PP), and the ImageJ image analysis software. It is important that the abilities and limitations of each technique are understood so that the results they provide may be correctly interpreted. Therefore, the following sections briefly describe each technique, how it may be applied to film analysis, and information about the specific tools and methods used in this work. More in-depth

discussions of major techniques' fundamentals are available in other works, such as the text by Brundle, Evans, and Wilson [Bru92].

3.4.1 Cross-Section Transmission Electron Microscopy

Transmission Electron Microscopy (TEM) is a technique which can be used to obtain images, diffraction patterns, and composition information from a sample. To image a sample with TEM, a beam of monochromatic electrons is focused on a very thin sample (typically less than 200 nm thick). As the beam of electrons passes through the sample, some electrons are inelastically scattered due to electron-atom interactions. Heavier atoms cause a stronger interaction, which leads to increased scattering. The transmitted electrons may then be imaged using a phosphorus screen or digital camera placed opposite and normal to the beam direction to provide precise images of the sample with very high magnification. The differently scattered electrons produce phase contrast in the image (areas of higher mass in the sample appear darker). Electron-atom interactions can also produce x-rays characteristic of the scattering atom. Characteristic x-rays may be captured by a dedicated detector and analyzed separately, a process which will be discussed in a later section. This technique, called Energy Dispersive X-Ray Spectroscopy (EDS), provides information about the atoms present in the analyzed region.

For analysis of nickel germanosilicide films, XTEM imaging is especially useful for determining the thickness of the film as layers are directly measured (as opposed to calculated or simulated from models with fitting parameters). The technique can also provide limited information about the morphology of the film, such as the size and distribution of grains in the layer, though it is important to consider that estimating these characteristics from cross-section is much less preferred than using a plan-view analysis technique. When combined with EDS analysis, the composition of the sample within a region of the image defined by the spot size of the beam can also be semi-quantitatively determined.

In this work, two TEMs located at the Major Analytical Instrumentation Center (MAIC) at the University of Florida were utilized for sample analysis. For low-magnification images, a JEOL 200CX was used. For high resolution images, a JEOL 2010F was used. XTEM samples in this work were produced using a FEI DB 235 Focused Ion Beam (FIB) mill to shape membranes approximately 8 microns long, 5 microns tall, and 150 nm thick from the parent material. The membrane was oriented such that its major plane was perpendicular to the surface of the material and oriented such that the [110] direction was normal to the sample plane. Once milled and fully cut away from the parent sample, XTEM samples were extracted using an ex-situ micromanipulator and placed on 3mm nickel grids backed with carbon films for imaging in the TEM. The XTEM samples were imaged in bright field along the $\langle 110 \rangle$ axis and/or in bright field using a two beam condition with $\langle 220 \rangle$ g vector.

3.4.2 Scanning Electron Microscopy

Scanning Electron Microscopy (SEM) is a versatile technique which can provide a variety of information about a sample. In SEM, a beam of energetic electrons is rastered (scanned) across the surface of a sample. The electrons interact with the sample and produce secondary electrons (SE), backscattered electrons (BSE), and characteristic x-rays; the signal associated with each of the interactions can then be captured with an appropriate detector. Secondary electrons, produced when primary electrons are inelastically scattered by atoms in the sample, provide topographical imaging of the surface of the sample. Depressed areas, such as pits and crevices, trap SE while raised areas, such as ridges and bumps, release more SE causing the areas to be darker and brighter, respectively, in the image. Backscattered electrons, produced when primary electrons are elastically scattered by atoms in the sample, provide images showing phase contrast in the sample. The phase contrast occurs due to the higher likelihood of electrons being elastically scattered by atoms with higher atomic numbers. Thus, regions with more massive

atoms will appear brighter in the BSE image. Finally, as in TEM analysis, characteristic x-rays can also be produced when the primary beam interacts with the sample. The EDS analysis of these x-rays is identical to that of those produced in TEM analysis and will be discussed in the next section.

Both SE and BSE imaging modes can be used to analyze nickel germanosilicide films. Plan-view SE imaging of the film surface and interfaces revealed by etching can provide information about qualitative surface roughness. Plan-view BSE imaging of the films is especially useful for monitoring the stability and size of the grains in the film as any non-uniform changes in composition difference can create contrast in the image. Plan-view measurement of grain size in either imaging mode also can provide direct measurements of grain size and distribution over a relatively large sampling area defined by the magnification of the image. As with TEM, when combined with EDS analysis the composition of the sample within a region of the image defined by the spot size of the beam can also be semi-quantitatively determined.

In this work, a JEOL 6335F field emission SEM located at MAIC was used to image samples. Plan-view samples for SEM analysis were prepared by cleaving small regions from thermally processed wafer pieces. The small regions were then mounted to an aluminum SEM puck using double sided carbon dots. The puck and samples were then coated with ~10 nm of carbon to prevent charging of the sample during imaging. Samples were imaged at $9.63\text{E-}5$ Torr in BSE mode with a working distance of 9 mm, a probe current of $12\ \mu\text{A}$, and accelerating voltage of 15 kV. Three images of each sample for quantitative analysis were taken at a magnification of 30,000x and a scan speed of 23 seconds/frame. Image processing and quantification is discussed in a later section of this chapter. While the reproducibility of the imaging quantification process was unable to be studied due to limitations in personnel time and

availability, an analysis of the repeatability of the SEM imaging method used in this work is presented in Appendix A.

3.4.3 Electron Dispersive Spectroscopy

As mentioned previously in the sections discussing TEM and SEM techniques, when a high energy primary electron interacts with an atom a characteristic x-ray can be produced. In this process, the primary electron causes the removal of an inner shell electron from the atom. To compensate for the loss, an electron in a higher energy shell in the atom fills the inner vacant position and after releasing its excess energy through the formation of an x-ray. The x-ray's energy is characteristic of the atom as the difference between the two energy levels (inner and outer) is, with few exceptions, different for each atomic species. If there are still higher energy shells, the process will repeat until only the outermost shell is missing an electron. Thus, a single strike may lead to the generation of a number of characteristic x-rays. The intensity of the x-rays can then be detected and plotted as a function of their energy. From this graph, the atomic species present in the sampled area can be identified and their relative concentrations semi-quantitatively determined. It is important, however, to note that characteristic x-rays are also produced throughout an interaction volume. Thus, depending on the spot size and energy of the beam, signal may also be produced by adjacent regions such as neighboring grains or underlying layers. These possible additional contributions must be considered when analyzing and interpreting EDS results. It is also important to mention that EDS cannot provide absolute phase identification (as can XRD analysis) since its results are semi-quantitative and lack any information about the actual structure of the analyzed region.

For the study of nickel germanosilicide films, EDS offers a local analysis method capable of determining the types and concentrations of atoms present within individual grains and, with high-resolution tools, in proximity to grain boundaries and interfaces. These results, when used

in conjunction with SEM and/or TEM analysis, can provide greater insight into the imaged structures in both cross-section and plan-view.

EDS analysis of XTEM samples in this work was performed using an Oxford Inca EDS system on the JEOL2010F TEM located in the MAIC. A 1 nm nominal spot size was used for point composition analysis, though a more accurate lateral resolution would be slightly higher as both beam drift and beam spreading effects must be taken into consideration. Semiquantitative analysis of the spectra was performed using the Cliff Lorimer thin ration section. The ratio of the relevant atomic species (disregarding C, Cu signal from the TEM grid) was then determined to arrive at an approximate local composition. It should be noted, however, that this process is very approximate and significant error is likely present in the results. EDS analysis of plan view SEM samples was performed using an Oxford Inca EDS system on the JEOL SEM 6400 located in the MAIC. A nominal spot size of 5 nm was used for this analysis. The ratio method described above was also used to determine approximate local composition for the plan view SEM samples.

3.4.4 Secondary Ion Mass Spectroscopy

Compositional profiling of films is also possible using SIMS analysis; the technique is especially appropriate for measuring smooth, continuous, multilayered structures. During SIMS analysis, the sample is bombarded with a stream of ions which sputter particles, including “secondary” ions, from the sample’s surface. A mass spectrometer then measures the mass-to-charge ratio of the secondary ions and this information is used to determine the average elemental composition of the sputtered layer. As the sputtering process continues, more material is removed and analysis moves deeper into the sample. In this manner, a raw SIMS profile of ion intensity per unit time is obtained. The raw data may then be converted into a quantitative composition profile as a function of depth by using a three step process. First, elemental signal

intensity is converted into elemental concentration based on variables including secondary ion sputtering yield and detection efficiency. Next, sputtering time is converted into sputter depth via calculations involving substrate sputtering rate. Finally, a depth resolution function (DRF) must be assessed and used to reconstruct the original distribution of the atomic species.

Thus, SIMS analysis can be used to profile the composition of nickel germanosilicide films as a function of depth. It is important to remember, however, that since SIMS analysis averages the composition of each sputtered layer over the entire beam spot size a great deal of structural information is lost during analysis (i.e. lateral composition differences). If an interface is rough, SIMS analysis will also provide less-abrupt measurements of changes in concentration across the interface. Use of SIMS analysis should therefore be confined to germanosilicide films that are homogeneous and planar to provide optimal results.

SIMS analysis in this work was performed using a PHI Adept 1010 Dynamic SIMS system located at the Advanced Materials Processing and Analysis Center (AMPAC) at the University of Central Florida. Samples were analyzed using an 2 kV, 50 nA O_2^+ primary beam and raw data was converted into concentration vs. depth plots using the sputtering rate and ion yield of undoped or B-doped SiGe standards, as appropriate. Analysis was performed over a 300 μm square region with 10% detection area to avoid crater wall effects. It should be noted that with these conditions, analysis of Ti and Ni containing layers will be less precise (especially for thickness measurements).

3.4.5 Four Point Probe

Four point probe (4PP), also know as Kelvin probe, analysis can provide information about the resistivity of a sample. In this technique, four terminals are placed in contact with a sample along a straight line. The outer terminals and the sample form a circuit through which a set current is passed. The inner terminals and the sample form a separate circuit which is passed

across a voltmeter. The voltmeter measures the decrease in potential between the two inner probes and, with the knowledge of the sample geometry and applied current, can allow the resistivity of the sample to be measured. Commonly, however, the resistivity of a thin film is not reported. Instead, the sheet resistance of the film is often discussed. The sheet resistance of a thin film is defined as the resistance measured for a thin film of equal length and width (a square). Thus, sheet resistance is equal to the resistivity of the film divided by the film's thickness and will be constant for any sized square sample. The sheet resistance of a sample can be directly calculated from 4PP data and, with the use of geometrical correction factors, can also be determined for an irregularly sized sample. It should be mentioned, however, that sheet resistance alone cannot define all of the electronic properties of a film (i.e. contact resistance, etc.) Nevertheless, sheet resistance does present a good general idea of the suitability of a film as a current conductor.

Since the primary application of nickel germanosilicide films is to provide an intermediate conduction layer between the source/drain wells of a device and its interconnect metallization, knowledge of a film's electronic properties is of great importance. Due to its relatively easy measurement through use of 4PP analysis, sheet resistance is most often used to provide insight into the electronic properties of a film. While other analysis techniques are sometimes applied to determine additional electronic properties of the films, most of them require the formation of 2- or 3-D test structures which adds to the expense and complexity of the analysis.

In this work, 4PP analysis was performed using rectangular wafer sections with nominal measurements of 10 by 15 mm. Samples were analyzed using a Jandel Engineering multi height probe with a linear configuration of carbide tungsten tips at a uniform spacing of 1.016 mm. Samples were measured using a 900 μ A current. If voltage readings could not be successfully

obtained with that level of current, the current was adjusted as necessary until successful readings could be taken or the sample was determined to be non-conductive. Measurements were performed at room temperature with the probe axis parallel to the long side of the wafer sections in both forward and reverse current mode. A 10% difference in readings was allowed between the forward and reverse modes; otherwise the probe location was adjusted until measurements fell within the allowance. The average of both voltage (V) measurements was then used in conjunction with the appropriate geometry correction factor (F) found in Table 3-1 and the probe current (I) to calculate the sheet resistance (R_s) of each sample according to Ohm's law, given in equation 3-1.

$$R_s = \frac{V}{I} F \quad \text{Equation 3-1}$$

A gauge repeatability and reproducibility analysis of the 4PP analysis technique used in this work is included in Appendix B. It was determined from this analysis that a 95% confidence interval of +/- 2.19 Ohm/sq can be applied to each data point in order to capture any variation in the measurement process.

3.4.6 Image Processing and Quantification

Quantification of SEM images is notably absent in prior work discussing nickel germanosilicide thin films. Accordingly, a method of processing and quantifying images was developed for this work. The majority of these tasks were performed using ImageJ v. 1.38x, a public domain, Java-based image processing program developed at the National Institute of Health. The program, available at the time of writing at [http://rsb/info.nih.gov/ij/](http://rsb.info.nih.gov/ij/), contains a large number of post-processing and image analysis options which may be used for a wide array of purposes. In this work, ImageJ was first used to remove the area of the raw image containing the scale bar in the SEM/BSE images by selecting the area of interest and using the "crop"

(Image>Crop) command. The noise in each images was also reduced though use of the “despeckle” (Process>Noise>Despeckle) command and three applications of the “smooth”(Process>Smooth) option. An example of a raw image is shown in Figure 3-1(a) and the same image after processing is shown in Figure 3-1(b)

Once processed, a user-defined grayscale threshold was selected to differentiate between contrasting grains, eliminating shades of gray and creating a binary image of black and white. Selecting a threshold allows the area fraction and average size of the black or white areas in the image to be quantified. Depending on the anneal conditions in this work, two or three phases were visible in each image. Images with two phases present had a single threshold applied to differentiate the phases. Images with three phases present had two thresholds individually applied to distinguish either the lightest and darkest phase from the rest of the image. Examples of thresholds applied to both types of images are shown in Figure 3-2.

The average grain size (in arbitrary units) and area fraction (in percent) of the black regions was then calculated for each thresholded image using the “analyze particles” (Analyze>Analyze Particles) tool. Final quantification values were determined for each sample by averaging the results of three images taken of the same experimental sample. If present, the area fraction of the third phase (the medium shade) was determined by subtracting the area fractions of the other two phases from 100. Grain sizes of the third phase were not calculated for reasons which will be discussed later. Error bars for the quantified results were statistically determined to be +/- 3.35% for a 95% confidence interval; determination of this interval is discussed in Appendix A.

For selected samples, the tortuosity of a connected phase was also calculated. Tortuosity, in its simplest form, is defined as the measure of the twisting of a path. The most basic method

to calculate tortuosity (τ) is to divide the actual path length, L, by the minimum distance between the endpoints of the path (its chord, C). This calculation is presented as Equation 3-2.

$$\tau = \frac{L}{C} \quad \text{Equation 3-2}$$

The quality of the SEM/BSE images in this work precluded the direct application of computer software to determine tortuosity. Specifically, the images were too grainy and the contrast too shallow for sufficiently accurate definition of individual grains and grain interfaces. Instead, the tortuosity was roughly calculated by hand. First, a line of given length was randomly drawn on a SEM/BSE image. The minimum length continuous path between the line endpoints within the desired phase was then estimated and its length measured. The tortuosity was then calculated by dividing the path length by the length of the initial line. An example of a SEM/BSE image with the initial path as a blue dashed line and the estimated continuous path as a solid red line is presented in Figure 3-3. This process was repeated three times for each image and the measurements averaged to determine the tortuosity. The error in the tortuosity measurement will be addressed in a later section.

3.4.7 Statistical Analysis

Statistical analysis of data was performed at many points in this work, including both paired t-tests and ANOVA analyses. A paired t-test (also known as a dependant t-test) is a basic statistical analysis technique which determines if the mean difference between two populations from which paired observations are drawn is likely different from a reference value, usually zero. For example, a paired t-test can be used to compare the grain size of samples with high and low levels of Ge content at each point of a thermal matrix. Using a reference value of zero, the test will determine whether it is statistically likely that changing Ge content affects grain size. By

pairing the samples, the test disregards the influence of anneal time and temperature and only calculates the influence of the Ge concentration factor.

To perform a t-test, a t-statistic is calculated from the data by first determining the difference ($D = X_2 - X_1$) between each pair of samples according to Equation 3-3. Next, a t-statistic is calculated from the values for D and the total number of paired samples (n) according to Equation 3-4.

$$D = X_2 - X_1 \quad \text{Equation 3-3}$$

$$t = \frac{\sum D}{\sqrt{\frac{n \sum D^2 - (\sum D)^2}{n-1}}} \quad \text{Equation 3-4}$$

Once the t-statistic has been calculated, it is compared to a critical t-statistic found using the desired confidence level and degrees of freedom (equal to n-1) from a standard t-distribution table to determine if a statistically significant difference exists. Alternatively, a p-value may be calculated from the t-statistic and, with the desired confidence level, used to evaluate the data. To aid analysis, Minitab version 15.1.1.0 was used to perform the statistical calculations presented in this work

Analysis of Variance (ANOVA) analyses are also used in this work as they offer the ability to test whether there is a statistically significant difference between the levels of one or more factors in a single analysis. The analysis can also determine if multiple factors combine to create interactions (synergistic effects) in the response variable. Performing the calculations to determine p-values for the factor and interaction terms in an ANOVA analysis, however, is a complicated topic and the reader is referred to an introductory statistics text for a detailed discussion of the theory and methodology of the analyses. As with the paired t-tests, Minitab version 15.1.1.0 was used to the statistical calculations for the ANOVA analysis presented in this

work. Minitab analysis provides calculated p-values for each factor and interaction term and, with the desired confidence level, these p-values may be used to determine the significance of each factor.

3.5 Analysis of As-Grown Samples

Samples from the as-grown wafers used in this work were analyzed with XTEM to ensure proper growth of the experimental structures. A representative XTEM image is shown in Figure 3-4. Analysis of the images from the as-grown samples showed acceptable layer thicknesses of 150 +/- 3 nm, 10 +/- 1nm, and 10 +/- 1 nm for the Si_{1-x}Ge_x, Ni, and TiN layers, respectively. Interfaces in the as-grown samples were found to be smooth and abrupt. The presence of dislocations at the Si_{1-x}Ge_x/Si interface was noted in all samples. While XRD analysis of the Si_{1-x}Ge_x layer strain state was not performed on samples in this work, it is known that the thickness of the Si_{1-x}Ge_x layer in each sample exceeds the critical value established for strain relaxation [Mat74, Peo85]. It can be concluded, therefore, that the Si_{1-x}Ge_x layers in this work are relaxed and any influence of strain on agglomeration will not be present in the samples.

SIMS analysis was also performed to confirm the Ge concentrations and B doping levels of the as-grown wafers; the results from the analysis are presented in Table 3-2. Analysis of the results indicates correct growth of the experimental structures. While the doped structure at the lower Ge level showed a slightly lower Ge concentration than the undoped structure at the same level, the difference is only ~2 at%. This difference is unlikely to cause significant variation in the experimental results. The Ge distribution in the Si_{1-x}Ge_x layer was also found to be uniform and continuous in the plots of concentration vs. depth, not included here. Analysis of the B doped samples showed homogeneous, uniform doping levels of 4.58E19 and 4.33E19 atoms/cm³ for the low and high Ge level samples, respectively. This doping level represents the maximum possible doping using the available reactors and processing time. With the XTEM results, these

findings allow the conclusion that the experimental structures used in this work were correctly grown and may be directly compared.

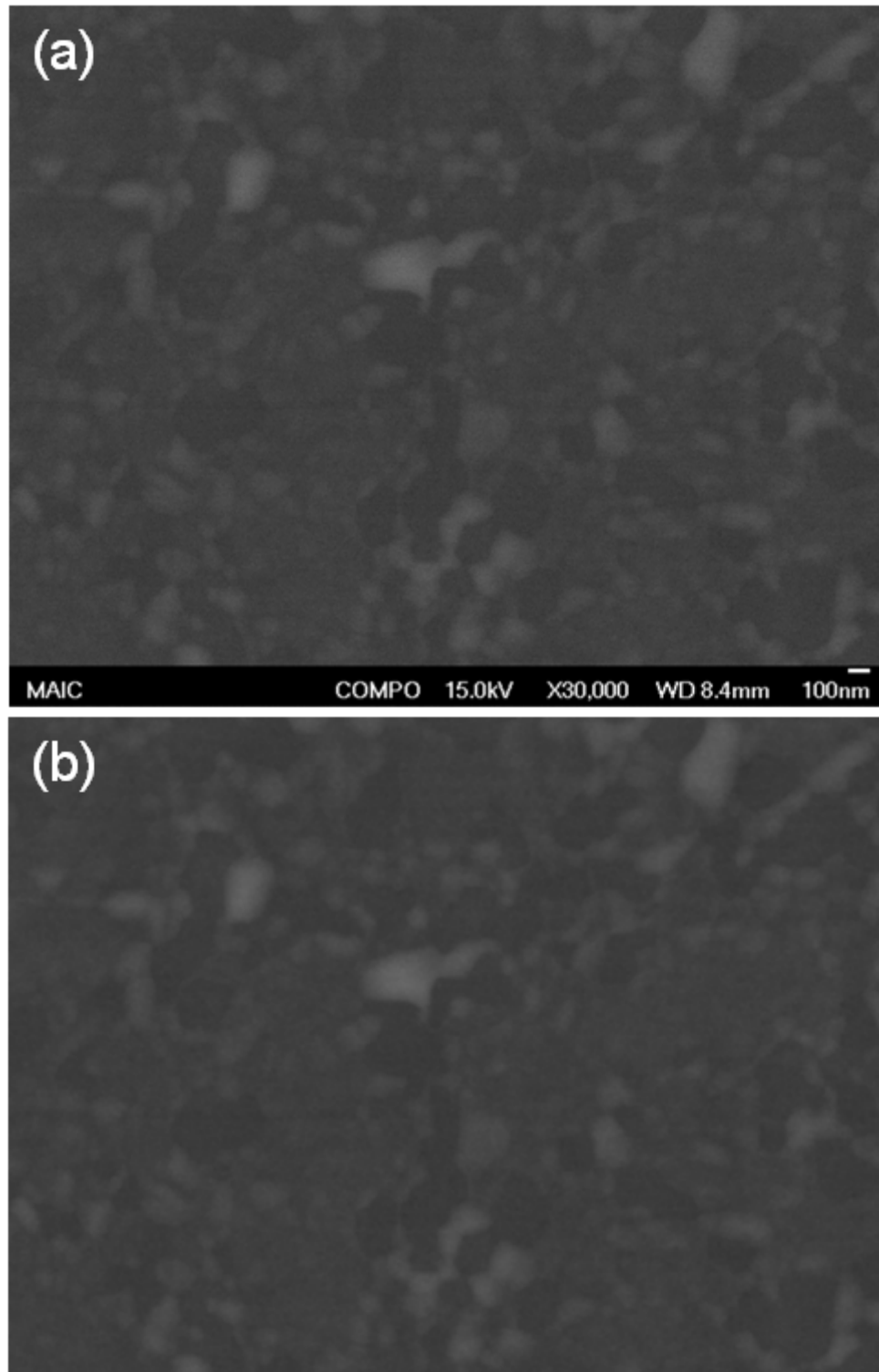


Figure 3-1: SEM/BSE image from this work (a) prior to Image J processing and (b) after processing.

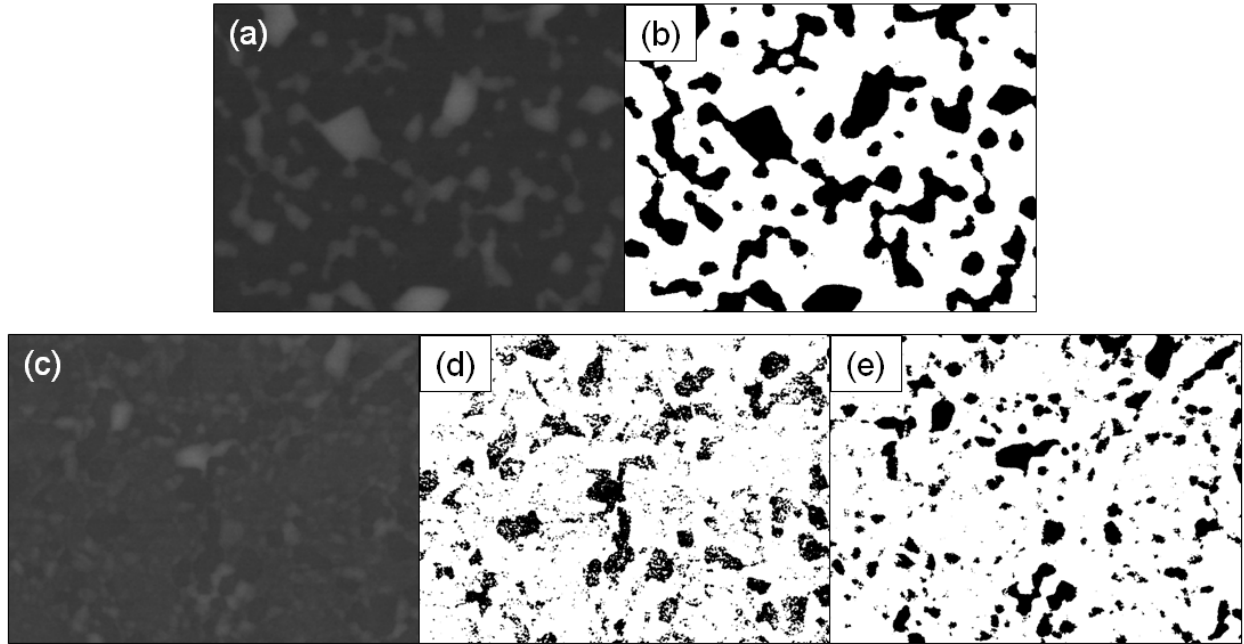


Figure 3-2: Examples of images from this work before and after Image J threshold operation. Images include (a) two phase image before, (b) two phase image after, (c) three phase image before, (d) three phase image after with darkest regions selected, and (e) three phase image after with lightest regions selected.

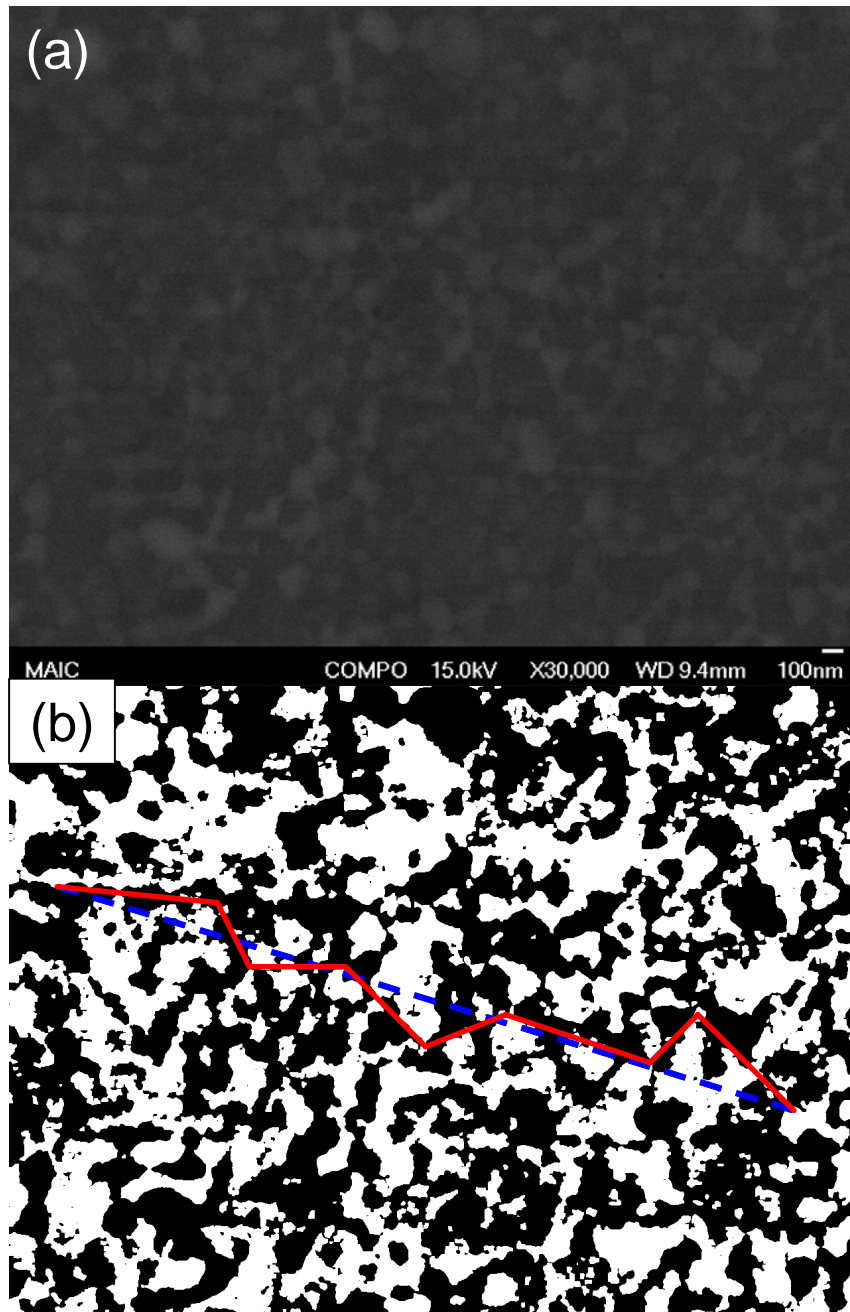


Figure 3-3: Example tortuosity measurement showing (a) raw SEM/BSE image of the undoped 25% Ge sample annealed at 450 °C for 1020 minutes and (b) the image after application of a $\text{Si}_{1-z}\text{Ge}_z$ threshold by ImageJ and with a randomly placed line (blue dashed line) and the estimated minimum continuous path around the phase (red solid lines).

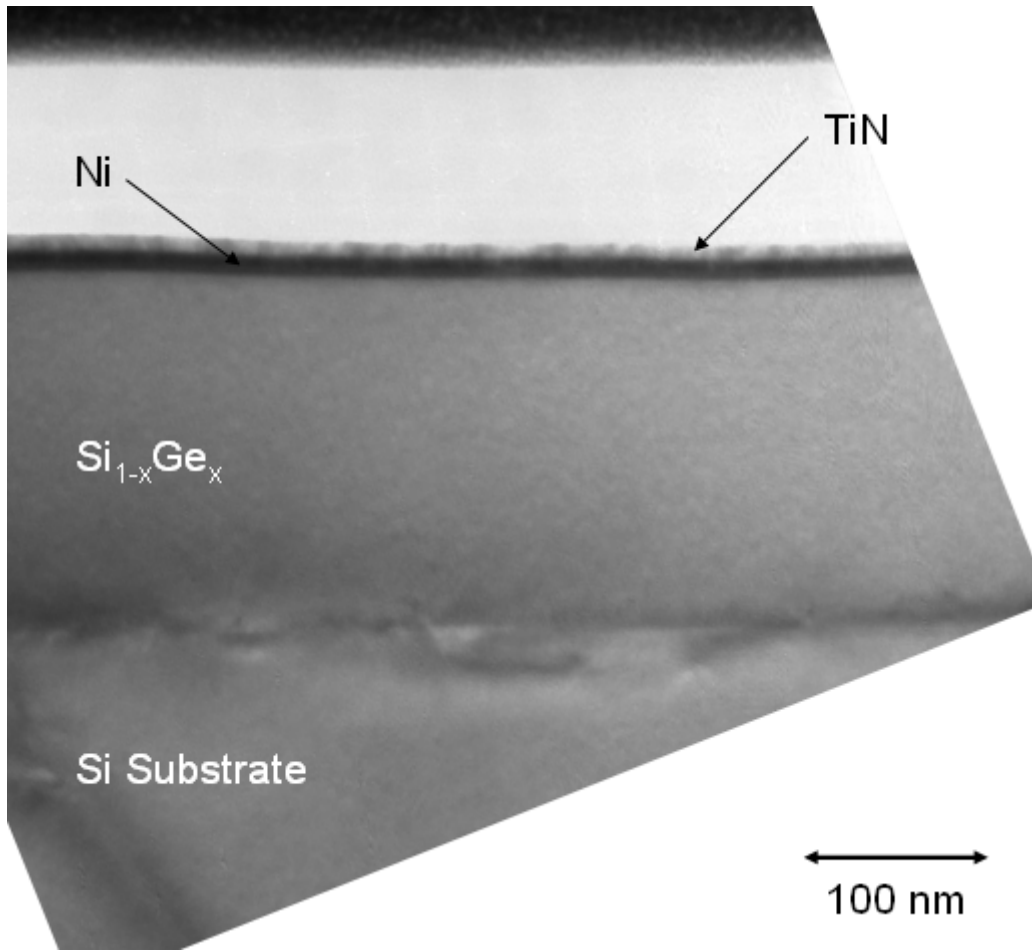
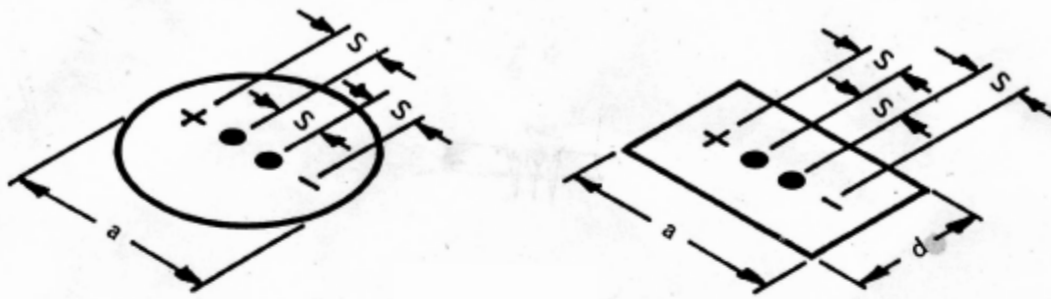


Figure 3-4: XTEM image of sample from as-grown wafer with $x = 25$ at% Ge and no B doping.

Table 3-1: Table of sheet resistance correction factors



$\frac{d}{s}$	CIRCLE	$\frac{a}{d} = 1$	$\frac{a}{d} = 2$	$\frac{a}{d} = 3$	$\frac{a}{d} > 4$
1.00				0.9988	0.9994
1.25				1.2467	1.2248
1.50			1.4788	1.4893	1.4893
1.75			1.7196	1.7238	1.7238
2.00			1.9454	1.9475	1.9475
2.50			2.3532	2.3541	2.3541
3.00	2.2662	2.4575	2.7000	2.7005	2.7005
4.00	2.9289	3.1137	3.2246	3.2248	3.2248
5.00	3.3625	3.5098	3.5749	3.5750	3.5750
7.50	3.9273	4.0095	4.0361	4.0362	4.0362
10.00	4.1716	4.2209	4.2357	4.2357	4.2357
15.00	4.3646	4.3882	4.3947	4.3947	4.3947
20.00	4.4364	4.4516	4.4553	4.4553	4.4553
40.00	4.5076	4.5120	4.5129	4.5129	4.5129
inf	4.5324	4.5324	4.5324	4.5324	4.5324

Table 3-2: Results from SIMS analysis of as-grown samples

Nominal Ge Concentration (at%)	B doping	Actual Ge Concentration (at%)	Actual B Doping (atoms/cm ²)
15	No	15	0
15	Yes	13	4.58E19
25	No	25	0
25	Yes	25	4.33E19

CHAPTER 4 INFLUENCE OF GE, B ON MICROSTRUCTURE AND KINETICS

This chapter explores the influence of both Ge content and the presence of homogeneous in-situ B doping in the initial $\text{Si}_{1-x}\text{Ge}_x$ layer on the microstructure and kinetics of nickel germanosilicide thin films. It has been previously reported in literature that increasing Ge content increases film sheet resistance by enhancing film agglomeration [Ok03, Zha04] and that incorporation of high levels of in-situ doped B stabilizes sheet resistance by suppressing agglomeration [Liu05]. None of these works, however, provide thorough microstructural analysis, focusing mainly on cross section Transmission Electron Microscopy (XTEM) analysis. XTEM analysis alone can provide good information concerning the depth distribution of phases. Combined with EDS analysis, XTEM can also provide local phase composition and thus limited information about the size and area fraction of phases present. While some works did apply plan view Scanning Electron Microscopy (SEM), which provides good information about grain size and phase area fraction, the technique was performed at relatively high magnification and without quantification of the results. In the case of the work by Liu and Ozturk, direct observation of the reported stabilization effect is not made at all; the presented conclusion was based on sheet resistance measurements and roughness measurements of the nickel germanosilicide/ $\text{Si}_{1-x}\text{Ge}_x$ interface. Without quantitative analysis, conclusive determination of effects and relationships is not possible.

Prior work has also been generally confined to single isochronal rapid thermal anneals for durations of 30 or 60 seconds. This limitation has prohibited the analysis of the reaction kinetics. By annealing the samples in this work over a large thermal matrix of both time and temperature, the kinetics of the nickel germanosilicide phase transformation from $\text{Ni}(\text{Si}_{1-x}\text{Ge}_x)$ to Si-rich $\text{Ni}(\text{Si}_{1-u}\text{Ge}_u)$ and Ge-rich $\text{Si}_{1-z}\text{Ge}_z$ can also be investigated.

To accomplish these investigations, Ge content in the initial $\text{Si}_{1-x}\text{Ge}_x$ layer was varied at levels of 10 and 25 at% and the layers were either undoped or doped with $\sim 4.5 \times 10^{19}$ atoms/cm³ of B during growth. Microstructure analysis was performed on samples annealed in a quartz tube furnace under N_2 ambient at temperatures between 450 and 650 °C in increments of 50 °C for 10, 30, 90, 270, and 1020 minutes. Analysis included XTEM and SEM/BSE imaging as well as limited application of EDS. Additional information on the experimental structure, processing, and analysis methods was previously presented in Chapter 3. The follow sections discuss the results from the analysis techniques to determine both the general microstructure evolution of the samples as well as the kinetics of the transformation process, including both the reaction order and activation energy.

4.1 Analysis using XTEM/EDS

As XTEM analysis provides limited information on film morphology, only selected samples in this work were imaged using the technique. The analyzed samples were selected such that they could be compared to prior work, ensuring that the films in this work behaved in a consistent manner. Specifically, it was of interest to verify that at low anneal times and temperatures the nickel germanosilicide film initially formed a homogeneous layer of $\text{Ni}(\text{Si}_{1-x}\text{Ge}_x)$ and then, at higher times and temperatures, this layer agglomerated into Si-rich $\text{Ni}(\text{Si}_{1-u}\text{Ge}_u)$ and Ge-rich $\text{Si}_{1-z}\text{Ge}_z$ grains. Accordingly, samples with 25% Ge content with and without B doping were XTEM analyzed after anneals of 450 °C for 10 min and 550 °C for 10 and 1020 minutes. For better comparison to literature, which extensively uses 30 to 60 second RTA anneals, samples with 25% Ge content with and without B doping were also RTA annealed for 60 seconds at 600 °C. Samples with 15% Ge content were not selected for analysis as it has been previously shown that agglomeration increases with increasing Ge content [Ok03]. Thus, any effect will be greatest, and most easily observed, in the 25% Ge samples.

Figure 4-1 presents an on-axis $\langle 110 \rangle$ XTEM images of 25% Ge undoped and doped samples annealed at 450 °C for 10 minutes. It is apparent from the images that the films in this work form a homogeneous nickel germanosilicide layer approximately 20 nm thick. These results agree well with prior literature that reports the initial formation of a granular, continuous, homogenous $\text{Ni}(\text{Si}_{1-x}\text{Ge}_x)$ layer of uniform thickness [Zha02, Jon04, Ok04, Ko06, Yao07] prior to the agglomeration process. It is also evident from the images that the presence of the homogeneous B doping used in this work does not significantly affect film behavior at this time and temperature, as the qualitative appearance of both images is identical.

On-axis $\langle 110 \rangle$ images of 25% Ge samples with and without B doping annealed at 550 °C for 10 and 1020 minutes are shown in Figure 4-2. It is apparent from the phase contrast between adjacent grains that the germanosilicide layers in the samples annealed at 550 °C for 10 minutes have begun to transform into Si-rich $\text{Ni}(\text{Si}_{1-x}\text{Ge}_x)$ and Ge-rich $\text{Si}_{1-z}\text{Ge}_z$ grains. The transformation is much more advanced, and evident, in the films annealed for 1020 minutes. These samples show large, distinct grains of dark-contrast Si-rich $\text{Ni}(\text{Si}_{1-x}\text{Ge}_x)$ interspaced with thin grains of light contrast Ge-rich $\text{Si}_{1-z}\text{Ge}_z$ (the relationship between grain contrast and composition was confirmed by EDS, discussed later in this section). The features in these images agree well with the intermediate and advanced stages of the phase transformation previously reported in literature [Zha02, Pey02, Ok03, Pey04, Jin05]. As noted previously, the addition of the homogeneous B doping in this work does not appear to affect the morphology of the films in cross section.

For improved comparison to the XTEM/EDS results of prior literature, additional doped and undoped 25% Ge samples were RTA annealed at 600 °C for 60 seconds. Figure 4-3 presents the XTEM images of these samples taken at a tilt of 10° from the $\langle 110 \rangle$ zone axis (necessary for

EDS analysis on the TEM used in this work). As with the samples annealed at 550 °C for 1020 minutes, these images show a microstructure with large, distinct grains with dark contrast interspersed between thin grains with lighter contrast. EDS analysis was performed on several locations for both samples; the results are also shown in Figure 4-3. As previously mentioned, the results indicated that the grains with dark contrast were Si-rich $\text{Ni}(\text{Si}_{1-u}\text{Ge}_u)$ and the regions with light contrast were Ge-rich $\text{Si}_{1-z}\text{Ge}_z$. Additionally, the EDS analysis of the remaining $\text{Si}_{1-x}\text{Ge}_x$ layers agreed well with the SIMS analysis performed on the as-grown structures (22 and 23 vs. 25 and 25 at% for the undoped and doped samples, respectively). Overall, the EDS results were found to agree well with previously reported germanosilicide film cross-section analyses [Zha02, Pey02, Ok03, Pey04, Jin05]. It was also noted in the EDS analysis that the initial TiN capping layer had oxidized to TiO_2 .

In summary, it can be concluded from the XTEM/EDS analyses presented in this section that the evolution of the germanosilicide films in this work generally agrees with the progression outlined in prior literature. Initially, at short annealing time and temperature, a homogeneous layer of nickel germanosilicide forms. At higher times and temperatures, the homogeneous layer transforms into grains of Si-rich $\text{Ni}(\text{Si}_{1-u}\text{Ge}_u)$ and Ge-rich $\text{Si}_{1-z}\text{Ge}_z$.

4.2 Plan View SEM Analysis

While XTEM analysis can provide valuable information about the cross section of a sample, such as layer thicknesses, the technique is not well-suited to monitoring grain size or the relative area fraction of phases present during a phase transformation. Hence, this work used extensive plan view SEM analysis to monitor the microstructure of the nickel germanosilicide films as they underwent the phase transformation from a homogeneous layer to an agglomerated Si-rich $\text{Ni}(\text{Si}_{1-u}\text{Ge}_u)$ and Ge-rich $\text{Si}_{1-z}\text{Ge}_z$ structure.

4.2.1 Phase Identification using EDS

As previously seen in the XTEM analysis, nickel germanosilicide films that are undergoing a phase transformation from a homogeneous layer to an agglomerated structure show phase contrast between the Si-rich $\text{Ni}(\text{Si}_{1-u}\text{Ge}_u)$ and Ge-rich $\text{Si}_{1-z}\text{Ge}_z$ grains. Similar phase contrast was also observed in plan view SEM images taken in both SE and BSE modes. An example of the observed phase contrast is shown in Figure 4-4, where SE and BSE images of an undoped 25% Ge sample annealed at 550 °C for 1020 minutes are shown. To identify the phases, an EDS line scan of a undoped 25% Ge sample annealed at 550 °C for 1020 minutes was performed. The results from this line scan, also presented in Figure 4-4, indicate that light contrast regions were rich in Ni while the Si and Ge signal are relatively constant due to the influence of the underlying $\text{Si}_{1-x}\text{Ge}_x$ layer. These results indicate that the phase contrast seen in the SEM images was the reverse of that seen in the XTEM images. The correct identification for the SEM results is that light contrast regions correspond to Si-rich $\text{Ni}(\text{Si}_{1-u}\text{Ge}_u)$ grains and dark regions to Ge-rich $\text{Si}_{1-z}\text{Ge}_z$ grains.

4.2.2 Imaging and Phase Quantification using SEM/BSE

The microstructure of all samples annealed from 450 to 650 °C in 50 °C increments at times of 10, 30, 90, 270, and 1020 minutes were plan view imaged in BSE mode according to the method outlined in Chapter 3. As will be presented later, these samples capture the region of the thermal matrix in which sheet resistance was decreased by the presence of B doping. It was of interest, therefore, to determine if the B-doped samples in this region exhibited less agglomeration according to the theory proposed by Liu and Ozturk [Liu05]. Additionally, as will also be later discussed, this region of the thermal matrix also encompasses all successful sheet resistance measurements of undoped samples. These samples were, therefore, of

maximum interest as their microstructure would allow a structure/property relationship to be determined for both the doped and undoped samples (discussed in Chapter 5).

Figures 4-5, 4-6, and 4-7 present BSE images of the samples annealed for 10, 90 and 1020 minutes at temperatures of 450, 550, and 650 °C, respectively. In general, the samples all show a similar morphological evolution with increasing time and temperature. At the lowest times and temperatures used in this study, no contrast is evident in the images. This corresponds to the homogenous initial film of $\text{Ni}(\text{Si}_{1-x}\text{Ge}_x)$ previously seen in cross section in Figure 4-1(a) and (b). As the time and temperature of the anneals increases, the images begin to show regions of light and dark contrast which have been shown by Figure 4-4 to correspond to Si-rich $\text{Ni}(\text{Si}_{1-u}\text{Ge}_u)$ and Ge-rich $\text{Si}_{1-z}\text{Ge}_z$ grains, respectively. At yet higher times and temperatures, the medium grey regions of $\text{Ni}(\text{Si}_{1-x}\text{Ge}_x)$ disappear as the amount of Si-rich $\text{Ni}(\text{Si}_{1-u}\text{Ge}_u)$ and Ge-rich $\text{Si}_{1-z}\text{Ge}_z$ increases further. Finally, at the highest times and temperatures, the grains of Si-rich $\text{Ni}(\text{Si}_{1-u}\text{Ge}_u)$ appear to begin to agglomerate. The evidence of agglomeration was further investigated by imaging samples annealed at 750 °C for 10, 30, 90, 270, and 1020 minutes. The BSE images of the samples annealed for 10, 90, and 1020 minutes are presented in Figure 4-8. Distinct agglomeration is evident in these series of images; the samples annealed for 1020 minutes are qualitatively fewer in quantity and much more circular than those annealed at lower times and temperatures. Therefore, it is expected that the agglomeration of the grains is resulting in an increase in grain thickness. Support for this conclusion can be observed in the XTEM images previously presented in Figure 4-2, where the $\text{Ni}(\text{Si}_{1-u}\text{Ge}_u)$ grains are much thicker in the samples annealed for 1020 minutes than in the samples annealed for 10 minutes.

While prior studies of nickel germanosilicide films have relied on the qualitative analysis of images, such as that leading to the previously discussed description of the evolution process,

this work makes extensive use of quantitative image analysis. As one of the main goals of this work is to monitor the decomposition (usually referred to as agglomeration) of nickel germanosilicide films, a quantitative metric linked to the process must be established. For this work, that metric was selected to be the area fraction (or, occasionally, grain size) of the Ge-rich $\text{Si}_{1-z}\text{Ge}_z$ phase present in an image. As Ge-rich $\text{Si}_{1-z}\text{Ge}_z$ is a product of the film transformation process, the area fraction of this phase will increase with increasing agglomeration.

Accordingly, many of the analyses in this work will discuss the agglomeration process in terms of the amount of Ge-rich $\text{Si}_{1-z}\text{Ge}_z$ present.

4.2.2.1 Influence of Ge content

Prior works by Ok et al. [Ok03] and Zhang et al. [Zha04] have qualitatively established that increasing the Ge content of the initial $\text{Si}_{1-x}\text{Ge}_x$ layer increases nickel germanosilicide agglomeration. The works, however, did not quantify the microstructures presented in their results. While a qualitative comparison of the SEM/BSE images presented in Figures 4-5 through 4-8 of the samples with initial $\text{Si}_{1-x}\text{Ge}_x$ layer concentrations of 15 and 25% Ge supports their conclusions, the images in this work were also quantitatively analyzed.

Figure 4-9(a) and (b) plot a 95% confidence interval for the area fraction of Ge-rich $\text{Si}_{1-z}\text{Ge}_z$ as a function of annealing time for temperatures of 450, 550, and 650 for the undoped and doped samples, respectively. Calculation of the area fraction range required for the 95% confidence interval is presented in Appendix A. It should be noted, however, that while for simplicity a single error range (established in Appendix A) was used for all values in these plots, the actual error decreases with increasing area fraction. The quantitative results further support the conclusion that increasing Ge content worsens film stability. At lower temperatures (450-550 °C), the area fraction of precipitated Ge-rich $\text{Si}_{1-z}\text{Ge}_z$ is much lower for the 15% vs. the 25% Ge samples for both the undoped and doped structures. At higher temperatures, however, the

difference in Ge-rich $\text{Si}_{1-z}\text{Ge}_z$ area fraction between the 15 and 25% Ge samples is much less. This trend is also consistent in the quantitative analysis of the isothermal series not shown in the figures (500, 600, 750 °C).

For further analysis, a paired t-test can be used to statistically compare the differences in Ge-rich $\text{Si}_{1-z}\text{Ge}_z$ area fraction at each point in the thermal matrix. A single paired t-test was applied to all points on the thermal matrix for both the undoped and doped samples (i.e. comparing the 15% Ge 500 °C 90 minute sample with the 25% Ge 500 °C 90 minute sample, and also comparing the 15% Ge + B 500 °C 90 minute sample with the 25% Ge + B 500 °C 90 minute sample in the same statistical test). Accordingly, a total of 36 paired data points were used in the analysis. The results from the analysis, presented in Figure 4-10, show that the difference in Ge-rich $\text{Si}_{1-z}\text{Ge}_z$ area fraction between the samples with 15 and 25% is statistically significant at a 99.999% level ($p=0.000$), with the 15% Ge samples having a generally lower area fraction (and hence less agglomeration). It is interesting, however, to note the range of the difference in area fraction. The difference ranges from the 15% samples showing over 60% (absolute) less area fraction to them having 3% (absolute) more. This range highlights the fact that, while increasing Ge content definitively increases agglomeration at lower times and temperatures, the effect is not consistent across the entire thermal matrix. The increase in agglomeration is only present at lower times and temperatures. The cause of this discrepancy, however, will be addressed in a later section.

4.2.2.2 Influence of B content

Previous work by Liu and Ozturk [Liu05] has suggested that the presence of high levels of homogeneous B doping reduced nickel germanosilicide film agglomeration and led to the stabilization of film sheet resistance. The previous work, however, lacked any direct observation of the microstructure effect and instead formulated the theory from AFM measurement of the

germanosilicide/Si_{1-x}Ge_x interface and SIMS compositional depth profiles. A main objective of this work was to determine, through direct, quantitative microstructure observation using plan view SEM/BSE imaging, if this theory could be substantiated. While the homogeneous B doping level in this work was limited by the ability of the reactor used to grow the experimental structures, it will be presented in Chapter 4 that the B doped samples in this work exhibited a similar decrease in sheet resistance when compared to undoped samples annealed at the same time and temperature. Accordingly, a difference between sample microstructures for the doped vs. undoped structures in this work was expected. The SEM/BSE images presented in Figures 4-5 to 4-8, however, do not qualitatively support Liu and Ozturk's theory. The area fractions, grain sizes, and interconnectivity of the phases present do not appear to differ between the undoped and doped samples at any time or temperature for either the 15 or 25% Ge samples.

Quantitative analysis of the images provides further evidence that there is no difference in area fraction or grain size between the undoped and doped samples in this work. Figure 4-11(a) and (b) plot a 95% confidence interval for the area fraction of Ge-rich Si_{1-z}Ge_z as a function of annealing time for temperatures of 450, 550, and 650 °C for the 15 and 25% Ge samples, respectively. Calculation of the area fraction range required for the 95% confidence interval is presented in Appendix A. It should be again noted that while for simplicity a single error range was used for all values in these plots, the actual error decreases with increasing area fraction. The plots for the undoped and doped samples appear to largely overlap within the experimental error at all times and temperatures for both the 15 and 25% Ge samples. In fact, it appears if the area fraction of Ge-rich Si_{1-z}Ge_z for the doped samples may be consistently slightly higher than that of the undoped samples, suggesting that doped samples may display more agglomeration than the equivalent undoped samples.

The validity of these conclusions may be further established by performing a paired t-test to statistically compare the differences in Ge-rich $\text{Si}_{1-z}\text{Ge}_z$ area fraction at each point in the thermal matrix. Accordingly, a single paired t-test was applied to all SEM/BSE imaged points on the thermal matrix for the 15 and 25% Ge samples ($n = 36$). The results from this analysis, presented in Figure 4-12(a), show that there is no statistically significant difference in Ge-rich $\text{Si}_{1-z}\text{Ge}_z$ area fraction between the undoped and doped samples at a 95% confidence level.

While area fraction provides information on the quantity of a phase present in a microstructure, the metric does not offer any information on the size or distribution of that phase. A difference in grain size (with constant area fraction) could suggest that the interconnectivity of grains may be altered with the addition of B doping. While this property appears qualitatively identical in the SEM/BSE images of the undoped and doped samples presented in Figures 4-5 to 4-7, statistical analysis was also performed to determine if a quantitative difference existed. Specifically, a single paired t-test as previously outlined for area fraction was used as the statistical analysis method. The results from this analysis, presented in Figure 4-12(b), again show that there is no statistically significant difference between the undoped and doped samples at a 95% confidence level. Thus, in conjunction with qualitative observation of the images, it can be concluded that the addition of B doping to the samples did not affect agglomeration, either through an increase in the area fraction of the precipitated phase or by varying the grain sizes of the precipitated (or any other) phase.

The quantitative results and statistical analysis in this work, therefore, strongly contradict the conclusions drawn by Liu and Ozturk on the influence of homogeneous B doping in the initial $\text{Si}_{1-x}\text{Ge}_x$ layer. No statistically significant difference in either grain size or area fraction of the Ge-rich $\text{Si}_{1-z}\text{Ge}_z$ phase was determined at a 95% confidence level. While their results

indicate that the addition of B doping may decrease the roughness of the germanosilicide/Si_{1-x}Ge_x interface, the decrease in roughness does not correlate to a decrease in agglomeration. Instead, an alternate mechanism must lead to the reduction of sheet resistance in the B doped samples observed in both works. This mechanism, and the structure/property relationship between agglomeration and sheet resistance, is further addressed in Chapter 5.

4.3 Reaction Kinetics

The reaction kinetics of nickel germanosilicide agglomeration have not been established as most published work has been confined to short, isochronal anneal series of 30 or 60 seconds. Accordingly, without a full thermal matrix including anneals of multiple times and temperatures, the reaction rate as a function of time and temperature cannot be calculated. This, in turn, prevents the activation energy of the reaction to be established. Accordingly, this work utilized a large thermal matrix incorporating a large range of times and temperatures in order to be able to investigate the kinetics of the reaction process.

It should be noted that published literature (and, at times, this work) generally refers to the “agglomeration” of nickel germanosilicide films. As shown in the SEM/BSE images in the previous section, this term is somewhat of a misnomer. Agglomeration, according to the Merriam-Webster dictionary, refers to “the action or process of collecting in a mass” [Mer04]. In materials science terminology, agglomeration is usually applied to a process in which a precipitate, thin film, or other structure becomes more spherical in order to reduce the energy of its interface. While XTEM micrographs of the nickel germanosilicide films in this work do show some signs of spheroidization (and hence agglomeration in its strictest definition), it is well established in both prior literature and this work that the film also rejects Ge and forms Ge-rich grains of Si_{1-z}Ge_z. The process, therefore, was not and should not be treated as a pure agglomeration process but instead be treated as (at least partially) a solid state transformation

reaction: the initial $\text{Ni}(\text{Si}_{1-x}\text{Ge}_x)$ film transforms into Si-rich $\text{Ni}(\text{Si}_{1-u}\text{Ge}_u)$ and Ge-rich $\text{Si}_{1-z}\text{Ge}_z$ grains. Parallel or subsequent agglomeration of either phase may, in fact, need to be handled as a separate event.

Transformation reactions have been widely studied across a variety of materials systems, and a number of theories have been advanced to describe their kinetic processes. One kinetic theory of transformation for a nucleation and growth process was proposed by M. Avrami [Avr39, Avr40, Avr41] and well discussed in the text by J.W. Christian [Chr02]. This theory considers the case where transformation begins at several points (nuclei) in a material. As the transformed regions grow outwards from the nuclei, they eventually impinge on each other and create a common interface over which growth ceases (though it will continue normally elsewhere). Assuming an isotropic growth rate and a constant or decreasing nucleation rate per unit volume, Avrami proposed a general relation for a three dimensional nucleation and growth process. This relation, presented in Equation 4-1, relates the volume fraction transformed (ζ) to a rate constant (k), time (t), and the reaction order (n).

$$\zeta = 1 - \exp(-kt^n) \quad \text{Equation 4-1}$$

An extensive discussion of the theory behind the relationship is included in the text by Christian [Chr02] and is beyond the scope of this work. It should be noted, however, that confining the transformation within a 2-D film (and hence including the effects of a free surface) will modify the reaction order by up to 1 (i.e. decrease $n = 3$ for a bulk system to $n = 2$ for a thin film).

Isothermal transformation curves of a process obeying the Avrami relationship will have a sigmoidal shape on a linear plot of ζ vs. t . It is difficult, however, to fit linearly plotted sigmoidal data in order to determine n and k for a set of experimental results. Accordingly,

Equation 4-1 may be mathematically transformed to produce the relationship given by Equation 4-2.

$$\log(\log((1-\zeta)^{-1})) = n(\log(t)) + \log(k) \quad \text{Equation 4-2}$$

It can be seen from Equation 4.2 that a plot of $\log(\log((1-\zeta)^{-1}))$ vs. $\log(t)$ will produce a straight lines with slope n and y-axis intercept of $\log(k)$ for an isothermal transformation curve of a process that obeys the Avrami relationship. Thus, experimental data from a process thought to obey Avrami kinetics is often graphed on such a plot and analyzed using linear regression analysis after the appropriate transformations have been made.

The isothermal transformation curves in Figures 4-9 and 4-11 do not show a classic sigmoidal shape as the curves are increasing in value from the earliest time. The lack of classic shape, however, does not preclude the process obeying Avrami kinetics, however. Instead, it illustrates that the initial nucleation period may be very short (i.e. the first part of the sigmoidal shape may lie below 10 minutes). It was of interest, therefore, to determine if the nickel germanosilicide transformation obeyed the Avrami theory. As the volume fraction of transformed phase was not determined in this work, the area fraction of the phase was substituted. This substitution is justified as the reaction can be generally assumed to be confined in a thin layer (as shown by the XTEM in Figures 4-1 and 4-2). Plots of $\log(\log((1-AF)^{-1}))$ vs. $\log(t)$ will still produce straight lines with slope n and y-axis intercept of $\log(k)$ for a process obeying Avrami kinetics. As mentioned previously, however, the reaction order will be reduced by up to 1.

4.3.1 Reaction Order

To determine n , the reaction order, the $\log(\log((1-AF)^{-1}))$ of all imaged sample conditions were plotted as a function of $\log(t)$. The plots are presented in Figure 4-13 for the undoped and doped 15% Ge samples and in Figure 4-14 for the undoped and doped 25% Ge samples. As it

was determined in the preceding discussion that, while Ge content influenced film microstructure, homogeneous B doping did not, the undoped and doped samples were considered and analyzed as a single case (though the provenance of each data point was maintained on the graphs). Restated, while the undoped and doped samples are plotted separately on the graphs, single statistical regressions containing all data points (both undoped and doped) was performed for each combination of Ge composition and anneal temperature. It should also be noted that, due to the mathematical transformation, the error bars plotted for the transformed $\log(\log((1-AF)^{-1}))$ values are not constant, as shown, but actually vary with area fraction. A more comprehensive explanation of this effect and the reasoning behind the selection of the displayed error ranges is contained in Appendix C.

It is evident from Figures 4-13 and 4-14 that while most temperature series appear to be linear, all anneal temperatures do not share a constant slope in either plot. Furthermore, the results from the 600 °C anneal series for the 15% Ge samples and the 550 °C series for the 25% Ge samples do not appear to be linear. An explanation for this effect can be determined by analysis of a plot of the area fraction of the initial $Ni(Si_{1-x}Ge_x)$ phase as a function of Ge-rich $Si_{1-z}Ge_z$ area fraction, presented in Figure 4-15. It is evident from this figure that for all samples, regardless of Ge or B content, the initial $Ni(Si_{1-x}Ge_x)$ phase disappears by ~60% Ge-rich $Si_{1-z}Ge_z$ area fraction. When transformed for the Avrami plots, the $\log(\log((1-AF)^{-1}))$ of 60% area fraction corresponds to a value of -0.400. A horizontal line of this value plotted on the graphs shown in Figures 4-13 and 4-14 would divide the graphs into two regions. Above and below this line, the slopes of all temperature series appear to be qualitatively equal, including the corresponding sections of the 550 and 600 °C plots. These results, along with the earlier observation of the film

morphology in plan view SEM/BSE, confirm that the nickel germanosilicide film evolution must be considered as two separate reactions: precipitation and agglomeration.

4.3.1.1 Precipitation reaction

Figure 4-16(a) and (b) present the sections of the Avrami plots lying below 60% area fraction Ge-rich $\text{Si}_{1-z}\text{Ge}_z$ for the 15% and 25% samples, respectively. These regions of the plot correspond to the precipitation stage of the transformation reaction, where the Ge-rich $\text{Si}_{1-z}\text{Ge}_z$ phase is being formed through Ge rejection from the initial $\text{Ni}(\text{Si}_{1-x}\text{Ge}_x)$ phase and reaction with the remaining $\text{Si}_{1-x}\text{Ge}_x$ layer. Linear regression analysis for every temperature series appearing in each plot was performed using the Minitab software; the results from the regression analysis are presented in Table 4-1 and the best fit equation lines are plotted in Figure 4-16(a) and (b). The average value of n for the 15% Ge samples was determined to be 0.676 ± 0.142 for a 95% confidence level. For the 25% Ge samples, n was determined to be 0.491 ± 0.106 for the same confidence level. With the previously mentioned influence of a 2-D film on n , it can be concluded that the equivalent n for this reaction in a bulk material would be between ~ 0.5 and 1.5 . This value for n can be compared to a table of values from the text of Christian [Chr02], presented in Table 4-2, for diffusion controlled reactions obeying Avrami behavior. While several types of growth have n values between 0.5 and 1.5 , the only reaction which can describe the morphology seen in Figures 4-5 to 4-7 is that of “all shapes growing from small dimensions, zero nucleation rate” which has $n = 1.5$. It can be concluded, therefore, that the first stage of the nickel germanosilicide transformation is of this type. This conclusion is further supported by the prior work of Yao et al. [Yao07] who showed that Ge enrichment occurred at grooves formed between neighboring germanosilicide grains (see Figure 2-15). These results, which suggest that grain boundary nucleation is occurring, support the conclusion that a zero nucleation rate is in

effect, as no new grain boundaries are likely to be formed during the reaction in unreacted regions.

4.3.1.2 Agglomeration reaction

Figure 4-17(a) and (b) present the sections of the Avrami plots lying above 60% area fraction Ge-rich $\text{Si}_{1-z}\text{Ge}_z$ for the 15% and 25% samples, respectively. These regions of the plot correspond to the agglomeration stage of the transformation reaction, where the Ge-rich $\text{Si}_{1-z}\text{Ge}_z$ area fraction increases as the Si-rich $\text{Ni}(\text{Si}_{1-x}\text{Ge}_x)$ phase agglomerates. Linear regression analysis for every temperature series appearing in each plot was performed using the Minitab software; the results from the regression analysis are presented in Table 4-3 and the best fit equation lines are plotted in Figure 4-17(a) and (b). The average value of n for the 15% Ge samples was determined to be 0.067 ± 0.023 for a 95% confidence level. For the 25% Ge samples, n was determined to be 0.056 ± 0.015 for the same confidence level. With the previously mentioned influence of a 2-D film on n , it can be concluded that the equivalent n for this reaction in a bulk material would be between ~ 0.05 and 1.05 . This value for n can be compared to the table of values from the text of Christian [Chr02], formerly presented in Table 4-2, for diffusion controlled reactions obeying Avrami behavior. The results of this comparison suggest that the reaction is the diffusion controlled “thickening of very large plates (e.g. after complete edge impingement)” which has a bulk n of 0.5. This conclusion is supported by the previously presented XTEM (Figure 4-2) and SEM/BSE images (Figures 4-5 to 4-7) in this work and in prior work (Figure 2-16) which show both the Ge-rich $\text{Si}_{1-z}\text{Ge}_z$ and Si-rich $\text{Ni}(\text{Si}_{1-x}\text{Ge}_x)$ to have large, plate-like morphologies.

4.3.2 Activation Energy

The linear regression analyses necessary to determine the order of the reactions also provided values for $\log(k)$. These values, reported in Tables 4-1 and 4-3 for the precipitation and

agglomeration reactions, respectively, may be mathematically converted to $\ln(k)$ and used to determine the activation energy (E_a) of each reaction according to the Arrhenius equation, which is presented as Equation 4-3:

$$\ln(k) = -E_a (1/KT) + \ln(A) \quad \text{Equation 4-3}$$

From this equation, where K is Boltzmann's constant (8.67×10^{-5} eV/K), it is apparent that on a plot of $\ln(k)$ vs. $(1/KT)$, E_a will be equal to the negative slope of the line. Figure 4-18(a) and (b) present such plots for the precipitation and agglomeration reactions, respectively. While each data point on these graphs has a unique error range (calculated from the standard error of $\log(k)$ in Tables 4-1 and 4-3), the error for each reaction series was found to be relatively consistent. Hence, for simplicity, a single error range corresponding to a 95% confidence interval for the average standard error was presented for each series on the graphs in Figure 4-18. The error ranges are equal to ± 0.680 , 0.459 for the 15 and 25% Ge precipitation reactions and ± 0.117 , and 0.078 for the 15 and 25% Ge agglomeration reactions, respectively. Linear analyses were performed on the reaction series shown in Figure 18; the results from the analyses are presented in Table 4-4 and will be discussed in the following paragraphs.

4.3.2.1 Precipitation reaction

For the precipitation reaction, Figure 4-18(a) and the results in Table 4-4 show that the activation energy for the 15% Ge samples was higher than for the 25% Ge samples. A two-sample t-test using the appropriate data from Table 4-4 shows the nominal difference in activation energy to be 1.196 eV, with a 95% confidence interval for the difference ranging between 0.595 and 1.797 eV. While this analysis is formed using somewhat limited data (four points for the 15% sample and three for the 25% sample), the difference is significant and the error range for the data relatively small. It is unlikely, therefore, that additional data points would cause enough of a shift in the linear regression to eliminate the difference in activation

energies. It can be concluded, accordingly, that a statistically significant difference in activation energies for the precipitation reaction exists when Ge content is increased.

It is evident from these results that the activation energy of this reaction is concentration dependant; increasing Ge content from 15 to 25% in the initial $\text{Si}_{1-x}\text{Ge}_x$ layer decreased the activation energy by ~ 1.2 eV. The precise cause of this decrease is not known. Many steps of the reaction, however, have been found to be concentration dependant in other systems. Such steps include the bonding energy between atoms (which must be broken to switch from Ni-Ge to Ni-Si), and the diffusion of atoms in an alloy. An example of a concentration influence on bonding energy can be found in the work by J. Tersoff, where bond strength was calculated to decrease with increasing Ge content in $\text{Si}_{1-x}\text{Ge}_x$ [Ter89]. Experimental evidence of this effect has also been reported [Cros03]. An example of concentration dependant diffusion activation energy has been shown by Zangenburg et al., who studied the diffusion of Ge in $\text{Si}_{1-x}\text{Ge}_x$ alloys [Zan01]. Their work showed that the activation energy of Ge diffusion in silicon germanium alloys decreases with increasing Ge content. It can be extrapolated from their results that the activation energy decreases from 4.33 to 3.92 eV for a change in composition from 15 to 25% Ge, a difference of 0.42 eV.

It is likely, therefore, that the influence of Ge on activation energy could be accounted for by similar concentration dependent effects, as the initial (metastable) $\text{Ni}(\text{Si}_{1-x}\text{Ge}_x)$ films contain different compositions of Ge based upon the concentration of the $\text{Si}_{1-x}\text{Ge}_x$ layer being silicided. Additional research into the bond strengths and mobility of Ni, Si, and Ge in nickel germanosilicide films is needed, however, to determine if a single concentration dependant effect dominates and creates the difference in activation energy, or if the difference is a compilation of

two or more lesser effects. The concentration dependency should also be studied over a greater range of Ge compositions to determine the other composition ranges to establish a stronger trend.

4.3.2.2 Agglomeration reaction

Figure 4-18(b) and the results in Table 4-4 show approximately equal activation energies for the 15 and 25% Ge samples undergoing the agglomeration reaction. A two-sample t-test using the appropriate data from Table 4-4 shows the nominal difference in activation energy to be 0.044 eV, with a 95% confidence interval for the difference ranging between -0.0054 and 0.0931 eV. It can be concluded, therefore, that no statistical difference between the reactions exists at the 95% confidence level. While this analysis is formed using somewhat limited data (three points for the 15% sample and four for the 25% sample), the nominal difference is small in relation to the error of the data. It is unlikely, therefore, that additional data points would cause enough of a shift in the linear regression to cause significant difference in the activation energies.

Thus, unlike for the precipitation reaction, this work found no statistically significant difference in activation energy for the agglomeration reaction between the 15% and 25% Ge samples. It can be concluded, therefore, that this reaction does not have a dependency on Ge concentration. The lack of concentration dependence, however, is not unreasonable. The agglomeration reaction does not result in any composition changes. Instead, it is likely driven solely by the minimization of free energy through geometric rearrangement of the $\text{Ni}(\text{Si}_{1-u}\text{Ge}_u)$ grains (i.e. minimizing surface area to volume ratio); a conclusion also supported by observation of the generally circular shape of the $\text{Ni}(\text{Si}_{1-u}\text{Ge}_u)$ grains after annealing at high times and temperatures. With consideration of the fact that the compositions of the $\text{Ni}(\text{Si}_{1-u}\text{Ge}_u)$ grains for both the 15 and 25% Ge samples are very close (less than ~ 1 at%) at the completion of the precipitation reaction (and hence the start of the agglomeration reaction), it is possible that the rearrangement is occurring by a mechanism which occurs within the $\text{Ni}(\text{Si}_{1-u}\text{Ge}_u)$ grains. Thus,

the mechanism would not be influenced by the external variations in Ge concentration. As with the precipitation reaction, however, not enough information about the Ni-Si-Ge system (mobility, diffusivity) is known to draw a firm conclusion as to the exact nature of the mechanism beyond the fact that it is not very temperature dependant as indicated by the small activation energy.

4.4 Summary

A number of important conclusions can be drawn from the work presented in this chapter. First, the general cross-section and plan-view morphology of the nickel germanosilicide films in this work agree well with those reported in prior literature. Second, while prior work has generally described the film evolution as “agglomeration,” two distinct reactions have been captured by the anneal matrix used in this work. Initially, Ge-rich $\text{Si}_{1-z}\text{Ge}_z$ grains precipitate from the parent film as Ge is rejected to the grain boundaries. This process continues until the parent film has completely transformed in to Ge-rich $\text{Si}_{1-z}\text{Ge}_z$ and Si-rich $\text{Ni}(\text{Si}_{1-u}\text{Ge}_u)$ grains. Complete transformation corresponds to ~60% area fraction Ge-rich $\text{Si}_{1-z}\text{Ge}_z$ for all samples in this work. Once the transformation is complete, the Si-rich $\text{Ni}(\text{Si}_{1-u}\text{Ge}_u)$ grains begin to agglomerate. Third, increasing Ge content in the initial $\text{Si}_{1-x}\text{Ge}_x$ film from 15 to 25% increases the amount of transformation observed for equivalent anneals, likely due to the increase in activation energy for Ge rejection with increasing Ge content. Fourth, the addition of $\sim 4.5 \times 10^{19}$ atoms/cm² homogeneous B doping during $\text{Si}_{1-x}\text{Ge}_x$ layer growth does not affect nickel germanosilicide film microstructure for any anneal. Finally, Avrami reaction kinetics can be used to model the isothermal transformation curves of nickel germanosilicide thin films. Two separate reaction orders were observed, corresponding to the precipitation and agglomeration reactions. By analysis of the reaction order, the precipitation reaction was determined to be diffusion controlled growth with a zero nucleation rate. The agglomeration reaction was similarly determined to be diffusion controlled thickening of very large plates. The activation

energies of the reactions were also able to be calculated and showed that for the precipitation reaction, E_a was 1.96 and 0.76 eV for the 15 and 25% Ge samples, respectively. For the agglomeration reaction, E_a was determined to be 0.14 and 0.10 eV, respectively (though statistically these values were found to be equal).

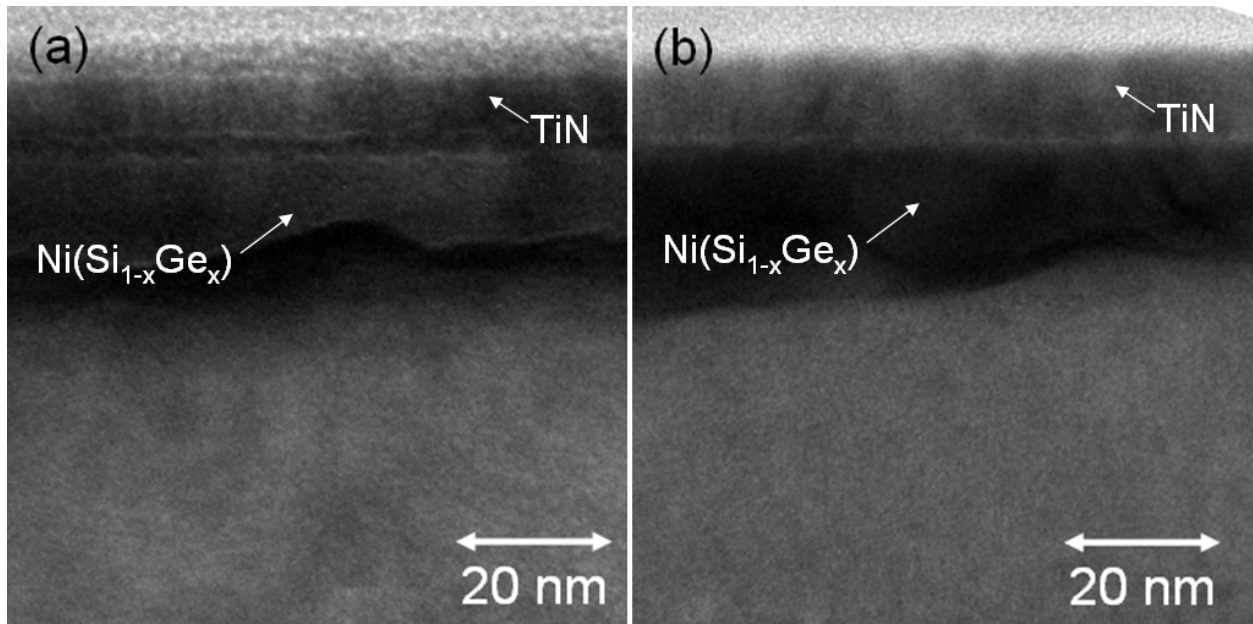


Figure 4-1: On-axis $\langle 110 \rangle$ XTEM images of 25% Ge samples annealed at 450 °C for 10 minutes with (a) no doping and (b) B doping

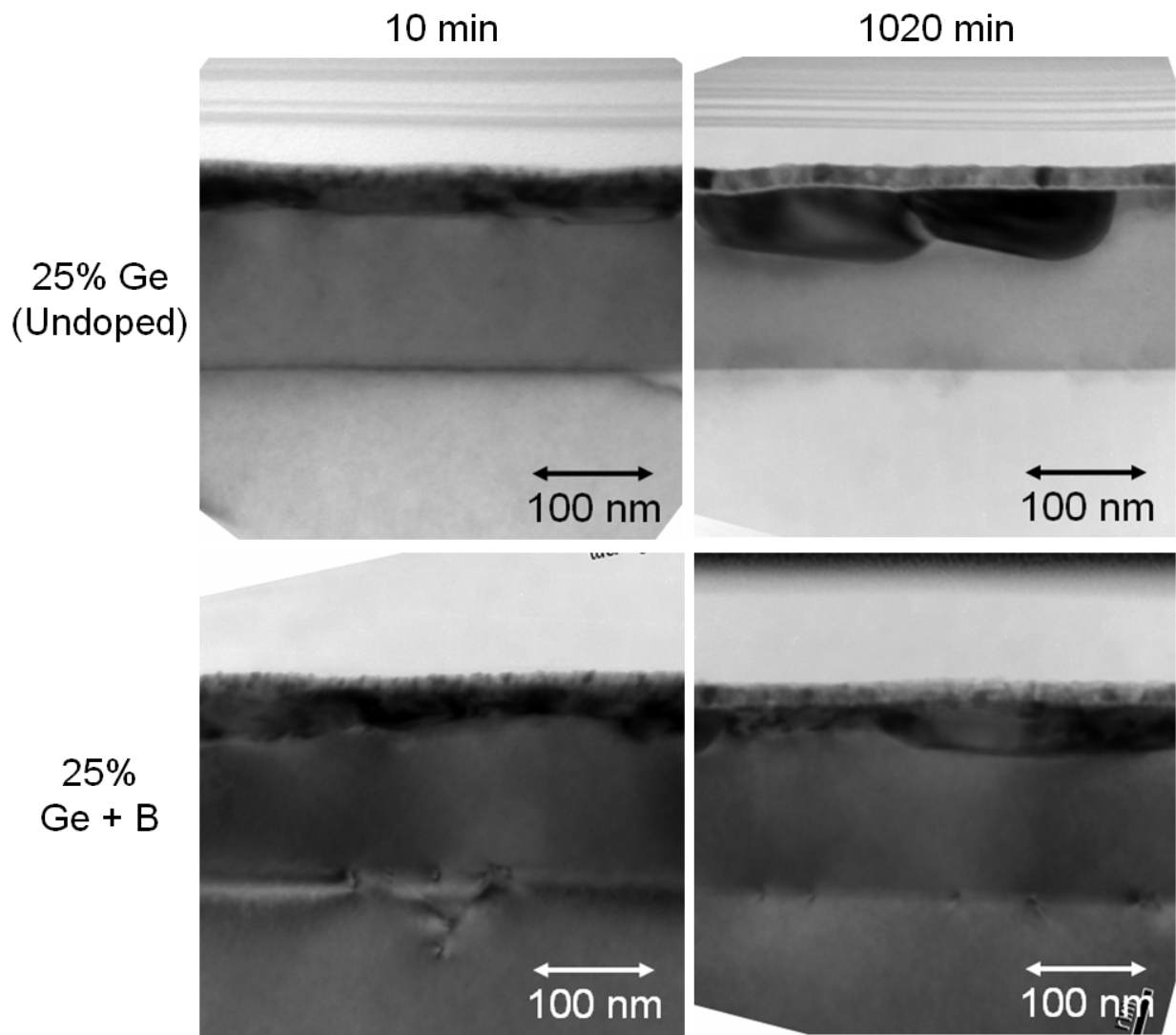


Figure 4-2: On-axis $\langle 110 \rangle$ images of 25% Ge samples with and without B doping annealed at 550°C for 10 or 1020 minutes.

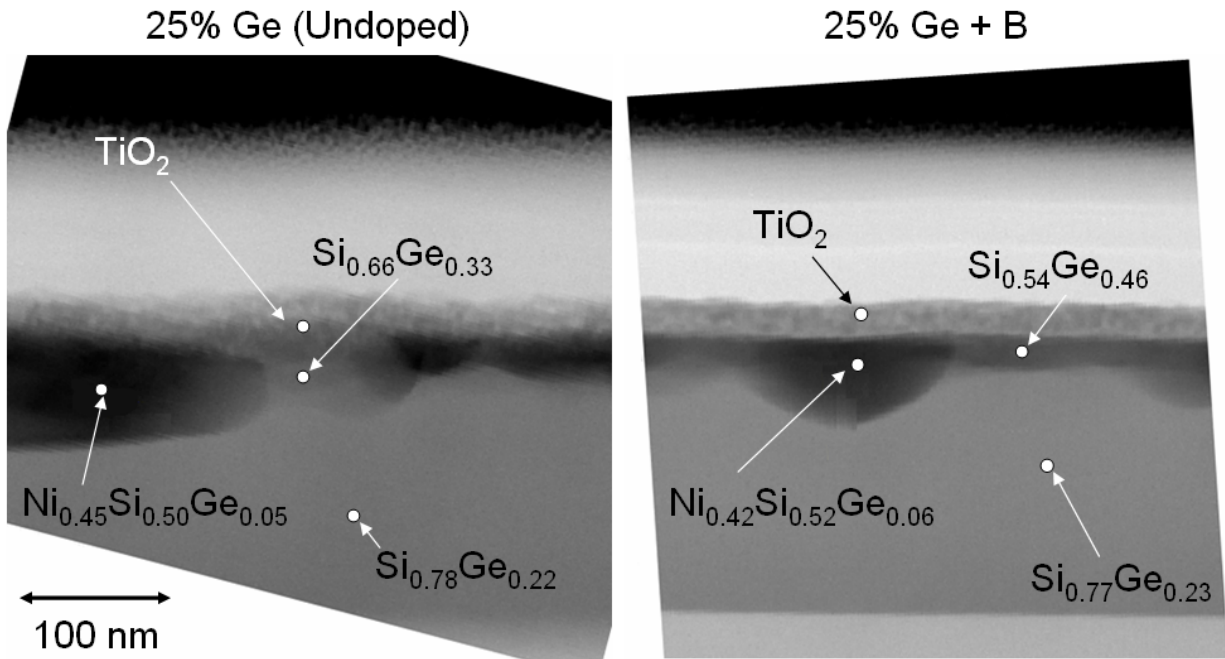


Figure 4-3: XTEM images taken at 10° tilt from $\langle 110 \rangle$ zone axis of undoped and doped 25% Ge samples RTA annealed at 600°C for 60 seconds. The locations and results of EDS analysis are indicated on the image.

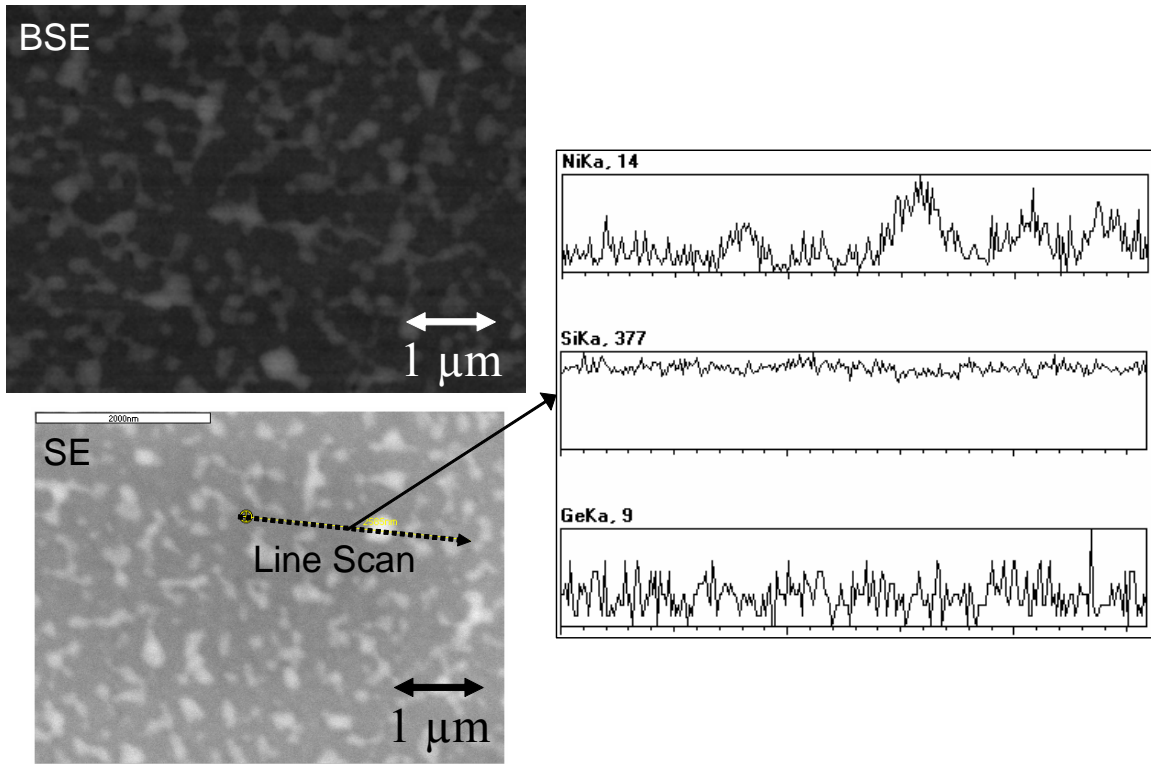


Figure 4-4: SEM images of undoped 25% Ge sample after 1020 minute anneal at 550 °C in SE and BSE modes. The location of the line scan and the resulting spectra are also shown. Note that the SE and BSE images show different regions of the same sample.

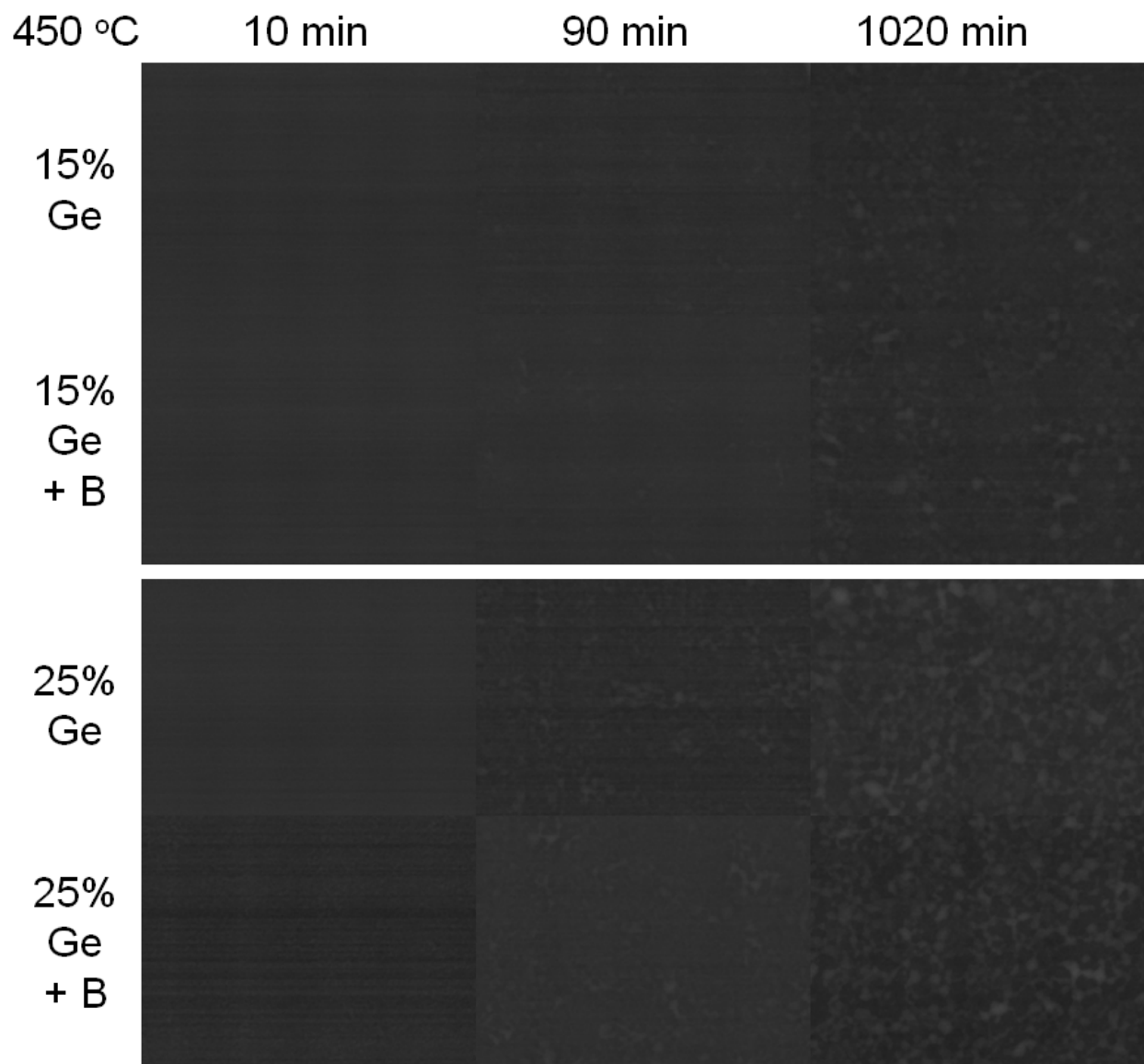


Figure 4-5: SEM/BSE images of samples annealed at 450 °C

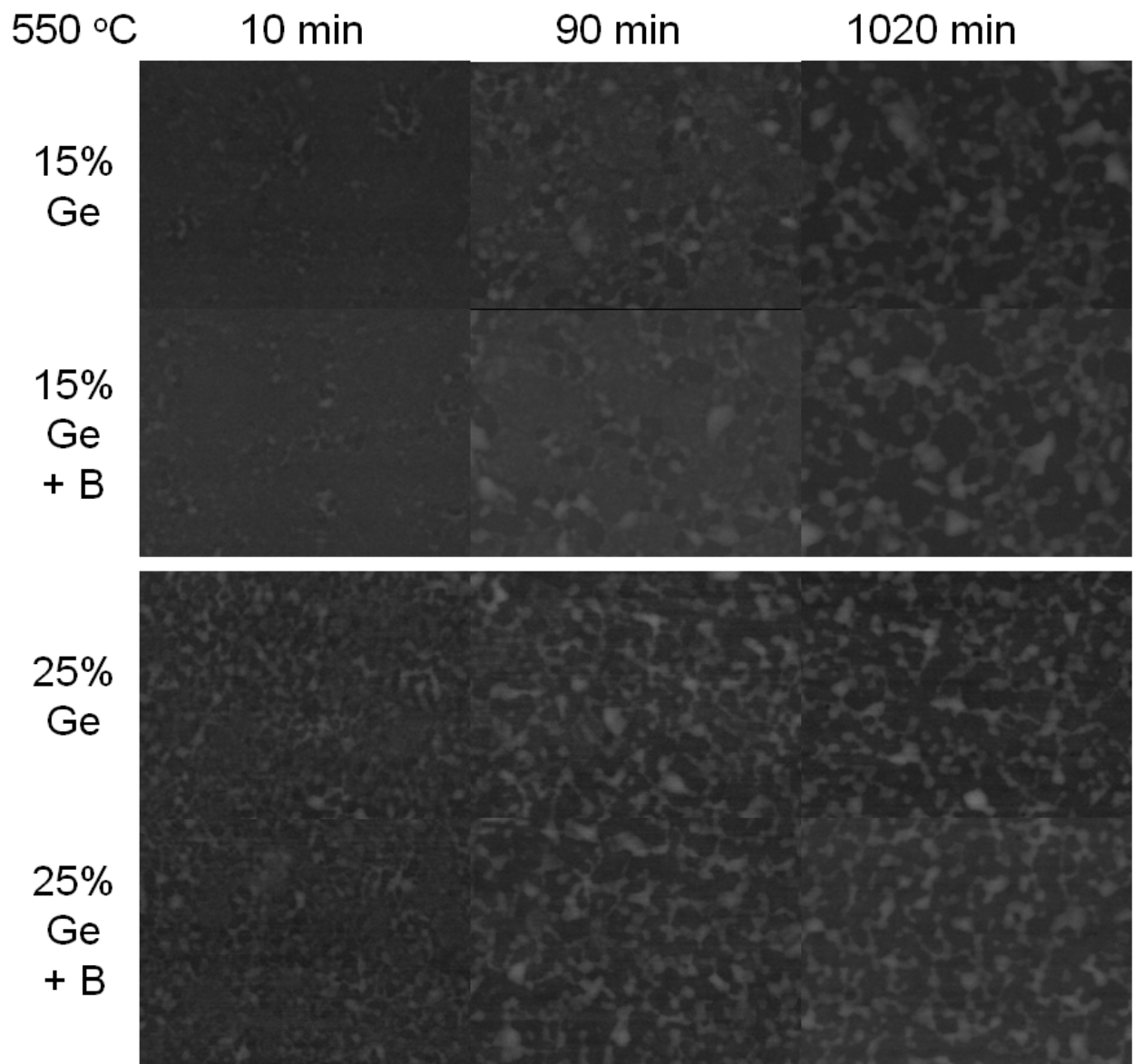


Figure 4-6: SEM/BSE images of samples annealed at 550 °C

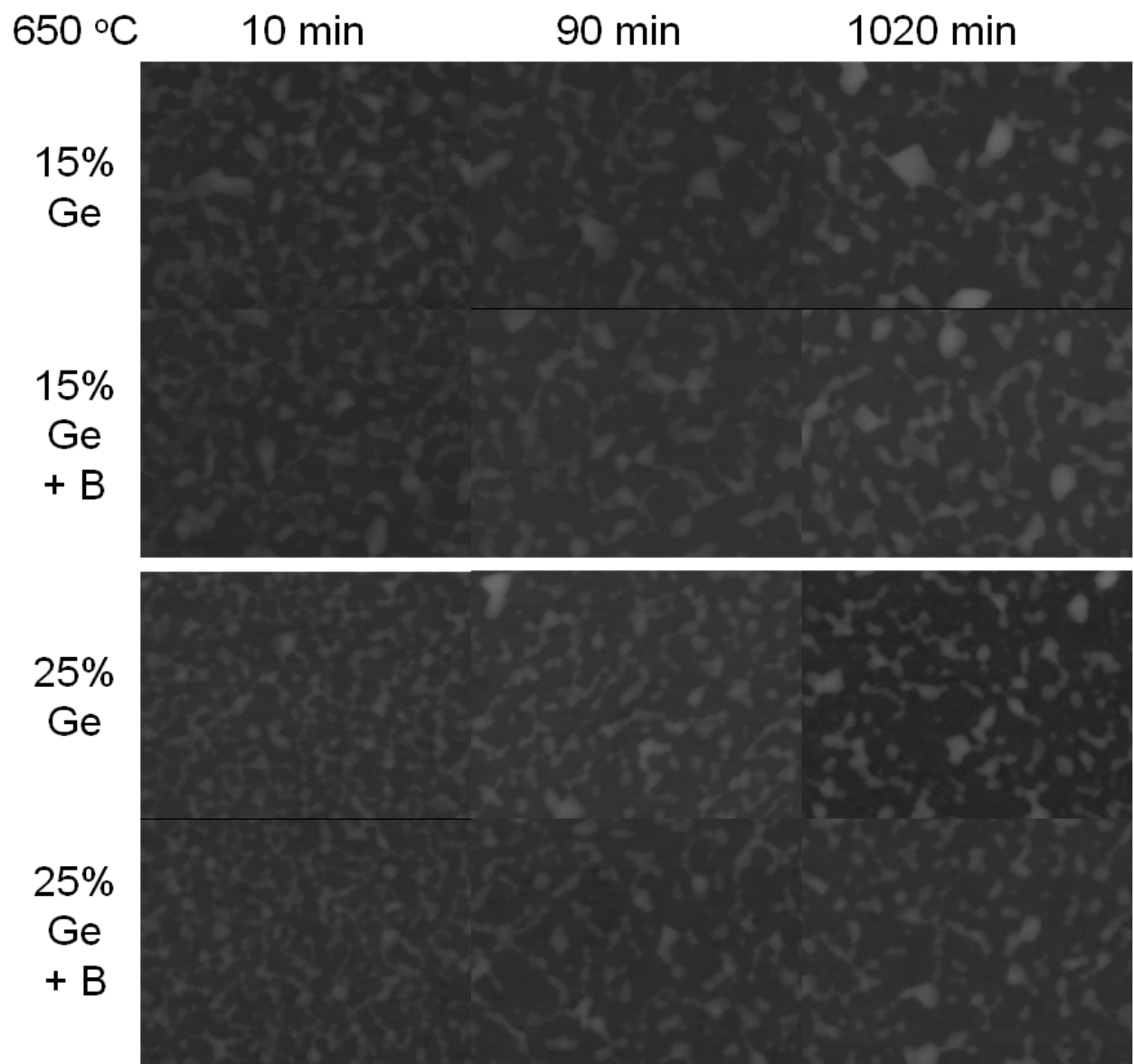


Figure 4-7: SEM/BSE images of samples annealed at 650 °C

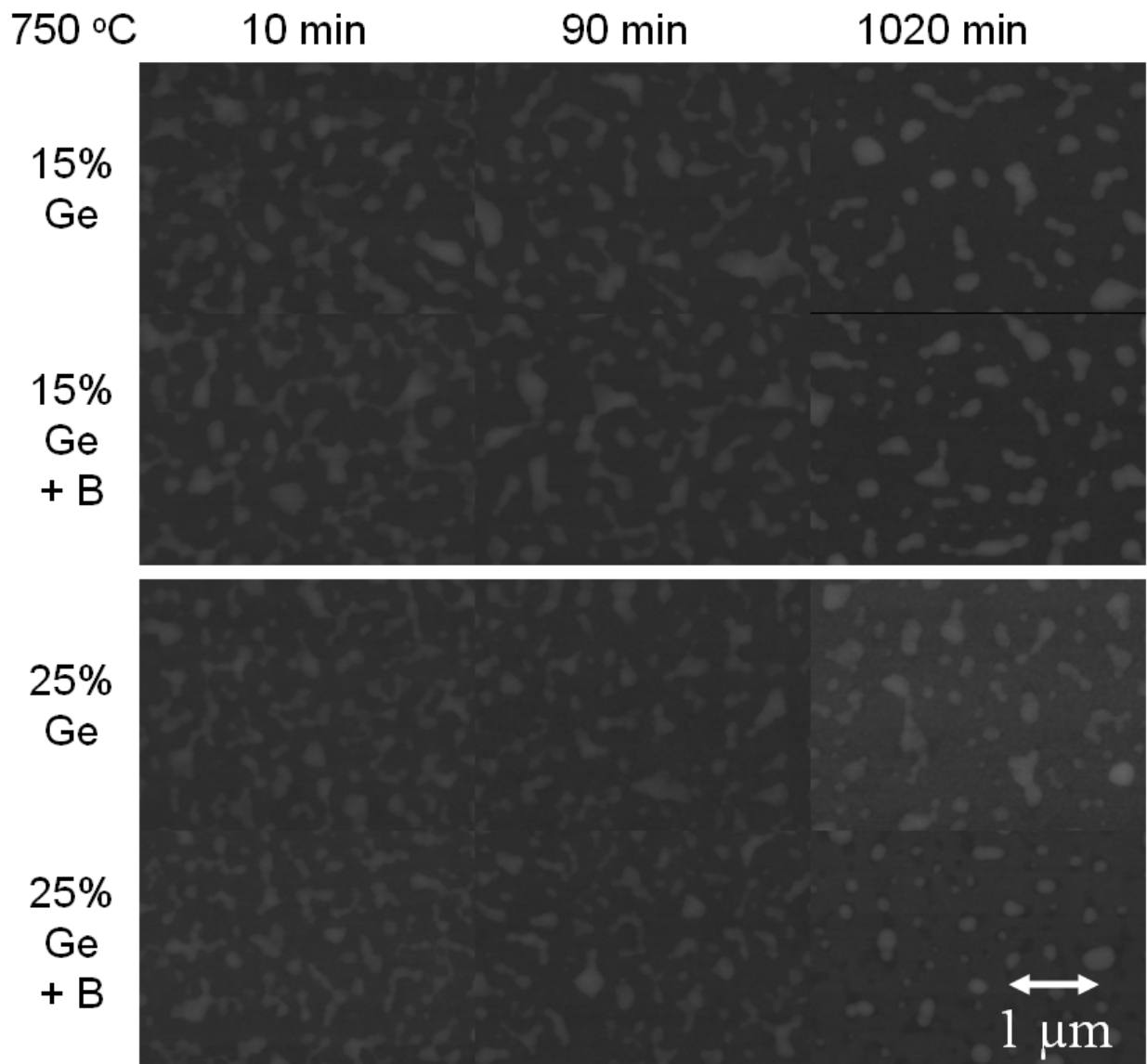


Figure 4-8: SEM/BSE images of samples annealed at 750 °C

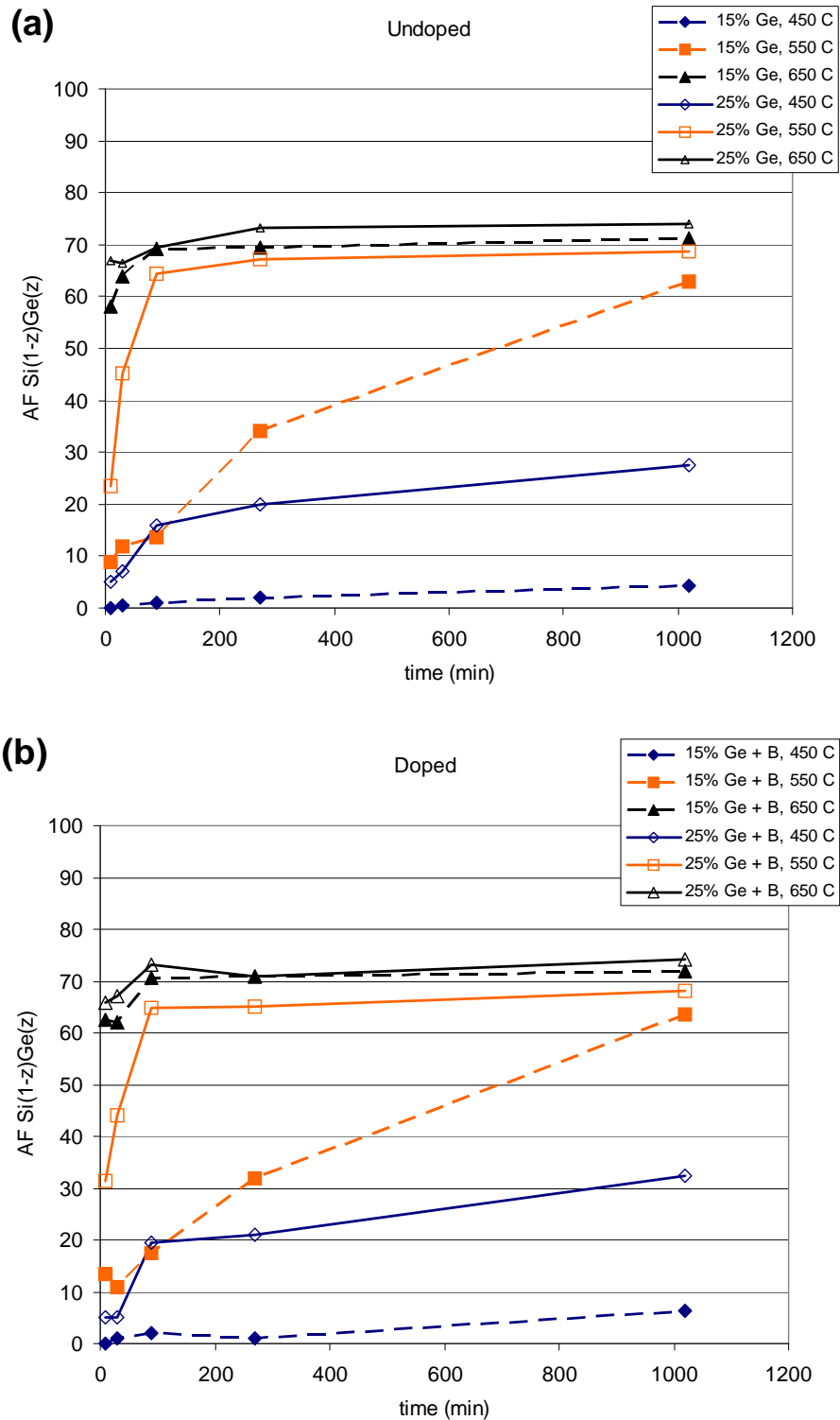


Figure 4-9: Area fraction of Ge-rich $\text{Si}_{1-z}\text{Ge}_z$ phase as a function of anneal time at temperatures of 450, 500, and 650 °C for (a) undoped samples and (b) doped samples.

$\mu = -15.05$
95% CI for μ : (-20.99, -9.11)
P-Value (for $\mu = 0$) = 0.000

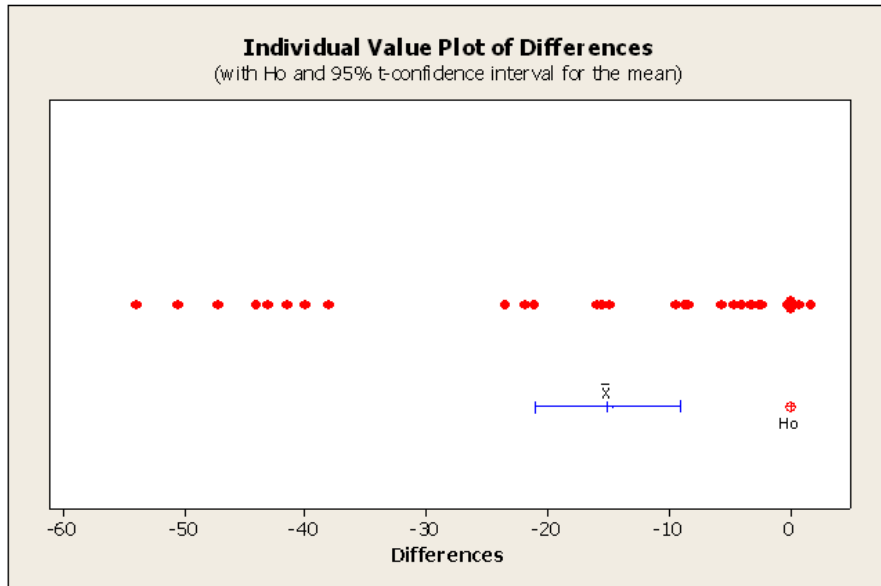


Figure 4-10: Paired t-test results (n=36) comparing the Ge-rich $\text{Si}_{1-z}\text{Ge}_z$ area fraction of 15 and 25% Ge samples at all points on the thermal matrix imaged with SEM/BSE.

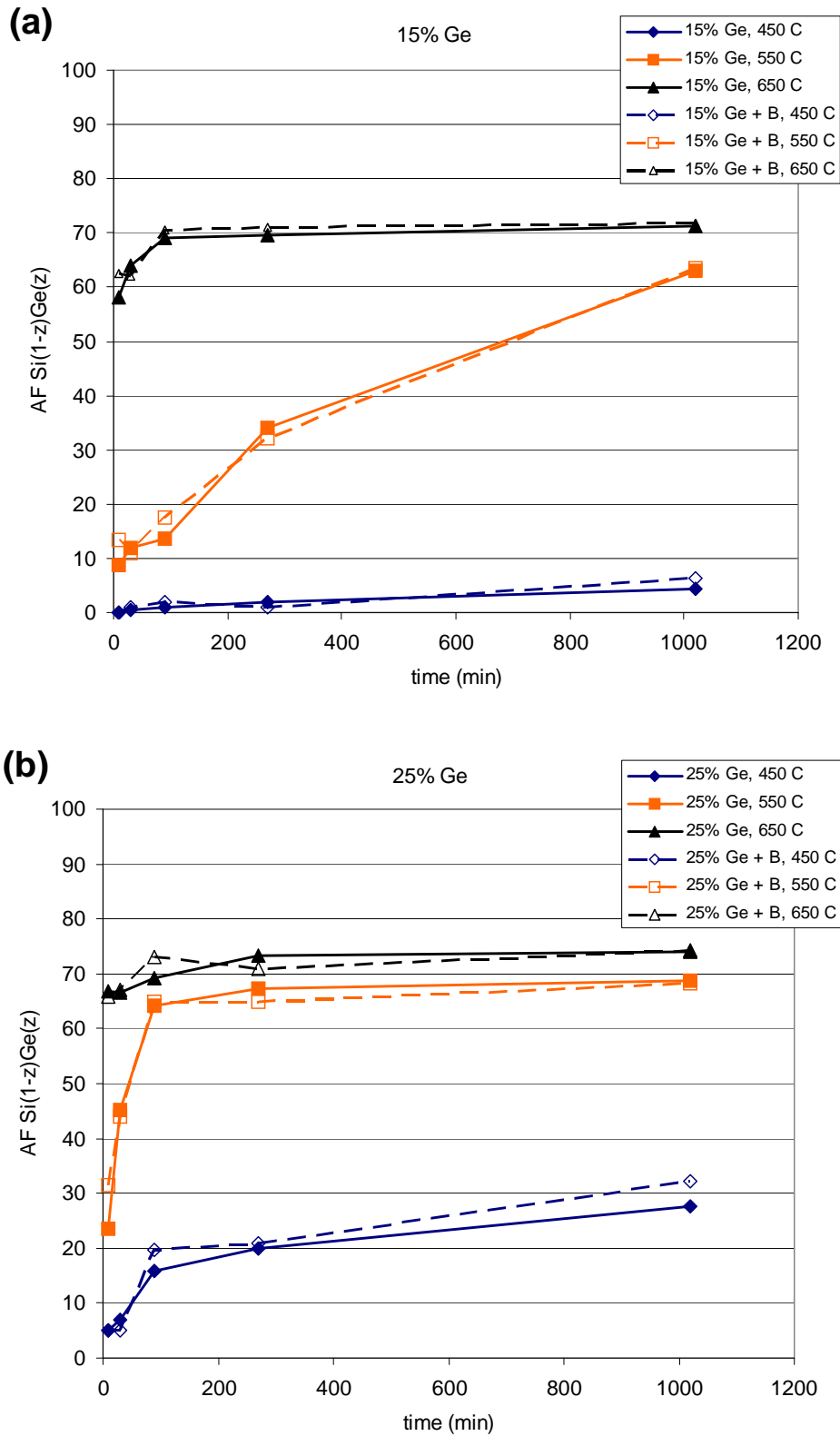
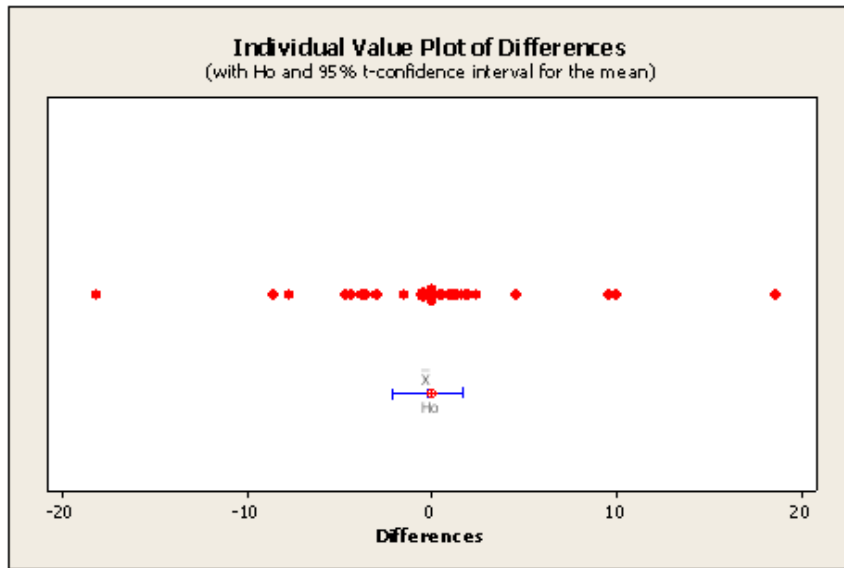


Figure 4-11: Area fraction of Ge-rich $\text{Si}_{1-z}\text{Ge}_z$ phase as a function of anneal time at temperatures of 450, 500, and 650 °C for (a) 15% Ge samples and (b) 25% Ge samples.

- (a) $\mu = -0.247$
95% CI for μ : (-2.195, 1.700)
P-Value (for $\mu = 0$) = 0.798



- (b) $\mu = -141$
95% CI for μ : (-408, 126)
P-Value (for $\mu = 0$) = 0.290

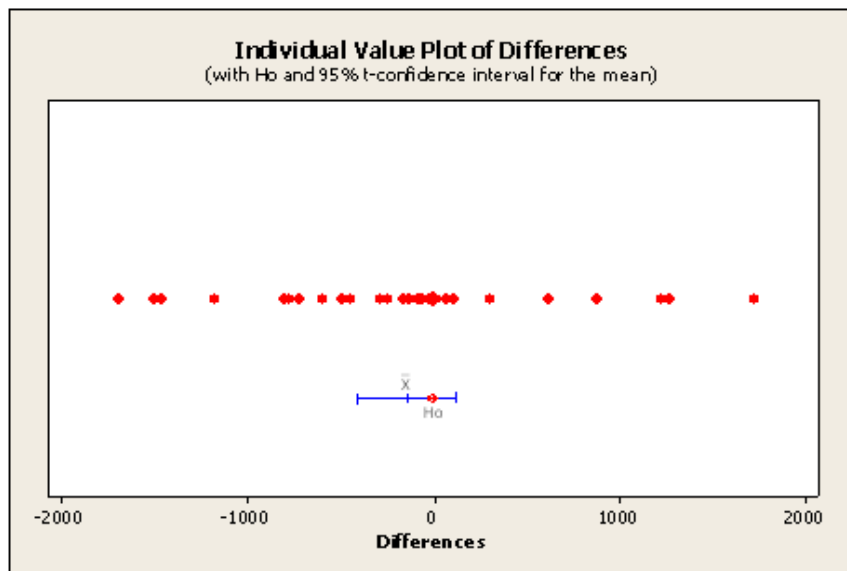


Figure 4-12: Paired t-test results ($n=36$) comparing the undoped and doped samples at all conditions imaged with SEM/BSE for (a) Ge-rich $\text{Si}_{1-z}\text{Ge}_z$ area fraction and (b) Ge-rich $\text{Si}_{1-z}\text{Ge}_z$ grain size.

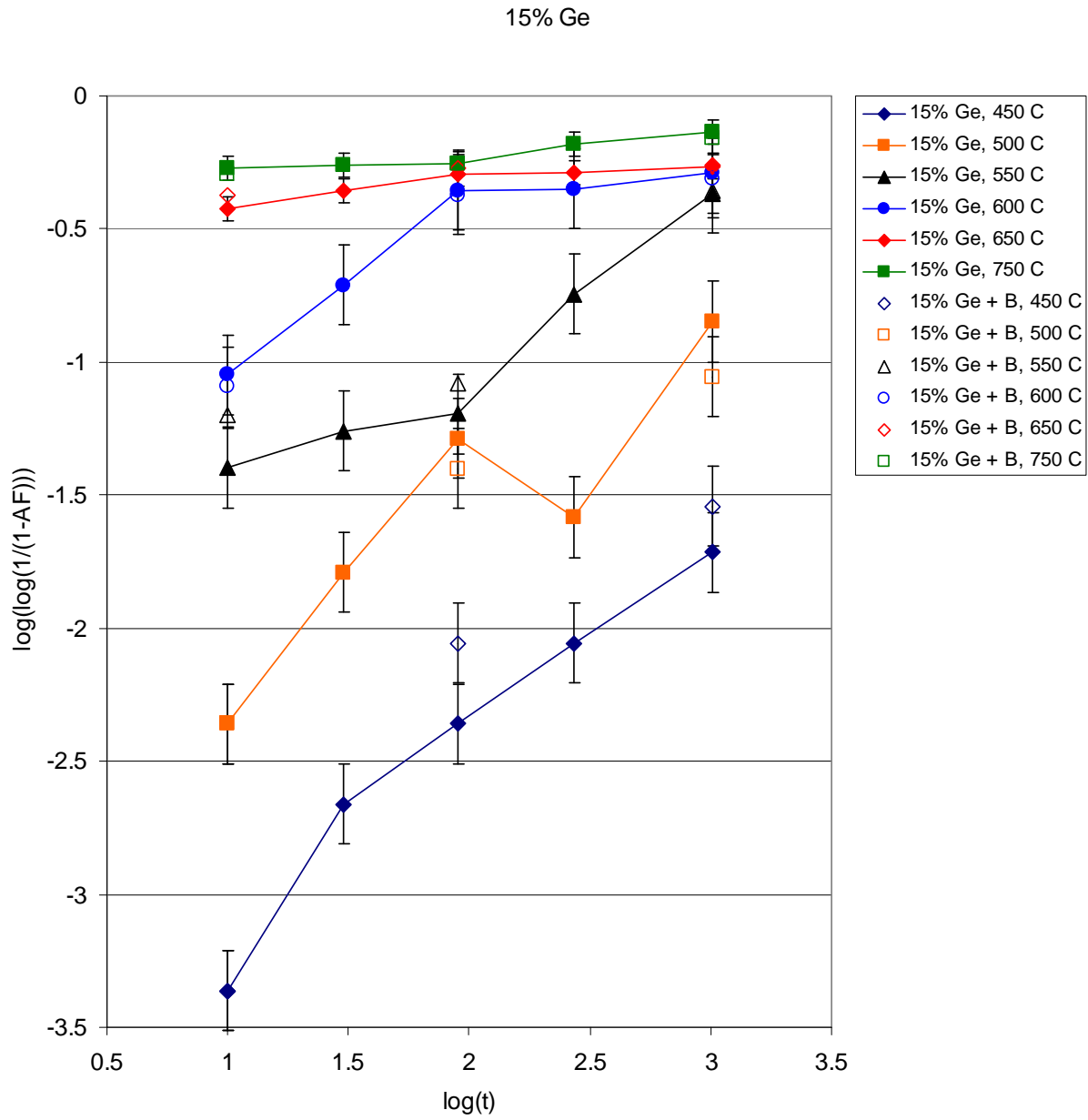


Figure 4-13: Plot of $\log(\log(1/(1-AF)))$ vs. $\log(t)$ for samples containing 15% Ge

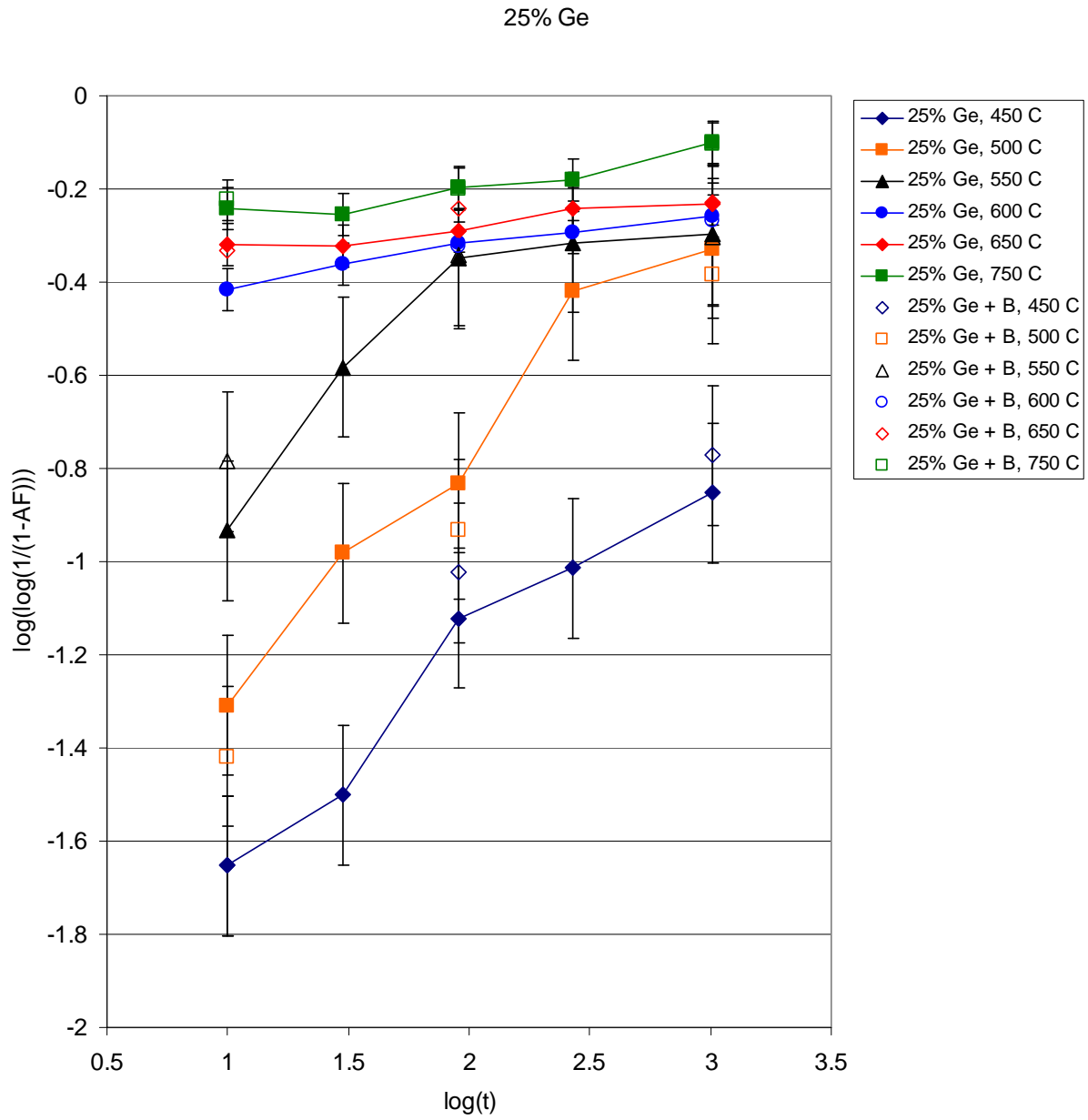


Figure 4-14: Plot of $\log(\log(1/(1-AF)))$ vs. $\log(t)$ for samples containing 25% Ge

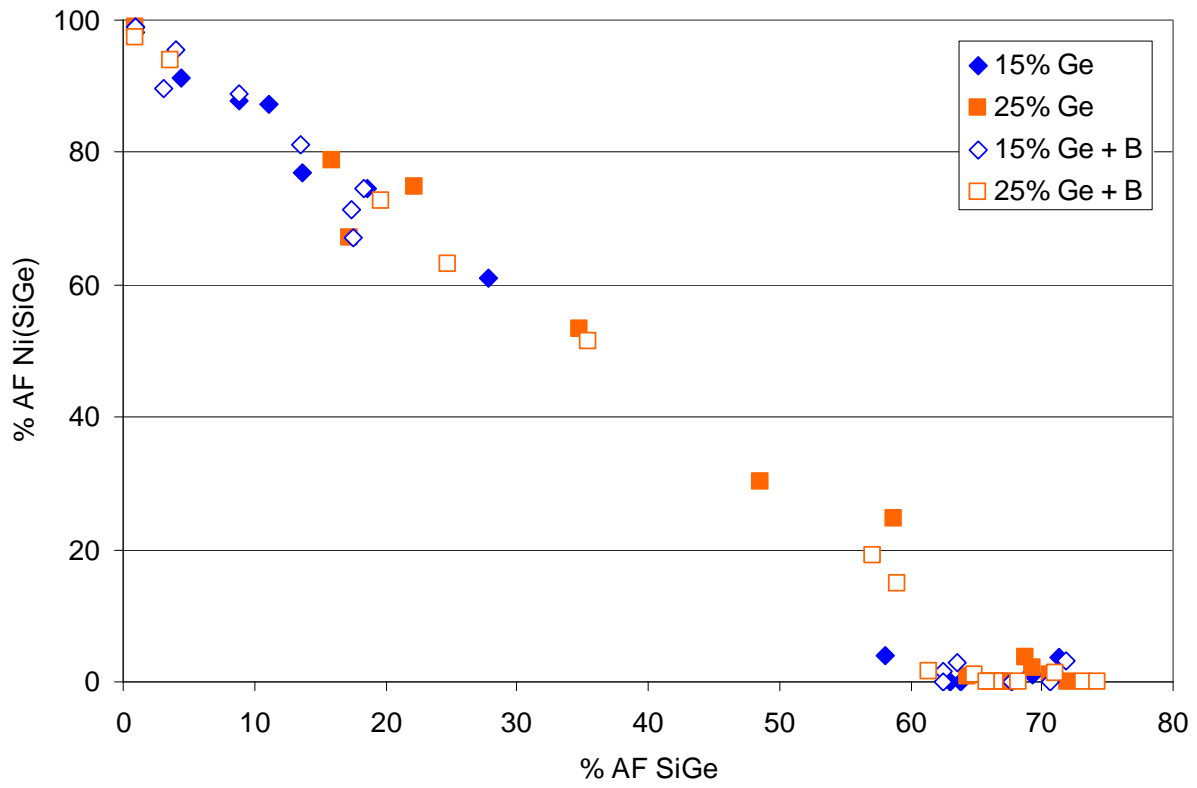


Figure 4-15: Plot of area fraction of initial Ni(Si_{1-x}Ge_x) phase present as a function of Ge-rich Si_{1-z}Ge_z area fraction.

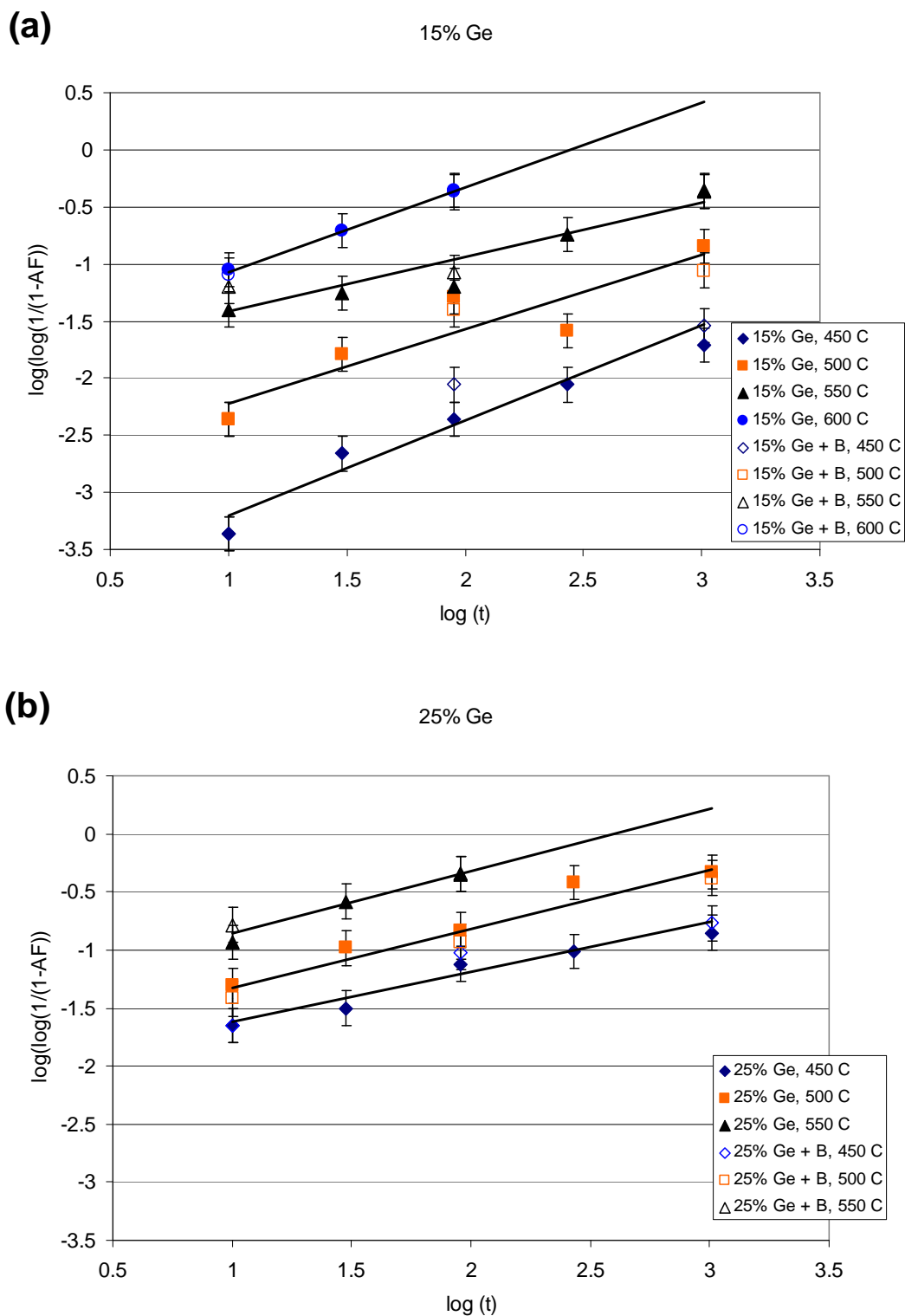


Figure 4-16: Plot of $\log(\log(1/(1-AF)))$ vs. $\log(t)$ for Ge-rich $\text{Si}_{1-z}\text{Ge}_z$ area fractions less than 60% (corresponding to precipitation reaction) for (a) 15% Ge and (b) 25% Ge samples.

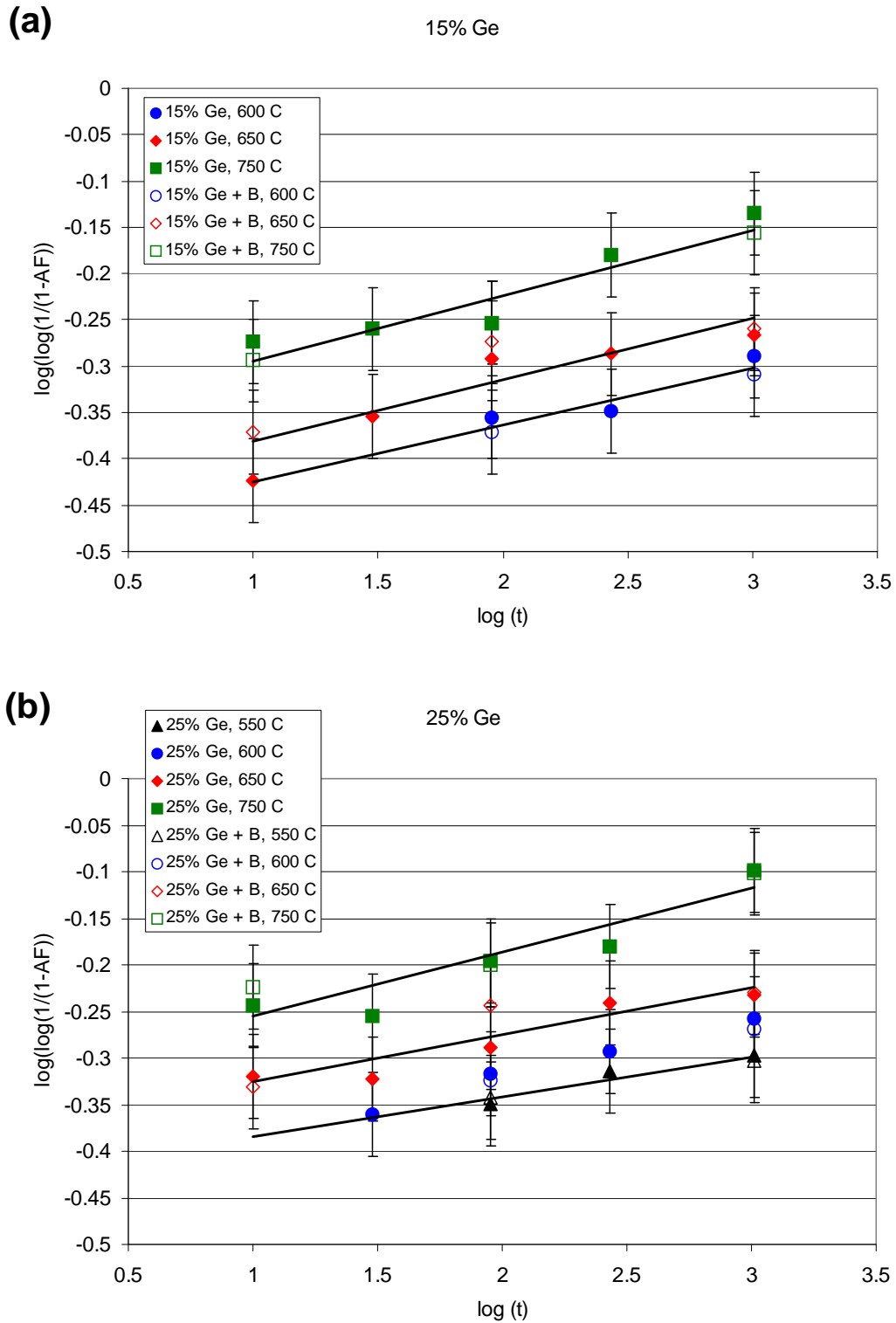


Figure 4-17: Plot of $\log(\log(1/(1-AF)))$ vs. $\log(t)$ for Ge-rich $\text{Si}_{1-z}\text{Ge}_z$ area fractions greater than 60% (corresponding to agglomeration reaction) for (a) 15% Ge and (b) 25% Ge samples.

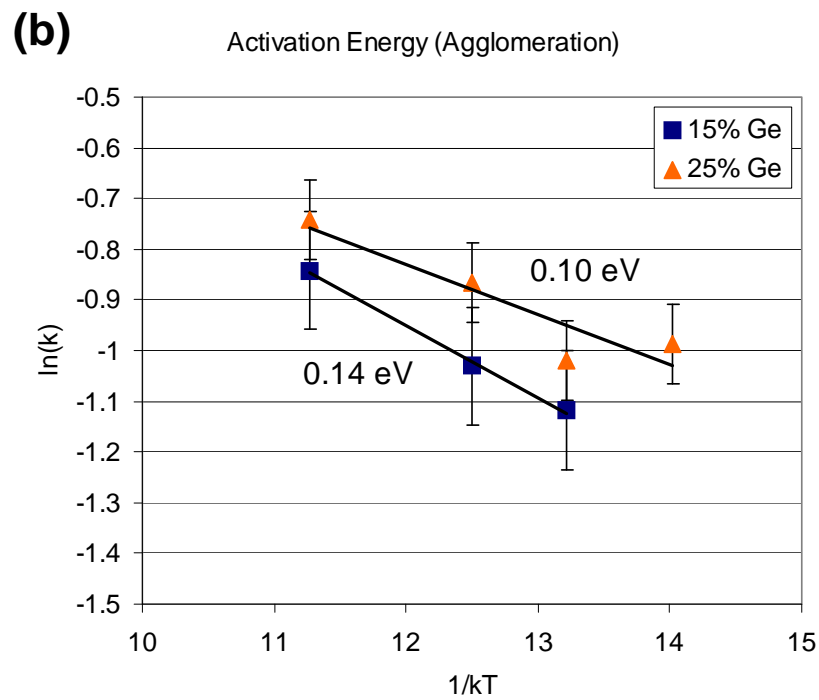
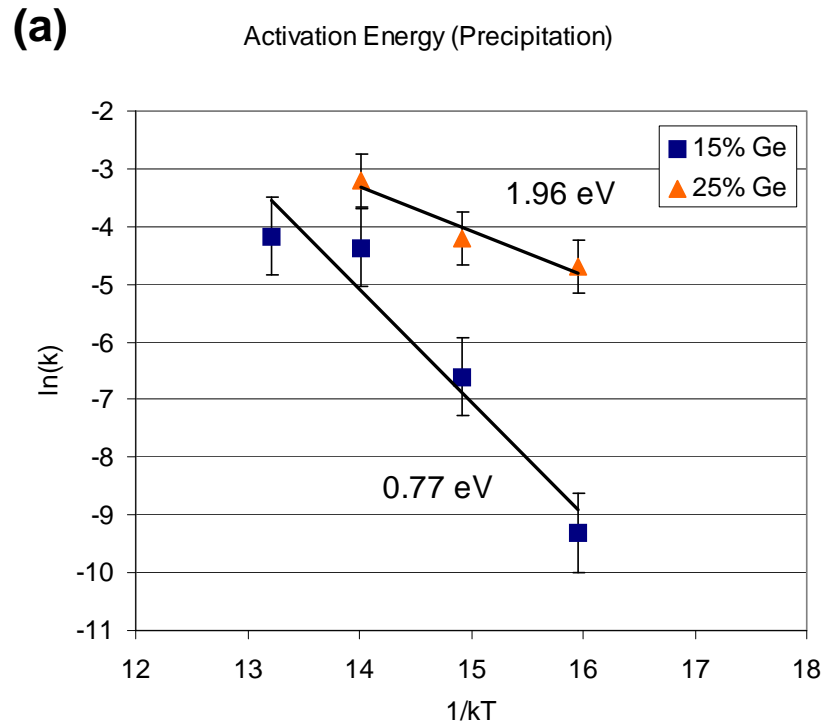


Figure 4-18: Plots of $\ln(k)$ vs. $1/(kT)$ for the (a) precipitation and (b) agglomeration reactions.

Table 4-1: Linear regression results for isothermal transformation curves plotted on a graphs of $\log(\log(1/(1-AF)))$ vs. $\log(t)$ for the precipitation reaction.

	n	standard error n	log(k)	standard error log(k)
15% Ge, 450 C	0.834	0.093	-4.041	0.197
15% Ge, 500 C	0.648	0.106	-2.869	0.223
15% Ge, 550 C	0.479	0.072	-1.897	0.152
15% Ge, 600 C	0.741	0.020	-1.810	0.031
15% Ge (average)	0.676	0.073	-2.654	0.151
25% Ge, 450 C	0.426	0.048	-2.042	0.101
25% Ge, 500 C	0.509	0.050	-1.832	0.105
25% Ge, 550 C	0.537	0.065	-1.392	0.099
25% Ge (average)	0.491	0.054	-1.755	0.102

Table 4-2: Values of n (reaction order) for reactions obeying Avrami kinetics [Chr02].

TABLE IX. VALUES OF n IN KINETIC LAW $\zeta = 1 - \exp(-kt^n)$

(a) Polymorphic changes, discontinuous precipitation, eutectoid reactions, interface controlled growth, etc.

Conditions	n
Increasing nucleation rate	>4
Constant nucleation rate	4
Decreasing nucleation rate	3-4
Zero nucleation rate (saturation of point sites)	3
Grain edge nucleation after saturation	2
Grain boundary nucleation after saturation	1

(b) Diffusion controlled growth

Conditions	n
All shapes growing from small dimensions, increasing nucleation rate	$>2\frac{1}{2}$
All shapes growing from small dimensions, constant nucleation rate	$2\frac{1}{2}$
All shapes growing from small dimensions, decreasing nucleation rate	$1\frac{1}{2}-2\frac{1}{2}$
All shapes growing from small dimensions, zero nucleation rate	$1\frac{1}{2}$
Growth of particles of appreciable initial volume	$1-1\frac{1}{2}$
Needles and plates of finite long dimensions, small in comparison with their separation	1
Thickening of long cylinders (needles) (e.g. after complete end impingement)	1
Thickening of very large plates (c.g. after complete edge impingement)	$\frac{1}{2}$
Precipitation on dislocations (very early stages)	$\sim \frac{2}{3}$

Table 4-3: Linear regression results for isothermal transformation curves plotted on a graphs of $\log(\log(1/(1-AF)))$ vs. $\log(t)$ for the agglomeration reaction

Agglomeration				
	n	standard error n	log(k)	standard error log(k)
15% Ge, 600 C	0.061	0.012	-0.485	0.030
15% Ge, 650 C	0.067	0.014	-0.448	0.029
15% Ge, 750 C	0.071	0.009	-0.366	0.020
15% Ge (average)	0.066	0.012	-0.433	0.026
25% Ge, 550 C	0.043	0.006	-0.428	0.016
25% Ge, 600 C	0.060	0.005	-0.442	0.012
25% Ge, 650 C	0.051	0.009	-0.377	0.019
25% Ge, 750 C	0.068	0.011	-0.323	0.024
25% Ge (average)	0.056	0.008	-0.392	0.017

Table 4-4: Activation energies derived from linear regression of series on the plot of $\ln(k)$ vs. $(1/KT)$

Precipitation		
	Ea	s.e. Ea
15% Ge	-1.961	0.376
25% Ge	-0.765	0.186

Agglomeration		
	Ea	s.e. Ea
15% Ge	-0.143	0.009
25% Ge	-0.100	0.029

CHAPTER 5 RELATIONSHIP OF SHEET RESISTANCE AND MICROSTRUCTURE AND THE INFLUENCE OF GE AND B

This chapter explores the influence of both Ge content and homogeneous in-situ B doping of the initial $\text{Si}_{1-x}\text{Ge}_x$ layer on the sheet resistance of nickel germanosilicide thin films. Using the results from the quantitative microstructure analysis performed in the previous chapter, this chapter also investigates the structure/property relationship between sheet resistance and microstructure. The influence of Ge content and B doping on the relationship is also addressed.

Prior work has widely utilized four point probe (4PP) sheet resistance measurements to characterize the electrical quality of nickel germanosilicide thin films. Isochronal sheet resistance measurements of undoped films, such as the one previously shown in Figure 2-19, have been reported by many researchers [Pey02, Zha02, Cha04, Cha04b, Zha04, Seg04, Liu05, Cho06, Ko06, Lau06, Yao06]. In each case, the isochronal sheet resistance curves show a relatively sharp increase in value around $\sim 700^\circ\text{C}$. In the absence of a high-resistivity digermanosilicide (analogous to the NiSi_2 phase), this increase is attributed to the agglomeration of the film. However, due to the limited thermal matrix and common lack of quantitative microstructure analysis, any direct structure/property relationship between sheet resistance and the microstructure has not been established.

Also of interest is determining how both Ge content and homogeneous in-situ B doping of the initial $\text{Si}_{1-x}\text{Ge}_x$ layer may affect the structure/property relationship. While it has been established in prior work [Ok03, Zha04] and confirmed in the previous chapter of this work that increasing Ge content increases film agglomeration, it is unknown whether Ge content would affect any microstructure/sheet resistance relationship. Prior work by Liu and Ozturk [Liu05] has shown that incorporation of high levels of in-situ doped B stabilizes sheet resistance. Their explanation for the cause of the stabilization (a reduction in agglomeration), however, was not

seen in the B doped samples of this work. Thus, it is of interest to first determine whether similar stabilization occurred in the samples in this work and, if so, how any structure/property relationship between sheet resistance and microstructure may have been altered.

To investigate the sheet resistance, structure/property relationship, and influence of Ge and B, the nickel germanosilicide films were formed at a range of thermal conditions. The Ge content in the initial $\text{Si}_{1-x}\text{Ge}_x$ layer of the structures was varied at levels of 10 and 25 at% and the layers were undoped or incorporated $\sim 4.5 \times 10^{19}$ atoms/cm³ of homogeneous in-situ B doping. The samples were annealed in a quartz tube furnace under N_2 ambient at temperatures between 450 and 800 °C in increments of 50 °C for 10, 30, 90, 270, and 1020 minutes. Once annealed, the sheet resistance of the samples was measured using a 4PP and the method previously presented in Chapter 3. It should be noted that, with the exceptions of the additional thermal series at 700 and 800 °C, the samples from the previous chapter were used for the analysis presented in this chapter.

5.1 Sheet Resistance Analysis

The sheet resistance of all samples was measured using the 4PP method outlined in Chapter 3. In keeping with prior work, the values of sheet resistance were plotted as a function of anneal temperature (isochronal series). It is important to note, however, that all samples were not able to be successfully measured for all times and temperatures. Instead, at higher values of temperature (generally over ~ 600 °C), some undoped samples were determined to be nonconductive. In this case, the plots of sheet resistance for those samples show a dashed line extrapolating to infinity after the last successful measurement of the isochronal series. The following sections discuss the sheet resistance measurement results in terms of Ge and B content to determine the respective influences of each variable.

5.1.1 Influence of Ge

The sheet resistance measurements for the undoped 15 and 25% Ge samples are presented in Figure 5-1(a) as a function of anneal temperature (isochronal series). Only the 10, 90, and 1020 minute anneal series are shown for clarity. It is apparent from the plot that increasing Ge content caused earlier increases in sheet resistance for all anneal series. The difference between the sheet resistances at each point in the thermal matrix was also calculated by subtracting the sheet resistance value of the 15% Ge sample from that of the 25% Ge sample, shown in Figure 5-1(b) for the isochronal 10, 90, and 1020 minute series. Dotted lines in the figure represent extrapolation to infinite sheet resistance (i.e. the next point in the series was unable to be successfully measured). It is evident from this plot that increasing Ge content increased the sheet resistance of the film by 10s to 100s of Ohm/sq. The intermediate isochronal series that were not shown in Figure 5-1 (30 and 270 min) displayed similar trends. The trend seen in these results agree well with those shown in prior work, where increasing Ge content was shown to result in poorer thermal stability of sheet resistance [Ok03, Zha04].

Isochronal sheet resistance measurements for the doped 15 and 25% Ge samples are presented in Figure 5-2(a). As with the undoped case, only the 10, 90, and 1020 minute anneal series are shown for clarity. It is apparent from the plot that, similar to the undoped samples, increasing Ge content caused an increase in sheet resistance for all anneal series. Figure 5-2(b) plots the differences between the sheet resistance values of the 25 and 15% Ge samples. It is evident from this plot that increasing Ge content increased the sheet resistance of the film by ~2 to ~70 Ohm/sq. In comparison with the undoped samples, these increases were generally smaller and more consistent across the thermal matrix. The intermediate isochronal series that were not shown in Figure 5-2 (30 and 270 min) displayed similar trends. This experiment was the first time the effect of Ge content on samples with homogeneously B doped $\text{Si}_{1-x}\text{Ge}_x$ layers was

investigated; the work by Liu and Ozturk [Liu05] did not vary Ge concentration (though it did vary initial Ni layer thickness). It is important to observe, therefore, that the trend of increasing Ge content increasing sheet resistance seen in undoped samples is also present in the doped samples, though to a lesser degree.

5.1.2 Influence of B

Previous work has shown that the addition of dopants to the initial $\text{Si}_{1-x}\text{Ge}_x$ prior to silicidation may [Liu05] or may not [Cha04] affect the sheet resistance of nickel germanosilicide thin films. Isochronal sheet resistance measurements for the undoped and doped 15% Ge samples in this work are presented in Figure 5-3(a). Only the 10, 90, and 1020 minute anneal series are shown for clarity. It is apparent from the plot that the B doped samples have a lower sheet resistance than the corresponding undoped samples at all times and temperatures. It is also apparent that the addition of B stabilized the sheet resistance measurements to much higher temperatures; as previously shown, no doped sample registered as non-conductive in this work. Figure 5-3(b) plots the differences between the sheet resistance values of the doped and undoped 15% Ge samples. It is evident from this plot that the addition of B doping initially provides a small decrease in sheet resistance. However, once the sheet resistance of the undoped sample begins to rapidly increase the addition of B doping results in a large decrease of sheet resistance. The magnitude of the decrease was eventually equal to infinity as the undoped samples read as open circuits and the doped samples maintained values less than ~ 120 Ohm/sq. The intermediate isochronal series that were not shown in Figure 5-2 (30 and 270 min) displayed similar trends.

Isochronal sheet resistance measurements for the undoped and doped 25% Ge samples are presented in Figure 5-4(a) and their differences in (b). These results are very similar to those discussed for the undoped and doped 15% Ge samples with the exception that the stabilization begins earlier (due to the influence of Ge content). As with the 15% Ge samples, the addition of

B stabilized the sheet resistance measurements to much higher temperatures. The difference between the sheet resistances of corresponding undoped and doped samples was also initially small and then rapidly grew, approaching infinity.

These results confirm that both the 15 and 25% Ge structures used in this work show the stabilizing effect on sheet resistance of the addition of high levels of homogeneous B doping during $\text{Si}_{1-x}\text{Ge}_x$ layer growth reported by Liu and Ozturk [Liu05]. While the level of B doping in this work ($\sim 4.5 \times 10^{19}$ atoms/cm³) is less than that used in their published work ($\sim 2.1 \times 10^{21}$ atoms/cm³), it is reasonable to assume that the same mechanism is causing the reduction and stabilization of sheet resistance for both works. Liu and Ozturk proposed that the cause for the effect was due to a reduction in agglomeration caused by strain-relieving effects of the high levels of B. The previous chapter of this work, however, showed that no difference in sample microstructure or evolution was caused by the addition of B doping. Thus, the effects of B on sheet resistance cannot be explained by its influence on film microstructure. A different proposed mechanism, and the influence of B doping on any sheet resistance/microstructure relationship, will be discussed in the following sections.

5.2 Sheet Resistance/Microstructure Relationship

Apart from the specific influences of Ge and B content, Figures 5-1 to 5-4 show a general trend of increasing thermal annealing causing an increase in sheet resistance (to a greater or lesser degree, dependent on Ge and B content). Similar trends have been extensively reported in literature and are generally ascribed to the worsening of film morphology with increasing anneal time and temperature (e.g. “agglomeration”) [Pey02, Zha02, Cha04, Cha04b, Zha04, Seg04, Liu05, Cho06, Ko06, Lau06, Yao06]. In general, however, prior literature has lacked quantitative analysis of film morphology in plan view, as well as having been confined to a single isochronal series. These limitations have precluded establishment of any direct,

quantitative structure/property relationship between film morphology and sheet resistance. Instead, only a circumstantial, qualitative relationship has been established. This work, however, performed quantitative microstructure analyses of a large number of anneal times and temperatures. These results, presented in the previous chapter, can be used in conjunction with the corresponding sheet resistance measurements presented in the preceding sections of this chapter to investigate the structure/property relationship between film microstructure and sheet resistance in a quantitative manner.

Film microstructures in Chapter 4 were quantified using three metrics: Ge-rich $\text{Si}_{1-z}\text{Ge}_z$ grain size, Si-rich $\text{Ni}(\text{Si}_{1-u}\text{Ge}_u)$ area fraction, and Ge-rich $\text{Si}_{1-z}\text{Ge}_z$ area fraction. Each of these three metrics was evaluated for suitability in establishing a structure/property relationship by plotting the sheet resistance of each sample as a function of the metric. Figure 5-5 presents the result of plotting sheet resistance as a function of Ge-rich $\text{Si}_{1-z}\text{Ge}_z$ grain size for all four structure types. Analysis of the plot shows that data from each sample type is widely scattered and intermixed with the other types, no discernable patterns are apparent. It is evident from this figure that Ge-rich $\text{Si}_{1-z}\text{Ge}_z$ grain size is not a suitable metric for establishing a quantitative relationship. Next, sample sheet resistance was plotted as a function of Si-rich $\text{Ni}(\text{Si}_{1-u}\text{Ge}_u)$ area fraction, shown in Figure 5-6(a). While this plot shows stronger trends than Figure 5-5, consistent relationships are not readily observed. Finally, sample sheet resistance was plotted as a function of Ge-rich $\text{Si}_{1-z}\text{Ge}_z$ area fraction, shown in Figure 5-6(b). This plot shows strong, consistent trends for all sample series which are clearly superior to those generated using the other metrics. It was determined, therefore, that Ge-rich $\text{Si}_{1-z}\text{Ge}_z$ area fraction was the best metric for use in establishing a structure/property relationship. It should be noted that Figure 5-6(b), and the plots derived from it throughout this chapter, is a plot of two experimentally

measured parameters. Accordingly, each data point has error in both the x (Ge-rich $\text{Si}_{1-z}\text{Ge}_z$ area fraction) and y (sheet resistance) axes of the plot. For the x-axis, error remains as discussed previously and in Appendix A, with a 95% confidence interval of 3.35%. The y-axis error, as determined in Appendix B, however, is narrow enough in range (~ 2.2 Ohm/sq for a 95% confidence interval) in comparison to the magnitude of the measurements that the error bars are not visible on the plot.

It is clearly evident from Figure 5-6(b) that a structure/property relationship between Ge-rich $\text{Si}_{1-z}\text{Ge}_z$ area fraction and film sheet resistance can be established. Both area fraction and sheet resistance are area properties. Hence, it could be expected that the sheet resistance of an anisotropic, non-textured two-phase microstructure (such as that evident in the SEM/BSE images of Figures 4-5 to 4-8) would vary linearly between the values of each phase. This relationship, however, is clearly not shown by the series in Figure 5-6(b). The discrepancy can be further illustrated by Figure 5-7(a), which shows the experimental relationship for the doped 15% Ge samples versus a linear interpolation between the values for the homogeneous nickel germanosilicide film (~ 10 Ohm/sq) and the B-doped $\text{Si}_{1-x}\text{Ge}_x$ layer (~ 120 Ohm/sq).

While, on initial observation, it may be attractive to model the microstructure/sheet resistance relationships for the sample series as exponential functions, the results from the microstructure analysis performed in Chapter 4 should be considered first. It was previously shown in Figure 4-15 that the area fraction of the initial $\text{Ni}(\text{Si}_{1-x}\text{Ge}_x)$ phase decreases with increasing Ge-rich $\text{Si}_{1-z}\text{Ge}_z$ area fraction. If this same plot is added on a secondary axis to a plot of the structure/property relationships, as is shown in Figure 5-7(b), it can be seen that the inflection point in the relationship corresponds to the disappearance of the initial $\text{Ni}(\text{Si}_{1-x}\text{Ge}_x)$ phase (at $\sim 60\%$ area fraction of Ge-rich $\text{Si}_{1-z}\text{Ge}_z$). The analysis in Chapter 4 also showed that it

is at this point that the morphological evolution of the film should be separated into two stages: precipitation and agglomeration. With this consideration, it is apparent that the structure/property relationships should be modeled as two sets of linear functions, one for each of the stages of microstructure evolution. These two stages, called Stage I for the precipitation reaction and Stage II for the agglomeration reaction, are shown in Figure 5-7(b). These structure/property relationships, and the influence of Ge and B on them, will be discussed in the following sections.

5.2.1 Stage I (Precipitation)

Figure 5-8 presents the sheet resistance of the sample series as a function of Ge-rich $\text{Si}_{1-z}\text{Ge}_z$ area fraction for area fractions less than 60%, corresponding to the precipitation stage of the microstructure evolution process. It is evident from this figure that the distribution of data points is not even, but skewed towards lower area fractions (less than ~25%). This is a result of the anneal sequences not being tailored to produce evenly spaced steps in area fractions, as the necessary rate calculations to engineer such a spacing were not available. It is also evident from the figure that there appears to be more spread in the data as the area fraction increases. Both of these observations will become important in the following sections as the influences of Ge and B are considered.

5.2.1.1 Influence of Ge

The influence of initial $\text{Si}_{1-x}\text{Ge}_x$ layer Ge content on the structure/property relationship of the undoped samples was determined by plotting the area fraction of Ge-rich $\text{Si}_{1-z}\text{Ge}_z$ area fraction versus sheet resistance, shown in Figure 5-9(a). Linear regression analysis of the series was also performed and the best fit lines shown on the plot. The linear regression analysis provided a best fit line with an R^2 value of 0.7454 and 0.8431 for the 15 and 25% Ge samples, respectively. The regression results including slope, slope standard error, intercept, and intercept

standard error, are presented in Table 5-1. These results, in combination with the R^2 values, indicate that the accuracy of the linear regressions for the undoped samples are hampered by the relatively few data points and large scatter above $\sim 25\%$ $\text{Si}_{1-z}\text{Ge}_z$ area fraction, especially for the 15% Ge samples. Nevertheless, it can be concluded that increasing Ge-rich $\text{Si}_{1-z}\text{Ge}_z$ area fraction causes an increase in sheet resistance.

Figure 5-9(b) presents a plot of the area fraction of Ge-rich $\text{Si}_{1-z}\text{Ge}_z$ area fraction versus sheet resistance for the doped 15 and 25% Ge samples. As with the undoped samples, linear regression analysis was performed and the best fit line shown for each series, with R^2 values of 0.8663 and 0.8423 for the 15 and 25% Ge series, respectively. The numerical regression results for these lines are also given in Table 5-1. These results indicate that the doped samples have a stronger linear trend than their undoped counterparts. Less disparity between the regression lines for the two series is also qualitatively apparent for the doped samples when compared to the undoped ones. As with the undoped series, however, the accuracy of the results is still hampered by the relative scarcity of data between ~ 25 and 60% Ge-rich $\text{Si}_{1-z}\text{Ge}_z$ area fraction, especially for the 15% Ge samples.

The values for the regression intercepts and their 95% confidence intervals are shown in Figure 5-10(a) and for each of the four sample series. Using 2-sample t-tests, it can be shown that no statistically significant differences in intercept value exist at the 95% confidence level between any of the sample series. This result was expected, as at low times and temperatures all samples exhibited a homogeneous, continuous film of $\text{Ni}(\text{Si}_{1-x})\text{Ge}_x$. It would be expected, therefore, that the intercept value of each plot of area fraction Ge-rich $\text{Si}_{1-x}\text{Ge}_x$ vs. sheet resistance would be equal to each other and the sheet resistance of this initial film (where there is 0% area fraction $\text{Si}_{1-z}\text{Ge}_z$). The average intercept value of $\sim 8 \pm 3$ Ohm/sq does in fact agree

well with the previously reported values for a such a film which have usually averaged between 5 and 12 Ohm/sq dependent upon initial Ni layer thickness, etc [Ok03, Cha04, Zha04, Liu05].

The values for the regression slopes and their 95% confidence intervals are shown in Figure 5-10(b) and for each of the four sample series. While 2-sample t-tests cannot statistically prove that the slopes for the 15 and 25% Ge samples are equivalent, this is likely due to the uncertainty introduced by the aforementioned scatter and lack of data at area fractions between 25 and 60%, especially for the 15% Ge samples. Qualitatively, however, the slope regression results for the 15 and 25% Ge series appear to be fairly similar for either the undoped or doped samples. These observations are further reinforced by observation of Figure 5-9(a) and (b) where the data points for both the 15 and 25% Ge samples appear to be well-interspersed for both the undoped and doped samples. It can be tentatively concluded, therefore, that increasing Ge content of the initial $\text{Si}_{1-x}\text{Ge}_x$ layer does not affect the structure/property relationship between precipitated Ge-rich $\text{Si}_{1-z}\text{Ge}_z$ area fraction and sheet resistance. This conclusion, however, requires further experimentation to provide statistically significant support; the needed experimentation will be discussed in a later section.

5.2.1.2 Influence of B

Figure 5-11 presents a plot of film sheet resistance vs. Ge-rich $\text{Si}_{1-z}\text{Ge}_z$ area fraction for all four sample series. The analysis in the previous section showed that it can be tentatively concluded that varying Ge content in undoped and doped nickel germanosilicide thin films does not affect the relationship between film morphology and sheet resistance. This section, therefore, grouped together the data from the 15 and 25% Ge samples when considering the influences of homogeneous B doping of the initial $\text{Si}_{1-x}\text{Ge}_x$ layer on the structure/property relationship. Linear regression analysis was accordingly performed on the grouped 15 and 25% Ge samples for the undoped and doped cases and the best fit regression lines shown on Figure 5-

11. The numerical regression results are included in Table 5-2 and the regression intercepts, slopes, and respective 95% confidence intervals of the lines are presented in Figure 5-12(a) and (b).

Comparison of the regression intercept values with a 2-sample t-test shows that there is no difference between the undoped and doped samples at a 95% confidence level. As in the previous section, the average intercept value of 9.7 ± 2 Ohm/sq agrees well with prior literature. Comparison of the regression slope values, however, shows that there is a significant difference between the undoped and doped samples at a 95% confidence level with the doped samples having a slope approximately ~60% less than the undoped samples. It can be concluded, therefore, that the addition of homogeneous B doping influences the fundamental structure/property relationship between film microstructure and sheet resistance. The cause for this influence is likely the addition of a more conductive current path provided by the B doped samples. The specific nature and location of this conductive path will be addressed separately in a later section.

5.2.1.3 Tortuosity Analysis

The previous sections have established that the sheet resistance of nickel germanosilicide thin films increases approximately linearly with increasing $\text{Si}_{1-z}\text{Ge}_z$ area fraction within this stage of the overall microstructure evolution (less than 60% AF $\text{Si}_{1-z}\text{Ge}_z$). Figure 5-7(a) has previously shown, however, that the effect cannot be described by a linear interpolation between the sheet resistance of the initial film and the substrate. It is of interest, therefore, to determine if the underlying cause for the relationship can be determined.

When considering possible mechanisms, it is important to remember that the defining characteristic of the first stage of the microstructure evolution is the presence of initial $\text{Ni}(\text{Si}_{1-x}\text{Ge}_x)$ phase which has not yet fully rejected Ge and transformed into Si-rich $\text{Ni}(\text{Si}_{1-u}\text{Ge}_u)$ and

Ge-rich $\text{Si}_{1-z}\text{Ge}_z$. Thus, it can be qualitatively observed in the SEM/BSE images that within this stage, the highly conductive $\text{Ni}(\text{Si}_{1-x}\text{Ge}_x)$ and Si-rich $\text{Ni}(\text{Si}_{1-u}\text{Ge}_u)$ phases form a continuous network which is disrupted by grains of relatively less conductive Ge-rich $\text{Si}_{1-z}\text{Ge}_z$. This observation leads to the suggestion that the conductive phases may be carrying the majority of the current and that the less conductive Ge-rich $\text{Si}_{1-z}\text{Ge}_z$ grains are disrupting the current path, causing an increase in sheet resistance with increasing area fraction (and hence interference) of $\text{Si}_{1-z}\text{Ge}_z$.

It was of interest, therefore, to determine how the conductive path tortuosity and the area fraction of $\text{Si}_{1-z}\text{Ge}_z$ were related. Accordingly, the tortuosity of selected doped and undoped 25% Ge samples was calculated according to the method described in Chapter 3. Figure 5-13 shows a example image and estimated continuous conductive path across the sample. The samples used in this analysis, and their $\text{Si}_{1-z}\text{Ge}_z$ area fraction, tortuosity, and sheet resistance are presented in Table 5-3. The samples were selected such that they covered the entire range of $\text{Si}_{1-z}\text{Ge}_z$ area fractions within the first stage of microstructure transformation. It is important to note that, due to the requirement of manual calculation, sample tortuosity was calculated using the average of three random measurements of a single image for each sample condition. The small sample size and relatively inaccurate calculation (when compared to computer modeling), therefore, resulted in substantial error in the tortuosity measurement. The average tortuosity range for the three measurements of each image was determined to be 0.0333. The measurement error, therefore, was estimated by dividing this value by the square root of the sample size (3) according to the work of Kyker [Kyk83] which showed that for normal distributions, this calculation would estimate the true standard deviation within 10-15%. For the tortuosity

calculations in this work, the resulting 95% confidence interval based on the error estimation proposed by Kyker was determined to be ± 0.0377 .

Figure 5-14(a) presents a plot of conductive path tortuosity vs. $\text{Si}_{1-z}\text{Ge}_z$ area fraction for the selected undoped and doped 25% Ge samples. It is evident from this plot that conductive path tortuosity increases linearly with increasing area fraction of $\text{Si}_{1-z}\text{Ge}_z$. It is also apparent without statistical analysis that B doping does not influence the relationship between the two properties. A single linear regression was therefore performed for all data points and the best fit regression line and equation shown in the figure. While the tortuosity of the 15% Ge samples was not studied, the same relationship is expected due to the similarity in microstructure evolution observed in the previous chapter. Additional work should be performed, however, to confirm this expectation and strengthen the observed relationship by reducing the error in tortuosity measurement.

The direct relationship between tortuosity and sheet resistance was also explored; the sheet resistance of the undoped and doped 25% Ge samples was plotted as a function of conductive path tortuosity and is presented in Figure 5-14(b). While observation of this plot shows that there is a distinct relationship between the two properties, it is not evident (due to the few data points and large error) either through qualitative or statistical analysis whether the relationship is of an exponential nature or linear relationship. The R^2 values for an exponential relationship are 0.864 and 0.874 for the undoped and doped 25% Ge samples, respectively. For a linear relationship, the values are 0.830 and 0.817, respectively. Regardless, the stabilization caused by B doping is clearly evident in the figure as the doped samples have smaller sheet resistance values than the undoped samples of equal tortuosity. While additional analysis is necessary to better establish the relationship, these results support the theory that the mechanism behind the

structure/property relationship in this stage of the film's microstructural evolution is likely related to the disruption of the conductive path through the Ni(Si_{1-x}Ge_x) and Si-rich Ni(Si_{1-u}Ge_u) grains by the precipitation of less conductive Si_{1-z}Ge_z. It is also probable, therefore, that the addition of B doping reduces the magnitude of this disruption by providing an alternative conduction path; as mentioned before, the nature and location of this path will be addressed in a later section. It is also important to note that the linear relationship between conductive path tortuosity and Si_{1-z}Ge_z area fraction suggests that the properties may be co-dependant variables. If so, conductive path tortuosity may be a better predictor of sheet resistance than Si_{1-z}Ge_z area fraction.

5.2.2 Stage II (Agglomeration)

The structure/property relationship between film microstructure and sheet resistance was also considered within the agglomeration stage of the film transformation. The samples in this stage had Si_{1-z}Ge_z area fractions above 60% and no sample in the study exhibited an area fraction greater than 78.16%. It is expected, however, that samples with significantly greater area fractions than this value will not occur, as while Ni(Si_{1-u}Ge_u) grains are agglomerating in this stage to reduce their interface energies resulting in the deepening of grains and through conservation of mass an associated reduction in projected size, eventually an equilibrium will be reached in this process. More simply put, the area fraction of Si_{1-z}Ge_z will never reach 100% as long as grains of Ni(Si_{1-u}Ge_u) are present in the film. Thus, the analyses in the following sections, which consider the influences of Ge and B, are likely representative of the entire reaction stage and not just a single segment or subset thereof.

5.2.2.1 Influence of Ge

Figure 5-15(a) presents a plot of the sheet resistance of the undoped 15 and 25% Ge samples as a function of Si_{1-x}Ge_z area fraction. Error ranges are omitted for clarity. The data in

this plot, which is shown on a logarithmic plot due to the substantial disparity in sheet resistance measurements, shows a wide degree of scatter for the 25% Ge samples. Additionally, only two data points are included for the 15% Ge samples. The scarcity of data may be attributed to the fact that the sheet resistance of only two of the ten 15% Ge samples with $\text{Si}_{1-x}\text{Ge}_x$ area fractions contained in this stage of the reaction was able to be successfully measured. Likewise, only ten of the seventeen 25% Ge samples were able to be measured. The cause for this difficulty will be addressed in the following section. It should also be noted that the analysis in Appendix B showed that 4PP measurement of sheet resistances above ~ 500 Ohm/sq showed much greater variability than those at lower values. Accordingly, no influence of Ge content may be determined for the undoped samples.

Figure 5-15(b) presents a plot of the sheet resistance of the doped 15 and 25% Ge samples as a function of $\text{Si}_{1-x}\text{Ge}_x$ area fraction with error bars omitted for clarity. It is evident from this plot that the sheet resistance of the doped samples in this range has a linear relationship with $\text{Si}_{1-x}\text{Ge}_x$ area fraction. Accordingly, linear regression of the data series was performed; the best fit lines are shown in the figure and the regression results given in Table 5-4. Analysis of the regression results using a 2 sample t-test shows that the slope and intercept of the best fit lines for the doped 15 and 25% Ge are not equal at a 95% confidence level. Thus, it can be concluded that, unlike within the first transformation stage, increasing Ge content in this stage affects the structure/property relationship.

5.2.2.2 Influence of B

Figure 5-16 presents a plot of the sheet resistance of all four sample series as a function of $\text{Si}_{1-z}\text{Ge}_z$ area fraction. It should be noted that a log scale was used for the y-axis of the plot (sheet resistance) to display all data points within reasonable proximity and that error bars were omitted for clarity. Observation of this figure shows that the doped samples have much smaller

sheet resistances than their undoped counterparts for all $\text{Si}_{1-z}\text{Ge}_z$ area fractions, as well as a much stronger structure/property relationship. Thus, the addition of B doping has a significant effect on the relationship between microstructure and sheet resistance.

The cause for the significant stabilization of sheet resistance by the addition of B doping within this stage is clarified by considering representative images of the film. Figure 5-17(a) and (b) show an image of a doped 25% Ge sample after annealing at 650 °C for 10 minutes before and after application of a contrast threshold, respectively. This sample has a $\text{Si}_{1-z}\text{Ge}_z$ area fraction of 64%, at the low end of the range within this stage. Figure 5-17(b) and (c) show an image of a doped 25% Ge sample after annealing at 750 °C for 10 minutes before and after application of a contrast threshold, respectively. This sample has a $\text{Si}_{1-z}\text{Ge}_z$ area fraction of 73.7%, at the high end of the range within this stage. Both samples show that within this stage of the transformation process, individual grains of Si-rich $\text{Ni}(\text{Si}_{1-u}\text{Ge}_u)$ are isolated from each other by regions of $\text{Si}_{1-z}\text{Ge}_z$. For the undoped samples, no highly conductive current path is available between these islands. Hence, it is extremely difficult for current to pass through the film and the measured sheet resistance is very high or the sample reads as an open circuit. Conversely, for the B doped samples, a conductive current path between Si-rich $\text{Ni}(\text{Si}_{1-u}\text{Ge}_u)$ grains is likely available through a B doped region. This leads to the much lower sheet resistances measured for these samples.

Unlike the precipitation stage, determination of the conduction path of least resistance for the doped samples is complicated by the fact that the path will, up to a certain island separation, likely utilize the low resistivity $\text{Ni}(\text{Si}_{1-u}\text{Ge}_u)$ grains for portions of the path (i.e. jump between $\text{Ni}(\text{Si}_{1-u}\text{Ge}_u)$ grains). However, as area fraction of $\text{Si}_{1-z}\text{Ge}_z$ increases with increasing agglomeration of the $\text{Ni}(\text{Si}_{1-u}\text{Ge}_u)$ grains, the distance between $\text{Ni}(\text{Si}_{1-u}\text{Ge}_u)$ grains increases.

This effect is shown in the SEM/BSE images of the microstructure; the sample in Figure 5-17(a) with area fraction of 64% is clearly less agglomerated than the sample in Figure 5-17(c) with area fraction of 73.7%. The increasing separation between highly conductive grains will therefore cause the observed increase in sheet resistance with $\text{Si}_{1-z}\text{Ge}_z$ area fraction as an increasing percentage of the total conduction path is spent between the $\text{Ni}(\text{Si}_{1-u}\text{Ge}_u)$ grains. Eventually, this path may become so tortuous that it becomes favorable for it to pass directly through the B doped regions and intersect only the $\text{Ni}(\text{Si}_{1-u}\text{Ge}_u)$ grains which happen to lie on a line directly along the chord of the path (i.e. directly between the terminals of a 4PP). If this occurs, it would be expected that the plot of sheet resistance vs. $\text{Si}_{1-z}\text{Ge}_z$ area fraction would show an inflection point as the relationship would become relatively insensitive to agglomeration. While no such point is visible in Figure 5-15(b), it is possible that the $\text{Si}_{1-z}\text{Ge}_z$ area fractions obtained in this work are not large enough. Additional work should be performed, therefore, to see if such a point exists at area fractions greater than 75%.

5.2.3 Boron Conduction Path

Prior sections of this chapter have suggested that doped regions of the experimental structures containing homogeneous B doping are providing an alternative conduction path for current flow, thereby reducing the sheet resistance of the film. In some cases, such as during the precipitation reaction, the amount of reduction is relatively low. In other cases, such as during the agglomeration reaction, the amount of reduction is large (even approaching infinity). The nature and location of the alternative path, however, has not yet been addressed.

Published literature has shown that full silicidation (FUSI) of doped polysilicon gates using Ni metal can lead to improved device performance through tuning of the gate work function and reduction of gate tunneling effects [Mas05]. The improvements are attributed to silicidation induced dopant segregation leading to high concentrations of dopants in proximity to

the gate oxide. Specifically, literature has shown that nickel silicidation of a B implanted Si sample past the initial implant depth results in the pile-up of B at the silicide/silicon interface. Zhang et al. performed an experiment where a 2 keV 3×10^{15} atoms/cm² B implant was performed into bulk silicon resulting in an initial peak concentration 10 nm below the sample surface. After deposition of excess Ni metal, the implanted samples were annealed at 500 °C for 90 seconds under a N₂ atmosphere. The samples were then analyzed using SIMS; the results are shown in Figure 5-18. It is evident from this figure that silicidation induced dopant segregation has moved the peak dopant concentration from a depth of ~10 nm to ~80 nm leaving only residual B doping of the silicide.

Silicidation induced dopant segregation has not been studied in the nickel germanosilicide system. It is plausible, however, to expect that similar segregation occurs in this system as well. To determine if any dopant segregation was observed in the B doped samples in this work, SIMS analysis of the doped 25% Ge sample annealed at 450 °C for 10 minutes was performed. This sample was selected for analysis as it has the most homogeneous layer compositions (beneficial for SIMS analysis) and any silicidation induced dopant segregation would have already occurred (as the segregation would occur during the formation of the silicide layer). An XTEM image of the sample is presented in Figure 5-19(a) and the SIMS results are shown in Figure 5-19(b). While evidence of dopant segregation is apparent in the SIMS results, due to the interface roughness observed in the XTEM image the SIMS results are of overall poor quality (as evidenced by the large concentration tails). Thus, another technique less susceptible to interface effects should be used to confirm the presence of dopant segregation.

5.2.3.1 Potential Conduction Paths

Assuming that silicidation induced dopant segregation does occur for the B doped samples in this work, three potential conduction paths can be proposed for the structure. As shown in

Figure 5-20, silicidation induced dopant segregation would result in a residually doped nickel germanosilicide silicide layer, the first possible conduction path. Assuming that the segregated B doping is fully electrically active (which is conservative, as it the mechanism by which segregation occurs is not understood), the region with the segregated dopant would form a second path. Finally, the unreacted, actively doped $\text{Si}_{1-x}\text{Ge}_x$ layer will offer a third conduction path.

The potential sheet resistance of each of the three potential conduction paths was estimated for the doped 15% Ge sample. The sheet resistance of the doped 15% Ge sample annealed at 450 °C for 10 minutes was measured to be ~10 Ohm/sq. This value is accordingly approximately equal to the sheet resistance of a 20 nm homogeneous nickel germanosilicide layer. A wafer without deposited Ni was also available for this experimental structure; 4PP measurement of this wafer's 150 nm B doped $\text{Si}_{0.85}\text{Ge}_{0.15}$ layer showed that the sheet resistance of the layer was 120 Ohm/sq. Sheet resistance (R_s) and sample resistivity (ρ) are related according to Equation 5-1 when the ratio of sample length (L) to width (W) is equal to 1.

$$R_s = \frac{\rho}{t} \left(\frac{L}{W} \right) \quad \text{Equation 5-1}$$

Equation 5-1 shows, therefore, that dividing the sheet resistance of the layer by its thickness (150 nm) allowed the resistivity of the layer to be calculated as 1.8E-5 Ohm*m. As the resistivity of a semiconductor is inversely proportional to its level of doping, assuming that all segregated dopant from the ~20 nm germanosilicide layer is contained within a 10 nm layer below the interface, the layer containing the pileup of segregated dopant would have three times the nominal dopant concentration and thus an estimated resistivity of 6E-6 Ohm*m (one-third of the nominal resistivity). The estimated sheet resistance of the region with the pileup of segregated dopant can accordingly be calculated as ~600 Ohm/sq. The estimated sheet resistance of the

remaining 120 nm layer of unreacted, nominally B doped $\text{Si}_{0.85}\text{Ge}_{0.15}$ layer would then be equal to 150 Ohm/sq (due to its reduced thickness). It should also be noted that if the dopant pileup caused by silicidation induced dopant segregation is not electrically active, the expected sheet resistance of the remaining 130 nm of nominally B doped $\text{Si}_{0.85}\text{Ge}_{0.15}$ would have a sheet resistance of 140 Ohm/sq.

Comparison of the calculated sheet resistance values for the 10 nm region with the pileup of segregated B dopant and the remaining 120 nm of unreacted, nominally B doped $\text{Si}_{0.85}\text{Ge}_{0.15}$ layer indicates that, while the concentration of active dopant in the region with pileup is potentially 3 times higher than that of the unreacted, nominally doped layer, the differences in layer thicknesses cause the sheet resistance of the region with pileup to be significantly higher (600 Ohm/sq. vs. 150 Ohm/sq, respectively). When considered as resistors in parallel, however, the combined resistance of the two layers decreases to 120 Ohm/sq according to Equation 5-2:

$$R_{\text{parallel}} = \frac{1}{\frac{1}{R_1} + \frac{1}{R_2}} \quad \text{Equation 5-2}$$

Thus, if pileup of active dopant does occur due to silicidation induced dopant segregation, the measured sheet resistance of the non-germanosilicide layers would be expected to be ~120 Ohm/sq. If pileup does not result in increased amounts of active dopant, the measured sheet resistance of the non-germanosilicide layers would be expected to be ~140 Ohm/sq (equal to the sheet resistance of 130 nm of nominally doped $\text{Si}_{0.85}\text{Ge}_{0.15}$).

5.2.3.2 Evaluation of Potential Paths

The previous section calculated the expected sheet resistance values of several potential conduction paths. As shown in Figure 5-20, it is expected that silicidation induced dopant segregation leads to the pileup of B dopant at the nickel germanosilicide/ $\text{Si}_{1-x}\text{Ge}_x$ interface for

the B doped samples in this work, leaving the initially homogeneous germanosilicide film with low levels of residual doping. As B diffusivity has been shown to be very low at the times and temperatures used in this work [Rad06], the $\text{Si}_{1-z}\text{Ge}_z$ grains which precipitate from the germanosilicide are thus likely only lightly doped, at best. It is expected, therefore, that the initial low resistance path provided by the germanosilicide layer will be significantly degraded with increasing anneal time and temperature. Unlike the undoped samples, however, the doped samples in this work exhibited lower, more stable sheet resistance measurements. Thus, an alternative conduction path must be provided by the B doped regions. Expected sheet resistance values for two possible conduction paths (10 nm highly doped $\text{Si}_{1-x}\text{Ge}_x$ plus 120 nm of nominally doped $\text{Si}_{1-x}\text{Ge}_x$ in parallel (120 Ohm/sq), or 130 nm of nominally doped $\text{Si}_{1-x}\text{Ge}_x$ (150 Ohm/sq)) were calculated in the previous section for the doped 15% Ge samples. By comparing the estimated values to experimental results, the more likely path may be determined.

Figure 5-21 presents a plot of the sheet resistance of the doped 15% Ge samples for isochronal anneal series of 10, 90, and 1020 minutes for temperatures ranging from 450 to 800 °C. The calculated sheet resistance values for the homogeneous nickel germanosilicide film and the two possible conduction paths are also presented in the figure. It is evident from the plot that the sheet resistance of the samples at low times and temperatures is equal to that of the homogeneous nickel germanosilicide film. As anneal time and temperature increases, the sheet resistance of the samples increases past 120 Ohm/sq and begins to asymptote at a value around 140 Ohm/sq. These results indicate that any piled up dopant is not electrically active and the most likely alternative conduction path is through 130 nm of nominally doped $\text{Si}_{0.85}\text{Ge}_{0.15}$.

In context of previous work, the determination that the dopant pileup is likely electrically inactive can explain why the work of Chamirian et al. [Cha04] found no effect of implanted

dopants on film sheet resistance. Silicidation induced dopant segregation likely resulted in the pileup of inactive dopants at the germanosilicide/Si_{1-x}Ge_x interface. Unlike this work or the work of Liu and Ozturk [Liu05], the Si_{1-x}Ge_x layer in the study by Chamirian et al. was not doped. Accordingly, no alternate, actively doped conduction path was available in the latter work and the sheet resistance of the films behaved identically to the undoped case.

It should be noted that these conclusions suggest that the influence of Ge content on the structure/property relationship between film microstructure and sheet resistance during the agglomeration reaction are most likely due to differences in the resistivity of the underlying Si_{1-x}Ge_x film due to differences in B dopant incorporation or activation with increasing Ge content. As this path is a major contributor to overall sample sheet resistance for this stage of the film transformation, a significant difference in sheet resistance with Ge content was seen. For the precipitation stage of the reaction, however, the contribution of the alternative conduction path to sample sheet resistance is much smaller, accordingly any difference in the resistance of the alternative path was negligible and no influence of Ge content was seen. The resistivity of the doped Si_{0.75}Ge_{0.25} layer was unable to be determined as no structure without Ni and TiN deposition was available for this sample conditions. Efforts to chemically or physically remove the Ni and TiN layers without damage to the doped Si_{0.75}Ge_{0.25} layer were attempted but were unsuccessful.

5.3 Summary

Several important conclusions can be drawn from the work presented in this chapter. First, as previously shown in literature, increasing the Ge content of the initial Si_{1-x}Ge_x layer was found to worsen sheet resistance. Second, as shown by Liu and Ozturk [Liu05], the addition of homogeneous B doping to the initial Si_{1-x}Ge_x layer resulted in the decrease and stabilization of sheet resistance values for both the 15 and 25% Ge samples used in this work. Third, a

quantitative structure/property relationship can be established between area fraction of Ge-rich $\text{Si}_{1-z}\text{Ge}_z$ and sheet resistance for both the precipitation and agglomeration stages of the film's microstructure evolution. For the precipitation stage, Ge composition was not determined to influence the structure/property relationship for either the undoped or doped samples. The addition of homogeneous B doping, however, was found to significantly affect the relationship. Overall, the general increase in sheet resistance for all samples in this stage of the transformation can be attributed to the increasing tortuosity of the conduction path with increasing $\text{Si}_{1-z}\text{Ge}_z$ precipitation. The decreased sheet resistance of the B doped samples in this stage is likely due to the samples containing an alternative conduction path that reduces the influence of the increasing tortuosity. For the agglomeration stage of the film transformation, the sheet resistance of the undoped samples was found to rapidly increase to large (or infinite) values unrelated to the amount of $\text{Si}_{1-z}\text{Ge}_z$ present. The influence of Ge content on the structure/property relationship for these samples was therefore unable to be conclusively determined. This effect was determined to be due to the absence of a continuous conduction path between isolated Si-rich $\text{Ni}(\text{Si}_{1-u}\text{Ge}_u)$ grains for these sample. For the doped samples in the agglomeration stage, the sheet resistance of the samples was found to increase linearly with increasing area fraction of $\text{Si}_{1-z}\text{Ge}_z$, resulting in a predicative structure/property relationship for these samples. These results suggested that an alternative conduction path between the isolated Si-rich $\text{Ni}(\text{Si}_{1-u}\text{Ge}_u)$ was provided by B doped regions. It was also determined that increasing initial Ge concentration influenced the relationship, with the 25% Ge samples having higher sheet resistance values than the corresponding 15% Ge samples. Fourth, the alternative conduction path for the B doped samples was determined to most likely be the unreacted, nominally B doped $\text{Si}_{1-x}\text{Ge}_x$ layer below the nickel germanosilicide layer. It was also determined that differences in the sheet resistance

of the $\text{Si}_{1-x}\text{Ge}_x$ layer with Ge content is the most likely cause for the influence of Ge noted in the agglomeration stage of the film transformation.

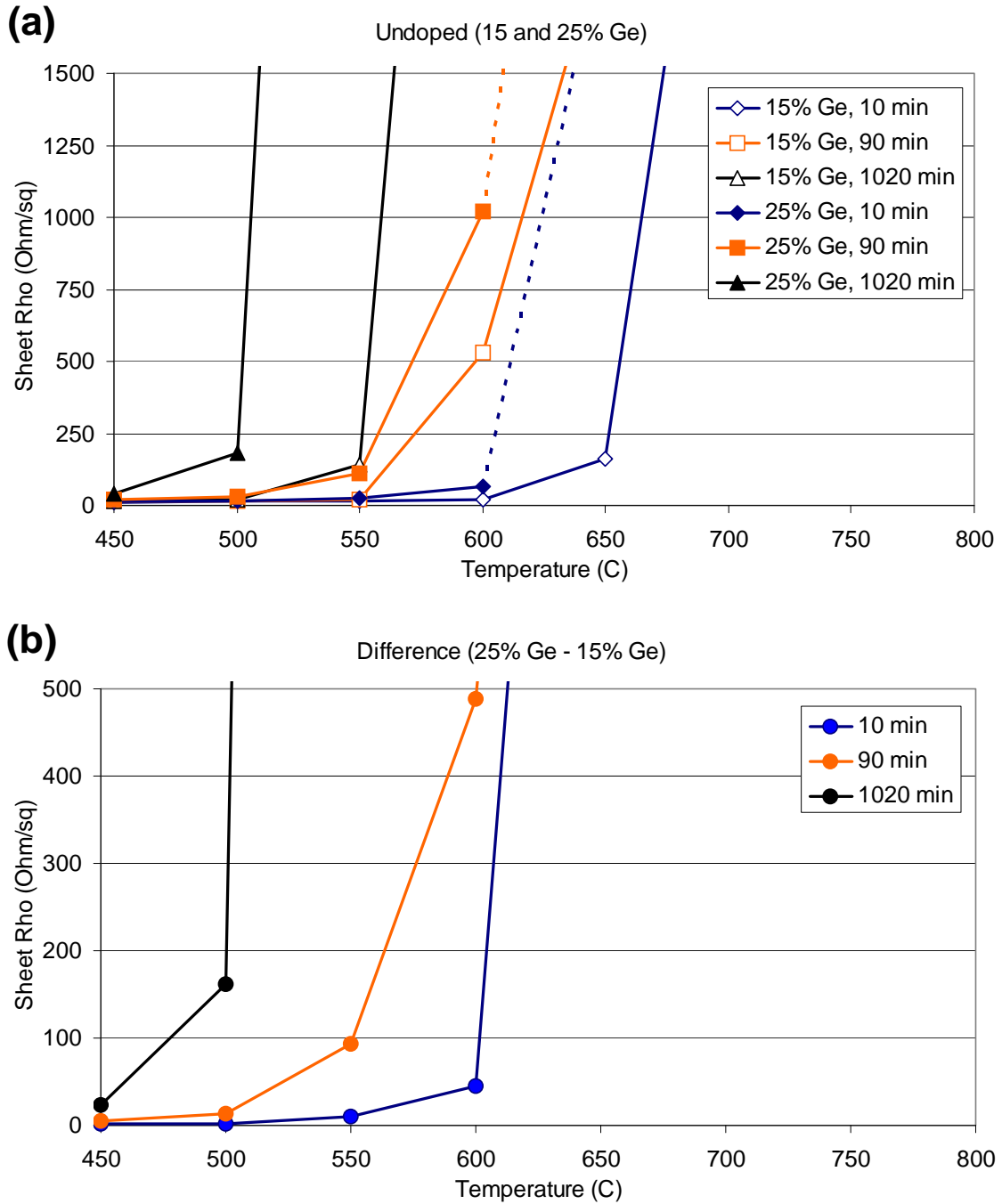


Figure 5-1: Isochronal anneal series of (a) sheet resistance of undoped 15 and 25% Ge samples and (b) difference in sheet resistance between 25 and 15% Ge samples. Note that dotted lines are extrapolations to infinity indicating that subsequent samples in the series read as open circuits.

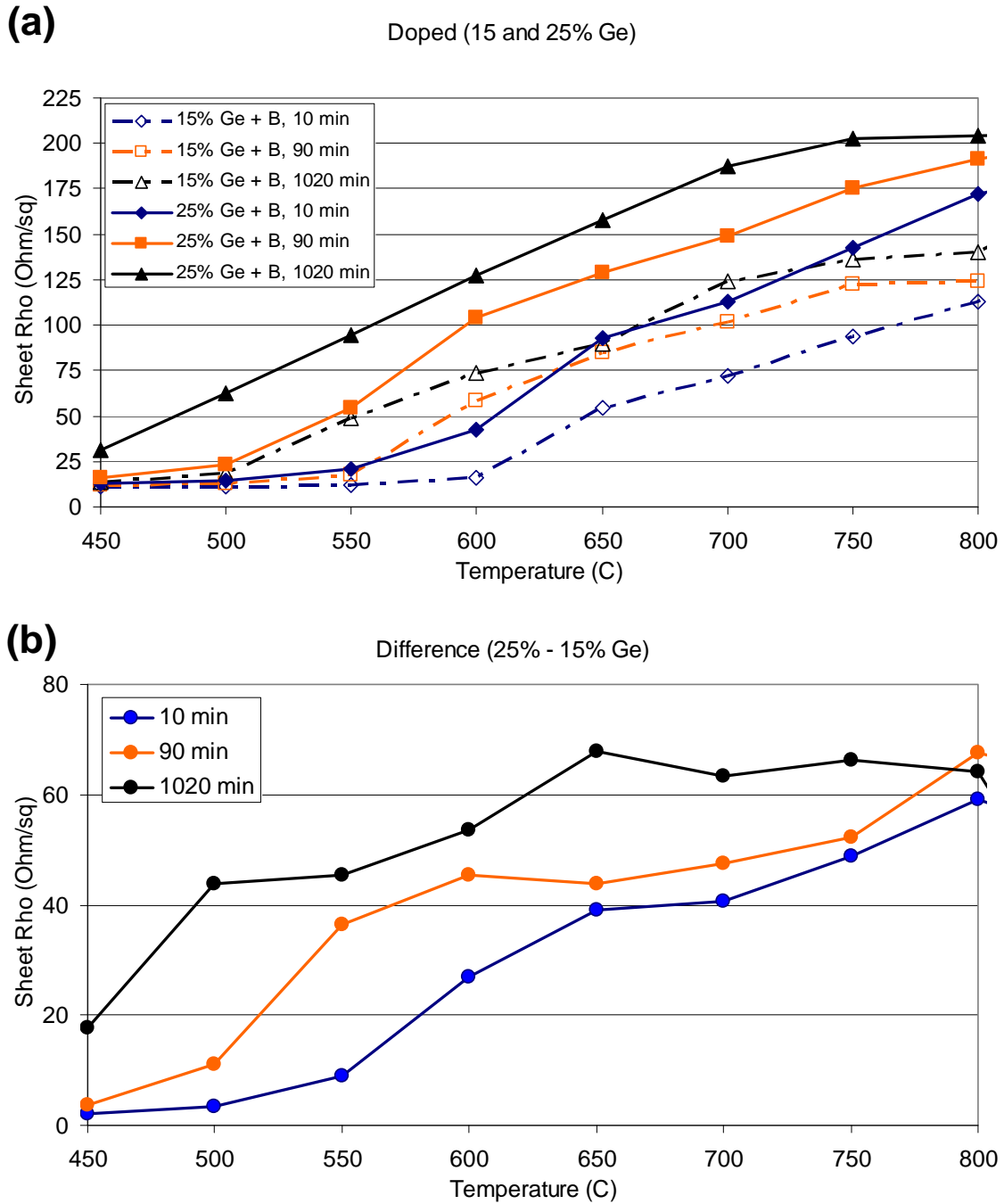


Figure 5-2: Isochronal anneal series of (a) sheet resistance of doped 15 and 25% Ge samples and (b) difference in sheet resistance between 25 and 15% Ge samples.

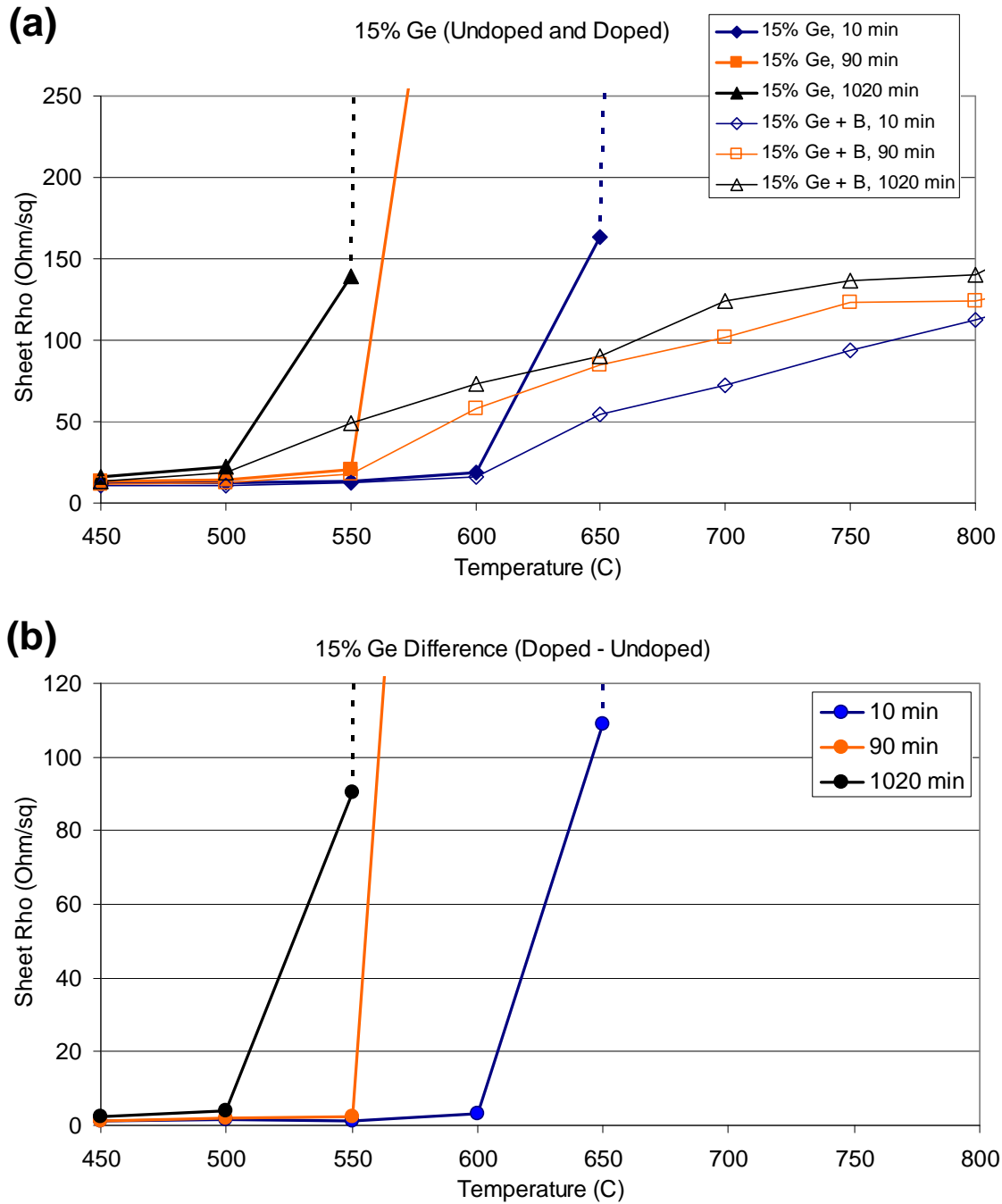


Figure 5-3: Isochronal anneal series of (a) sheet resistance of undoped and doped 15% Ge samples and (b) difference in sheet resistance between the doped and undoped samples. Note that dotted lines are extrapolations to infinity indicating that subsequent samples in the series read as open circuits or that an infinite difference was calculated.

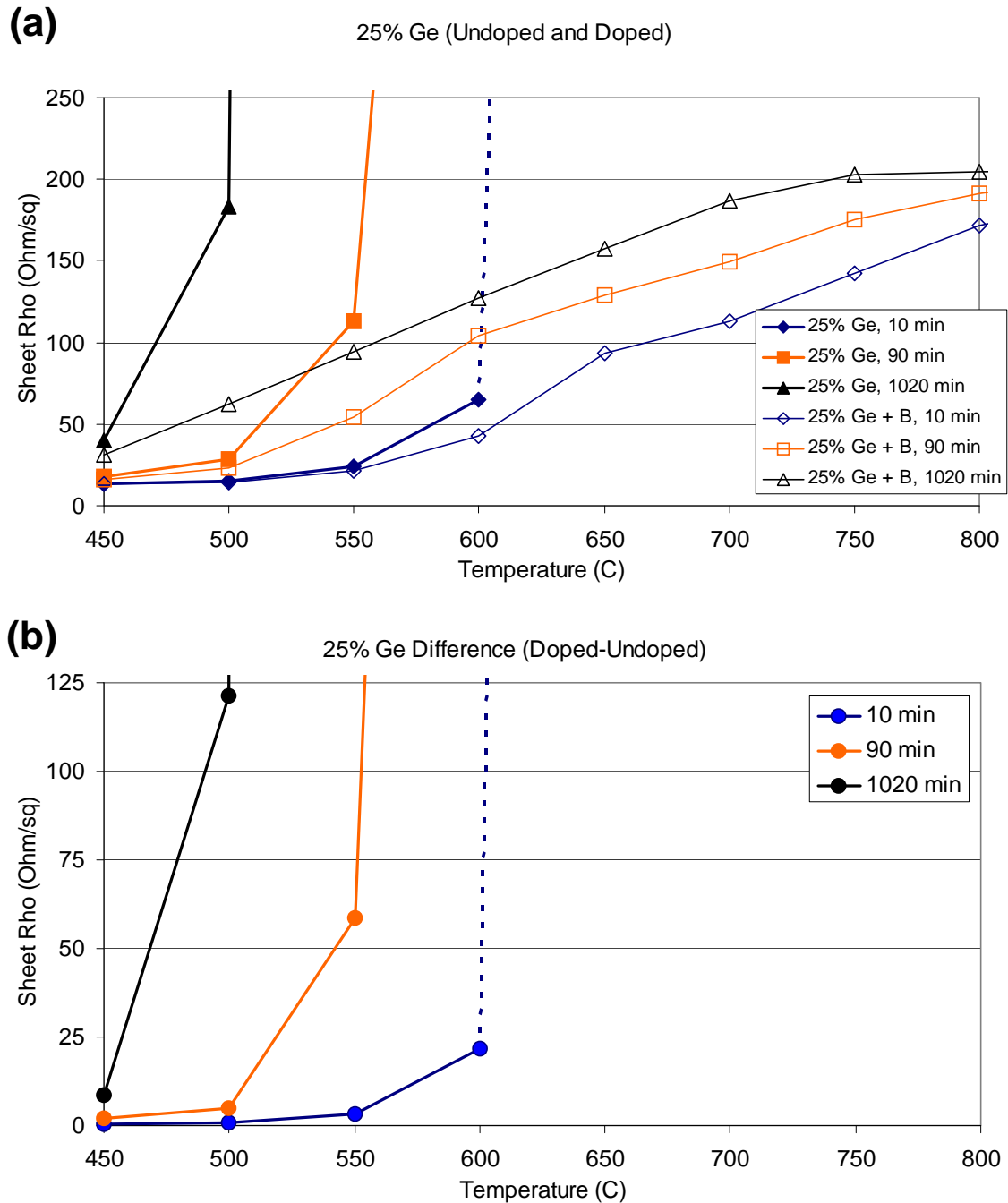


Figure 5-4: Isochronal anneal series of (a) sheet resistance of undoped and doped 25% Ge samples and (b) difference in sheet resistance between the doped and undoped samples. Note that dotted lines are extrapolations to infinity indicating that subsequent samples in the series read as open circuits or that an infinite difference was calculated.

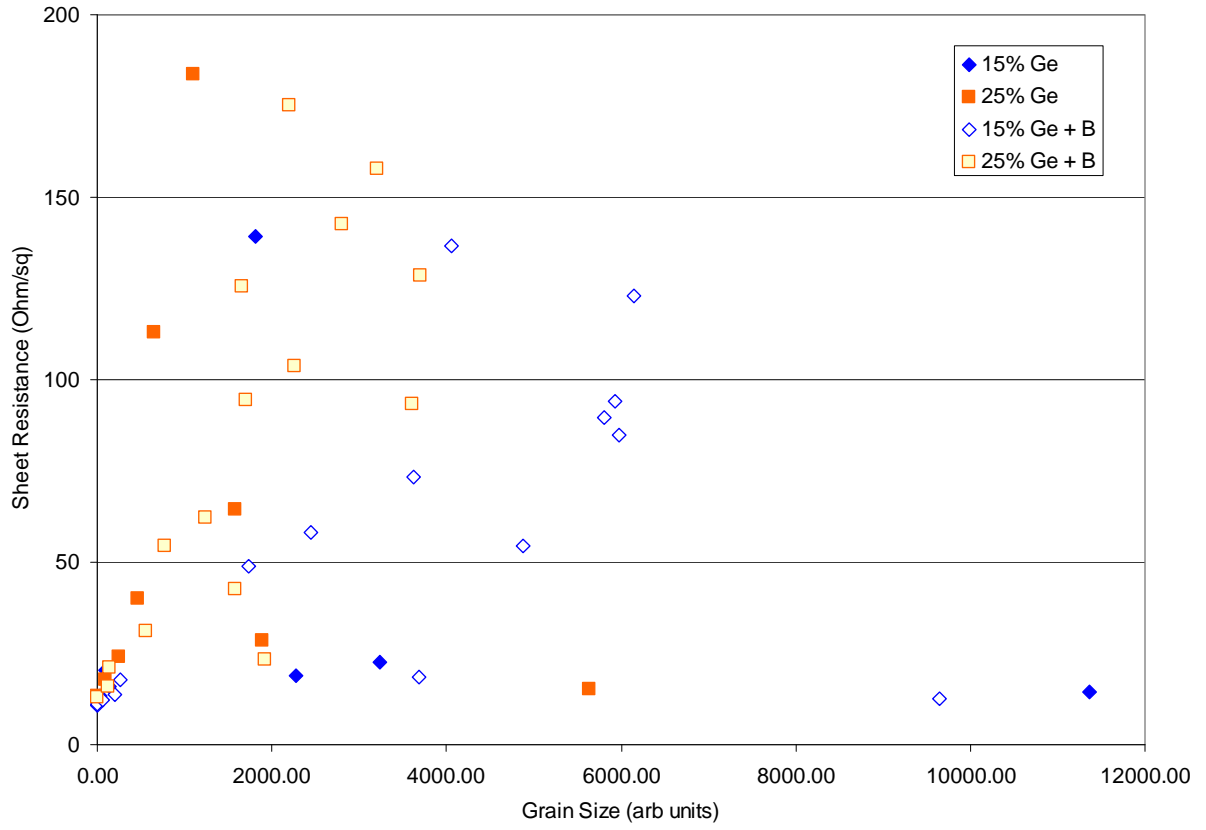


Figure 5-5: Plot of sample sheet resistance vs. $\text{Si}_{1-z}\text{Ge}_z$ grain size.

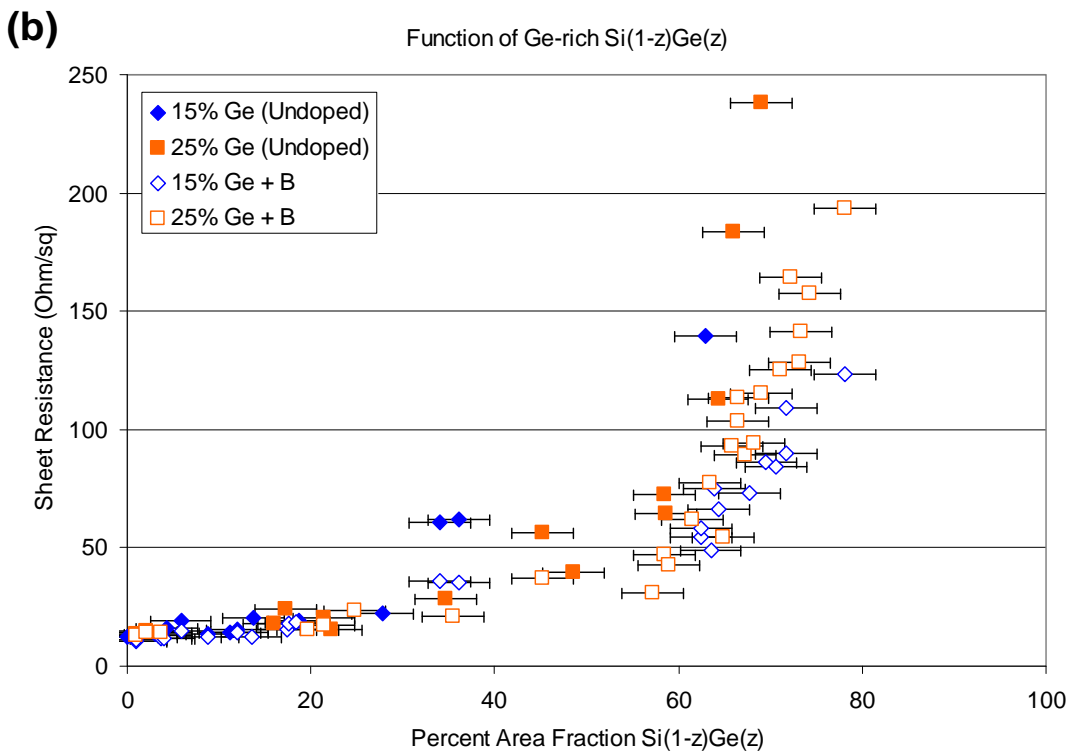
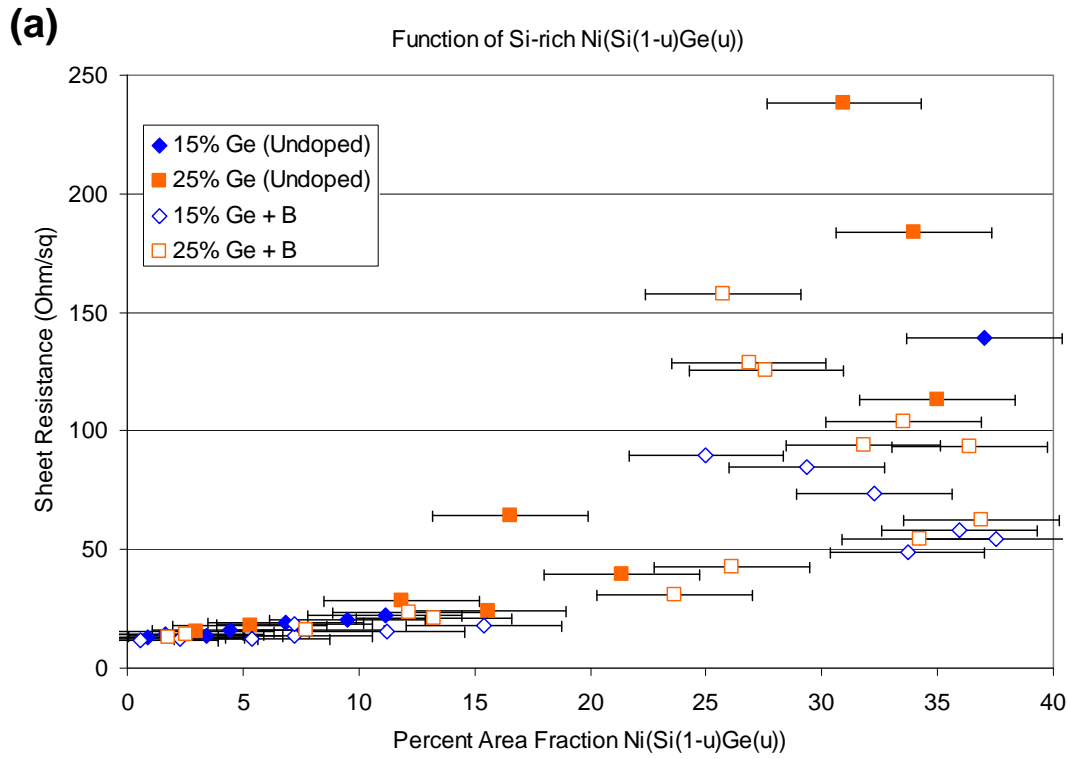


Figure 5-6: Plot of sample sheet resistance vs. area fraction of (a) Ni(Si_{1-u}Ge_u) and (b) Si_{1-z}Ge_z.

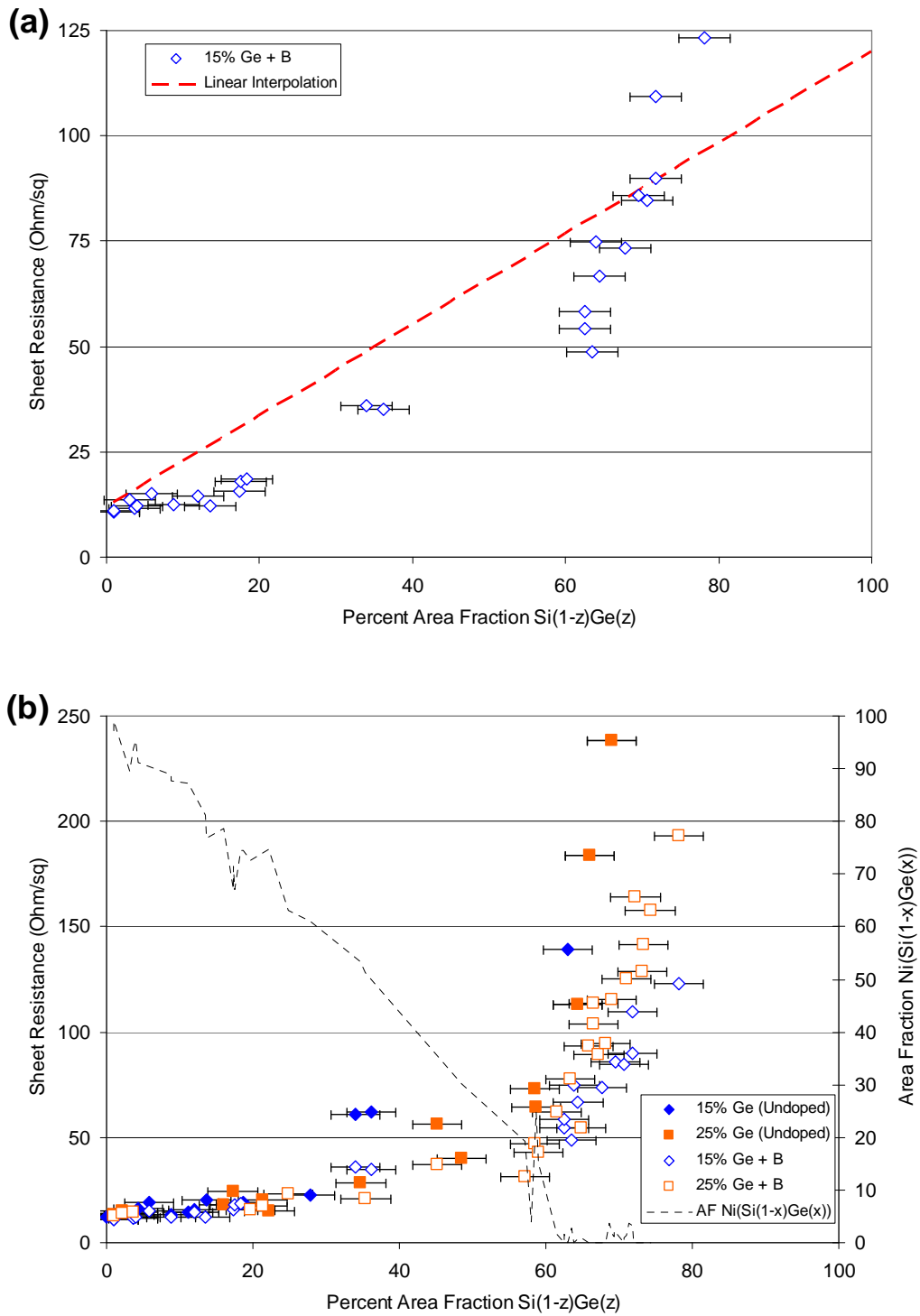


Figure 5-7: Plot of sample sheet resistance vs. area fraction of $\text{Si}_{1-z}\text{Ge}_z$ for (a) doped 15% Ge samples with linear interpolation of film and substrate sheet resistance values and (b) for all samples with area fraction of remaining initial $\text{Ni}(\text{Si}_{1-x}\text{Ge}_x)$ layer and divisions into reaction stages.

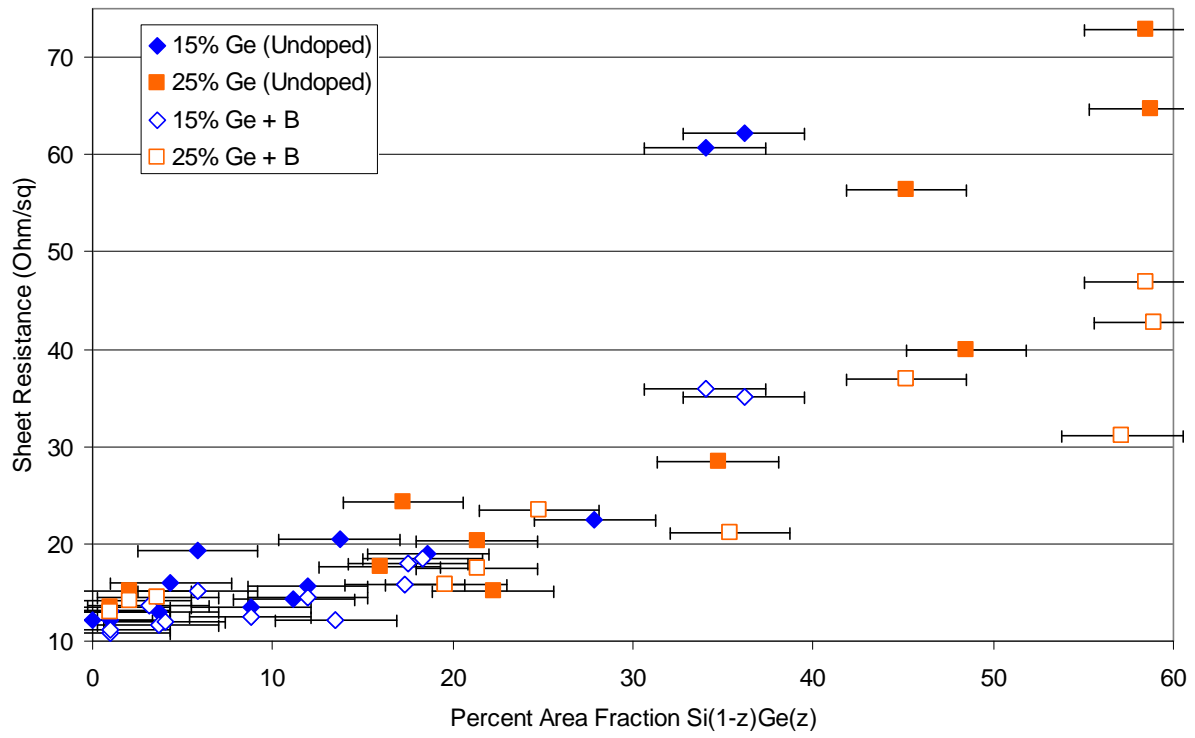


Figure 5-8: Plot of sample sheet resistance vs. area fraction of $\text{Si}_{1-z}\text{Ge}_z$ for the precipitation stage (Stage I) of the transformation.

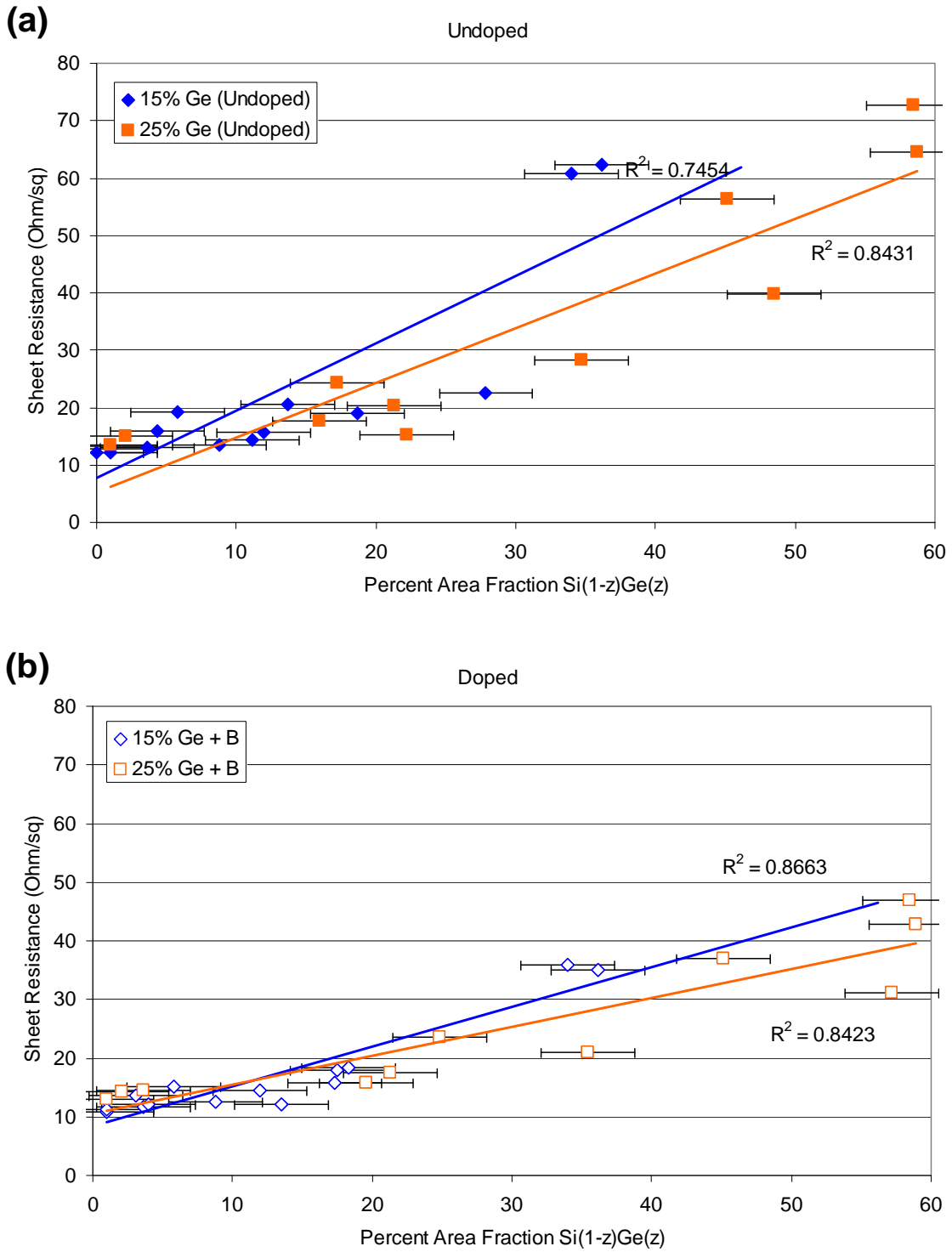


Figure 5-9: Plot of Stage I sample sheet resistance vs. area fraction of $\text{Si}_{1-z}\text{Ge}_z$ for (a) undoped and (b) doped samples. Best fit linear regression lines are also shown.

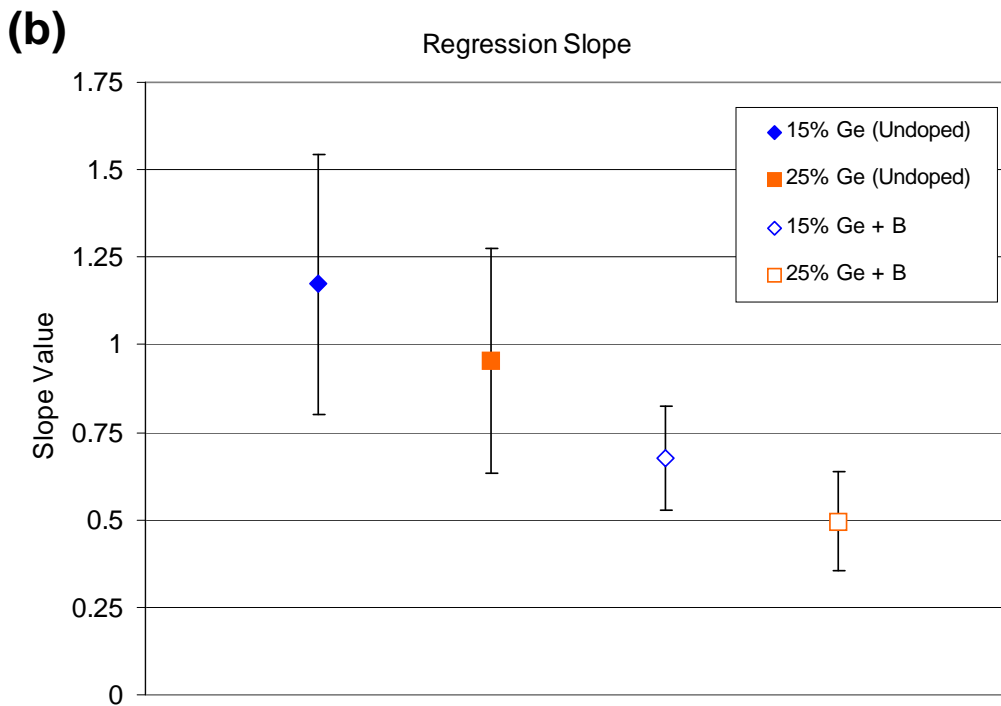
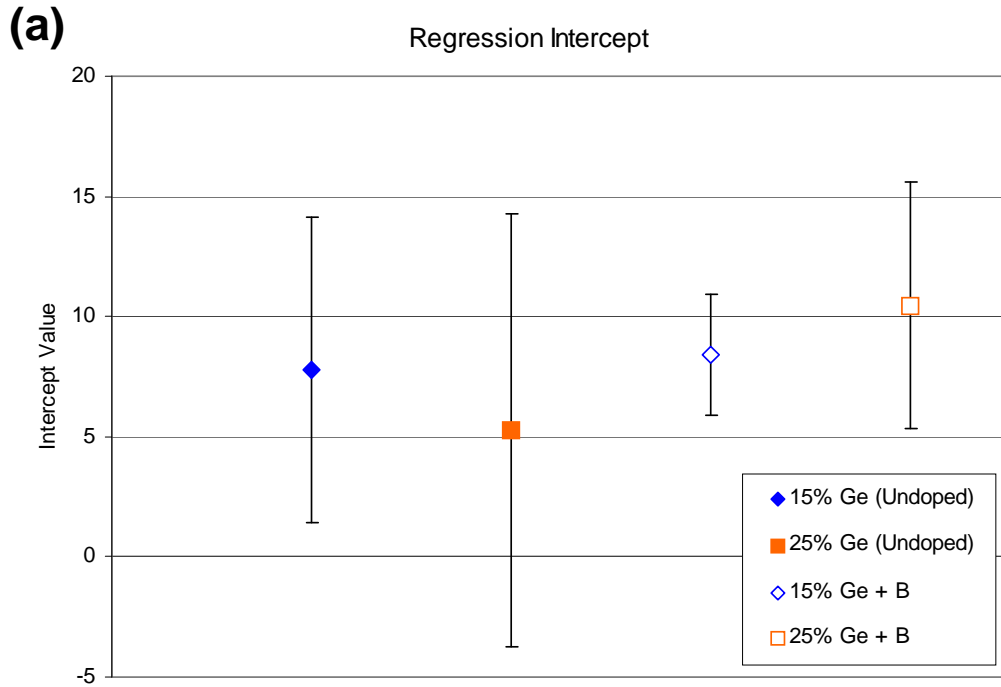


Figure 5-10: Plot of Stage I linear regression (a) intercept and (b) slope of the results given in Table 5-1. The 95% confidence interval for each value is also shown.

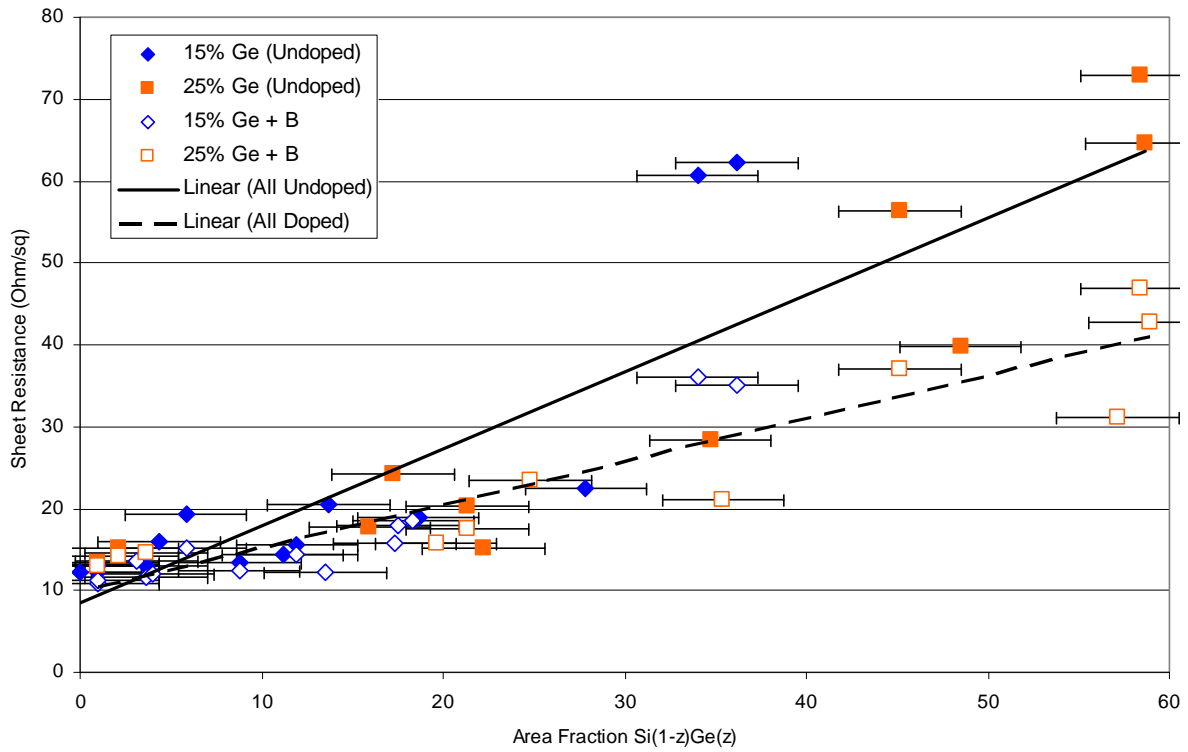


Figure 5-11: Plot of Stage I sample sheet resistance vs. area fraction of $\text{Si}_{1-z}\text{Ge}_z$ for all samples. Best fit linear regression lines for the compiled undoped and doped samples are also shown.

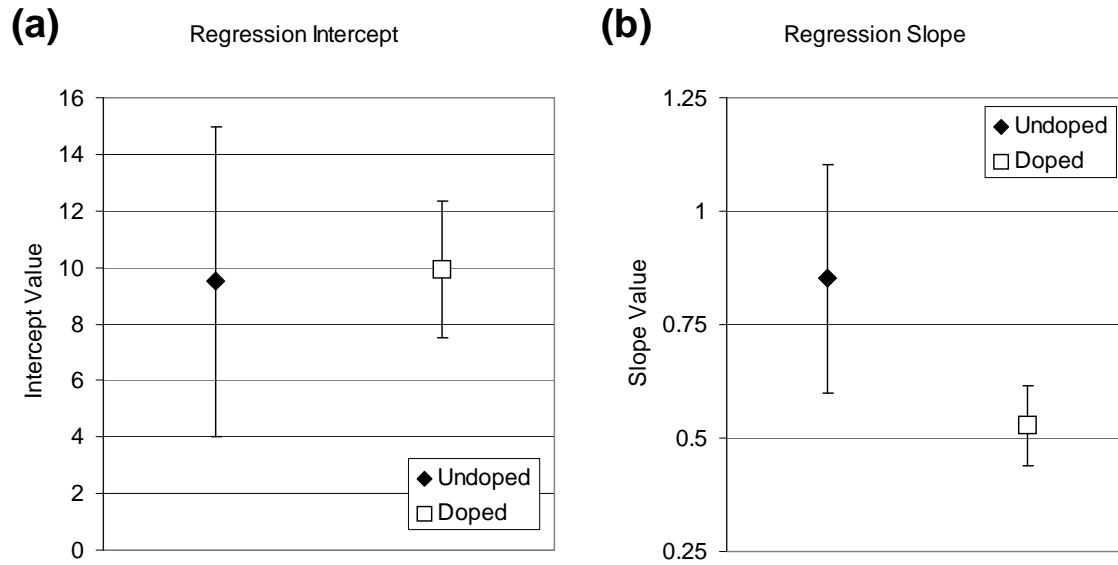


Figure 5-12: Plot of linear regression (a) intercept and (b) slope of the results given in Table 5-2. The 95% confidence interval for each value is also shown.

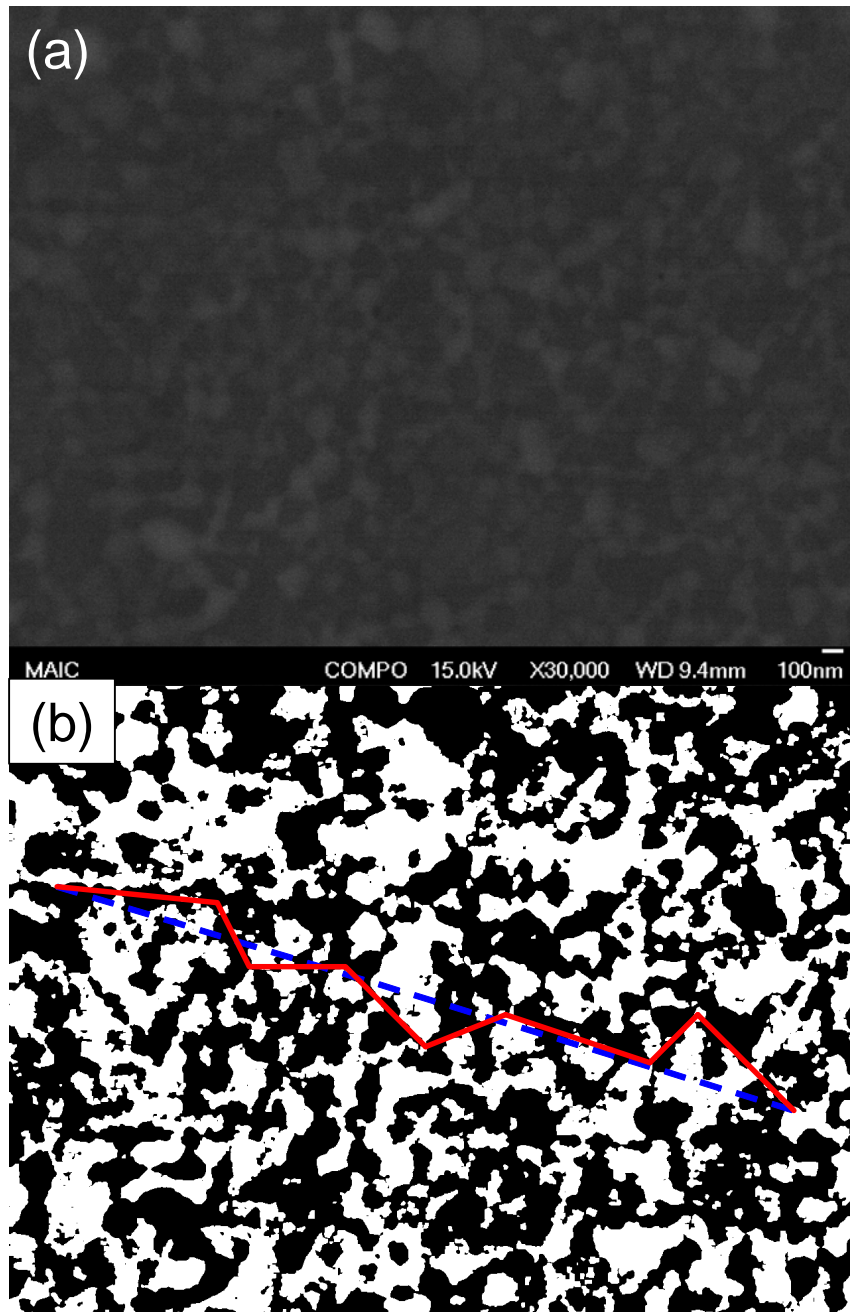


Figure 5-13: Images of (a) raw SEM/BSE image for undoped 25% Ge sample annealed at 450 °C for 1020 minutes and (b) image of same sample after ImageJ processing and threshold application with example tortuosity calculation shown.

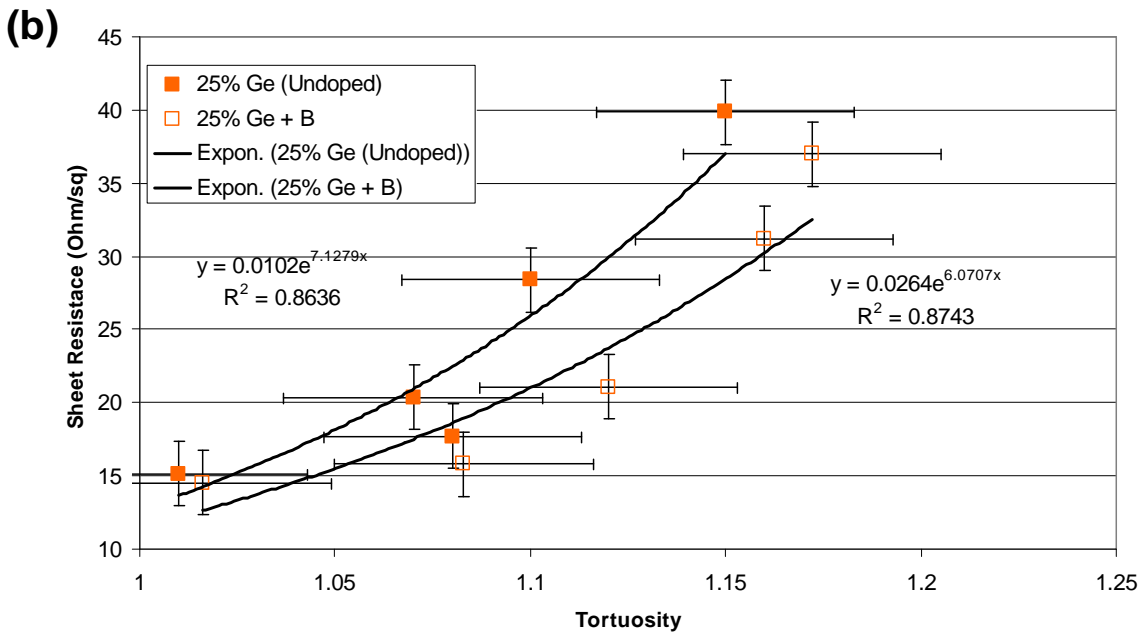
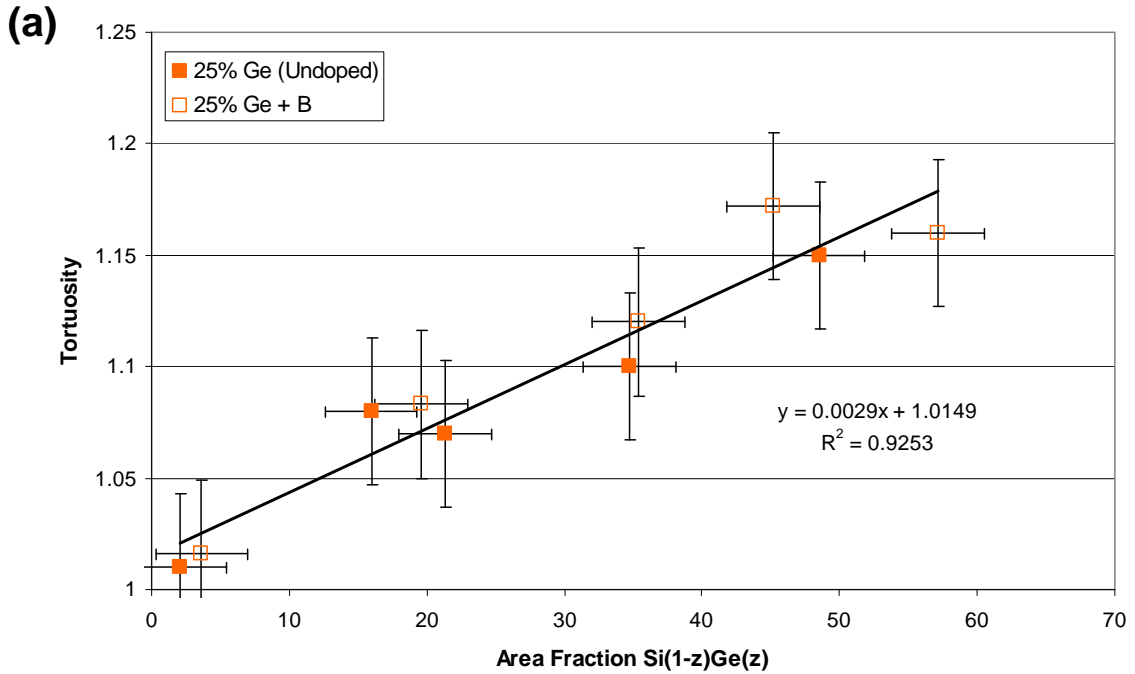


Figure 5-14: Plots of (a) conductive path tortuosity vs. area fraction $\text{Si}_{1-z}\text{Ge}_z$ and (b) sample sheet resistance vs. tortuosity for selected undoped and doped 25% Ge samples. Best fit linear regression line for compiled undoped and doped samples is shown in (a).

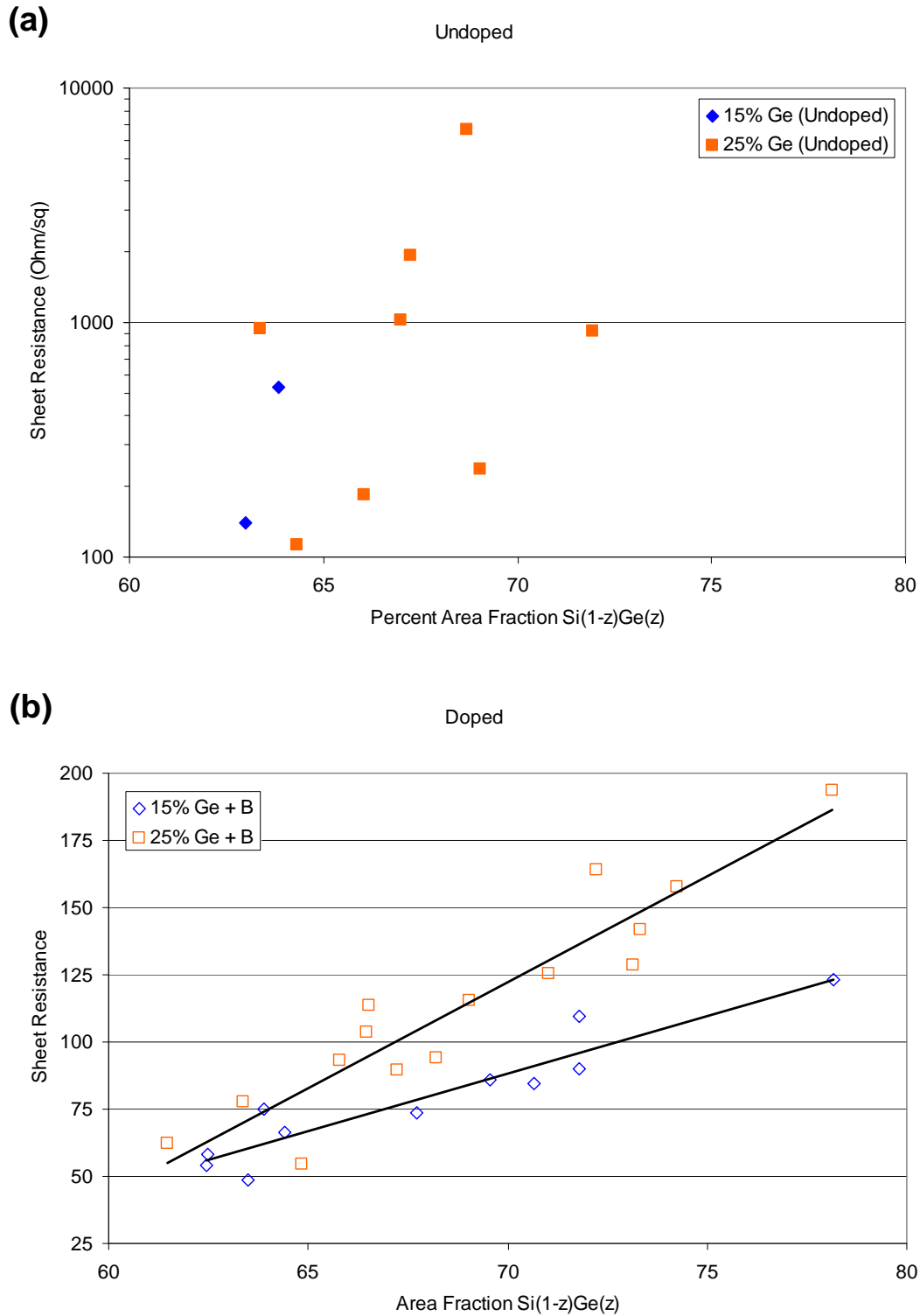


Figure 5-15: Sheet resistance of (a) undoped and (b) doped 15 and 25% Ge samples as a function of $\text{Si}_{1-z}\text{Ge}_z$ area fraction for the agglomeration stage (Stage II) of the film transformation. Best fit linear regression lines for 15 and 25% Ge samples are shown in (b).

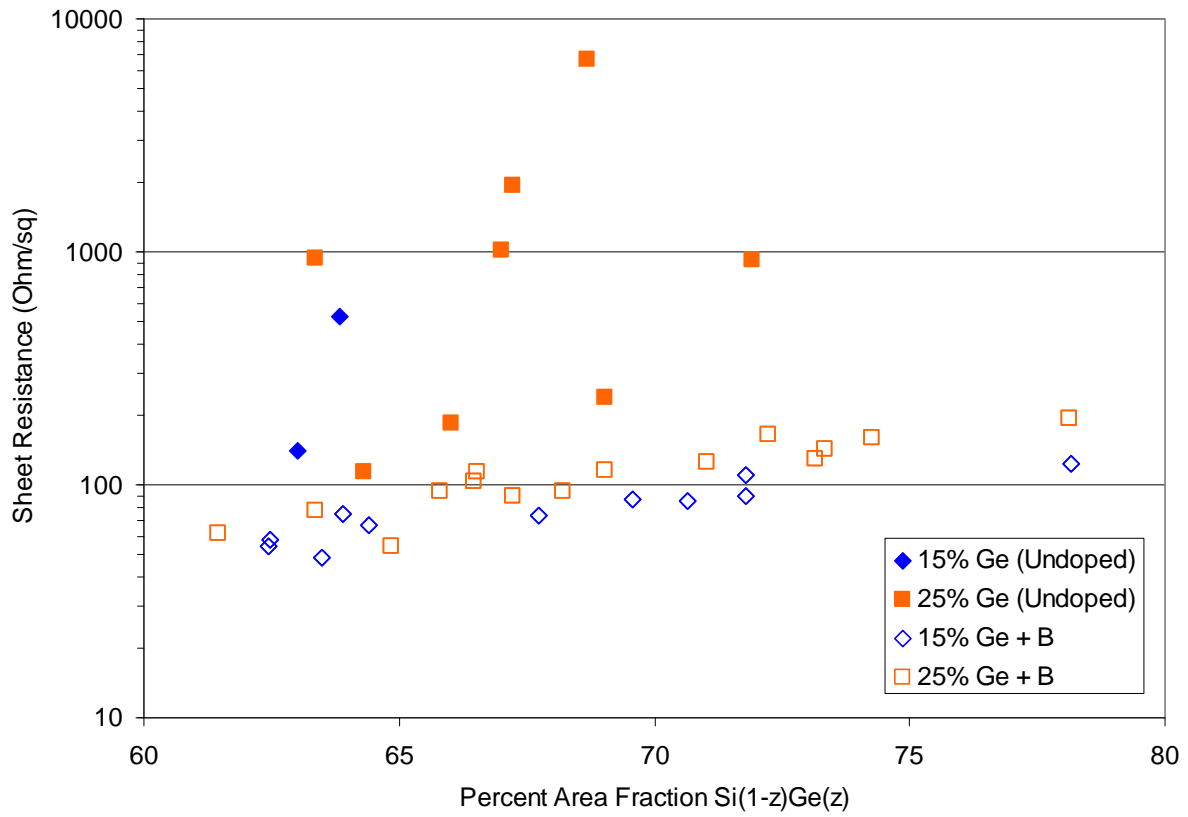


Figure 5-16: Sheet resistance as a function of $\text{Si}_{1-z}\text{Ge}_z$ area fraction for all samples in Stage II (agglomeration) of the film transformation.

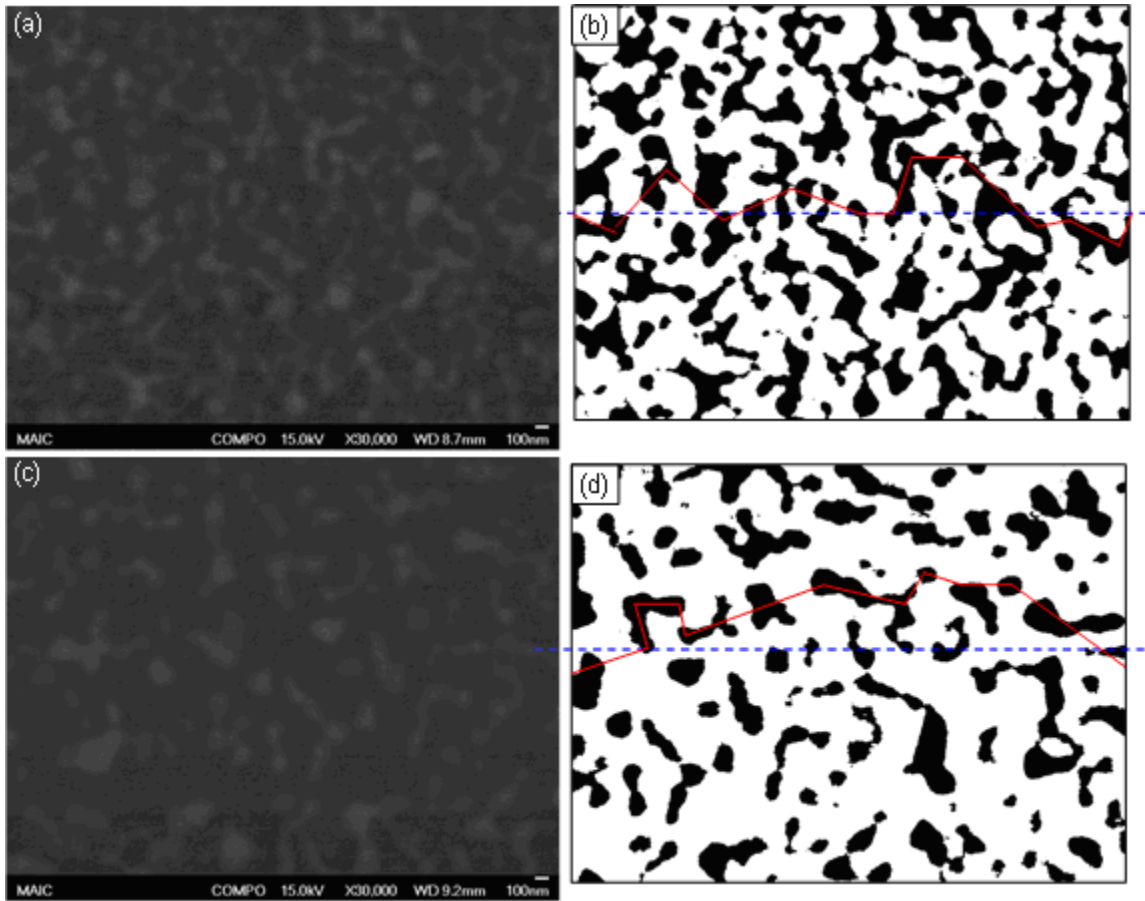


Figure 5-17: Images of (a) raw SEM/BSE for undoped 25% Ge sample annealed at 650 °C for 10 minutes, (b) previous sample after ImageJ processing, (c) raw SEM/BSE image annealed at 750 °C for 10 minutes, and (d) previous sample after ImageJ processing. Possible conduction paths vs. chord lines are shown in (b) and (d).

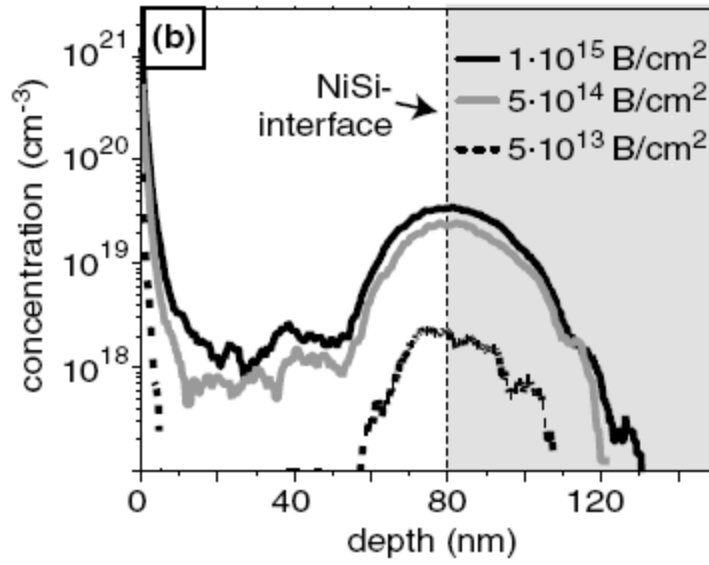


Figure 5-18: SIMS analysis results of B doping distribution after silicidation with Ni metal showing silicidation induced dopant segregation [Zha06].

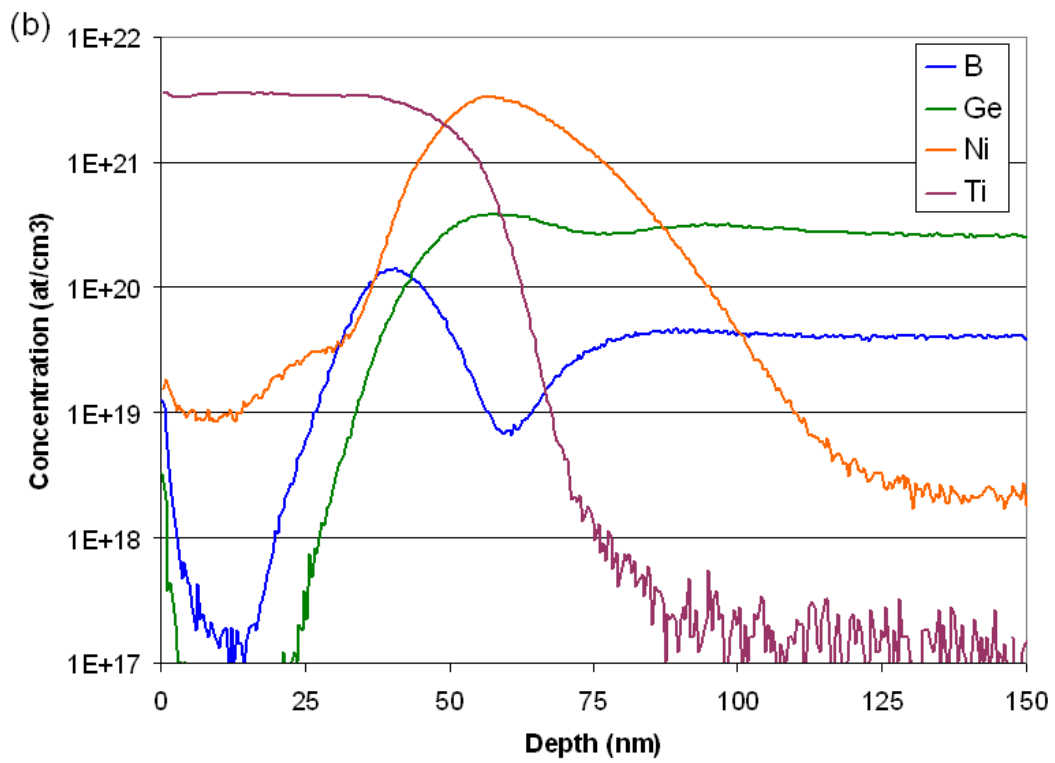
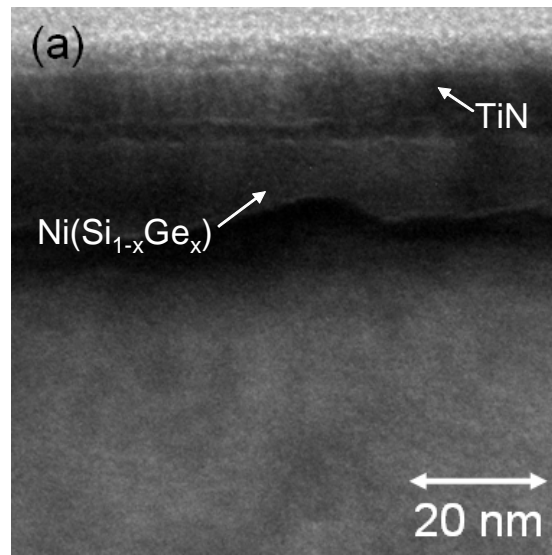


Figure 5-19: (a) XTEM and (b) SIMS analysis results for doped 25% Ge sample annealed at 450 °C for 10 minutes

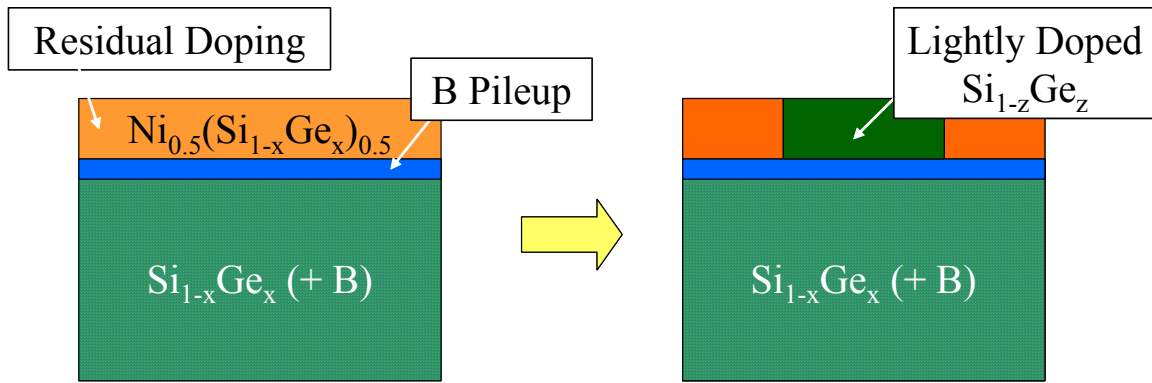


Figure 5-20: Cartoon schematics of nickel germanosilicide samples exhibiting segregation induced dopant segregation of initial $\text{Si}_{1-x}\text{Ge}_x$ B dopants before and after precipitation of $\text{Si}_{1-z}\text{Ge}_z$ grains.

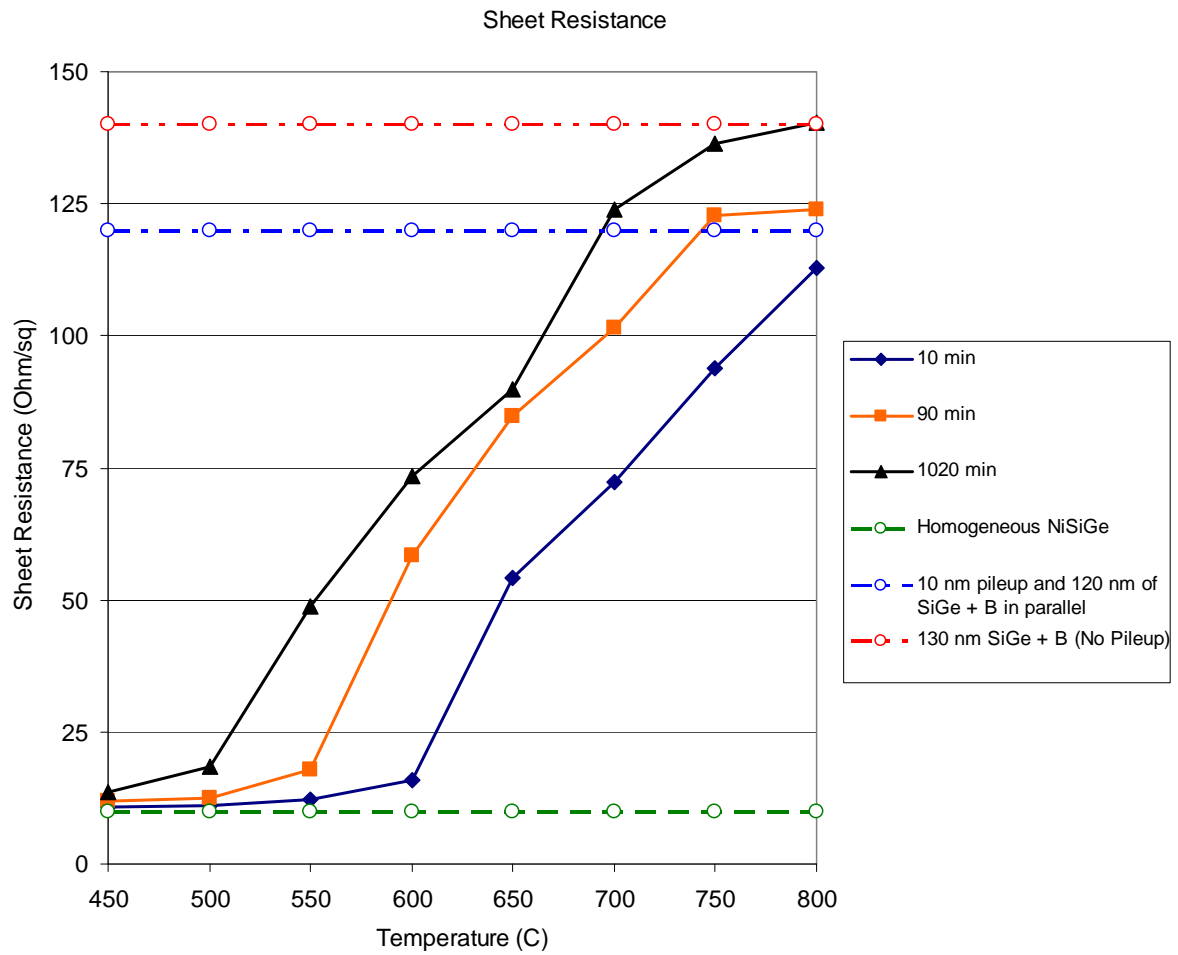


Figure 5-21: Isochronal anneal series of doped 15% Ge samples with calculated sheet resistance values for the potential alternative conduction paths.

Table 5-1: Linear regression results for best fit lines shown for Stage I (precipitation reaction) in Figure 5-9.

	Intercept	Standard Error Intercept	Slope	Standard Error Slope
15% Ge (Undoped)	7.788	3.178	1.173	0.190
25% Ge (Undoped)	5.274	4.889	0.954	0.137
15% Ge + B	8.395	1.278	0.676	0.077
25% Ge + B	10.459	2.632	0.495	0.071

Table 5-2: Stage I (precipitation reaction) linear regression results for the compiled undoped and doped data shown in Figure 5-11.

	Intercept	Std. Error Intercept	Slope	Std. Error Slope
Undoped	9.497	2.787	0.851	0.129
Doped	9.929	1.231	0.528	0.045

Table 5-3: Measurements of $\text{Si}_{1-z}\text{Ge}_z$ area fraction, tortuosity, and sheet resistance for selected undoped and doped 25% Ge samples.

	Temperature (C)	Time (min)	% AF $\text{Si}(1-z)\text{Ge}(z)$	Tortuosity	Sheet Resistance (Ohm/sq)
15% Ge (Undoped)	450	30	2.10	1.010	15.14
15% Ge (Undoped)	450	90	15.95	1.080	17.69
15% Ge (Undoped)	450	1020	48.50	1.150	39.85
15% Ge (Undoped)	500	30	21.33	1.070	20.35
15% Ge (Undoped)	500	90	34.73	1.100	28.39
25% Ge (Undoped)	450	90	19.60	1.083	15.79
25% Ge (Undoped)	450	1020	57.15	1.160	31.19
25% Ge (Undoped)	500	10	3.63	1.016	14.53
25% Ge (Undoped)	550	10	35.40	1.120	21.08
25% Ge (Undoped)	550	30	45.17	1.172	37.00

Table 5-4: Regression results for Stage II (agglomeration reaction) best fit lines shown in Figure 5-15.

	Intercept	Std. Error Intercept	Slope	Std. Error Slope
15% Ge + B	-211.27	34.78	4.28	0.51
25% Ge + B	-429.23	57.90	7.88	0.84

CHAPTER 6 CONCLUSIONS AND FUTURE WORK

The stated objective of this work was to clarify certain outstanding issues regarding the morphological stability and electronic properties of nickel germanosilicide thin films. The following sections discuss the results and conclusions determined by this work in the context of these outstanding issues. A discussion of potential future work which would complement the results of this work is also included.

6.1 Conclusions

Three major research objectives were addressed by the experimentation in this work. The three objectives included clarification and quantification of the structure/property relationship which published literature had proposed to exist between nickel germanosilicide film agglomeration and increases in film sheet resistance, further investigation of the influence of high levels of homogeneous B doping on the relationship, and expansion of the thermal matrix in which films were studied in order to gain information about the kinetics of the agglomeration process. The following sections discuss the findings of the experiments performed in this work in terms of these three objectives.

6.1.1 Microstructure and Kinetics

Prior studies available in literature have utilized isochronal experiments with very short annealing times (30 to 60 seconds). This work aimed to expand the knowledge of the behavior of nickel germanosilicide films over a much larger range of anneal times and temperatures, including both isochronal and isothermal series. Through analysis of samples annealed at temperatures ranging from 450 to 800 °C and times from 10 minutes to 1020 minutes, information about the kinetics of the phase transformation was obtained.

Results from the analysis of the annealed samples showed that the general cross-section and plan-view morphology of the nickel germanosilicide films in this work agreed well with those reported in prior literature. Also, while prior work has generally described the film evolution as “agglomeration,” two distinct reactions were captured by the anneal matrix used in this work. Initially, Ge-rich $\text{Si}_{1-z}\text{Ge}_z$ grains precipitated from the parent film as Ge was rejected (presumably to the grain boundaries). This process continued until the parent film had completely transformed in to Ge-rich $\text{Si}_{1-z}\text{Ge}_z$ and Si-rich $\text{Ni}(\text{Si}_{1-u}\text{Ge}_u)$ grains. Complete transformation corresponded to ~60% area fraction Ge-rich $\text{Si}_{1-z}\text{Ge}_z$ for all samples in this work. Once the transformation was complete, the Si-rich $\text{Ni}(\text{Si}_{1-u}\text{Ge}_u)$ grains then began to agglomerate. It was also shown that increasing Ge content in the initial $\text{Si}_{1-x}\text{Ge}_x$ film from 15 to 25% increased the amount of transformation observed for equivalent anneals, likely due to the increase in driving force for Ge rejection with increasing Ge content.

It was also determined that the reaction kinetics for both stages of the film transformation could be modeled using general Avrami isothermal transformation curves. Two separate reaction orders were observed, corresponding to the precipitation and agglomeration reactions. By analysis of the reaction order, the precipitation reaction was determined to be diffusion controlled growth with a zero nucleation rate. The agglomeration reaction was similarly determined to be diffusion controlled thickening of very large plates. The activation energies of the reactions were also able to be calculated and showed that for the precipitation reaction, E_a was 1.96 and 0.76 eV for the 15 and 25% Ge samples, respectively. For the agglomeration reaction, E_a was determined to be 0.14 and 0.10 eV, respectively (though statistically these values were found to be equal).

6.1.2 Structure/Property Relationship

Prior literature has proposed a qualitative link between the agglomeration of a nickel germanosilicide thin film and increases in the film's sheet resistance. The evidence in favor of the relationship, however, was circumstantial and no quantitative relationship had been established. Therefore, one objective this work was to clarify the relationship by determining if a direct, quantitative relationship could be established between a metric describing film agglomeration and sheet resistance. The influence of increasing Ge content was on the structure/property relationship was also studied.

The best metric for establishing a structure/property relationship between the film quality and its sheet resistance was determined to be the area fraction of Ge-rich $\text{Si}_{1-z}\text{Ge}_z$ present in the film. Use of this metric allowed a direct, quantitative relationship to be established in both the precipitation and agglomeration stages of the film transformation. For the precipitation stage of the transformation, the sheet resistance was found to increase linearly with increasing area fraction of $\text{Si}_{1-z}\text{Ge}_z$. Increasing Ge content in this stage of the reaction did not affect the relationship. It was determined, therefore, that the influence of increasing Ge on sheet resistance could be attributed solely to the increased agglomeration seen in these samples and not to a fundamental change in the structure/property relationship. Overall, the general increase in sheet resistance for all samples in this stage of the transformation was found to be attributable to the increasing tortuosity of the conduction path with increasing $\text{Si}_{1-z}\text{Ge}_z$ precipitation. For the agglomeration stage of the film transformation, the sheet resistance of the undoped samples was found to rapidly increase to large (or infinite) values unrelated to the amount of $\text{Si}_{1-z}\text{Ge}_z$ present and no quantitative structure/property was able to be established. The influence of Ge content was similarly unable to be determined. This effect was determined to be due to the absence of a continuous conduction path between isolated Si-rich $\text{Ni}(\text{Si}_{1-u}\text{Ge}_u)$ grains for these sample. The

doped samples, however, showed a linear trend of increasing sheet resistance with increasing area fraction $\text{Si}_{1-z}\text{Ge}_z$, though with a greater slope than seen in the precipitation stage of the reaction.

6.1.3 Influence of Homogeneous B Doping

Prior literature has proposed that high levels of homogeneous B doping in the initial $\text{Si}_{1-x}\text{Ge}_x$ layer can suppress the agglomeration process and thus stabilize sheet resistance. The prior work, however, did not utilize direct measurement techniques when evaluating film agglomeration and so the degree of suppression, if any, is not well quantified. Accordingly, this work aimed to confirm the presence of agglomeration suppression using plan-view SEM imaging. This work also aimed to determine if the quantitative relationship between agglomeration and sheet resistance was maintained for B doped samples.

Analysis of the samples in this work showed that the addition of $\sim 4.5\text{E}19$ atoms/cm² homogeneous B doping during $\text{Si}_{1-x}\text{Ge}_x$ layer growth did not affect the morphology of the nickel germanosilicide film microstructure for any anneal time or temperature. The doped samples, however, showed a decrease and stabilization of sheet resistance values for both the 15 and 25% Ge samples used in this work in accordance with prior literature. This effect was determined to be present in both the precipitation and agglomeration stages of the film transformation, though the magnitude of the effect was much larger in the latter stage. Overall, these results suggested that a mechanism other than a decrease in agglomeration, most likely an alternative conduction path in the B doped structures, was responsible for the effects. This path was also determined to most likely be the unreacted, nominally B doped $\text{Si}_{1-x}\text{Ge}_x$ layer below the nickel germanosilicide layer. This conclusion also suggested that differences in the sheet resistance of the $\text{Si}_{1-x}\text{Ge}_x$ layer with changing Ge content, though unconfirmed, caused the difference in structure/property relationship for the doped samples within the agglomeration stage of the transformation.

6.2 Future Work

While this work clarified many of the outstanding questions concerning the stability and behavior of nickel germanosilicide thin films, some questions were also raised by this work. Specifically, the cause for the increase of activation energy for the precipitation reaction with increasing Ge content is not known. Also, the existence of segregation induced dopant segregation was not directly observed for the samples in this work, nor was the distributions of the B dopant determined within the structure for each anneal time and temperature. These points could possibly be clarified by performing additional investigations of the nickel germanosilicide system using Local Electrode Atom Probe (LEAP) analysis.

LEAP analysis has been shown to be able to provide three dimensional maps of atomic distributions for semiconducting samples [Kel04,]. The technique has also been shown to be sensitive enough to investigate the lateral distribution of a gate structure implanted with B dopant [Moo08]. It is expected, therefore, that LEAP analysis of samples similar to those used in this work could provide information about B and Ge distributions in proximity to the grain boundaries of the germanosilicide grains. With such information, the mechanism by which Ge is rejected from the sample (i.e. via bulk or grain boundary diffusion) could possibly be clarified. The cause for the concentration dependence of the activation energy might, in turn, also be clarified. The B dopant distribution, specifically confirmation of whether silicidation induced dopant segregation is present, could definitely be determined through LEAP analysis. Information about the doping of the precipitated $\text{Si}_{1-z}\text{Ge}_z$ grains could also be determined through this type of analysis. This information would, in turn, allow confirmation of the alternative conduction path for the B doped samples.

Another area of potential future research would be the continued investigation of the relationship between area fraction of precipitated $\text{Si}_{1-z}\text{Ge}_z$, conduction path tortuosity, and

sample sheet resistance. The tortuosity investigations in this work were performed using manual measurement and calculations. It is expected, therefore, if computer software was used to measure tortuosity measurement error would decrease. The more rapid speed of software-based calculations would also allow both a larger number of samples at each anneal time and temperature to be studied as well as a larger overall number of anneal times and temperatures. Additionally, software aided analysis may allow the modeling of the conductive path for the doped samples in the agglomeration stage of the relationship to explain the linear dependence of sheet resistance on area fraction of $\text{Si}_{1-z}\text{Ge}_z$. Both of these analyses will require higher resolution, less noisy SEM images of the samples, as the graininess of the images (and the resulting difficulty of defining the grain edges) was the primary reason such analyses were not attempted in this work.

Performing these additional investigations would continue to develop the scientific knowledge of the behavior of nickel germanosilicide thin films. This knowledge, in turn, can then be used to address the use of such films as intermediate layers between semiconductor devices and metallization layers.

APPENDIX A ERROR IN SEM/BSE IMAGE QUANTIFICATION

SEM/BSE images in this work were mainly quantified using ImageJ software. To validate the repeatability of the SEM/BSE image quantification in this work, as well as explore the repeatability of the anneal process and regional sample variation, samples of the undoped, 15% Ge samples were annealed at 550 °C for 90 minutes on three separate occasions. Between each anneal, the furnace was set to another temperature and then re-set back to 550 °C. While it does not represent an exact center point in the experimental matrix, the data point (undoped, 15% Ge, 550 °C, 90 minute) selected for replication was chosen as it displays the most complex intermediate morphology with all three phases, Ni(Si_{1-x}Ge_x), Ni-rich Ni(Si_{1-u}Ge_u), and Ge-rich Si_{1-z}Ge_z, present in the image. It is expected, therefore, that the variation in this sample would be the highest in the experiment due to the difficulty in quantizing the complex microstructure. By applying the variation found at this data point to the entire matrix, a conservative estimate of variation would be included in the data analysis. Additional data points for replication were not chosen due to time and resource constraints.

Once annealed, each of the replicates was imaged at 30,000x magnification using SEM/BSE five times in two separate regions on each sample, for a grand total of 30 images. This nested design allowed both sample-to-sample and region-to-region comparisons to be made. The area fraction of Ni-rich Ni(Si_{1-u}Ge_u) and Ge-rich Si_{1-z}Ge_z phases present in each image was then quantified using ImageJ and the results analyzed with Minitab to determine the variation in the process.

Individual value plots of the area fraction values divided by sample and region are shown in Figure A-1 for both response variables. The plots indicate the qualitative presence of some variation, both between and within each sample. To determine if the apparent variation was

statistically significant, a fully nested ANOVA analysis was performed on the data for each response variable using sample and region as the predictive factors in the model. The ANOVA results, presented in Figure A-2, show that there is no statistically significant difference between samples for either response variable at a 95% confidence level (p-values of 0.335, 0.375). While no statistically significant difference is seen between regions for the area fraction of Ni-rich Ni(Si_{1-u}Ge_u) (p = 0.438) at the 95% confidence level, a significant difference is noted for the regional variation of Ge-rich Si_{1-z}Ge_z (p = 0.003). It is not known why regional variation is seen for one phase and not the other; however it is unsurprising that some local variations in phase quantity exist due to the relatively small sampling area contained by an image at 30,000x magnification. Nevertheless, this level of magnification is necessary to resolve the small grains involved in the phase transformation.

The maximum total variance in the nested ANOVA analysis was found to be 8.761. As three images were independently analyzed and their values averaged to determine the area fraction of each phase at each data point in the experiment, the variance of the averaged data is calculated according to Equation A-1:

$$Var(\bar{X}) = \frac{\sigma^2}{n} \quad \text{Equation A-1}$$

The variance for the averaged data was thus found to be 2.92, corresponding to a standard deviation of 1.71%. For a 95% confidence interval, this equates to a range of +/- 3.35%. This conservative estimate takes into account both sample-to-sample and local variations. Error from image processing and selection of contrast threshold for quantification analysis is also contained in this term. It should be noted, however, that experimental results suggest that actual error decreases with increasing area fraction and that this confidence interval results in very conservative error estimation at high area fraction contents (greater than ~ 60% AF).

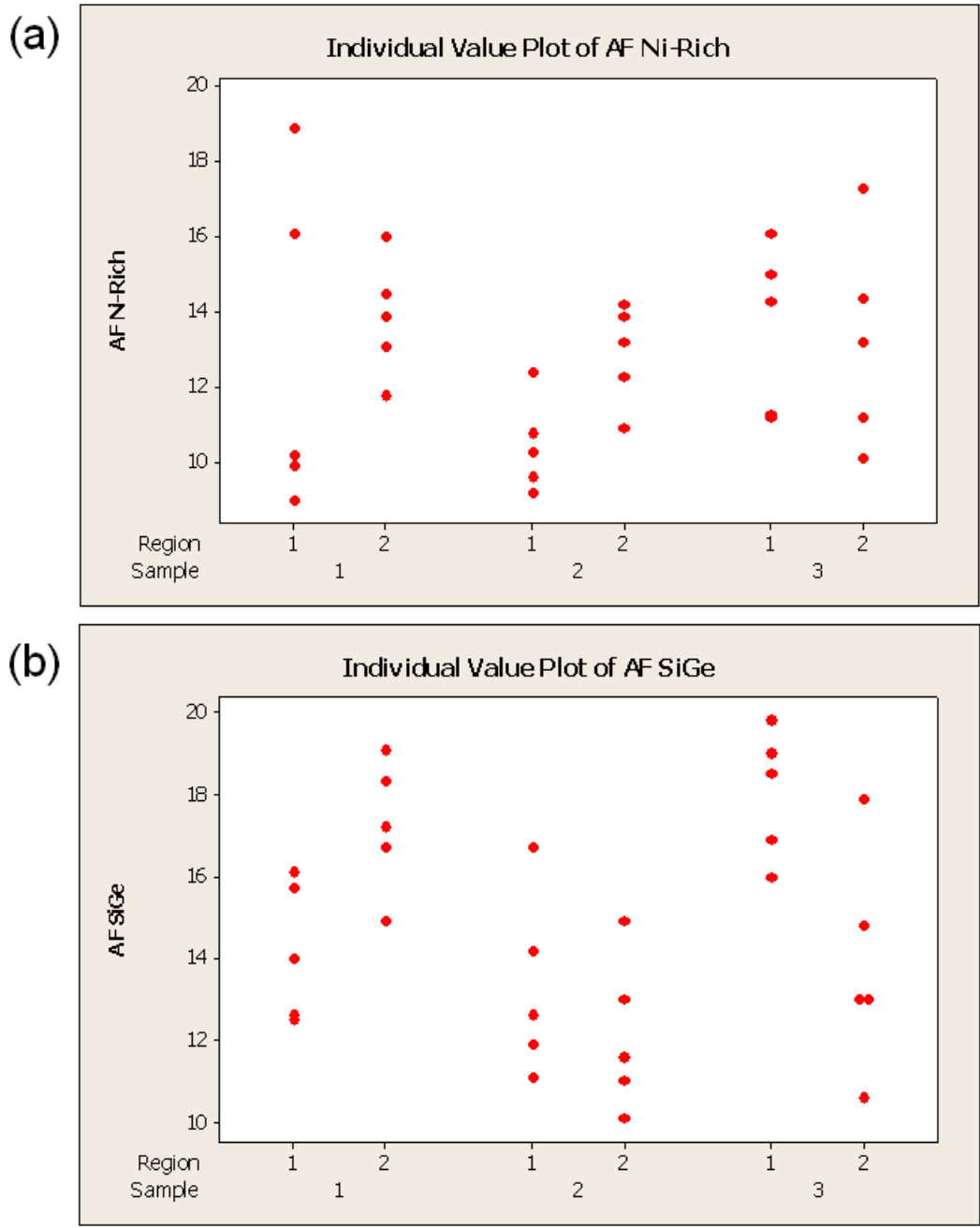


Figure A-1: Individual plot results divided by sample and region for (a) area fraction of Ni-rich phase and (b) area fraction of Ge-rich SiGe phase

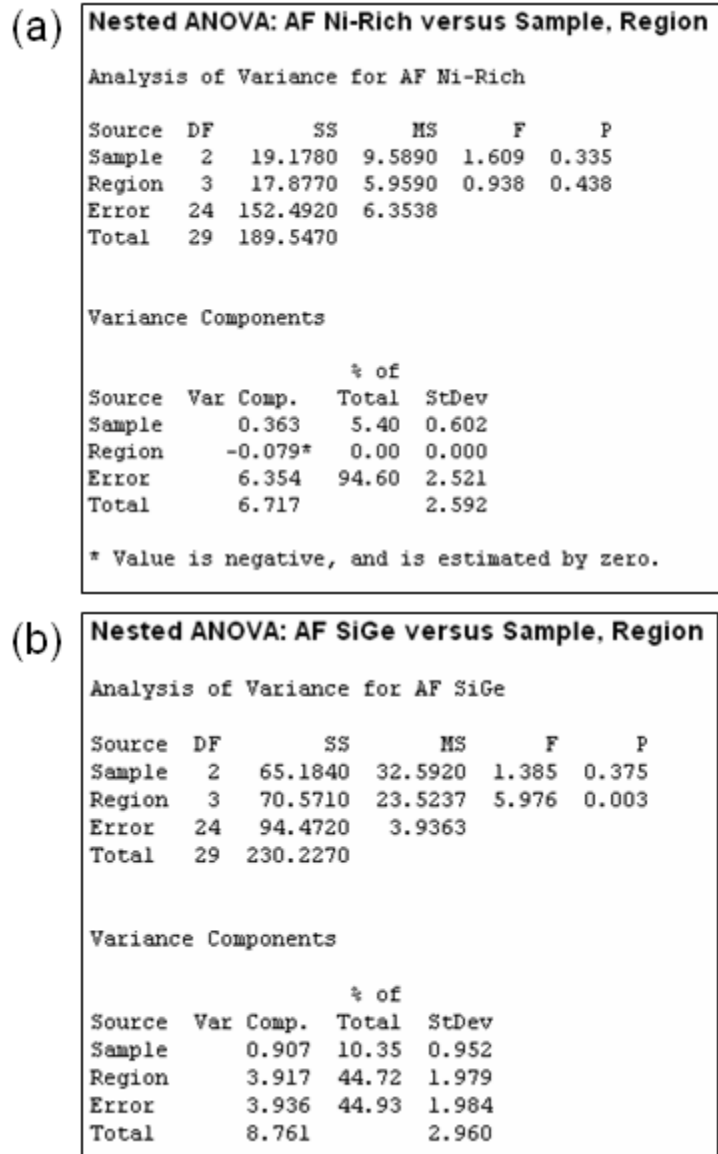


Figure A-2: Minitab results for fully nested ANOVA results for (a) area fraction of Ni-rich phase and (b) area fraction of Ge-rich SiGe phase

APPENDIX B GAUGE REPEATABILITY AND REPRODUCIBILITY ANALYSIS OF 4PP MEASUREMENT

A full gauge repeatability and reproducibility study (gauge R&R) was performed on the four point probe (4PP) sheet resistance measurement technique used in this work. For this study, 10 samples were selected at random from the full anneal matrix used in this work. Three operators then measured the sheet resistance of each sample in random order. This process was then repeated twice (with the order of the samples randomly re-arranged between each repetition) for a total of 3 repetitions and a grand total of 90 measurements.

Of the three operators, only one operator (the author of this work) was able to successfully measure every sample for each of the three repetitions. In total, only 5 of the 10 samples were successfully measured for all repetitions by all operators. For the five samples that were not completely successfully measured, some samples were successfully analyzed by an operator for none, one, or two repetitions. These results indicate problems with both the repeatability and reproducibility of the measurement process.

Data from the five samples that were completely successfully measured was analyzed using a Gauge R&R ANOVA package contained in the Minitab 15.1.1.0 software. The results, presented in Figure B-1, indicate very low contributions to the total study deviation by both measurement repeatability and reproducibility. These results are very interesting when taken in conjunction with the fact that many samples could not be successfully measured by some operators. Thus, it can be concluded that while an operator may have a difficult time obtaining a successful measurement of a sample, if a measurement is obtained it is of good quality.

While this finding is of general interest regarding the measurement process, all sheet resistance measurements presented in this work were taken by a single operator (the author). Hence, a deeper understanding of the repeatability of the measurement process by this operator is

of interest when analyzing the results in this work. Accordingly, a one-way ANOVA analysis was performed on the results from this operator. As this operator successfully obtained measurements for all samples in the study, data from all 10 samples was used in the analysis. The ANOVA results from this analysis, presented in Figure B-2, indicate that both repeatability and part-to-part variation contribute to the total overall variance in the study. It can also be observed in the results that one sample, number 9, has a sheet resistance several orders of magnitude higher than the other samples in the study. It is also apparent that the sheet resistance measurements of this sample varied over a considerable range (from ~2000 to ~6500 Ohm/sq). This observation suggests that measurement repeatability may suffer for samples with very high sheet resistances. To further explore this supposition, the data from sample 9 was eliminated from the study and the ANOVA analysis performed again. The results from the revised analysis are presented in Figure B-3 and show that the contribution of repeatability to the study variation has decreased to less than 5% of the overall value. It can be concluded, therefore, that the sheet resistance measurement process is repeatable for this operator (the author) for most samples. If a sample presents a very high sheet resistance value (on the order of thousands of Ohm/sq), however, it should be cautioned that significant variation in the results may be present. Nevertheless, most samples in this work have sheet resistance values below ~200 Ohm/sq. For these samples, based on the results from the revised ANOVA analysis of the first operator (the author of this work), a 95% confidence interval of +/- 2.19 Ohm/sq can be applied to capture any variation in the measurement process.

Two-Way ANOVA Table With Interaction

Source	DF	SS	MS	F	P
Part	4	11897.5	2974.37	26034.3	0.000
Operator	2	0.2	0.11	1.0	0.426
Part * Operator	8	0.9	0.11	1.2	0.335
Repeatability	30	2.9	0.10		
Total	44	11901.5			

Alpha to remove interaction term = 0.25

Two-Way ANOVA Table Without Interaction

Source	DF	SS	MS	F	P
Part	4	11897.5	2974.37	29891.2	0.000
Operator	2	0.2	0.11	1.1	0.346
Repeatability	38	3.8	0.10		
Total	44	11901.5			

Gage R&R

Source	Study Var	%Study Var
Total Gage R&R	0.3164	1.899
Repeatability	0.3154	1.893
Reproducibility	0.0248	0.149
Operator	0.0248	0.149
Part-To-Part	18.1790	109.074
Total Variation	18.1817	109.090

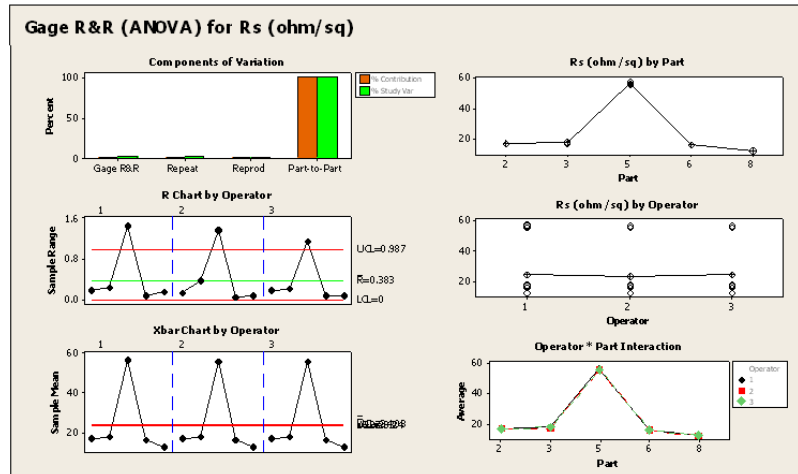


Figure B-1: Gauge R&R ANOVA analysis of sheet resistance measurements for the five samples which all operators measured successfully in all trials.

One-Way ANOVA Table

Source	DF	SS	MS	F	P
Part	9	37565140	4173904	6.38368	0.000
Repeatability	20	13076805	653840		
Total	29	50641945			

Alpha to remove interaction term = 0.25

Gage R&R

Source	VarComp	%Contribution (of VarComp)
Total Gage R&R	653840	35.78
Repeatability	653840	35.78
Part-To-Part	1173355	64.22
Total Variation	1827195	100.00

Source	Study Var	StdDev (SD)	(6 * SD)	%Study Var (%SV)
Total Gage R&R	808.60	4851.62	59.82	
Repeatability	808.60	4851.62	59.82	
Part-To-Part	1083.21	6499.29	80.13	
Total Variation	1351.74	8110.43	100.00	

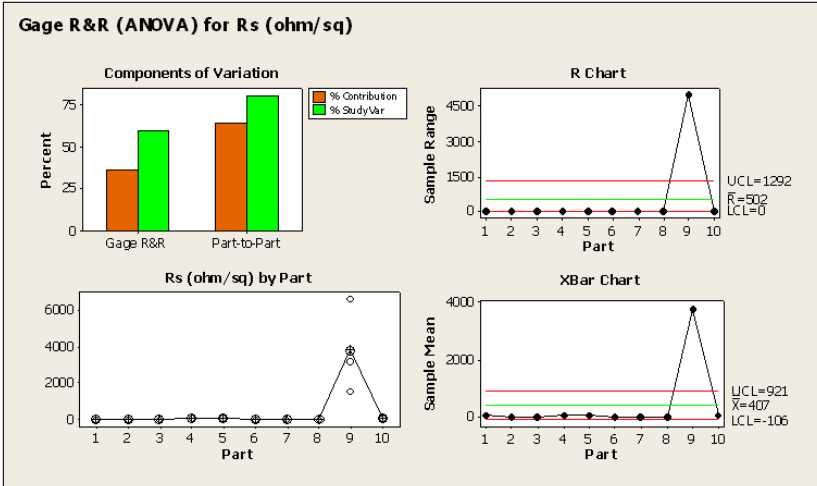


Figure B-2: Gauge R&R ANOVA analysis of sheet resistance measurements including data from all 10 samples for the operator (the author) who successfully measured all samples for all trials.

One-Way ANOVA Table

Source	DF	SS	MS	F	P
Part	8	13627.0	1703.38	1368.99	0.000
Repeatability	18	22.4	1.24		
Total	26	13649.4			

Alpha to remove interaction term = 0.25

Gage R&R

Source	VarComp	%Contribution
Total Gage R&R	1.244	0.22
Repeatability	1.244	0.22
Part-To-Part	567.378	99.78
Total Variation	568.622	100.00

Source	Study Var	StdDev (SD)	(6 * SD)	%Study Var
Total Gage R&R	1.1155	6.693	4.68	
Repeatability	1.1155	6.693	4.68	
Part-To-Part	23.8197	142.918	99.89	
Total Variation	23.8458	143.075	100.00	

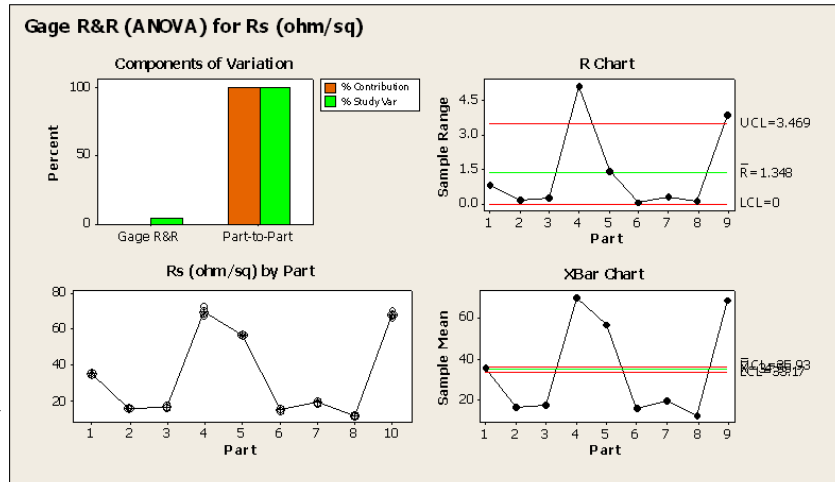


Figure B-3: Gauge R&R ANOVA analysis of sheet resistance measurements, excluding data from sample 9, for the operator (the author) who successfully measured all samples for all trials.

APPENDIX C AVRAMI PLOT ERROR

Generating error bars for a sigmoidal function plotted on a graph of $\log(\log((1-AF)^{-1}))$ vs. $\log(t)$ is complicated by the transformation mathematics. While it was determined in Appendix A that a constant error of $\pm 3.35\%$ should be used for a 95% confidence interval of area fraction in this work, the transformation of this interval for use on a $\log(\log((1-AF)^{-1}))$ vs. $\log(t)$ results in significantly varying error with the nominal (mean) value of area fraction. This complication is graphically shown in Figure C-1. In the figure, the resulting upper and lower confidence error bounds for the transformed interval are shown as a function of nominal area fraction. For small area fractions (less than $\sim 15\%$), the transformed error range is very large. For moderate area fractions (~ 15 to 85%), the error range is relatively small, and for large area fractions (greater than $\sim 85\%$), the error range again increases.

An example of the non-linear nature of transformed error on this type of plot is as follows. Consider a sample with 5% AF. For a 95% confidence interval in this work, the resulting range of AF lies between 1.65% and 8.35%. The resulting range on the transformed plot would therefore span between -2.28 and -1.39, a range of 0.88. For a sample with 50% AF, the linear range of 46.65% to 53.35% corresponds to a span of -0.57 to -0.47 on the transformed plot, a range of only 0.10.

Thus, a constant error range on a linear plot of area fraction vs. time can be shown to be much more difficult to handle after mathematical transformation for use with a plot of $\log(\log((1-AF)^{-1}))$ vs. $\log(t)$. For simplicity, this work therefore uses a constant error term of ± 0.15 for the data points that lie below 60% area fraction. For points with greater than 60% area fraction, a term of ± 0.045 was used. These values were selected according to their representation of the average error in their respective ranges (based on Figure C-1).

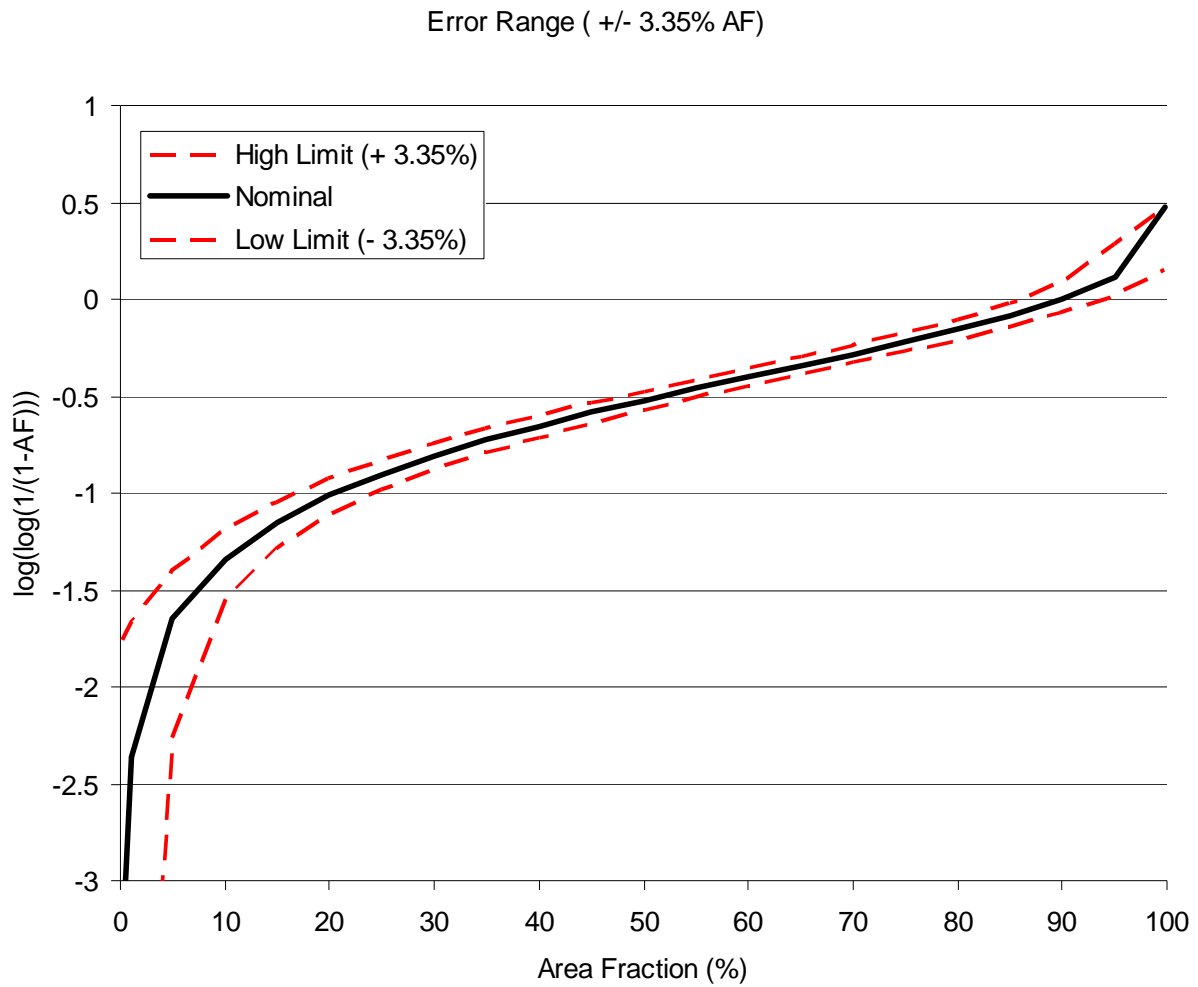


Figure C-1: Transformed error range for a constant +/- 3.35% range of area fraction as a function of nominal area fraction.

LIST OF REFERENCES

- [Aub05] V. Aubry-Fortuna, P. Dollfus, S. Galdin-Retailleau, *Solid-State Electron.* 49, 1320 (2005)
- [Avr39] M. Avrami, *J. Chem. Phys.* 7, 1103 (1939)
- [Avr40] M. Avrami, *J. Chem. Phys.* 8, 212 (1940)
- [Avr41] M. Avrami, *J. Chem. Phys.* 9, 177 (1941)
- [Bai04] P. Bai et al., *IEDM Tech. Dig.* 2004, 657 (2004)
- [Bar87] J.C. Barbour, A.E.M.J. Fischer, J.F. van der Veen, *J. Appl. Phys.* 62, 2582 (1987)
- [Cha04] O. Chamirian, A. Lauwers, J.A. Kittl, M. Van Dal, M. De Potter, R. Lindsay, K. Maex, *Mic. Eng.* 76, 297 (2004)
- [Cha04b] S. Chattopadhyay, L.D. Driscoll, K.S.K. Kwa, S.H. Olsen, A.G. O'Neill, *Solid State Electron.* 48 1407 (2004)
- [Che97] J. Chen, J.P. Colinge, D. Flandre, R. Gillon, J.P. Raskin, D. Vanhoenacker, *J. Electrochem. Soc.* 144(7), 2437 (1997)
- [Chi04] P.R. Chidambaram, B.A. Smith, L.H. Hall, H. Bu, S. Chakravarthi, Y. Kimm *VLSI Symp. Tech. Dig.* Honolulu, HI, 48 (2004)
- [Cho06a] Saurabh Chopra, Mehmet C. Ozturk, Veena Musra, Kris McGuire, Laurie E. McNeil, *App. Phy. Lett.* 88, 202114 (2006)
- [Cho06b] Saurabh Chopra, Mehmet C. Ozturk, Veena Musra, Kris McGuire, Laurie E. McNeil, *App. Phy. Lett.* 89, 202118 (2006)
- [Chr02] J.W. Christian, *The Theory of Transformations in Metals and Alloys, Part I*, Pergamon, Oxford (2002)
- [Cro03] R.T. Crosby et al., *Mat. Sci. in Semicond. Proc.* 6, 205 (2003)
- [dHe82] F. d'Heurle, C.S. Petersson, L. Stolt, B. Stritzker, *J. Appl. Phys.* 53, 5678 (1982)
- [dHe84] F.M. d'Heurle, C.S. Petersson, J.E.E. Baglin, S.J. LaPlaca, C. Wong, *J. Appl. Phys.* 55, 4208 (1984)
- [dHe89] F.M. d'Heurle, *J. Vac. Sci. Technol. A* 7, 1467 (1989)
- [dHe86] F.M. d'Heurle *P. Gas, J. Mater. Res.*, 1(1), 205 (1986)
- [Dis54] J.P. Dismukes, L. Ekstrom, R.J. Paff, *J. Phys. Chem.* 68(10), 3021 (1964)

- [Fin81] T.G. Finstad, *Phys. Status Solidi*. 63(a), 223 (1981)
- [Gam98] J.P. Gambino, E.G. Colgan, *Mat. Chem. Phys.* 52, 99 (1998)
- [Gan93] E. Ganin, S. Wind, P. Ronshei, A. Yapsir, K. Barmak, J. Bucchingnano, R. Assenz, *Rapid Thermal and Integrated Processing II*, Vol. 303, Materials Research Soc. Puttsburgh, PA, 109 (1993)
- [Gan00] S. Gannavaram, N. Pesovic, M.C. Ozturk, in: *Proceedings of the IEDM 2000*, p.347 (2000)
- [Gas98] P. Gas, F. d'Heurle, *Numerical Data and Functional relationships in Science and Technology Volume III*, Landolt-Bornstein, Berlin 33A (1998)
- [Ger04] P. Gergaud, C. Rivero, M. Gaillanou, O. Thomas, B. Froment, H. Jaouen, *Mater. Sci. Eng. B* 114-115, 67 (2004)
- [He05] J.H. He, W.W. Wu, L.J. Chen, *Nuc. Ins. Meth. Phys. Resch. B* 237, 174 (2005)
- [Hel97a] P.E. Hellberg, S.L. Zhang, C.S. Peterson, *IEEE Elec. Dev. Lett.* 18(9), 456 (1997)
- [Hel97b] P. E. Hellberg, A. Gagnor, S.L. Zhang, C.S. Peterson, *J. Electrochem. Soc.* 144, 3968 (1997)
- [Hsi88] Y.F. Hsieh, L.J. Chen, E.D. Marshall, S.S. Lau, *Thin Solid Films* 162, 287 (1988)
- [Hua95] F.Y. Huang, X. Zhu, M.O. Tanner, K.L. Wang, *Appl. Phys. Lett.* 67(4), 566 (1995)
- [Ish03] C. Isheden, J. Seger, H. Radamson, S.L. Zhang, M. Ostling, *Mater. Res. Soc. Symp. Proc.* 745, N4.9 (2003)
- [Iwa85] M. Iwami, A. Hiraki, *Jpn. J. Appl. Phys.* 24, 530 (1985)
- [Iwa02] Hiroshi Iwai, Tatsuya Ohguro, Shun-ichiro Ohmi, *Mic. Eng.* 60, 157, (2002)
- [Jar02] T. Jamar, J. Seger, F. Ericson, D. Mangelick, U. Smith, S.L. Zhang, *J. App. Phy.* 92(12), 7193 (2002)
- [Jia92a] H. Jiang, C.M. Osburn, Z.G. Xiao, D. Giffis, G. McGuire, G.A. Rozgonyi, *J. Electrochem. Soc.* 139, 196 (1992)
- [Jia92b] H. Jiang, C.M. Osburn, Z.G. Xiao, G. McGuire, G.A. Rozgonyi, B. Patniak, N. Parikh, M. Swanson, *J. Electrochem. Soc.* 139, 206 (1992)
- [Jia92c] H. Jiang, C.M. Osburn, Z.G. Xiao, G. McGuire, G.A. Rozgonyi, *J. Electrochem. Soc.* 139, 211 (1992)
- [Jin04] L.J. Jin, K.L. Pey, W.K. Choi, E.A. Fitzgerald, D.A. Antoniadis, A.J. Pitera, M.L. Lee, D.Z. Chi, C.H. Tung, *Thin Solid Films*, 462, 151 (2004)

- [Jin05] L.J. Jin, K.L. Pey, W.K. Choi, E.A. Fitzgerald, D.A. Antoniadis, A.J. Pitera, M.L. Lee, D.Z. Chi, Md. A. Rahman, T. Osipowicz, C.H. Tung, *J. Appl. Phys.* 98, 033520 (2005)
- [Kel04] T. Kelly et al., *Microsc. Microanal.* 10, 373 (2004)
- [Ko06] H. Ko, *J. Vac. Sci. Technol. A*, 24(4), 1468 (2006)
- [Kyk83] G.C. Kyker, Jr., *Am. J. Phys.* 51, 852 (1983)
- [Las91] J.B. Lasky, J.S. Nakos, O.J. Cain, P.J. Geiss, *IEDM Trans. Electron. Devices*, ED-3458, 262 (1991)
- [Lau06] A. Lauwers, M.J.H. van Dal, P. Verheyen, O. Chamirian, C. Demeurisse, S. Mertens, C. Vrancken, K. Verheyden, K. Funk, J.A. Kittl, *Mic. Eng.* 83, 2268 (2006)
- [Lav03] C. Lavoie, F.M. d'Heurle, C. Detavernier, C. Cabral, *Micro. Eng.* 70, 144 (2003)
- [Lee05] S.G. Lee et al. *Mater. Sci. Semicond. Process.* 8, 215 (2005)
- [Li89] J. Li, Q.Z. Hong, J.W. Mayer, *J. Appl. Phys.* 67, 2506 (1989)
- [Liu05] Jung Liu, Mehmet C. Ozturk, *IEEE Trans. Ele. Dev.* 52(7), 1535 (2005)
- [Mae93] K. Maex, *Mater. Sci. Eng. Rev.* R11, 53 (1993)
- [Man98] D. Mangelick, P.E. Hellberg, S.L. Zhang, F.M. d'Heurle, *J. Electrochem. Soc.* 145, 2530 (1998)
- [Mas90] T.B. Massalski, *Binary Alloy Phase Diagrams*, ASM International, Materials Park, OH (1990)
- [Mas05] W.P. Maszara, *J. Electrochem. Soc.* 152 (7), G550 (2005)
- [Mat74] J.W. Matthreus and A.E. Blakeslee, *J. Cryst. Growth*, 29, 273 (1974)
- [Mei04] D.L. Mei, J.C. Li, J. Zhang, W.J. Xu, K.Z. Tan, M.H. Yang, *Microelectron. J.* 35, 969 (2004)
- [Moo08] J.S. Moore et al., *Ultramicroscopy*, 108(6), 536 (2008)
- [Mor84] Cpt. Morgan, Diageo, (1984)
- [Nat04] R. Nath, M. Yeadon, *Electrochem. Solid-State Lett.* 7(10), G231 (2004)
- [Nem06] F. Nemouchi, D. Mangelinck, J.L. Labar, M. Putero, C. Bergman, *P. Gas, Mic. Eng.* 83, 2101 (2006)
- [NTR97] 1997 National Technology Roadmap for Semiconductors, Semiconductor Industry Association, San Jose, CA (1997)

- [Nyg91] S. Nygren, D. Caffin, M. Ostling, F.M. d'Heurle, *App. Surf. Sci.* 53, 87 (1991)
- [Ok03] Young-Woo Ok, S.H. Kim, Y.J. Song, K.H. Shim, Tae-Yeon Seong, *Sem. Sci. Tech.* 19, 285 (2003)
- [Ok04] Young-Woo Ok, S.H. Kim, Y.J. Song, K.H. Shim, Tae-Yeon Seong, *J. Vac. Sci. Technol. B* 22(3), 1088 (2004)
- [Pat94] J. Ken Patterson, B.J. Park, K. Ritley, H.Z. Xiao, L.H. Allen, A. Rockett, *Thin Solid Films* 253, 456 (1994)
- [Pea86] T.P. Pearsall, J.C. Bean, *IEEE Electron. Device Lett.* EDL-7, 308 (1986)
- [Peo85] R. People and J.C. Bean, *Appl. Phys. Lett.* 47, 322 (1985)
- [Pey02] K.L. Pei, W.K. Choi, S. Chattopadhyay, H.B. Zhao, E.A. Fitzgerald, D.A. Antoniadis, P.S. Lee, *J. Vac. Sci. Technol. A* 20(6) 1903 (2002)
- [Pey04] K.L. Pey, S. Chattopadhyay, W.K. Choi, Y. Miron, E.A. Fitzgerald, D.A. Antoniadis, T. Osipowicz, *J. Vac. Sci. Technol. B* 22(2) 853 (2004)
- [Pon00] Youri V. Ponomarev, Peter A. Stolk, Cora Salm, *IEEE Trans. Elect. Dev.* 47(4) 848 (2000)
- [Raa99] Ivo J. Raaijmakers, Hessel Sprey, Arjen Storm, Timo Bergman, Joe Italiano, Doug Meyer, *J. Vac. Sci. Technol. B* 17(5) 2311 (1999)
- [Rad06] L. Radic, PhD Dissertation for the University of Florida (2006)
- [Sal97] C. Salm, D.T. van Veen, D.J. Gravesteijn, J. Holleman, P.H. Woerlee, *J. Electrochem. Soc.* 144, 3665 (1997)
- [Seg02] J. Seger, S.L. Zhang, D. Mangelick, H.H. Radamson, *Appl. Phys. Lett.* 81(11), 1978 (2002)
- [Seg03] J. Seger, S.L. Zhang, *Thin Solid Films* 429, 216 (2003)
- [Seg04] J. Seger, T. Jarmar, Z.B. Zhang, H.H. Radamson, F. Ericson, U. Smith, S.L. Zhang, *J. App. Phy.* 96(4), 1919 (2004)
- [Tak00] Hirotsugu Takizawa, Kyota Uheda, Tadashi Endo, *J. All. Com* 305, 306 (2000)
- [Ter89] J. Tersoff, *Phys. Rev. B* 39, 5566 (1989)
- [Tho88] R.D. Thompson, K.N. Tu, J. Angillelo, S. Delage, S.S. Iyer, *J. Electrochem. Soc.* 135, 3161 (1988)
- [Tho02] S. Thompson et al. *IEDM Tech. Dig.* 2002, 61 (2002)

- [Tho04] S.E. Thompson, G. Sun, K. Wu, J. Lim, T. Nishida, IEDM Tech. Dig. 2004, 221 (2004)
- [Tol04] N. Toledo, P. Leeb, K. Pey, Thin Solid Films, 462-463, 202 (2004)
- [Uch06] K. Uchida, T. Krishnamohan, K.C. Saraswat, Y. Nishi, IEDM Tech. Dig. 2006: San Francisco, CA (2006)
- [Ver94] Sopia Verdonckt-Vandebroek, Emmanuel F. Crabbe, Bernard S. Meyerson, David L. Hareme, Phillip J. Restle, Johannes M.C. Stork, Jeffrey B. Johnson, IEEE Trans. Elect. Dec. 41(1) 90 (1994)
- [Wan95] Zhihai Wang, D.B. Aldrich, Y.L. Chen, D.E. Sayers, R.J. Nemanich, Thin Solid Films, 270, 555 (1995)
- [Web05] J. Weber, L. Nebrick, F. Bensch, K. Neumeier, G. Vogg, R. Wileland, D. Bonfert, P. Ramm, Microelectron. Eng. 82, 215 (2005)
- [Won04] L.H. Wong et al. Thin Solid Films 462-463, 76 (2004)
- [Yao07] H.B. Yao, M. Bouville, D.Z. Chi, H.P. Sun, X.Q. Pan, D.J. Srolovitz, D. Mangelinck, Electrochem. Solid State Lett. 10(2) H53 (2007)
- [Zan01] N.R. Zangenberg et al. Phys. Rev. Lett. 87(12), 125901 (2001)
- [Zha02] H.B. Zhao, K.L. Pey, W.K. Choi, S. Chattopadhyay, E.A. Fitzgerald, D.A. Antoniadis, P.S. Lee, J. Appl. Phys. 92(1) 214 (2002)
- [Zha03] S.L. Zhang, Mic. Eng. 70, 174 (2003)
- [Zha04] Q.T. Zhao, D. Buca, St. Lenk, R. Loo, M. Caymax, S. Mantl, Mic. Eng. 76, 285 (2004)
- [Zha05] Qingchun Zhang, Nan Wu, Thomas Osipowicz, Lakshmi Kanta Bera, Chunxianh Zhu, Jap. J. of Appl. Phys., 44(45), 1389, (2005)

BIOGRAPHICAL SKETCH

John Samuel Moore, who publishes as J.S. Moore, received his B.S. cum laude from the University of Florida in 2004, with a major in materials science and engineering (metals specialty) and a minor in business administration. After entering graduate school at UF, he received his M.S. in materials science and engineering in 2006 and continued with doctoral studies. He graduated with a Ph.D. in 2008 in materials science and engineering (electronic materials specialty) and a minor in industrial engineering. During his years at the University of Florida, he was active in both engineering and student government societies including terms as the President of the Society of Automotive Engineers (Spring 2002 to Spring 2003) and Treasurer of the Benton Engineering Council (2004-2005).